



**HAL**  
open science

# Microwave experiments on atypical transport phenomena induced by spatial and spectral wave shaping

Julian Böhm

► **To cite this version:**

Julian Böhm. Microwave experiments on atypical transport phenomena induced by spatial and spectral wave shaping. Other [cond-mat.other]. COMUE Université Côte d'Azur (2015 - 2019), 2016. English. NNT: 2016AZUR4048 . tel-01437569

**HAL Id: tel-01437569**

**<https://theses.hal.science/tel-01437569>**

Submitted on 17 Jan 2017

**HAL** is a multi-disciplinary open access archive for the deposit and dissemination of scientific research documents, whether they are published or not. The documents may come from teaching and research institutions in France or abroad, or from public or private research centers.

L'archive ouverte pluridisciplinaire **HAL**, est destinée au dépôt et à la diffusion de documents scientifiques de niveau recherche, publiés ou non, émanant des établissements d'enseignement et de recherche français ou étrangers, des laboratoires publics ou privés.

**UNIVERSITÉ NICE SOPHIA ANTIPOLIS** - UFR Sciences  
École Doctorale de Sciences Fondamentales et Appliquées (ED n°364)

## **THÈSE**

pour obtenir le titre de  
**Docteur en Sciences**  
de l'UNIVERSITÉ Nice Sophia Antipolis

Spécialité : **Physique**

présentée et soutenue par

**Julian BÖHM**

**Phénomènes de transport originaux  
dans des expériences micro-ondes  
via la mise en forme spatiale et spectrale**

---

**Microwave experiments  
on atypical transport phenomena  
induced by spatial and spectral wave shaping**

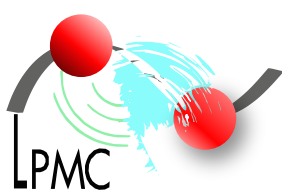
Thèse dirigée par Ulrich KUHL

Soutenue le 15 septembre 2016

à 13h30 au Laboratoire de Physique de la Matière Condensée

Jury :

M. Steven ANLAGE	-	Professeur, University of Maryland
M. Geoffroy LEROSEY	-	Chargé de recherche CNRS, Institut Langevin
M. Eric AKKERMAN	-	Professeur, Israel Institute of Technology (Technion)
M. Philippe BESNIER	-	Directeur de recherche CNRS, INSA (Rennes)
M. Sylvain GIGAN	-	Professeur, Université Pierre et Marie CURIE
M. Ulrich KUHL	-	Professeur, Université Nice Sophia Antipolis



Thèse préparée au  
**Laboratoire de Physique de la Matière Condensée**  
CNRS UMR 7336  
Université Nice-Sophia Antipolis  
Parc Valrose  
06108 Nice CEDEX 2

*”What I cannot create,  
I do not understand.”*  
- Richard Feynman

# Acknowledgements

---

I would like to express my gratitude to "L'Agence Nationale de la Recherche" (ANR) which laid the financial basis for the work presented in this thesis.

During the three years of my PhD I have gotten in contact with so many people, who helped me in so many ways to finally successfully finish my PhD. In case someone, who feels to have contributed, is not mentioned explicitly in the following, I want to apologise to him or her.

Firstly, I would like to thank my jury for investing their time in reading and reflecting on the manuscript. I very much appreciated their open questions and their interest in my work. I thank **Philippe Besnier** for being the president of my jury, **Steven Anlage** and **Geoffroy Lerosey** for being my rapporteurs and for their detailed opinion on my manuscript and finally **Eric Akkerman** and **Sylvain Gigan** for judging my work during the PhD-defence.

I have to pay tribute to my supervisor **Ulrich Kuhl** for being my guide throughout my whole PhD. I am glad that he gave me the chance to follow my own ways in doing things and to make my own experiences. His criticism on my work really helped me improving not only my own understanding of the subject but also the way I can present it to others. Also **Fabrice Mortessagne**, the director of the lab, has been an important adviser. His mind is working incredibly fast. He does not only recognize problems or difficulties at an early stage, he also comes up with an elegant solution.

The last two mentioned persons are just one part of our research team (*Groupe: "Physique Mésoscopique"*). I am happy that I had the chance to work together with **Mathieu Bellec**, **Claire Michel**, **Jean-Baptiste Gros**, **Valérie Doya**, **Khalid Oubaha**, **Olivier Legrand** and **Martin Richter**. The discussions with them and their suggestions helped me to overcome the situations in which my work seemed stuck. Also the common time we shared attending several conferences was very pleasant (food and drink tastings).

I have also to thank the guys from the workshop (= Les mecs de l'atelier: **Frédéric Lippi**, **Jean-Luc Vanni** and **Christophe Pitiot**) and our electronic expert **Grégory Sauder**. Without them I would be quite clueless how to realise my experimental set-ups.

This was the technical part. As I entered a foreign country to obtain my PhD-diploma, there was also a lot of bureaucracy I had to deal with. Since I spoke no french at all at the beginning of my PhD, I was totally lost. Countless times I visited the offices of "*les filles*" to look for help. **Nathalie Koulechhoff** alias '*Tata*' was

very patient with me and explained me everything a hundred times (french tax system, social security etc.). Also the other secretaries (**Christine Chassagneux**, **Madalena Neri-Martinez**, **Denise Siedler** and **Christine Boudard-Morteau**) helped me as best as they could by inviting me for their dinner parties for example.

The lunch/IT-gang **Bernard Gay-Para** and **Jérôme Mauro** were always ready to cheer me up with some uplifting jokes and when at lunchtime the "jamjam-jam" sound in the corridors appeared they joined our lunch crew (members: **Yann Bouret**, **Pascal Baldi**, **Nathalie Fraysse**, **Stanislaw Trzesien** and **Michèle Ude**) and together we went to the cafeteria of the french tax office (thank you french administration for letting me eat there).

I am very grateful to **Christophe Raufaste**, who offered me not only a place to stay for the first months of my PhD but he also supported me whenever all these "living in France problems" seemed overwhelmingly huge (Sometimes France can smack you). I guess without him there would have been a moment for me to quit and to call off this PhD-project.

The first people who introduce you to the PhD world are of course your office mates and of course your office mates are just the best ones. The same applies to me and my office mates. I was very lucky, because I never had to leave my office. So it is time to thank my friends and office mates **Mathieu**, **El Bang**, **Khalid**, **Florent** alias "**Le petit**", **Sissi** alias "*Don't touch my desk*", **Chiara** and **Martina** my cheerful coffee partners who had always an open ear to lend.

I came here as a stranger but I will leave with many stories to tell from my welcoming PhD-colleagues, who made my stay a wonderful adventure. So my thanks goes to: **Manu**, **Jeff** and **the JB-brothers** for the "gaming nights", **Amanchine**, **Panos**, **Djeylan**, **Bruno** for the nice weekends and especially for those evenings which finished in *Pompei*.

Finally I have to thank my family and to apologise to them at the same time, because there were a lot's of events I missed. Thank you for your constant support and your trust in me.

# Table of Contents

---

<b>General Introduction and Executive Summary</b>	<b>3</b>
<b>Introduction générale</b>	<b>9</b>
<b>1 Introduction to Transport with Microwaves</b>	<b>15</b>
1.1 Electromagnetic Systems . . . . .	16
1.2 Scattering Matrix . . . . .	18
1.3 Green Function and the Scattering Matrix . . . . .	20
<b>2 Quantum Search</b>	<b>23</b>
2.1 A Tight Binding Analogue . . . . .	24
2.1.1 <i>Microwave Set-up</i> . . . . .	24
2.1.2 <i>Dielectric Resonators</i> . . . . .	25
2.2 Quantum Search and its Experimental Implementation . . . . .	28
2.2.1 <i>Theoretical Basis</i> . . . . .	28
2.2.2 <i>Quantum Search on a Linear Chain</i> . . . . .	31
2.2.3 <i>The Honeycomb Lattice</i> . . . . .	36
2.2.4 <i>Graphene</i> . . . . .	40
2.2.5 <i>Quantum Search on the Graphene-lattice</i> . . . . .	42
2.3 Conclusion . . . . .	45
<b>3 The <math>Q</math>-Operator</b>	<b>47</b>
3.1 Wigner-Smith Time Delay Operator . . . . .	48
3.2 The Derivation of the $Q$ -Operator . . . . .	49
3.3 Eigenvalues of the $Q$ -Operator . . . . .	50
3.4 Construction of the $Q$ -Operator - A Practical Approach . . . . .	52
<b>4 Wave Front Shaping</b>	<b>55</b>
4.1 The Basic Idea . . . . .	56
4.2 Quasi-One-Dimensional Waveguide . . . . .	57
4.2.1 <i>Experimental Realisation</i> . . . . .	57
4.2.2 <i>Theoretical Description</i> . . . . .	59
4.2.3 <i>The Empty Waveguide</i> . . . . .	63
4.2.4 <i>IQ-Modulators</i> . . . . .	70
4.2.5 <i>Waveguide Filled with Scatterers</i> . . . . .	72
4.2.6 <i>Mode Tuning</i> . . . . .	73
4.3 Realising $Q$ -States . . . . .	76
4.3.1 <i>Transmission Matrix in a Scattering Environment</i> . . . . .	76
4.3.2 <i>Generating <math>Q</math>-States</i> . . . . .	77
4.3.3 <i>Experimental Realisation of <math>Q</math>-States</i> . . . . .	79
4.3.4 <i>A Coherent Perfect Absorber</i> . . . . .	83
4.4 Conclusion . . . . .	86

## Table of Contents

---

<b>5</b>	<b>Dynamical Encircling of an Exceptional Point</b>	<b>87</b>
5.1	Exceptional Points and their Experimental Realisation . . . . .	88
5.2	Dynamical Encircling with a Waveguide . . . . .	92
5.2.1	<i>Bloch Modes</i> . . . . .	92
5.2.2	<i>Using Perturbation Theory</i> . . . . .	94
5.3	Experimental Realisation in a Waveguide . . . . .	96
5.4	Microwave Set-up . . . . .	100
5.5	The Dynamical Encircling - Experimental Results . . . . .	102
5.6	Parametric Encircling . . . . .	105
5.7	Conclusion . . . . .	110
<b>6</b>	<b>Particle-like Scattering States</b>	<b>111</b>
6.1	Theoretical Background and Motivation . . . . .	112
6.1.1	<i>Group Delay and Dwell Time</i> . . . . .	112
6.1.2	<i>Particle-like Scattering States</i> . . . . .	115
6.2	Microwave Set-up . . . . .	118
6.3	Experimental Findings . . . . .	120
6.3.1	<i>Determining the <math>Q</math>-operator</i> . . . . .	120
6.3.2	<i>Generating Particle-like Scattering State 1</i> . . . . .	124
6.3.3	<i>Other Particle-like Scattering States</i> . . . . .	126
6.3.4	<i>Perturbation of Particle-like Scattering States</i> . . . . .	128
6.4	Conclusion . . . . .	131
	<b>General Summary</b>	<b>133</b>
	<b>Conclusion</b>	<b>135</b>
	<b>A The Central Eigenstate for a Resonator Chain</b>	<b>139</b>
	<b>Bibliography</b>	<b>141</b>
	<b>Abstract</b>	<b>153</b>





# *General Introduction and Executive Summary*

---

Wave transport is all around us. When you switch on your portable phone and it starts communicating with the basis antennas, when you are walking around in your flat to find the best place to establish a stable Wi-Fi-connection or when you are in the middle of a concert and sound speakers amplify the singer's voice.

All these wave based communication systems face more or less the same issues. How can one make these systems more efficient in terms of energy consumption and more secure in the case of Wi-Fi or mobile networks? Can we find a way to filter the transmitted signal so that we get only those components in which we are really interested?

Normally these communication systems such as the ones described above consist of three parts. An emitter (speakers, antennas, lasers, etc.) from where the wave signal is sent, a transporting medium (air, dielectrics, optical fibres, etc.) in which the wave can propagate so that it reaches the final part which is the receiver (ear, mobile phone, photo diode, etc.). A standard procedure to improve such systems is to try to improve one of these three components. One could develop, for example, new lasers needing less power to generate a cleaner and more powerful output or new optical materials featuring less loss. This is not what I am going to do in this work. I will not try to improve single components.

My aim is to find solutions for the mentioned issues using already available state of the art microwave technology. In principle all the mentioned wave based communication systems are in many ways similar, meaning that this restriction to microwaves is not a real one. The underlying physical principles of these different wave systems are very strongly related. One main difference is that they work on different scales. Optics is typically working on a nm-scale, whereas microwaves operate on a cm-scale. Thus, studying transport phenomena (or wave based communication) with microwaves is yet a clever approach. As already mentioned microwave systems feature cm-scaling. This scale is easily accessible by humans as we are capable of modifying objects within a precision of mm or  $\mu\text{m}$ , which takes us much less effort than manipulating things on nm-scale or a m-scale. This means that we can easily achieve a sub-wavelength precision giving us a very good control over the systems we are looking at.

The question remains: how do we address the raised issues of security and efficiency? The idea we have to answer this question is by shaping the emission of the signal on the emitter side in such a way that the transport of the wave through

the system follows an atypical behaviour. This is to say a behaviour like following the path of a classical particle, avoiding pre-selected regions or focussing on chosen spots. To do that one needs to deduce certain properties from the transporting medium first before being able to shape the emission in the right way. In this case we like to restrict ourselves exclusively to the investigation of the information we can obtain directly at the points where the signal is emitted and received. It is evident that if one wants to shape the emitted signal one needs certain controllable degrees of freedom, i.e., parameters which allow us to tune the emitted signal. These parameters can be represented on the one hand by multiple frequencies which are mixed together and sent from a single antenna (spectral wave shaping). On the other hand one can use multiple input antennas at a fixed frequency (spatial wave shaping), where one tunes each antenna signal individually. Having the possibility to introduce multiple sources is one thing. The other more important thing is to have the necessary control about each source and with control I refer here to the control of the amplitude, the phase and the frequency of the emitted signal. Such devices which offer such control are nowadays commercially available. For example, you can find them in optics as spatial light modulators (SLM, narrowband) or as IQ-modulator for microwaves (broadband).

We demonstrate that measuring the transport between a single/multiple input antenna/s and the output as a function of a parameter (frequency, position change of one obstacle/receiver) contains the necessary information to address the mentioned issues. More information about the scattering medium is not necessary. We do not need to know where obstacles are positioned, for example. We show that once we have done this basis measurement we are able to avoid certain regions, i.e., we can avoid possible intruders into our system which makes the communication more secure. We can even focus a signal onto a certain spot/receiver so we do not have to waste energy by sending a transmission signal in every possible direction in order to look out for possible receivers. With this we addressed two of the three mentioned points above; security and efficiency. The chapters in which we work on this idea are chapters 4, 5, 6 and 8.

The approach to build an effective filter follows a slightly different idea. To realise this we make use of the phenomena which arises when one approaches a so called exceptional point during the transport through the system. The shaping of the wave in this case is done by spatial modification of the scattering system itself, i.e., we have to shape the wave by manipulating the boundaries and the inside of the scattering system. This special shaped waveguide still consists of standard material (aluminium plus absorbing microwave material) but it will feature an effective filtering property. It is effective in the sense that it does not simply suppress the unwanted component. Instead it transforms the unwanted component into the favoured one (we are working with two components in the system). This other form of wave shaping is discussed in chapter 7.

---

## Chapter 3: Introduction to Transport with Microwaves

In this chapter I lay down basic fundamentals to understand our microwave experiments. I introduce the two types of experiments which are studied throughout this thesis: Rectangular waveguides and open cavities. Once we have understood how the electromagnetic field behaves in such a system and how it can be described with the help of the Helmholtz equation, I relate this propagation of waves to a scattering problem described by a scattering matrix  $S$ . I lay down the connection between  $S$  and the Green function of the system which incorporates the solution of the Helmholtz equation. I present the fact that performing a measurement can be seen as an opening of the system so that the observed solution is modified from the solution one would obtain if the system was fully closed.

## Chapter 4: Quantum Search

I apply the method of spectral wave shaping in order to focus a signal onto a specific target. Focusing energy onto a certain point with an unknown position can be understood as a search. The word 'quantum' comes into play as such searches are performed in systems like the tight-binding one [Wal47, Sla54] which is known from solid state physics. As this is the original name for this kind of search [Gro97, Amb04, Por13] it is used throughout this work although the underlying mechanism is a pure wave phenomenon [Gro02].

First I discuss in detail how the used open microwave cavity containing dielectric resonators is able to mimic a tight-binding system [Bar13, Bel13a, Bel13b, Bel14, Pol15, Vig16]. Then I give a brief introduction to quantum search with the focus on two dimensional continuous quantum search [Chi04, Hei09, Fou14]. I derive the necessity to perform the quantum search on graphene-like lattices (as it features a Dirac point [Cas09]). Performing the search on this kind of lattices makes the search significantly faster (search time  $\propto \mathcal{O}(\sqrt{N \ln N})$  [Fou14]) than the classical search (search time  $\propto N$ ).

We start our experimental observation with a linear chain of resonators and an additional search resonator studying the search time as a function of the number of used resonators. We demonstrate how a search for different sites can be realised using the chain arrangement of discs and two different search sites. Then we deepen the insights on graphene-lattices and implement a quantum search on this kind of lattices where we perform the search to identify two different items [Böh15].

## Chapter 5: The Q-Operator

To understand how the delay time of scattering states is encoded in the systems scattering matrix one has to look at the Wigner-Smith time delay matrix/operator

[Eis48, Boh51, Wig55, Smi60]. We modify this operator by replacing the scattering matrix  $S$  by the transmission matrix  $T$  and replacing energy by an arbitrary variable  $\alpha$ . This modified operator is called  $q$ -operator [Amb12, Bra16, Gir16].

We see in an alternative derivation why the  $q$ -operator has its specific form. Furthermore we look at the way to calculate its eigenvalues and we discuss their physical interpretation. The eigenvectors of the  $q$ -operator allow us then to define our input so that we can create scattering states which avoid or focus on regions or which form highly collimated beams on classical trajectories, so called particle-like scattering states.

## Chapter 6: Wave Front Shaping

The basic idea behind wave front shaping is to manipulate the input in such a way that the desired output features are significantly improved. This output tuning can be done by iteratively changing the input and observing the output as it is, for example, done in optics [Vel07, Mos12, His13, Nix13, Cha14, Ami16], in the microwave field [Kai14, Dup15] or in biomedicine [Hor15]. Using this kind of output optimization people could achieve very interesting results, such as focusing light through opaque media [Vel07, Vel08], transmitting images through opaque media [Pop10] or focusing/defocusing microwaves in cavities [Kai14, Dup15].

Our set-up is a rectangular microwave waveguide excited by an array of 10 antennas where each antenna can be addressed with an individual amplitude and phase using IQ-modulators. We characterise the used IQ-modulators performing test measurements. We start performing wave front shaping experiments by tuning specific sinusoidal modes at the output of the empty waveguide. In a second step we introduce scatterers and redo the mode tuning at the output verifying the functionality of our set-up [Böh16].

Since all these tests are successful, we move on and set up the  $q$ -operator where the parameter  $\alpha$  is the position of a metallic scatterer introduced in the cavity. Three different transmission matrix measurements for three different positions of the metallic scatterer (slight movements in the transversal direction) are enough to create scattering states (eigenstates of the  $q$ -operator) which focus on or avoid the region occupied by the metallic scatterer. These states stay almost unchanged whether the metallic scatterer is present or not. By looking on the eigenvalue of the corresponding focussing eigenstates we can impress a certain direction on the scattering state which refers to the main focussing direction. Since we have a very good control on our input we can even think of developing a so called coherent perfect absorber [Cho10b, Gma10, Wan11].

---

## Chapter 7: Dynamical Encircling of an Exceptional Point

In this chapter we build an asymmetric mode filter/switch based on non-adiabatic transition effects which occur while dynamically encircling an exceptional point (EP). We look into the description of exceptional points and their occurrence in a  $2 \times 2$  non-Hermitian Hamiltonian [Rot09, Moi11, Hei12]. Exceptional points are of current interest as they show atypical phenomena such as state flips, for example [Uzd11, Mil15, Gao15, Xu16, Din16]. We analyse this phenomenon in the context of parametric encircling theoretically [Kec03, Dem04, Mai05] and experimentally by looking at already existing experimental realisations [Dem01, Dem04, Ste04, Lee09, Cho10a].

To introduce non-adiabatic transitions we study the dynamical encircling of an EP. We translate the dynamical encircling into the realm of wave guide experiments where we realise a wavy waveguide (based on [Dop16b]) which is shaped in space in such a way that the incorporated Bloch modes undergo a dynamical encircling of an exceptional point. Due to the non-adiabatic transitions we observe a different scattering behaviour of the modes for the two injection directions leading to the creation of an asymmetric mode filter/switch.

To prove the encircling we relate our results to the ones one would obtain in the case of parametric encircling [Dem01, Dem04, Ste04, Lee09, Cho10a]. Therefore, we build five different wave guides each of them representing a point in parameter space defining the encircling trajectory. We obtain that the state flip behaviour is in good agreement with the results predicted by the  $2 \times 2$  Hamiltonian and numerical calculations. Thus, our experiment links in a nice way the parametric and the dynamical encircling of an EP [Dop16a].

## Chapter 8: Particle-like Scattering States

We revisit the Wigner-Smith time delay operator (WSTDO) and we describe in more detail its relation to the time delay, the group delay and the dwell time of a scattering state [Hau89, Win03a, Win03b, Ili09, Amb12]. Thereafter, we discuss special eigenstates of the WSTDO so called particle-like scattering states (PLSSs) as they are defined in [Rot11]. These states are of great interest as they show either very high transmission values (close to the maximum) or very low ones (close to the minimum). Therefore, they are also referred to as noiseless states [Two03, Sil03]. Another important property of these PLSSs is that their intensity is highly accumulated on trajectories corresponding to paths of classical particles. They are very robust against frequency changes and also against local perturbations, so they can be of great use for wave based communication systems.

We realise these states in a two dimensional chaotic scattering cavity where we attach an incoming lead with an antenna array of 16 antennas and an outgoing lead. Only using the transmission matrix information between these leads we can clearly

## General Introduction and Executive Summary

---

create the particle-like scattering state corresponding to the shortest classical path between incoming and outgoing lead. We can also observe other particle-like scattering states corresponding to longer classical paths. However, these states are degenerate in our geometry as their similar path lengths make them undistinguishable for the  $q$ -operator. We can also show that these states are robust against frequency changes by studying their spatial autocorrelation. Also the stability against local perturbation is investigated. To do that, we examine the transmitted intensity as a function of the position of additional scatterers. Only when the scatterers cross the classical path which is related to a specific state, the transmitted intensity of this state drops down.

# *Introduction générale*

---

Le transport des ondes nous entoure constamment. Lorsque vous allumez votre téléphone et qu'il commence à communiquer avec une antenne éloignée, lorsque vous marchez chez vous pour trouver une connection Wi-Fi stable, ou encore lorsque vous assistez à un concert et que les haut-parleurs amplifient la voix du chanteur.

Tous ces systèmes de communication basés sur le transport des ondes font face aux mêmes enjeux et posent les mêmes questions. Comment rendre ces systèmes moins gourmands en énergie, et plus sécurisés dans le cas des réseaux Wi-Fi ou de téléphonie mobile ? Pouvons-nous trouver une solution pour filtrer le signal transmis dans le but de ne détecter que les composantes désirées ?

Généralement, les systèmes de communication décrits ci-dessus se composent de trois parties. Un émetteur (haut-parleurs, antennes, lasers, etc.) duquel le signal est envoyé, un milieu de transport (air, diélectrique, fibre optique, etc.) dans lequel l'onde se propage jusqu'à la dernière composante, le récepteur (oreille, téléphone mobile, photodiode, etc.). Une procédure standard pour améliorer ces systèmes est de se concentrer sur l'amélioration de l'une des trois parties. On pourrait par exemple développer de nouveaux lasers nécessitant moins d'énergie pour générer un faisceau plus propre et plus puissant, ou encore de nouveaux composants optiques impliquant moins de pertes. Ce n'est pas ce que je prétends réaliser ici, dans le sens où je ne vais pas me concentrer sur l'amélioration de composants uniques.

Mon but est de trouver des solutions utilisant des technologies déjà acquises et disponibles dans le domaine des micro-ondes. Dans le principe, tous les systèmes de communication basés sur une approche ondulatoire sont très semblables, ce qui signifie que cette étude ne se limite pas aux micro-ondes mais sera applicable à d'autres dispositifs. En effet, les principes sous-jacents sont très similaires. Une différence importante cependant est la différence entre échelles caractéristiques. Par exemple, les distances typiques en optique sont de l'ordre de quelques nanomètres alors que l'on parle de quelques centimètres pour les micro-ondes. Il paraît ainsi pertinent d'étudier les phénomènes de transport (ou les communications basées sur la propagation d'ondes) avec des micro-ondes : l'échelle centimétrique est en effet aisément accessible, dans la mesure où modifier des objets à l'échelle du centimètre, avec une précision de l'ordre du mm ou du  $\mu\text{m}$  demande moins d'efforts que de modifier des objets à l'échelle du mètre ou du nanomètre. Cela implique que nous pouvons relativement facilement assurer une précision sub-longueur d'onde, permettant ainsi un bon contrôle sur les systèmes que nous étudions.

Mais la question persiste : comment répondre aux attentes en termes de sécurité et d'efficacité ? La piste que nous avons suivie pour répondre à cette question



est de mettre en forme le signal initial du côté de l'émetteur de manière à ce que son transport à travers le système suive une évolution atypique mais contrôlée, en adoptant le comportement d'une particule classique, soit en évitant des zones prédéfinies, ou encore en se focalisant en un point choisi au préalable. Pour ce faire, il est nécessaire de déterminer certaines propriétés du milieu de propagation avant de mettre en forme l'excitation, et nous posons dès lors une restriction : nous nous concentrons exclusivement l'information qui peut être extraite des points d'émission et de réception du signal. Il est évident que cela nécessite d'avoir un certain degré de liberté dans le contrôle des paramètres afin d'adapter finement le signal émis. Cela se traduit soit par l'utilisation de fréquences multiples qui seront mélangées et envoyées par une antenne unique (on parle alors de mise en forme spectrale de l'onde, "spectral wave shaping"), soit par l'utilisation d'antennes émettrices multiples à fréquence fixe (mise en forme spatiale de l'onde, "spatial wave shaping"), pour lesquelles le signal de chaque antenne est fixé individuellement. Cela implique bien sûr d'être capable d'introduire des sources multiples, mais surtout, il faut être capable de contrôler simultanément l'amplitude, la phase et la fréquence de chaque source. Des systèmes offrant ce contrôle sont commercialisés au jour d'aujourd'hui. Par exemple, il existe les modulateurs spatiaux de lumière ("Spatial Light Modulator", SLM, à spectre étroit) pour l'optique, ou les "IQ-modulators" (modulateurs en phase et en quadrature, à spectre large) pour les micro-ondes.

Nous démontrons ici que la mesure du transport entre une ou plusieurs antennes émettrices et le récepteur en fonction d'un paramètre donné (fréquence, position d'un obstacle ou du récepteur) contient toute l'information nécessaire pour répondre aux questions mentionnés plus haut. Détenir plus d'informations sur le milieu diffusant n'est alors pas indispensable. Nous n'avons par exemple pas besoin de connaître les positions d'éventuels obstacles. Nous montrons ainsi qu'une fois cette première calibration réalisée, nous serons capable d'éviter certaines régions, c'est-à-dire de neutraliser des tentatives d'intrusion dans notre système, ce qui rendra la communication plus sûre. Nous pourrons également focaliser à souhait le signal sur un point précis, ou sur un récepteur donné de manière à ne pas perdre d'énergie en envoyant l'information de manière isotrope en espérant en récupérer une petite partie. Nous répondons ainsi à deux des trois points relevés : la sécurité et l'efficacité. Les chapitres dans lesquels nous développons cette idée en détail ce travail sont les chapitres 4, 5, 6 et 8.

L'approche adoptée pour la mise en œuvre d'un filtre efficace suit un raisonnement un peu différent. Nous utilisons les conséquences de l'approche d'un « point exceptionnel » au cours du transport à travers le système. La mise en forme de l'onde dans ce cas est réalisée par une modification du système diffusant lui-même, c'est-à-dire en modifiant les bords et la structure même du milieu. Ce nouveau guide d'ondes spécifique est toujours constitué d'un matériau standard (aluminium et matériau absorbant dans la gamme des micro-ondes) mais il possède aussi les propriétés d'un filtre efficace. La notion d'efficacité vient du fait qu'il ne se contente pas de supprimer la composante indésirable mais la transforme plutôt en composante favorable (sachant que nous travaillons essentiellement avec deux composants). Cet autre type de mise en forme est discuté au chapitre 7.

---

## Chapitre 3: Introduction au transport dans les micro-ondes

Dans ce chapitre, je rappelle les principes fondamentaux nécessaires à la compréhension de nos expériences. J'introduis deux types d'expériences qui seront étudiées dans cette thèse : les systèmes à base de guides d'ondes rectangulaires et les cavités ouvertes. Une fois que nous aurons compris comment le champ électromagnétique se comporte dans de tels systèmes, et la description que nous en faisons à l'aide de l'équation de Helmholtz, nous pourrons aller vers l'étude de la propagation de ce champ dans un milieu diffusant à l'aide de la matrice de diffusion, notée  $S$ . Je décrirai aussi la connexion entre  $S$  et la fonction de Green du système qui prend en compte la solution à l'équation de Helmholtz. Je présente également dans ce chapitre le fait que le processus de mesure puisse être vu comme une ouverture du système, de sorte que la solution observée soit modifiée par rapport à la solution attendue pour un système fermé.

## Chapitre 4: “Quantum search” – algorithme de recherche quantique

Dans ce chapitre, j'applique la méthode de mise en forme spectrale dans le but de focaliser un signal sur une cible spécifique. Vouloir focaliser toute l'énergie sur un point dont on ne connaît pas la position peut être interprété comme une recherche. Le mot “quantum” dans la dénomination anglo-saxonne “quantum search” entre en jeu car tous les systèmes étudiés peuvent être traités par le modèle des liaisons fortes [Wal47, Sla54] couramment utilisé en physique du solide. Nous utilisons cette dénomination de “quantum search”, qui constitue la terminologie originelle pour ce type d'approche [Gro97, Amb04, Por13] mais il faut garder à l'esprit que notre étude est purement ondulatoire [Gro02].

Tout d'abord, je discute en détails le fait qu'une cavité micro-onde ouverte contenant des résonateurs diélectriques puisse reproduire un modèle de liaisons fortes [Bar13, Bel13a, Bel13b, Bel14, Pol15, Vig16]. Ensuite, j'introduis brièvement la notion de recherche quantique avec une attention particulière sur le cas à 2 dimensions continu [Chi04, Hei09, Fou14]. Puis, je discute de la nécessité d'appliquer cette méthode sur des réseaux de type graphène (dans la mesure où ces systèmes possèdent un point de Dirac [Cas09]). En effet, la méthode de recherche quantique sur ce type de réseau est beaucoup plus rapide (temps de recherche  $\propto \mathcal{O}(\sqrt{N \ln N})$  [Fou14]) qu'une recherche classique (temps de recherche  $\propto N$ ).

Nous commençons notre étude expérimentale par une chaîne linéaire de résonateurs agrémentée d'un résonateur additionnel à rechercher, et nous étudions le temps de recherche en fonction du nombre de résonateurs. Nous démontrons qu'il est possible de réaliser une recherche associée à plusieurs sites de types différents. Pour ce faire, nous utilisons notre chaîne linéaire et deux types de sites à chercher. Puis, nous allons plus loin en étudiant un réseau de type graphène et appliquons la méthode de recherche quantique pour à nouveau identifier deux différents types de sites [Böh15].

### Chapitre 5: Le “Q-operator”

Dans le but de comprendre comment le retard accumulé par des états de diffusion est encodé dans la matrice de diffusion du système, nous devons étudier la matrice/l’opérateur de retard de Wigner-Smith [Eis48, Boh51, Wig55, Smi60]. Nous modifions cet opérateur en remplaçant la matrice de diffusion  $S$  par la matrice de transmission  $T$  et l’énergie par une variable arbitraire  $\alpha$ . Cet opérateur modifié est appelé “ $q$ -operator ” [Amb12, Bra16, Gir16].

Nous verrons dans un développement alternatif pourquoi le  $q$ -operator possède une forme caractéristique. Par ailleurs, nous étudierons un moyen de calculer ses valeurs propres et discuterons de leur interprétation physique. Les vecteurs propres du  $q$ -operator nous permettront alors de définir une condition initiale pour créer des états de diffusion qui évitent ou au contraire visent certaines régions ou encore qui forment des faisceaux hautement collimatés le long de trajectoires classiques (états appelés “particle-like scattering states”).

### Chapitre 6: Mise en forme de front d’onde

L’idée de base à propos de la mise en forme de front d’onde est de manipuler la condition initiale de manière à ce que l’accord entre le signal souhaité et le signal effectivement reçu soit significativement amélioré. Ce réglage fin sur le signal sortant peut être effectué en changeant la condition initiale de manière itérative jusqu’à obtenir le résultat souhaité. C’est une méthode couramment utilisée par exemple en optique [Vel07, Mos12, His13, Nix13, Cha14, Ami16], pour les micro-ondes [Kai14, Dup15] ou encore pour la bio-médecine [Hor15]. A titre d’exemple, des résultats marquants comme la focalisation d’un signal optique [Vel07, Vel08], la transmission d’images [Pop10] à travers un milieu opaque ou encore la focalisation/défocalisation de micro-ondes en cavités [Kai14, Dup15] ont été obtenus.

Notre montage expérimental consiste en un guide de micro-ondes rectangulaire excité par un système de 10 antennes, chaque antenne ayant une phase et une amplitude imposée individuellement en utilisant un modulateur en phase et en quadrature (IQ-modulator). Les IQ-modulators que nous utilisons sont au préalable caractérisés par des mesures de test : dans un premier temps, nous commençons nos expériences de mise en forme de front d’onde en ajustant les modes sinusoïdaux spécifiques à la sortie du guide d’ondes à vide. Dans un second temps, nous introduisons les diffuseurs et recommençons l’adaptation de modes pour vérifier la validité du système expérimental [Böh16].

A partir du moment où tous ces tests sont validés, nous construisons le  $q$ -operator mentionné au chapitre précédent, où le paramètre  $\alpha$  correspond à la position d’un diffuseur métallique introduit dans la cavité. Trois matrices de transmission différentes sont enregistrées pour trois positions différentes du diffuseur (se différenciant par de petites translations dans le plan transverse), ce qui suffit pour créer des états de

---

diffusion (vecteurs propres du  $q$ -operator) qui se focalisent ou au contraire évitent la position occupée par le diffuseur métallique. A noter que ces états sont quasiment inchangés, que le diffuseur métallique soit présent ou non. En jouant sur la valeur propre correspondant à un état focalisé, nous pouvons imposer une certaine direction à l'état de diffusion qui correspond à la direction principale de focalisation. Comme nous avons un très bon contrôle sur notre injection nous pouvons également espérer développer un absorbant cohérent parfait [Cho10b, Gma10, Wan11].

## Chapitre 7: Encerclement dynamique d'un point exceptionnel

Dans ce chapitre, nous mettons en place un filtre/interrupteur asymétrique de modes basé sur des effets de transition non-adiabatique qui apparaissent lorsque nous encerclons dynamiquement un point exceptionnel (PE). Nous nous intéressons en particulier à la description des points exceptionnels et à leur apparition dans un hamiltonien non-hermitien  $2 \times 2$  [Rot09, Moi11, Hei12]. Les points exceptionnels sont des objets intéressants dans le sens où ils exhibent des phénomènes atypiques comme par exemple des changements brutaux d'états [Uzd11, Mil15, Gao15, Xu16, Din16]. Nous analysons ce phénomène des points de vue théorique [Kec03, Dem04, Mai05] et expérimental [Dem01, Dem04, Ste04, Lee09, Cho10a] dans le contexte de l'encerclement paramétrique.

Pour induire des transitions non-adiabatiques, nous étudions ensuite l'encerclement dynamique d'un PE. L'étude est adaptée pour traduire au mieux nos expériences de guides d'ondes qui consistent en la réalisation d'un guide ondulant (basé sur l'étude [Dop16b]) qui est mis en forme spatialement de manière à ce que les modes de Bloch du système subissent l'encerclement dynamique d'un point exceptionnel. Les effets de transition non-adiabatique résultent en un comportement différent pour des modes se propageant dans des directions opposées. Nous sommes ainsi en présence d'un filtre/interrupteur asymétrique permettant de filtrer les modes différemment en fonction de leur direction de propagation.

Pour prouver que ce résultat est bien relié à l'encerclement d'un point exceptionnel, nous comparons nos résultats à ceux obtenus dans le cas d'un encerclement paramétrique [Dem01, Dem04, Ste04, Lee09, Cho10a]. Pour ce faire, nous avons fabriqué cinq guides différents, chacun représentant un point dans l'espace des paramètres définissant la trajectoire d'encerclement. Nous obtenons alors que le comportement de saut d'un état à l'autre est en bon accord avec les résultats prédits par l'étude de l'hamiltonien  $2 \times 2$  et avec les simulations numériques. Ainsi, notre expérience relie de manière élégante les encerclements paramétrique et dynamique d'un point exceptionnel [Dop16a].

## Chapitre 8: "Particle-like scattering states"

Dans ce dernier chapitre, nous exploitons à nouveau la matrice de retard de Wigner-Smith ("Wigner-Smith time-delay matrix", WSTDm) et nous décrivons plus en

détails son lien avec le retard, le retard de groupe, et le temps de transit d'un état de diffusion [Hau89, Win03a, Win03b, Ili09, Amb12]. Ensuite, nous discutons de l'existence d'états propres particuliers de la WSTDMD appelés "Particle-like scattering states" (PLSSs) tels que définis dans [Rot11]. Ces états sont particulièrement intéressants dans la mesure où ils présentent à la fois des coefficients de transmission très importants (proches de la valeur maximale) et très faibles (proches de la valeur minimale). Ainsi, ils sont aussi parfois appelés « états sans bruit » [Two03, Sil03]. Une autre propriété importante de ces PLSSs est la forte localisation de leur intensité le long de trajectoires associées à des particules classiques. Ils sont très robustes aux changements de fréquence, ainsi qu'aux perturbations locales et peuvent ainsi être d'une grande utilité dans des systèmes de communications basés sur la propagation d'ondes.

Nous réalisons de tels états dans une cavité chaotique diffusante à deux dimensions à laquelle nous connectons un guide d'injection doté de 16 antennes ainsi qu'un guide de sortie. En utilisant exclusivement la matrice de transmission entre les guides d'entrée et de sortie, nous pouvons créer un état de type "particle-like" correspondant au chemin classique le plus court existant entre l'entrée et la sortie. Nous pouvons également observer d'autres états correspondant à des chemins plus longs. Cependant, ces états sont dégénérés pour notre géométrie dans la mesure où leurs longueurs de chemin similaires les rendent indiscernables pour le  $q$ -operator. Nous pouvons montrer que ces états sont robustes aux changements de fréquence en étudiant leur auto-corrélation spatiale. Nous étudions aussi leur stabilité face à des perturbations locales. Pour ce faire, nous examinons l'intensité transmise en fonction de la position de diffuseurs additionnels. Ce n'est que lorsqu'un diffuseur se positionne sur la trajectoire classique qui est reliée à un état spécifique que ce dernier voit son intensité de transmission chuter.

# 1

## *Introduction to Transport with Microwaves*

---

Propagation of electromagnetic waves are not only related to problems concerning transport through any kind of diffusive medium but also to studies which try to gain deeper insights on quantum mechanical questions such as quantum chaoticity [Stö90, Ste95], fidelity [Köb11, Sch05] and dynamical localisation [Sir00]. Working with electromagnetic systems, especially working with microwave systems has some distinct advantages. The system size is in the order of cm to m since the typical wavelength  $\lambda$  ranges from mm to a few cm. This means that such systems are handy and relatively easy to fabricate. The materials we use are metals like aluminium, copper, gold, dielectric material such as Teflon, absorbing foams and ceramics, which are standard materials for industries which makes them easily available. To understand the microwave experiments presented in this thesis, one must be familiar with certain terminologies, which will be introduced in this chapter.

## 1.1 ELECTROMAGNETIC SYSTEMS

At the start of the description of any electromagnetic system one always finds Maxwell's equations. If we assume that there are no source currents  $\vec{j}$  and no free charges the Maxwell equations are defined in the following way:

$$\vec{\nabla} \cdot \vec{D} = 0 \quad (1.1)$$

$$\vec{\nabla} \cdot \vec{B} = 0$$

$$\vec{\nabla} \times \vec{E} = -\frac{\partial \vec{B}}{\partial t} \quad (1.2)$$

$$\vec{\nabla} \times \vec{H} = \frac{\partial \vec{D}}{\partial t}.$$

$\vec{D}$  denotes the electric displacement field and  $\vec{B}$  the magnetic field which are related to the electric field  $\vec{E}$  and to the magnetising field  $\vec{H}$  via

$$\begin{aligned} \vec{D} &= \epsilon \vec{E}, & \epsilon &= \epsilon_r \epsilon_0 \\ \vec{B} &= \mu \vec{H}, & \mu &= \mu_r \mu_0, \end{aligned}$$

where  $\epsilon$  is the dielectric constant and  $\mu$  is the permeability.  $\epsilon_0$  and  $\mu_0$  are the vacuum permittivity and the permeability of free space, which are connected to  $\epsilon$  and  $\mu$  by material dependant parameters  $\epsilon_r$  and  $\mu_r$ . Please note whenever we speak about dielectric media in this chapter, we will assume a non-dissipative and homogeneous dielectric medium which can be described via its real and positive dielectric constant  $\epsilon$ .

Using  $\nabla \times (1.2)$ ,  $\nabla \times \nabla = \nabla(\nabla) - \Delta$  and (1.1) we derive the time dependant wave equation for the electric field

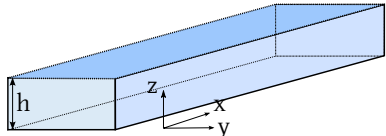
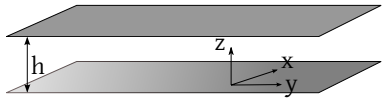
$$\Delta \vec{E} = \underbrace{\mu\epsilon}_{1/c^2} \frac{\partial^2 \vec{E}}{\partial t^2}, \quad (1.3)$$

where  $c$  is the speed of light for a medium with an index of refraction  $n = \sqrt{\mu_r \epsilon_r} = c_0/c$ .  $c_0$  indicates the vacuum speed of light given by  $c_0^2 = 1/(\mu_0 \epsilon_0)$ . In the same manner we can derive for the magnetic field  $\vec{B}$

$$\Delta \vec{B} = \mu\epsilon \frac{\partial^2 \vec{B}}{\partial t^2}. \quad (1.4)$$

We assume that the fields oscillate harmonically, i.e.,

$$\vec{E}(\vec{r}, t) = E(\vec{r})e^{-i\omega t} \quad \text{and} \quad \vec{B}(\vec{r}, t) = B(\vec{r})e^{-i\omega t}. \quad (1.5)$$

Rectangular waveguide	Open cylindrical cavity
	
<b>TE:</b> $B_z = 0$ $E_z = \Psi(x, y) \cos\left(\frac{l\pi}{h} z\right), l = 0, 1, 2, \dots$	$E_z = 0$ $B_z = \Psi(x, y) \sin\left(\frac{m\pi}{h} z\right), m = 1, 2, \dots$
<b>TM:</b> $E_z = 0$ $B_z = \Psi(x, y) \sin\left(\frac{m\pi}{h} z\right), m = 1, 2, \dots$	$B_z = 0$ $E_z = \Psi(x, y) \cos\left(\frac{l\pi}{h} z\right), l = 0, 1, 2, \dots$

**Table 1.1** – Sketches of the two types of systems investigated. The blue and grey surfaces symbolise metallic surfaces. TE denotes "Transversal Electric" and TM indicates "Transversal Magnetic". These definitions are done according to [Jac98].

Thus the time dependant equation reduces to

$$(\Delta + k^2)\vec{\Omega} = 0, \quad \text{with} \quad k^2 = \left(\frac{\omega}{c}\right)^2 = \left(\frac{2\pi f}{c}\right)^2, \quad \vec{\Omega} = \vec{E}, \vec{B}, \quad (1.6)$$

where  $k$  is often referred to as wavenumber and  $f$  denotes the frequency.

In this thesis I investigate two types of systems. One type is a open cavity with no boundary in the  $xy$ -plane and the other type is a waveguide where electromagnetic waves propagate in the  $x$ -direction. These two systems are shown in table 1.1. Table 1.1 shows that our systems are invariant with regard to the  $z$ -direction. The  $z$ -component of the electric field as well as the  $z$ -component of the magnetic field are described by a scalar field  $\Omega_z$  with

$$\Omega_z(x, y, z) = \Psi(x, y)f(z). \quad (1.7)$$

$\Omega$  can be replaced by  $E$  or  $B$  as it was defined in equation (1.6).

Electromagnetic waves have to fulfil certain boundary conditions. Especially at metallic surfaces they have to follow:

$$\vec{n} \cdot \vec{B} = 0, \quad \vec{n} \times \vec{E} = 0, \quad (1.8)$$

where  $\vec{n}$  is a unit normal vector pointing away from the metallic surface.

Throughout this work, we only investigate the  $z$ -component of the electromagnetic field, i.e., we work with two different field types called "Transversal Magnetic" (TM) and "Transversal Electric" (TE) in our experiments. Unfortunately two different conventions exist for these field types when one compares waveguide systems



with cavity systems. The two mentioned field types are explicitly defined for the two studied systems in table 1.1. The integers  $m, l$  in table 1.1 give raise to speak of a quantisation of this fields related to the confinement in the  $z$ -direction which imposes the mentioned boundary conditions above. Taking into account this quantisation one speaks of  $\text{TM}_i$  or  $\text{TE}_i$  modes, such as the  $\text{TE}_0$ -mode for example (which means  $l = 0$  in a waveguide system).

The function  $f(z)$  is well defined for the introduced field types (see equation (1.7) and compare with table 1.1) and we can simplify equation (1.6) by defining a wavenumber  $k_z$  such that

$$\frac{d^2}{dz^2} f(z) = -k_z^2 f(z) \quad \text{with} \quad k_z = \frac{n\pi}{h}, \quad n \in \mathbb{N}. \quad (1.9)$$

$n$  is an integer value referring to the different boundary conditions (see table 1.1) and  $\lambda$  denotes the wavelength of the wave. This yields a quasi two-dimensional problem of the form:

$$(\Delta_t + k^2 - k_z^2)\Psi(x, y) = 0 \quad (1.10)$$

$$\iff (\Delta_t + k_t^2)\Psi(x, y) = 0, \quad \text{with} \quad k_t^2 = k^2 - k_z^2, \quad (1.11)$$

where  $t$  denotes the transverse plane ( $xy$ -plane). This equation holds only for a fixed  $k_t$ . As one is also interested in the  $k_t$ -dependency of  $\Psi(x, y)$ ,  $\Psi$  can become a function of  $k_t$  such that  $\Psi = \Psi(x, y, k_t)$ . The word 'quasi' is used here to remind oneself that one has to be aware that the full problem is three-dimensional and that one should not totally forget about the  $f(z)$ -dependency (see equation (1.7)). Equation (1.11) is also referred to as two-dimensional Helmholtz equation. It got famous in the quantum chaotic community, because it represents an analogue to the two-dimensional Schrödinger equation with

$$(\Delta_t + k_s^2)\psi = 0, \quad \text{with} \quad k_s^2 = \frac{2m}{\hbar} \omega - \frac{2m}{\hbar^2} V(x, y), \quad (1.12)$$

where  $V(x, y)$  denotes a two-dimensional potential and  $\psi$  is the quantum mechanical wavefunction.

Equation (1.11) is the basis of our theoretical considerations in chapters 2, 4 and 5. To solve equation (1.11) can be a hard task as we will see for example in our open cavity system (see chapter 2), where we will introduce dielectric scatterers so that the dielectric constant  $\epsilon(\vec{r})$  gets position dependant.

## 1.2 SCATTERING MATRIX

Another important concept besides the concept of modes which we heard of in the previous section is the concept of the scattering matrix, that is briefly explained

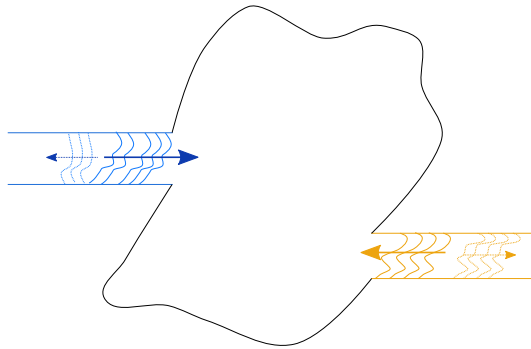


**Figure 1.1** – Sketch of a scattering system with two attached channels, in which incoming and outgoing waves enter or leave the scattering region/billiard.

here. Let us look at a system of the waveguide-type in the way it is described in figure 1.1, where we connected two waveguides to a central scattering part, which we call billiard.

These waveguides (or ports/antennas) attached to the billiard allow us to send (receive) waves in (from) the central scattering part. If the widths of the coupled waveguides are on the scale of a few wavelengths, the electromagnetic field  $\Upsilon$  within the  $n$ -th waveguide can be assumed to be a superposition of incoming and outgoing waves following

$$\Upsilon(\mathbf{r}, k) = a_i(\mathbf{r})e^{ik_i|\mathbf{r}-\mathbf{r}_i|} - b_i(\mathbf{r})e^{-ik_i|\mathbf{r}-\mathbf{r}_i|}, \quad (1.13)$$

where  $r_i$  denotes the point where the waveguide  $i$  touches the billiard.  $k_i$  are complex wavenumbers.  $a_i$  and  $b_i$  are complex numbers.  $a_i$  describes how waves are entering the billiard and  $b_i$  how they leave it. This entering and leaving is indicated with orange and blue arrows in figure 1.1.  $\mathbf{r}$  is a two-dimensional vector. Bold symbols and vectors are synonymously used throughout this work. Each waveguide can be assumed to correspond to exactly one so-called scattering channel (width of the waveguide much smaller than the billiard size). We can connect ingoing and outgoing channels via a matrix, which we call scattering matrix  $S$ . If we have  $N$  waveguides (ports) we can define two vectors  $\mathbf{a} = (a_1, \dots, a_N)^T$  and  $\mathbf{b} = (b_1, \dots, b_N)^T$  containing the amplitudes of the incoming and outgoing waves which are connected via the  $N \times N$  scattering matrix such as

$$\mathbf{b} = S\mathbf{a}. \quad (1.14)$$

The diagonal elements  $S_{ii}$  of  $S$  can be understood as reflection amplitudes as they describe the scattering back inside the port. The off-diagonal elements  $S_{ij}$  are the transmission amplitudes describing the transport between different ports. One can add additional (fictitious) channels to the system to account for loss. This is a well known assumption in theory [Fyo05, Sav06, Kuh13].

Especially in the field of microwave measurements, measured spectra obtained by antenna measurements are often linked to entries of the scattering matrix. Let us imagine that the two leads shown in figure 1.1 correspond to two antennas.

Then  $S$  would look like

$$S = \begin{pmatrix} S_{11} & S_{12} \\ S_{21} & S_{22} \end{pmatrix} = S = \begin{pmatrix} R_1 & T' \\ T & R_2 \end{pmatrix}. \quad (1.15)$$

$S_{11}$  and  $S_{22}$  describe the reflection of the signal back into the antenna 1 and antenna 2. In this thesis they are also called  $R_i$  or just  $R$ .  $S_{12}(S_{21})$  describe the transmission from antenna 2(1) to antenna 1(2). They can be alternatively denoted as  $T'$  and  $T$  in this thesis. In this case with just two attached channels  $R$ ,  $R'$ ,  $T$  and  $T'$  are simple numbers.

The scattering matrix in general gets more complicated once one works with multiple leads containing multiple modes, like multiple TE-modes for example. Such a scattering matrix can also be described in terms of  $R, R', T$  and  $T'$ . But these quantities become then matrix quantities themselves as we will see in section 6.1.2.

### 1.3 GREEN FUNCTION AND THE SCATTERING MATRIX

We will stick a little bit longer to the scattering system introduced in the previous section. Let  $\Psi$  be the electromagnetic field within this central scattering part which we refer to as 'billiard'.  $\Psi$  shall fulfil the Helmholtz equation. A possible way to solve this equation is to apply the Green function technique, i.e., one tries to find the billiards Green function  $G(\mathbf{r}, \mathbf{r}', k)$ . This Green function describes the field within the billiard with no ports attached. To find the Green function for the full problem one has to modify  $G(\mathbf{r}, \mathbf{r}', k)$  to account for the two attached leads (ports). The modified Green function  $\bar{G}(\mathbf{r}, \mathbf{r}', k)$  is defined as

$$\bar{G}(\mathbf{r}, \mathbf{r}', k) = \sum_n \frac{\bar{\Psi}(\mathbf{r})\bar{\Psi}(\mathbf{r}')}{k^2 - \bar{k}_n^2}, \quad (1.16)$$

where  $\bar{k}_n^2$  are the modified eigenvalues of the modified eigenfunctions  $\bar{\Psi}(\mathbf{r})$ . The functions  $\bar{\Psi}(\mathbf{r})$  are modified in the sense that they respect other boundary conditions than the original eigenfunctions  $\Psi_n$ , i.e.,  $\bar{\Psi}$  at the boundaries fulfils

$$\bar{\Psi}(\mathbf{r})|_b = 0, \quad \lim_{\mathbf{r} \rightarrow \mathbf{r}_w^-} \nabla_{\perp} \bar{\Psi}(\mathbf{r}) = \lim_{\mathbf{r} \rightarrow \mathbf{r}_w^+} \nabla_{\perp} \bar{\Psi}(\mathbf{r}), \quad (1.17)$$

where  $b$  in this equation stands for the boundary of the billiard.  $r_w$  denotes the positions where the waveguide openings touches the billiard.  $\nabla_{\perp}$  is the normal derivative pointing into the waveguide. Instead of speaking of the eigenvalue  $k_n$  one can also speak of the  $n$ th-resonance. The left (right) hand side of equation (1.17) is referred to as Dirichlet (Neumann) boundary conditions.  $\bar{G}$  is related to  $S$  [Stö99] via

$$S = \frac{1 - i\gamma\bar{G}}{1 + i\gamma\bar{G}} \quad (1.18)$$

### 1.3. Green Function and the Scattering Matrix

---

in which  $\gamma$  describes the coupling of the waveguides to the billiard. If the **resonances are isolated**, one can transform Equation (1.18) into

$$S_{ij} = \delta_{ij} - i\gamma \sum_n \frac{\bar{\Psi}(\mathbf{r}_i)\bar{\Psi}(\mathbf{r}_j)}{k^2 - \bar{k}_n^2 + i\Gamma_n} = \delta_{ij} - i\gamma \hat{G}(\mathbf{r}_i, \mathbf{r}_j, k) \quad (1.19)$$

$$\text{with } \hat{G}(\mathbf{r}_i, \mathbf{r}_j, k) = \sum_n \frac{\bar{\Psi}(\mathbf{r}_i)\bar{\Psi}(\mathbf{r}_j)}{k^2 - \bar{k}_n^2 + i\Gamma_n} \quad (1.20)$$

which has been shown in [Stö99]. Note that equations (1.19, 1.20) are also known as Breit-Wigner-formula in the context of nuclear physics [Bla52].  $\delta_{ij}$  denotes the Kronecker delta. The constants  $\gamma$  and  $\Gamma$  have been modified here to fit to the definition given in [Bel13a] (see details in section 2.2.4).  $\Gamma_n$  takes into account losses like ohmic losses induced by the metallic surfaces of the cavity for example but also losses due to the opening of the system, which is a consequence of the added waveguides/antennas. This result holds also when the attached waveguides are replaced by circular antennas [Ste95].

Looking at equations (1.19, 1.20) it becomes clear that one needs the transmission measurement between two antennas to recover the complete modified Green function, i.e., the sign of the modified eigenstates  $\bar{\Psi}_n$  [Ste95]. The reflection measurements give us only the information about the spectrum of the eigenstates and their modulus. [Stö90, Ste95] The transmission measurements corresponding to  $S_{ij}$  on the other hand help us to obtain the off diagonal elements containing especially the sign (phase) information of  $\bar{\Psi}_n$ .

Equations (1.19, 1.20) state that one never obtains the original or unperturbed resonances  $k_n$ . **The obtained resonances (eigenvalues) are shifted  $\bar{k}_n \neq k_n$  and broadened by the factor  $\Gamma_n$**  (more details in [Ste95]).



# 2 *Quantum Search*

---

## Contents

---

<b>2.1 A Tight Binding Analogue . . . . .</b>	<b>24</b>
2.1.1 <i>Microwave Set-up . . . . .</i>	24
2.1.2 <i>Dielectric Resonators . . . . .</i>	25
<b>2.2 Quantum Search and its Experimental Implementa- tion . . . . .</b>	<b>28</b>
2.2.1 <i>Theoretical Basis . . . . .</i>	28
2.2.2 <i>Quantum Search on a Linear Chain . . . . .</i>	31
2.2.3 <i>The Honeycomb Lattice . . . . .</i>	36
2.2.4 <i>Graphene . . . . .</i>	40
2.2.5 <i>Quantum Search on the Graphene-lattice . . . . .</i>	42
<b>2.3 Conclusion . . . . .</b>	<b>45</b>

---

The first system we want to look at, is the system of an open cavity, where we study our first transport phenomenon, the quantum search. Before I describe what a quantum search is, one has to describe the system with which one can study this phenomenon. The system to which we restrict ourselves is a tight binding analogue. I start describing our tight binding analogue where we use an arrangement of dielectric cylinders. Then I am more precise on the quantum search itself.

### 2.1 A TIGHT BINDING ANALOGUE

The tight binding model is a well-known theoretical description which was developed in the late 40s and 50s [Wal47, Sla54] in solid state physics to describe electronic properties of solids. Tight binding means that the electrons are tightly bound to the atoms forming the structure of the solid. The transport of electrons can be described as hopping from one atom to another. The wave function of the electron being bound to a specific atom does not differ from the orbital of an electron of a free atom described by the atomic Hamiltonian. Therefore it is assumed that the bound wave function is declining faster than  $1/r^2$  outside the potential boundary of its atom, so that it is not influencing the potential of neighbouring atoms. The coupling between electrons can be assumed to be weak as long as the overlap of their exponentially decreasing wave-functions is small. This assumptions gave rise to the tight binding model. It has been shown that this assumptions together with the idea of periodicity in atomic structures form a powerful tool to describe properties like band structure or conductance [Sin01, Kit53]. If one is interested in a system of electrons which all belong to the same orbital like it is the case for electrons in the  $p_z$ -orbital in graphene for example, the description of the system is analogue to the classical description of coupled oscillators [Tay05].

#### 2.1.1 Microwave Set-up

Our experiment is an open microwave cavity (see figure 2.1). It consists of two parallel aluminium plates. Onto the ground plate we place ceramic cylinders (TEMEX-ceramics, E2000 Series, ZrSnTiO) with a high index of refraction ( $n \approx 6$ ). They have a dielectric constant  $\epsilon_r$  of  $\approx 36$  and their permeability  $\mu_r$  is 1. Their height is 5 mm and they have a diameter of 8 mm ( $= 2r_d$ ). The placing of these cylinders is done by a computer controlled arm, which is movable and achieves a placing precision of 0.1 mm (see figure 2.2). To excite the  $TE_1$ -mode inside the cavity (see details in table 1.1), we use two kinds of antennas. A kinked antenna and a loop antenna, which are shown in figure 2.1. The upper plate is movable in the  $xy$ -plane, so that the magnetic field component in the  $z$ -direction  $B_z$  can be measured with the loop antenna at any given position inside the cavity. The microwave measurements are performed by a two port vector network analyser (VNA, ZVA-24 by Rohde & Schwartz) which is able to generate and to measure phase and amplitude of the microwave signal.

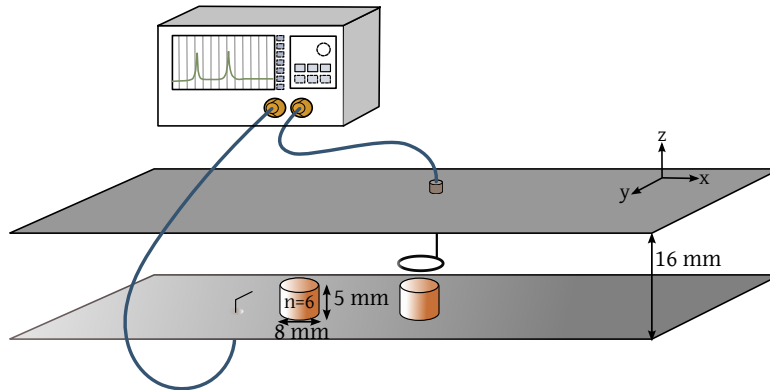


**Figure 2.1** – Set-up with two dielectric discs inside using a kinked and a loop antenna to measure microwave signals which are sent and received by a vector network analyser, which is able to measure phase and amplitude of the microwave signal. The whole top plate is movable in the  $xy$ -direction.

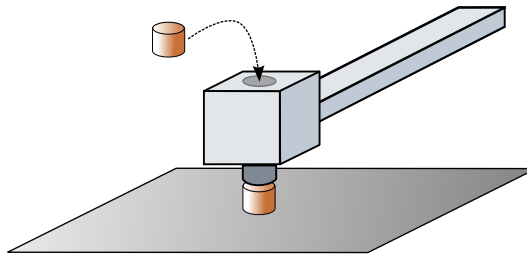


**Figure 2.2** – Computer controlled arm to position the dielectric discs. The disc is dropped in the hole and falls through a cylinder to the given position as indicated by the arrow. The arm is freely moveable in the  $xy$ -direction.

### 2.1.2 Dielectric Resonators

We have seen in chapter 1 that the TE-mode in the open cavity shows a magnetic field aligned in the  $z$ -direction. We have already seen that  $B_z$  obeys the Helmholtz equation. For the reason of convenience I would like to repeat equation (1.11) with the explicit parameters we have in the system:

$$(\Delta + k_t^2)\Psi(x, y) = 0, \quad \text{with} \quad k_t^2 = \left(\frac{\omega}{c_0}\right)^2 \mu_r \epsilon_r - \left(\frac{m\pi}{h}\right)^2 = k_0^2 \epsilon_r \mu_r - k_z^2, \quad (2.1)$$

where  $h$  denotes similarly to chapter 1 the height of the cavity.  $k_0$  is the wavenumber in free space  $k_0 = (\omega/c_0)^2$ . One observes that the lowest TE<sub>1</sub>-mode which exists in the system is captured within the dielectric disc. The transversal wavenumber  $k_t^2$  for the frequency  $\omega_{\text{TE}_1}$  of this lowest TE<sub>1</sub>-mode is greater than zero inside the disc, since  $\epsilon_r = 36$  and  $\mu_r = 1$ . Whereas, outside the disc, in air,  $k_t^2$  is smaller than zero ( $\epsilon_r = 1, \mu_r = 1$ ) leading to evanescent decay of the field outside the disc. The  $k_t$ -value describing the situation outside the disc will be denoted with  $k_t'$  in the following. Note that outside the discs also all the other TE <sub>$j$</sub> -modes with  $j \geq 1$  are



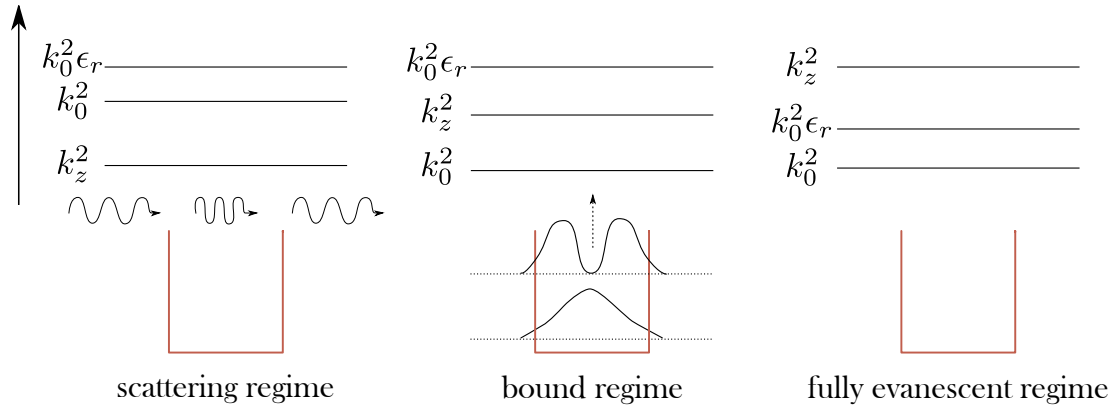


**Figure 2.3** – Different regimes defined by the relation between  $k_0$  (describing the situation outside the disc with  $\epsilon_r = 1$ ,  $\mu_r = 1$ ),  $k_0\epsilon_r$  (describing the situation inside the disc with  $\epsilon_r = 36$ ,  $\mu_r = 1$ ) and the quantisation number  $k_z$  (which accounts for the boundary conditions at the metallic plates). The bound states are discussed in detail in the main text. The two shown bound states are just sketches to convey the idea. In principle more bound states are possible, which is indicated by the arrow.

strongly suppressed due to the boundary conditions implied by the metallic walls (see section 1.1). This means that outside the discs the behaviour is really purely evanescent.

In fact this is exactly the electromagnetic analogue to what is known in quantum mechanics as a potential well. Let us forget for a moment about the  $y$ -direction and look at different configurations of  $k_0$ ,  $k_0\epsilon_r$  and  $k_z$  (see equation (2.1)) which are presented in figure 2.3.

In figure 2.3 we identified three different regimes. In the scattering regime, the disc acts primarily as a scatterer. In the bound regime the wave is located within the disc as it is the case in our experiment. In the fully evanescent regime the initially excited field declines exponentially from the point of the excitation so that a field only exists in the vicinity of the excitation position. From figure 2.3 one can understand the great flexibility of this experiment. Just by changing the frequency  $f = \omega/2\pi$  at which we are working we can switch between different regimes. We could either decide to use the dielectric discs as scatterers for the wave or we could change their behaviour totally to a system of localised bound states which are weakly coupled. The coupling in fact is small enough so that the localised bound states of the isolated discs are only slightly distorted, which has been shown experimentally in [Bar13, Bel13a]. In this case one can speak of a tight binding analogue.

Let us be more detailed on the last point and look at the explicit and fully two dimensional solution of equation (2.1). If we assume that the disc touches the upper plate, one can find a detailed solution in [Jac98], where the solution is derived using cylindrical coordinates  $(r, \Phi, z)$  and a separation of variables. The solution, which can be obtained, consists of two parts. One part states that  $B_z$  inside the disc-radius follows Bessel functions of the first kind  $J_m$ . The other part illustrates the exponential decline of  $B_z$  outside the disc. If one puts these parts together one gets

the bell-shaped curve shown in figure 2.4. Explicitly, the full solution for  $B_z$  looks like:

$$B_z = \begin{cases} \propto J_m(k_{t,m}r) e^{im\Phi} \sin(l\pi\frac{z}{h}) & \text{if } r < r_d \\ \propto K_{m'}(k'_{t,m'}r) e^{im'\Phi} \sin(l\pi\frac{z}{h}) & \text{if } r > r_d \end{cases} \quad (2.2)$$

$m, m'$  and  $l$  are integers denoting the angular quantisation and the quantisation in the  $z$ -direction.  $r, \Phi$  and  $z$  denote cylindrical coordinates. In the real set-up this ideal case described in equation (2.2) is not fulfilled since the disc does not touch the upper plate. Thus some modifications of equation (2.2) appear, which need to be discussed:

$$B_z = \begin{cases} \propto f(z) J_m(k_{t,m}r) e^{im\Phi} & \text{if } r < r_d \\ \propto \sum_l \alpha'_l \sin(l\pi\frac{z}{h}) K_{m'}(k'_{t,l,m'}r) e^{im'\Phi} & \text{if } r > r_d \end{cases} \quad (2.3)$$

The function  $f(z)$  takes the unknown  $z$ -dependence of  $B_z$  inside the disc-radius into account. The air gap between the top of the disc and the top plate of the cavity allows the excitation of a variety of evanescent  $K$ -modes. Therefore a summation over multiple  $K$ -modes with different  $k'_{t,l,m'}$  appears.

We can simplify the expression (2.3) by putting  $m = m' = 0$ , since only  $J_0$  and  $K_0$  type of modes are present in the frequency regime in which our experiment is working. This means the angular dependence drops out and we can finally write:

$$B_z \approx \begin{cases} \propto J_0(k_t r) & \text{if } r < r_d \\ \propto \sum_l \alpha_l K_0(k'_{t,l} r) & \text{if } r > r_d \end{cases} \quad (2.4)$$

The height where the magnetic field is measured, depends of the  $z$ -position  $z_{loop}$  of the loop antenna. Since this height is fixed in our experiment we can do a normalisation so that  $\alpha_l = \alpha'_l \sin(l\pi\frac{z_{loop}}{h})/f(z_{loop})$  and  $J_0(0) = 1$ .

In the following we clarify these theoretical considerations with actual experimental findings. The loop antenna scanned  $B_z$  above and around one disc. This disc is excited at its lowest resonance frequency  $\nu_0$  at 6.65 GHz [Bel13a]. Figure 2.4 shows the measured intensity profile  $|B_z|^2$ . One observes that the intensity is well confined within the discs and it declines exponentially outside the disc in the way we describe it theoretically. As shown in figure 2.4 by the fit we have to consider up to three evanescent  $K_0$ -modes to describe the evanescent behaviour outside the disc properly.

We want to establish a tight binding analogue with these kind of discs. Therefore it is necessary for us that the eigenfunctions  $J_0, K_0$  of a disc remain mainly unperturbed, when one brings other discs close to it. This has been confirmed in [Bel13a], where the  $B_z$ -field of two coupled discs was investigated. These two discs were coupled by bringing them spatially close together. The field of the coupled resonators still followed the description of a simple sum of two independent fields which corresponded to the  $B_z$ -field of an isolated disc [Bel13a]. This clarifies that we are really

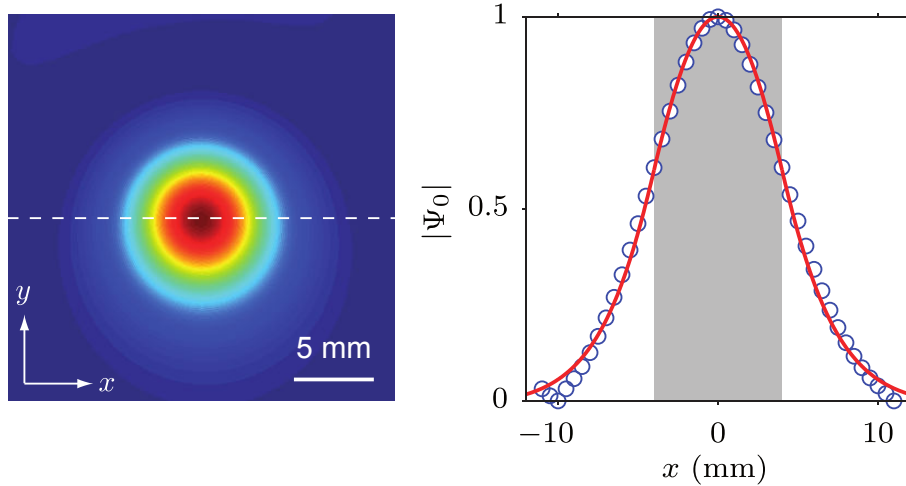


**Figure 2.4** – Intensity of the lowest disc resonance obtained with the loop antenna at 6.65 GHz which corresponds to  $J_0$  and  $\sum_l \alpha_l K$  (see main text). **Left:** Intensity  $|B_z|^2$  profile outside the disc (see normalisation in the text). **Right:** Intensity profile  $|B_z|^2$  according to the dashed white line on the left. The gray zone indicates the dielectric disc. The circles indicate the measured data points. The red line corresponds to a fit with  $k_t = 0.3341 \text{ mm}^{-1}$ ,  $k'_{t,1} = 0.1215 \text{ mm}^{-1}$ ,  $k'_{t,2} = 0.3423 \text{ mm}^{-1}$  and  $k'_{t,3} = 0.5366 \text{ mm}^{-1}$  and  $\alpha_1 = -0.1370$ ,  $\alpha_2 = 5.3816$  and  $\alpha_3 = -6.6585$  according to equation (2.4). Figure and fit from [Bel13a].

dealing with a tight binding analogue (see also [Bar13]). This system of coupled dielectric discs has already been proven to be a powerful tool. It is convenient to study the effects of disordered lattices like disorder in graphene lattices [Bar13] or to look at lattices with special boundary conditions [Bel14]. I realised a Penrose-tiled lattice a so called quasicrystals with this system [Fig16]. Also highly theoretical concepts like topological transitions of Dirac points in graphene [Bel13b] or topologically induced interface states [Pol15] can be addressed. In the following we perform a quantum search experiment using an arrangement of dielectric discs and we develop an idea of a possible application.

## 2.2 QUANTUM SEARCH AND ITS EXPERIMENTAL IMPLEMENTATION

### 2.2.1 Theoretical Basis

A very interesting point in the realm of quantum information and quantum computing is the field of quantum search algorithms. Such quantum computing algorithms are very powerful as they enable the user to carry out a large number of parallel computing processes. Such algorithms use the fact that a quantum mechanical system can exist simultaneously as superposition of multiple states. If one now carries out an operation on this superposition of states, this operation acts simultaneously

## 2.2. Quantum Search and its Experimental Implementation

---

on all included states, i.e., this operation corresponds to a huge parallel operation. Grover was the first to describe such a quantum type of search algorithm for an unstructured database [Gro97]. The underlying mechanism to describe such a search is done using the formalism of quantum walks in the way described in [Amb04, Por13].

One distinguishes in general between the discrete quantum walk and the continuous one. The difference can be seen on how the motion of the walker is described (see [Chi10] for more information):

$$\begin{aligned} \text{Discrete Quantum walk:} \quad p_t &= W^t p_0 \\ \text{Continuous Quantum walk:} \quad \frac{d}{dt} p(t) &= M p(t). \end{aligned}$$

$W$  describes the hopping probability matrix and  $M$  is the hopping probability matrix per unit time. Discrete quantum walks have also been implemented experimentally using laser pulses as stepping mechanisms [Sch10, Sch12]. The two mentioned descriptions of the quantum walk lead to two types of quantum search algorithms. The search problem described by such algorithms reads like the following: Assuming we have  $N$  unique distinguishable items in an arbitrary grid and we are looking for the position of a specific one. Classically we would need about  $N/2$  steps on average to find it when we apply a classical search algorithm. The idea of the quantum search is to 'excite' the grid itself in such a way that after a certain time the excitation energy localises on the item we searched for and therefore we can identify its position in the structure.

The search time classically scales with  $\mathcal{O}(N)$ . But with the quantum search algorithm using the power of de-localisation, the search time is typically proportional to  $\approx \sqrt{N}$ . This is due to the fact that the coupling between the search item and the grid takes into account the normalisation of the grid state which is used to perform the search. Typically one uses a uniform distributed grid-state and therefore the factor  $\sqrt{N}$  appears [Gro02]. The  $\sqrt{N}$ -behaviour describes well the search time for a small number of search sites. For larger systems one has to take into account corrections. The reason for that is discussed below. It turns out, however, that the factor  $\sqrt{N}$  is exact for the case of  $d$ -dimensional lattices with  $d > 2$  even in the large  $N$  limit. For two dimensional lattices the minimal search time is of the order of  $\sqrt{N \ln(N)}$  for the continuous walk/search [Fou14]. Note that the lattice in [Fou14] had to be manipulated in such a way that it contains a Dirac point, i.e. a linear growth of the density of states (such as in graphene [Cas09], see a detailed discussion in section 2.2.4), otherwise this minimal limit is not achieved. This is the result for the continuous quantum search. For the discrete one the number of necessary steps is  $\sqrt{N} \log(N)$  [Amb04]. In the following we restrict ourselves to the case of continuous quantum search.

The 'quantum' search is in fact a pure wave phenomenon relying only on interference of an distributed grid state with the localised state of the searched item as it has been described in detail by Grover himself in [Gro02] using coupled pendula to perform his quantum search algorithm.

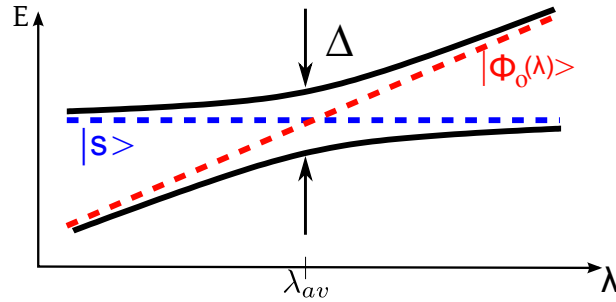


**Figure 2.5** – Avoided crossing between a distributed grid state  $\Phi_0$  which is dependant on a tuning parameter  $\lambda$  and the state of the search item  $s$ . The coupling of the two states is proportional to the minimal distance  $\Delta$  at the avoided crossing.

At the beginning of the quantum search, like for any other kind of search, stands the information about the item which should be searched for. Let us say that we look for an object which carries the eigenstate  $|s\rangle$  of energy  $E_s$ . In the following we will describe the search for this localised eigenstate, which is equivalent to the search for the object itself. Let us assume that  $|s\rangle$  is weakly coupled to a system whose dynamics is described by an Hamiltonian  $H$ . One can think of  $H$  as the Hamiltonian describing a tight binding model of  $N$  coupled resonators for example. Let us furthermore assume that the Hamiltonian is tunable with a parameter  $\lambda$  ( $H \equiv H(\lambda)$ ) so that there exists a tunable eigenstate  $|\Phi_0(\lambda)\rangle$  of  $H$ . This state must not necessarily be distributed over all items but it must be assured that  $|\Phi_0(\lambda)\rangle$  has a finite overlap with  $|s\rangle$  such as  $\langle s|\Phi_0(\lambda)\rangle \neq 0$  for a given interval of  $\lambda$  values. The easiest way to fulfil this condition is to use the totally symmetric state of the system, i.e, the state which is uniformly distributed over all search items. Since  $|\Phi_0(\lambda)\rangle$  is tunable we can shift its energy towards the energy of  $|s\rangle$  and since the overlap is non-zero, the two states will undergo an avoided crossing just as is shown in figure 2.5. Sufficiently close to each other the two states can exchange energy.

Let us assume that  $|\Phi_0(\lambda)\rangle$  denotes the uniform distributed state and that the minimal energetic distance between the two states is reached at  $\lambda = \lambda_{av}$ . If we prepare the system to evolve starting from  $|\Phi_0(\lambda_{av})\rangle$ , i.e, we excite the  $|\Phi_0(\lambda_{av})\rangle$ , we can follow the time-development of the system using  $\exp(iHt)|\Phi_0(\lambda_{av})\rangle$ . If  $|\Phi_0(\lambda_{av})\rangle$  and  $|s\rangle$  are sufficiently isolated from any other state of the system, the result of the time development is a beating pattern between the distributed state  $|\Phi_0(\lambda_{av})\rangle$  and  $|s\rangle$ . This beating time (or revival time of  $|\Phi_0(\lambda_{av})\rangle$ ) can be interpreted as twice the search time  $t_s$ , where  $t_s$  marks the time at which the intensity is 'fully' localised in  $|s\rangle$ . The minimal energetic splitting of the two states  $\Delta$  (see figure 2.5) is proportional to the coupling of the two states (see [Hei09] for a mathematical rigorous description). As shown in [Hei09] one can deduce that  $t_s \propto 1/\Delta \propto 1/\langle s|\Phi_0(\lambda)\rangle$  (see also figure 2.5 to understand the definition of  $\Delta$ ). If we assume that  $|\Phi_0(\lambda_{av})\rangle$  is the uniformly distributed state, one can calculate the coupling to state  $|s\rangle$  to be of the order  $1/\sqrt{N}$  (see [Gro02] for the case of coupled pendula). This square-root is, as already mentioned earlier, basically related to the normalisation of  $|\Phi_0(\lambda_{av})\rangle$  following the calculation in [Gro02]. This means that the search time  $t_s$  is of the order of  $\sqrt{N}$  if  $|\Phi_0(\lambda_{av})\rangle$  is distributed over  $N$  items.

## 2.2. Quantum Search and its Experimental Implementation

The critical reader might have already spotted the crucial point which is essential for the success of the algorithm. I said above that the two states  $|\Phi_0(\lambda_{av})\rangle$  and  $|s\rangle$  have to be sufficiently isolated. This, in general, can be very hard to achieve especially for  $d < 4$  as we see in the following. Let us do an estimation for the number of states with an energy less than  $E_c$  depending on the dimension  $d$ :

$$N(E)|_{E < E_c} = \int_0^{N(E_c)} dN \propto \int_0^{E_c} \frac{dN}{dE} dE \propto N_g \int_0^{E_c} E^{\frac{d-2}{2}} dE \propto N_g E_c^{\frac{d}{2}}, \quad (2.5)$$

where  $N_g$  represents the total number of states. Finally we derived that  $N(E) \propto N_g E_c^{d/2}$ . This means the first state above the ground state  $E_1$  is supposed to appear at  $2 \propto N_g E_1^{d/2} \leftrightarrow E_1 \propto N_g^{-2/d}$ . If we assume that we need an energy separation of the order  $N_g^{-1/2}$  between the ground state, which shall correspond to  $|\Phi_0\rangle$  in our example, and  $E_1$ , we have to perform the search in the space with  $d \geq 4$  (in the large  $N_g$  limit). If the search is carried out in a space of lower dimension, i.e.,  $d < 4$ , one has to readjust the coupling to ensure the 'property of isolation' of the two states. Readjusting means that one has to lower the coupling to minimise  $\Delta$  and this has to be paid by a larger search time  $t_s$ . This is the reason why for  $d = 2$  correction factors are needed which lead to no substantial speed up of the algorithms (see details in [Chi04]).

It turned out however that a good idea to substantially improve the performance of the algorithm is to perform the search in systems containing Dirac points (such as graphene, see more details below), where the energy scaling in the vicinity of these points is lowered to  $E_1 \propto N_g^{-1/2}$  due to the linear dispersion relation (see [Cas09]). A rigorous mathematical derivation for a graphene-like lattice showed that there are still some corrections which have to be included so that one obtains the search time to scale with  $\mathcal{O}(\sqrt{N \ln N})$  [Fou14] (see especially the supplementary material for the derivation of the logarithmic corrections). The idea in this chapter will be to present the first **proof of principle experiment** for a continuous two dimensional quantum search using a graphene-like lattice arrangement (also called artificial graphene according to [Bar13, Bel13a, Bel14]) of coupled dielectric disc resonators forming a system obeying the tight binding description.

### 2.2.2 Quantum Search on a Linear Chain

To understand the underlying process of bringing a distributed grid state in resonance with a localised search state, we will use a linear chain of disc resonators (grid) to which additional discs are coupled to. These additional discs are called search discs (**SDs**) and their eigenfrequencies differ from the ones of the chain. The localised eigenstate of each of the SDs is the one shown in figure 2.4. It corresponds to what was introduced as  $|s\rangle$  above. The search will be performed by exciting the grid in the way described above. At some point in time the excitation energy will be focused exclusively within the SD, i.e., in the localised eigenstate  $|s\rangle$  of the SD which is characterised by its individual eigenenergy  $E_s$  which translates in our case

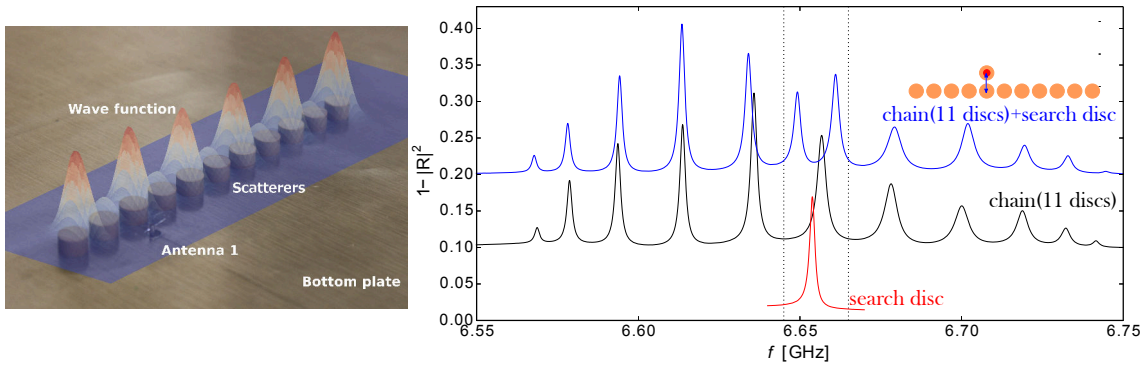


**Figure 2.6** – **Left:** Picture of the measurement of the chain containing 11 discs. Superimposed is the measured field  $|B_z|$  for the state which corresponds to the central frequency of the chain (called  $\Psi_c$  in the text). **Right:** Reflection spectra  $1 - |R|^2$  measured at antenna 1 (kink antenna) for the search disc, the chain containing 11 discs and for the chain containing 11 discs, where the search disc is coupled at. How this search disc is coupled to the chain is indicated by the inset in the upper right corner.

to the eigenfrequency. Once this has happened the search successfully reveals the SD with the eigenfrequency we have been looking for.

We start with a linear chain with a length of 11 disc resonators. The used chain discs have an eigenfrequency of  $\nu = 6.655 \pm 0.003$  GHz. If no SD is attached, the measured reflection spectra using the kink antenna (denoted antenna 1 in figure 2.6) looks like the one presented in figure 2.6 (black line). The spectrum is showing 11 resonances which correspond to the 11 non degenerated eigenvalues of the chain just like it is the case for 11 coupled mechanical pendula.

In the following we investigate the central eigenfrequency of the chain. This is the resonance (black line) between the two dashed lines in figure 2.6. The corresponding central eigenstate  $\Psi_c$  can be written as

$$\Psi_c = \frac{1}{\sqrt{\frac{(N+1)}{2}}} \cos\left(\frac{m+1}{2}\pi\right) \quad \text{with } m = 1, 2, \dots, N \text{ with } N \in 2\mathbb{N} + 1. \quad (2.6)$$

The eigenfrequency of this state coincides with the eigenfrequency of a single disc  $\nu$  (see appendix A for a detailed derivation of  $\Psi_c$  and its eigenfrequency). With the loop antenna we can measure the intensity profile of  $\Psi_c$ , which corresponds to  $B_z$  (see figure 2.6, left). We recognise that the measured pattern follows the theoretical cosine function illuminating every second disc, which is also reflected by its normalisation of  $1/\sqrt{(N+1)/2}$  (see appendix A). The resonance of the SD can also be measured (using the loop or the kink antenna). We can see from figure 2.6 that the resonance of the SD lies close to the central frequency of the chain. If we bring now the search disc (eigenfrequency  $\nu_1 = 6.654$  GHz) close to the chain in the manner shown by the inset in figure 2.6, we force the two states to undergo an avoided crossing. In our system we control the coupling of the SD to the chain by lowering or altering the distance between the SD and the chain. The distance

## 2.2. Quantum Search and its Experimental Implementation

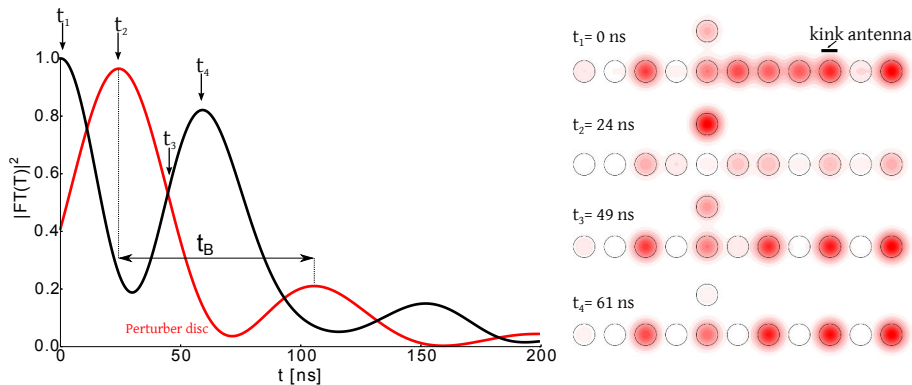


**Figure 2.7 – Left:** The result of the Fourier transform of the transmission signal  $T$ . The black line denotes the result of the chain discs integrated over each 2nd disc. This corresponds to  $|\Psi_c(t)|^2$ .  $t_B$  denotes the beating time which is the re-occurrence time of the signal at the SD. The result of the Fourier transform at the SD is shown in red. The signals are normalised such as  $|\Psi_c(0)|^2 = 1$ . **Right:** The intensities of the Fourier transformed signal which is obtained above each disc for given times  $t_i$ .

between the disc and the chain is fixed to 14.7 mm, whereas the distance between the chain discs is 11.4 mm assuring the strong coupling of the discs within the chain and the weak coupling of the SD to the chain (see [Bar10] for details on the coupling in such a system).

If we want to get from the frequency space to the time domain we have to apply a Fourier transform to the measured transmission signals. We position the loop antenna above each disc and measure the transmission from the kink antenna to the loop antenna and afterwards we take this data and we perform a Fourier transform in the frequency range indicated with the dotted lines in figure 2.6. The Fourier transform reveals how the intensities of the two states develops. The result of this Fourier transform for the chain with 11 discs, where an additional search site is coupled to, is shown in figure 2.7. In this figure we see how the system evolves in time. First, we excite the chain state  $\Psi_c$ , which is coupled to the SD. Then we obtain a beating pattern between  $\Psi_c$  and the localised state of the SD. As we look at intensities, figure 2.7 reflects only the envelope of the time development of the beating. At  $t_2 = 24$  ns the energy focuses in the localised eigenstate of the SD. At this point we have clearly found the SD within our system. The beating time  $t_B$  is defined as the time of the re-occurrence of the signal at the SD. This time can be understood as twice the search time  $t_s$ .

The question is how  $t_s$  is scaling with the number  $N$  which is the number of used discs in the chain. To account for the fact that just  $(N + 1)/2$  discs are enlightened we define an effective number of discs  $N' = (N + 1)/2$ . The discs which are not enlightened would be 'blind spots' anyway, i.e., to these discs we can not couple the search disc. If we would try to couple the SD to such a blind spot the search would fail.

We perform this kind of experiments for chain lengths ranging from  $N = 5$  to



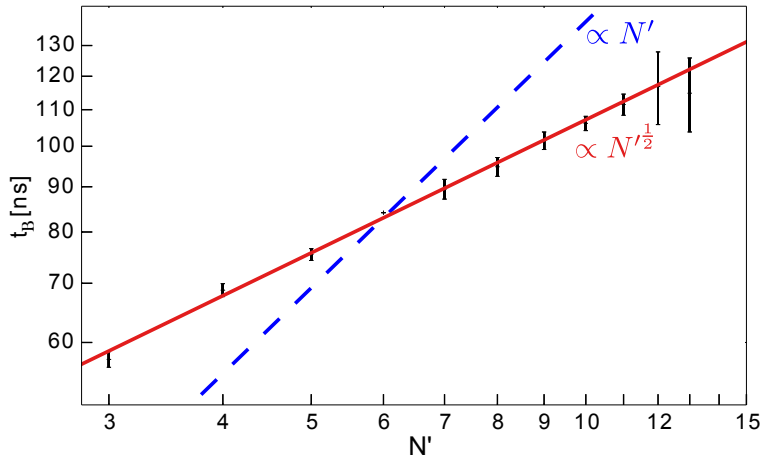


**Figure 2.8** – A log-log plot of the beating time  $t_B$  as a function of  $N' = (N + 1)/2$ . The errorbars are obtained taking multiple re-occurrences of the signal at the SD into account (up to 3). **Solid red line:** square root dependence. **Dashed line:** linear increase.

$N = 25$  discs. The positions of the kink antenna and of the SD stayed untouched throughout this process. Each time we performed a double Lorentzian fit for the two resonances obtained in the  $N + 1$  transmission measurements for the frequency range which is indicated with dotted lines in figure 2.6. That the resonances follow the description of Lorentzian functions can be seen from the Greens function defined in equation (1.20), which holds for isolated resonances as it is the case in the current set-up. This Lorentzian fit permits us to subtract the complex background coming from the  $TM_0$  mode which is always present in the system (see section 1.1 and especially table 1.1). Then the fitted Lorentzians are Fourier transformed to obtain  $t_s$ .

The error, which is indicated with errorbars in figure 2.8, is the standard deviation of the re-occurrence times  $t_B$  of up to 3 re-occurrences of the signal at the SD for different chain lengths. The obtained  $N'$  dependency is shown in figure 2.8. We see, that our obtained beating time  $t_B$  (twice the search time) follows a  $\sqrt{N'}$  behaviour. This  $\sqrt{N'}$  factor refers to the normalisation of the chain state  $\Psi_c$  as it was already discussed above. As long as we are not working in the large  $N$  limit, this normalisation factor is dominant. The enlargement of the chain by adding more and more discs will finally lead to the fact, that at some point another grid state will enter our fixed frequency window. In order to overcome this problem, one has to readjust the coupling, which in the end destroys the simple  $\sqrt{N'}$  behaviour for larger  $N$ . We notice this effect already in the presented experiment. The growing errorbar for growing  $N'$  is already an effect of other resonances coming close to the frequency interval where the avoiding crossing takes place and consequently the search becomes slower.

It turned out that working with the central frequency of the chain is a good idea since it is distributed over the whole chain and it corresponds to the eigenfrequency of the discs, i.e., we do not have to manipulate discs to change their eigenfrequency towards the frequency of the chain state. However, as we have seen in appendix A,

## 2.2. Quantum Search and its Experimental Implementation

---

this state is only dependent on the eigenfrequency of the discs. This means especially that it is not sensitive to a change of the coupling which would have been a nice tuning parameter. The tuning parameter  $\lambda$ , which remains for the modification of  $|\Psi_c\rangle$ , is the eigenfrequency of the discs forming the linear chain. One can think of changing them by modifying the boundary conditions of the discs by placing metallic objects on top as it was done in [Bar10]. One can even think about a mechanical device of an array of metallic pins for example which can be positioned simultaneously on top of the discs.

For a simple proof of principle experiment which should demonstrate how we could search for more than one SD we placed another disc (SD 2) with a different eigenfrequency of  $\nu_2 = 6.70$  GHz next to the chain (11 chain discs), where we set the distance of the SDs to the chain to be the same (14.7 mm), i.e, the coupling between the SDs and the chain is the same. Note that this added SD can not interact with the central state of the chain as its eigenfrequency is far away from eigenfrequency of central state  $\nu_{c_1} = 6.655$  GHz. We follow the procedure above and measure the transmission between the kink antenna and the loop antenna which is placed above each disc and perform a Fourier transform around the central frequency of the chain  $\nu_{c_1}$ . Just like in the case before all the energy is concentrated in the localised eigenstate of the upper SD demonstrating the actual identifying or finding of the SD. Then we exchange all chain discs, which corresponds to changing our tuning parameter  $\lambda$ , with 11 discs of an eigenfrequency around 6.695 GHz and we follow the same steps as before. This exchange of chain discs tunes the central eigenfrequency of the chain  $\nu_{c_2} \approx 6.695$  GHz to the resonance frequency of SD 2, i.e.,  $\nu_{c_2}$  is close to  $\nu_2$ .

As we can observe in figure 2.9 we do always find one of the search discs with almost the same beating frequency as we fixed the coupling to be the same (the error is in the  $1\sigma$ -limit).

This experiment shows the principle of searching for multiple discs by bringing a distributed grid state in resonance with a localised search state. This is always possible as long as one has precise information about the eigenfrequency of the search state and the control of a tuning parameter  $\lambda$  which one can tune to bring the grid state in resonance with the search disc.

The results presented so far depend strongly on the fact, that we are **not** working in the large N limit. Once one works with large system sizes, one has to use a grid structure which prohibits the appearance of a state close to the frequency region where the avoided crossing of the two relevant states takes place. This ensures that the correction factor due to the adjustment of the coupling stays sufficiently low so that the search time stays significantly below the one of a classical search. In the following we will investigate a two dimensional lattice structure, a two-dimensional honeycomb lattice, where we will show that this type of lattice is a good choice to perform such quantum search experiments for larger systems. The system in the following will contain about 10 times more discs than the system of the linear chain.

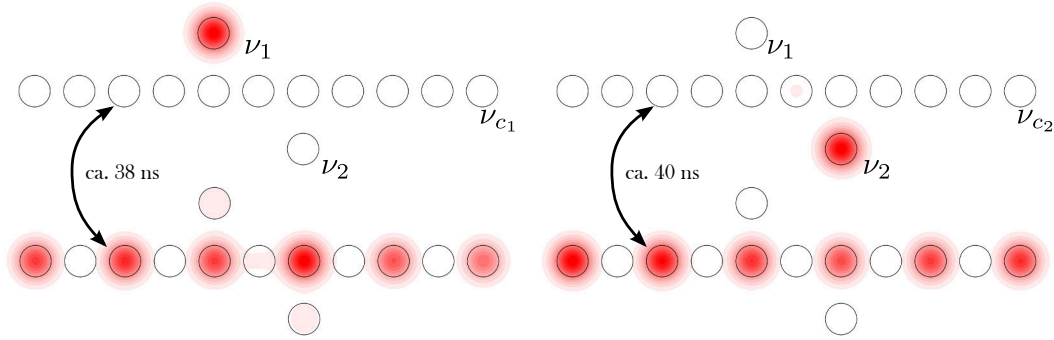


**Figure 2.9** – Intensity for the search of two different discs using a chain of 11 discs, where the eigenfrequency of the chain discs is tuned so that the central resonance of the chain undergoes an avoided crossing either with the upper disc (**Left**) or with the lower disc (**Right**). Starting point in time is when the signal arrives at the search disc for the first time, i.e., we neglect the initial transport coming from the  $\text{TM}_0$ -mode (as it can be seen in the intensity pictures in figure 2.8 for  $t_1 = 0$ ). We showed for each case two pictures. One is the picture where the total intensity is maximal for the localised eigenstate  $|s\rangle$  of the SDs characterized by their frequencies  $\nu_1$  or  $\nu_2$ . The other one shows the case for maximal intensity of  $|\Psi_c(t)|^2$ .

### 2.2.3 The Honeycomb Lattice

Since we have a formal correspondence between quantum mechanics and the electromagnetic system defined by disc resonators (see discussion above), we can make use of a well known concept in quantum mechanics, Bloch's theorem (A detailed introduction on this subject can be found in [Kit53]). Bloch's theorem comes into play, when one looks at a system of periodically arranged disc resonators which mimics a system of periodically arranged potentials (as already indicated in section 2.1.2 above).

The Hamiltonian  $H$  of such a system can be defined as

$$H = \sum_{l=1}^N H_l, \quad \text{with} \quad H_l = H_0 + \Delta V, \quad (2.7)$$

where  $\Delta V$  takes into account the contributions from neighbouring discs and  $H_0$  describes the Hamiltonian for a single isolated disc with its Bessel-like eigenfunctions (called  $\Phi^j$  in this section) described above.  $N$  is the total number of discs ( $N \gg 1$ ). Such an Hamiltonian is referred to as tight-binding Hamiltonian as it assumes that the total Hamiltonian can be described as a sum of the 'local' unperturbed Hamiltonian  $H_0$  and additional potential contributions  $\Delta V$  of neighbouring sites.

To solve the complete Schrödinger equation of the system  $H\Psi_{\mathbf{k}} = \epsilon_{\mathbf{k}}\Psi_{\mathbf{k}}$  we have to introduce Bloch functions  $\Psi_{\mathbf{k}}(\mathbf{r})$  ( $\mathbf{k}$  stands for the vector of the quasi-momentum in the Bloch formalism). For a system with two sites per unit cell we can write

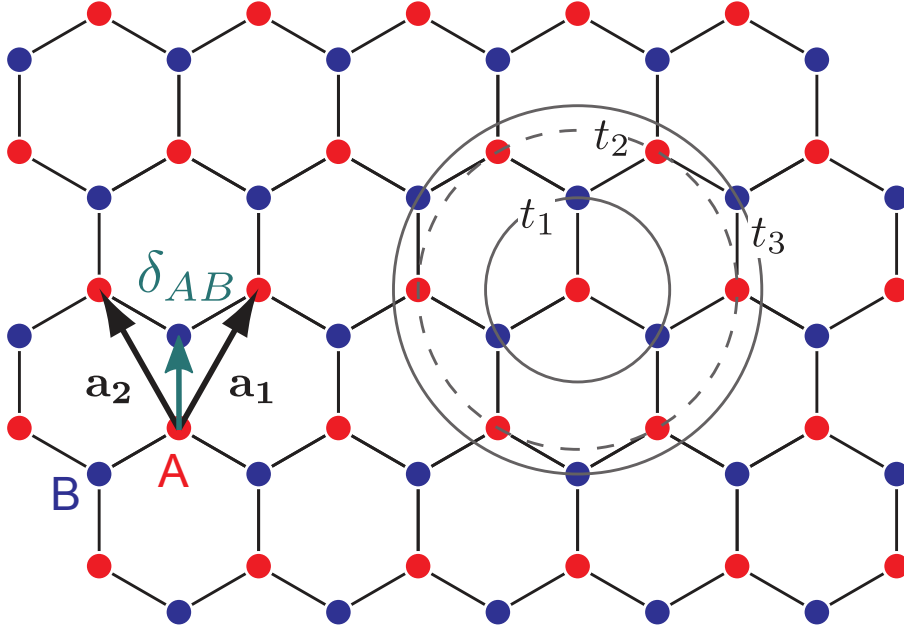


**Figure 2.10** – Sketch of the honeycomb lattice consisting of two sublattices  $A$  (red) and  $B$  (blue).  $\mathbf{a}_1$  and  $\mathbf{a}_2$  define the basis vectors of the unit cell of the Bravais lattice, which are connected to the lattice constant  $a$  via  $\mathbf{a}_1 = a/2(\sqrt{3}, 3)$  and  $\mathbf{a}_2 = a/2(-\sqrt{3}, 3)$ . The circles mark the first, second and third nearest neighbours together with their coupling parameters  $t_1$ ,  $t_2$  and  $t_3$  [Bell3a]

$\Psi_{\mathbf{k}}(\mathbf{r})$  as a superposition of two Bloch functions  $\Psi^A$  and  $\Psi^B$  such as

$$\Psi_{\mathbf{k}}(\mathbf{r}) = a_{\mathbf{k}}\Psi_{\mathbf{k}}^A + b_{\mathbf{k}}\Psi_{\mathbf{k}}^B, \quad \text{with} \quad \Psi_{\mathbf{k}}^j(\mathbf{r}) = \sum_{\mathbf{R}_l} e^{i\mathbf{k}\mathbf{R}_l} \phi^j(\mathbf{r} + \boldsymbol{\delta}_j - \mathbf{R}_l), \quad (2.8)$$

$$H_0\phi^j = \epsilon^j\phi^j, \quad \text{and} \quad \int d\mathbf{r}^2 \phi^{(j)\star}\phi^{(j)} = 1, \quad (2.9)$$

where  $j = A, B$  labels the atom of the sublattices  $A$  and  $B$ .  $\boldsymbol{\delta}_j$  is the vector which connects the Bravais lattice with the site of the  $j$  atom within the unit cell. The definition of  $\boldsymbol{\delta}_j$  will help us to simplify the equations later on as it allows us to connect the different sublattices.  $\mathbf{R}_l$  is composed of the Bravais lattice vectors  $\mathbf{R}_l = m_l\mathbf{a}_1 + n_l\mathbf{a}_2$ , where  $m_l$  and  $n_l$  are integers (see figure 2.10). We multiply the Schrödinger equation with  $\Psi_{\mathbf{k}}^*$  to obtain the hermitian Hamilton matrix  $\mathcal{H}_{\mathcal{TB}}$  in the Bloch basis ( $\mathcal{TB}$  indicates the tight binding approximation).

$$\Psi_{\mathbf{k}}^* H \Psi_{\mathbf{k}} = \epsilon_{\mathbf{k}} \Psi_{\mathbf{k}}^* \Psi_{\mathbf{k}} \iff (a_{\mathbf{k}}^*, b_{\mathbf{k}}^*) \mathcal{H}_{\mathcal{TB}} \begin{pmatrix} a_{\mathbf{k}} \\ b_{\mathbf{k}} \end{pmatrix} = \epsilon_{\mathbf{k}} (a_{\mathbf{k}}^*, b_{\mathbf{k}}^*) \mathcal{S}_{\mathcal{TB}} \begin{pmatrix} a_{\mathbf{k}} \\ b_{\mathbf{k}} \end{pmatrix}, \quad (2.10)$$

where the new Hamiltonian  $\mathcal{H}_{\mathcal{TB}}$  and  $\mathcal{S}_{\mathcal{TB}}$  are defined as

$$\mathcal{H}_{\mathcal{TB}} = \begin{pmatrix} \Psi_{\mathbf{k}}^{(A)\star} H \Psi_{\mathbf{k}}^{(A)} & \Psi_{\mathbf{k}}^{(A)\star} H \Psi_{\mathbf{k}}^{(B)} \\ \Psi_{\mathbf{k}}^{(B)\star} H \Psi_{\mathbf{k}}^{(A)} & \Psi_{\mathbf{k}}^{(B)\star} H \Psi_{\mathbf{k}}^{(B)} \end{pmatrix} = \begin{pmatrix} \mathcal{H}^{AA} & \mathcal{H}^{AB} \\ \mathcal{H}^{BA} & \mathcal{H}^{BB} \end{pmatrix} = \mathcal{H}_{\mathcal{TB}}^\dagger \quad (2.11)$$

$$\mathcal{S}_{\mathcal{TB}} = \begin{pmatrix} \Psi_{\mathbf{k}}^{(A)\star} \Psi_{\mathbf{k}}^{(A)} & \Psi_{\mathbf{k}}^{(A)\star} \Psi_{\mathbf{k}}^{(B)} \\ \Psi_{\mathbf{k}}^{(B)\star} \Psi_{\mathbf{k}}^{(A)} & \Psi_{\mathbf{k}}^{(B)\star} \Psi_{\mathbf{k}}^{(B)} \end{pmatrix} = \mathcal{S}_{\mathcal{TB}}^\dagger. \quad (2.12)$$

Explicitly for the entries of  $\mathcal{H}_{\mathcal{TB}}$  we find:

$$\mathcal{H}_{\mathcal{TB}}^{ij} = \sum_{\mathbf{R}_l \mathbf{R}_m} e^{i\mathbf{k}(\mathbf{R}_l - \mathbf{R}_m)} \int d\mathbf{r}^2 \phi^{(i)\star}(\mathbf{r} + \boldsymbol{\delta}_i - \mathbf{R}_m) H_{lm} \phi^{(j)}(\mathbf{r} + \boldsymbol{\delta}_j - \mathbf{R}_l) \quad (2.13)$$

$$= N \sum_{\mathbf{R}_l} e^{i\mathbf{k}\mathbf{R}_l} \int d\mathbf{r}^2 \phi^{(i)\star}(\mathbf{r}) [H_0 + \Delta V] \phi^{(j)}(\mathbf{r} + \boldsymbol{\delta}_{ij} - \mathbf{R}_l) \quad (2.14)$$

$$= N(\epsilon^{(j)} s_{\mathbf{k}}^{ij} + t_{\mathbf{k}}^{ij}), \quad (2.15)$$

where  $\boldsymbol{\delta}_{ij} = \boldsymbol{\delta}_j - \boldsymbol{\delta}_i$  is connecting site  $i$  with site  $j$  in the unit cell (see for example  $\boldsymbol{\delta}_{AB}$  in figure 2.10).  $s_{\mathbf{k}}^{ij}$  and  $t_{\mathbf{k}}^{ij}$  are defined as

$$s_{\mathbf{k}}^{ij} = \sum_{\mathbf{R}_l} e^{i\mathbf{k}\mathbf{R}_l} \int d\mathbf{r}^2 \phi^{(i)\star}(\mathbf{r}) \phi^{(j)}(\mathbf{r} + \boldsymbol{\delta}_{ij} - \mathbf{R}_l) = \mathcal{S}_{\mathcal{TB}}^{i,j}/N, \quad (2.16)$$

$$t_{\mathbf{k}}^{ij} = \sum_{\mathbf{R}_l} e^{i\mathbf{k}\mathbf{R}_l} \int d\mathbf{r}^2 \phi^{(i)\star}(\mathbf{r}) \Delta V \phi^{(j)}(\mathbf{r} + \boldsymbol{\delta}_{ij} - \mathbf{R}_l). \quad (2.17)$$

We introduce names to determine the couplings.  $f_1$ ,  $f_2$  and  $f_3$  name the first, second and third nearest neighbour coupling contribution, respectively. Couplings of higher order are not included in the following. Therefore the summation terms for  $\mathcal{H}_{\mathcal{TB}}^{ij}$  reduce to

$$\mathcal{H}_{\mathcal{TB}} = \begin{pmatrix} \epsilon^A + f_2(\mathbf{k}) & f_1(\mathbf{k}) + f_3(\mathbf{k}) \\ f_1(\mathbf{k}) + f_3(\mathbf{k}) & \epsilon^B + f_2(\mathbf{k}) \end{pmatrix}. \quad (2.18)$$

The two sublattices  $A$  and  $B$  are identical such that  $\epsilon^A = \epsilon^B = \epsilon_0$ . Note that we assumed

$$s_{\mathbf{k}}^{AB} = 0 \quad \text{assuming} \quad \int d\mathbf{r}^2 \phi^{(A)\star}(\mathbf{r}) \phi^{(B)}(\mathbf{r} + \boldsymbol{\delta}_{AB}) \approx 0, \quad (2.19)$$

which would lead to small corrections for the  $t_{\mathbf{k}}^{ij}$ , which are neglected in our case. If we assume an infinite honeycomb lattice, it is a good idea to take the symmetry of the lattice into account and to define coupling parameters  $t_1$ ,  $t_2$  and  $t_3$  (indices refer to the indices of  $f_i$ , see also figure 2.10) as

$$\begin{aligned} -t_1 &= \int d\mathbf{r}^2 \phi^{(A)\star}(\mathbf{r}) \Delta V \phi^{(B)}(\mathbf{r} + \boldsymbol{\delta}_{AB}), \\ -t_2 &= \int d\mathbf{r}^2 \phi^{(A)\star}(\mathbf{r}) \Delta V \phi^{(B)}(\mathbf{r} + \mathbf{a}_1), \\ -t_3 &= \int d\mathbf{r}^2 \phi^{(A)\star}(\mathbf{r}) \Delta V \phi^{(B)}(\mathbf{r} + \boldsymbol{\delta}_{AB} + (\mathbf{a}_1 - \mathbf{a}_2)). \end{aligned} \quad (2.20)$$

Refer to figure 2.10 for the definition of  $\boldsymbol{\delta}_{AB}$ .

This simplifies the definition of the  $f_i$  to

$$\begin{aligned}
 f_1(\mathbf{k}) &= -t_1(1 + e^{i\mathbf{k}\mathbf{a}_1} + e^{i\mathbf{k}\mathbf{a}_2}), \\
 f_2(\mathbf{k}) &= -2t_2\left(\cos(\mathbf{k}\mathbf{a}_1) + \cos(\mathbf{k}\mathbf{a}_2) + \cos(k(\mathbf{a}_1 - \mathbf{a}_2))\right), \\
 f_3(\mathbf{k}) &= -t_3(e^{i\mathbf{k}(\mathbf{a}_1+\mathbf{a}_2)} + e^{i\mathbf{k}(\mathbf{a}_1-\mathbf{a}_2)} + e^{i\mathbf{k}(\mathbf{a}_2-\mathbf{a}_1)}).
 \end{aligned} \tag{2.21}$$

The energy spectrum of  $\epsilon(k)$  of  $\mathcal{H}_{\mathcal{T}B}$  can immediately be determined by calculating the eigenvalue spectrum of  $\mathcal{H}_{\mathcal{T}B}$ , i.e.,

$$\epsilon(\mathbf{k}) - \epsilon_0 = f_2(\mathbf{k}) \pm |f_1(\mathbf{k}) + f_3(\mathbf{k})|. \tag{2.22}$$

We end up with two energy bands which touch for  $f_1 = f_3 = 0$ . This point is called Dirac point  $\mathbf{k} = \mathbf{K}_D$  and it is defined by  $\mathbf{K}_D \cdot \mathbf{a}_1 = \pm 2\pi/3$ ,  $\mathbf{K}_D \cdot \mathbf{a}_2 = \mp 2\pi/3$ . One can calculate that  $\epsilon_D = \epsilon(\mathbf{K}_D) = \epsilon_0 + 3t_2$  (compare with [Ben11, Kun11, Bel13a]). Once one has found a relation to describe the energy dispersion relation  $\epsilon(\mathbf{k})$  it is worth looking at the density of states (DOS), which denotes the number of states per energy unit as can be seen from its definition for the case of a continuous dispersion relation in two dimensions:

$$\text{DOS}(\epsilon) = \rho(\epsilon) \propto \int d^2\mathbf{k} \delta(\epsilon - \epsilon(\mathbf{k})), \tag{2.23}$$

where  $\delta$  denotes here the Dirac delta function. Figure 2.11 shows how the DOS for a honeycomb lattice looks like. Especially one can visualise the effect, when second and third nearest neighbour coupling ( $t_2$  and  $t_3$ ) kicks in. If second and third nearest neighbour coupling are considered,  $\epsilon_D$  is shifted and the former symmetrical shape of the bands is destroyed. This can also be observed experimentally for honeycomb lattices of our dielectric resonators [Bel13a].

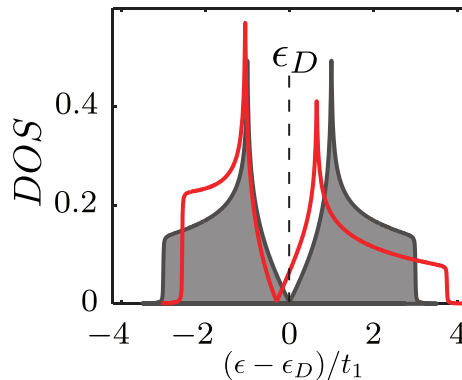


**Figure 2.11** – Density of states  $DOS$  for an infinite honeycomb lattice for two sets of coupling parameters  $t_i$ . **Gray area:**  $DOS$  for  $t_1 = -1$  and  $t_2 = t_3 = 0$ ; **Red curve:**  $DOS$  for  $t_1 = -1$ ,  $t_2 = -0.1$  and  $t_3 = -0.05$ .  $\epsilon_D$  denotes the Dirac point where the two energy bands touch [Bel13a]

### 2.2.4 Graphene

A famous material showing the honeycomb lattice structure described above is graphene. Graphene became famous for the possibility it offers to modify its charge carrier density by applying a simple gate voltage [Nov04]. From then on the idea was born to create electronic devices based on graphene structures. It was shown that the fabrication of graphene-based transistors is indeed feasible [Lin10].

Graphene is made from carbon atoms which form a two dimensional honeycomb lattice, exactly like the one shown above (see figure 2.10). The atomic ground state for carbon is  $1s^2 2s^2 2p^2$ , i.e., each orbital  $1s$ ,  $2s$  and  $2p$  (there are three p-orbitals  $p_x$ ,  $p_y$  and  $p_z$ ) is occupied with 2 electrons. The inner shell consists of  $1s$  and the outer shell of  $2s$  and  $2p$ . One possible excited state of carbon is  $\langle 2s, 2p_x, 2p_y, 2p_z \rangle$ . The excitation energy of this state is rather low  $\approx 4$  eV [Roh94]. This energy can be easily paid by forming covalent bonds with an hydrogen or an oxygen atom for example. This is why carbon forms the basis of organic chemistry.

Atomic orbitals can also hybridise to form other structures. The interesting hybridisation in the case of graphene is the  $sp^2$  hybridisation of the carbon atoms. This means the  $2s$  orbital and two  $2p$  orbitals form new hybridised orbitals ( $|sp_1^2\rangle$ ,  $|sp_2^2\rangle$  and  $|sp_3^2\rangle$ ) which are oriented in the  $xy$ -plane and which have a mutual angle of  $120^\circ$ . This angle enables the carbon to form honeycomb structures. An arrangement of six carbon atoms which are  $sp^2$  hybridised can form a perfect hexagon. If the remaining  $sp^2$  orbital is bond with an hydrogen atom, one speaks of benzene, which consists of 6 carbon atoms forming a hexagon and 6 added hydrogen atoms. The remaining  $p$ -orbital is oriented in the  $z$  direction and it is able to form an additional bonding ( $\pi$ -bond) with neighbouring carbon atoms. There are three of these  $\pi$ -bonds in benzene and they are delocalised.

The hydrogen atoms can be replaced by other carbon atoms which form themselves honeycomb structures and in the end one observes a two dimensional crystal of carbon-hexagons with totally delocalised  $p$ -electrons (forming the  $\pi$ -bonds). Such a crystal structure is called graphene. This was just a very brief introduction to graphene and its application. More information can be found in [Cas09, Ali16].

We already calculated the DOS of graphene (see section 2.2.3) when we investigated the honeycomb lattice. It remains the question: how can we measure this density of states in our experiment? In chapter 1 we showed that the scattering matrix entries can be obtained using antenna measurements. The local density of states  $\rho(\mathbf{r}, \epsilon)$  for a discrete number of isolated states follows [Stö99]:

$$\rho_l(\mathbf{r}, f) = -\frac{1}{\pi} \text{Im}(\hat{G}(\mathbf{r}, \mathbf{r}, f)) = \sum_n |\Psi_n(\mathbf{r})|^2 \delta(f - f_n). \quad (2.24)$$

We used here  $\hat{G}(\mathbf{r}, \mathbf{r}, f)$  and not  $\hat{G}(\mathbf{r}, \mathbf{r}, k)$  as it was defined in chapter 1. But this changes only constants and is not of greater importance. We replaced also  $\epsilon$  by  $f$  which also leads to changes in constants only. The local density of states contains

## 2.2. Quantum Search and its Experimental Implementation

---

only the information of such states with  $|\Psi_n(\mathbf{r})|^2 \neq 0$ . Assume for example you excite a two dimensional crystal at a point  $\tilde{\mathbf{r}}$ , where a certain state is 0 meaning that  $|\Psi_l(\tilde{\mathbf{r}})|^2 = 0$ . This state will not be accounted for in the local density of states. Thus, the full information of the DOS is only obtained measuring the local density of states throughout the whole crystal. The total density of states  $\rho(\epsilon)$  is then recovered using  $\int d\mathbf{r} \rho_l(\mathbf{r}, f)$ .

The connection between the observables in our experiment and the local density of states is the  $g$ -function [Bel13a]:

$$g(\mathbf{r}, f) = \frac{|S_{ii}(f)|^2}{\langle |S_{ii}(f)|^2 \rangle_f} \varphi'_{ii}(f) \quad (2.25)$$

$$\text{with } \varphi'_{ii} = \frac{\text{Im}(S'_{ii})\text{Re}(S_{ii}) - \text{Im}(S_{11})\text{Re}(S'_{ii})}{|S_{ii}|^2}. \quad (2.26)$$

The index  $i$  denotes the antenna such that 1 indicates the kink antenna and 2 denotes the loop antenna.  $S_{ij}$  follows the definition given in chapter 1 for attached antennas. Thus  $S_{22}$  corresponds in our set-up to the reflection measurement at the loop antenna. Variables which are derivatives with respect to the frequency are marked with a ( $'$ ). The brackets  $\langle \dots \rangle_f$  indicate an average over the whole frequency range. It was shown that  $g$  and  $\rho_l(\mathbf{r}, f)$  are linked following [Bel13a]:

$$g(\mathbf{r}, f) = -\frac{\gamma}{\Gamma \langle |S_{ii}|^2 \rangle} \rho_l(\mathbf{r}, f) = -\frac{\gamma}{\Gamma \langle |S_{ii}|^2 \rangle} \sum_n |\Psi_n(\mathbf{r})|^2 \delta(f - f_n). \quad (2.27)$$

The modulus of the eigenstate  $\Psi_n$  can be obtained by taking the maximum value of  $g$  at the frequency  $f_n$ . The factor  $-\gamma/(\Gamma \langle |S_{ii}|^2 \rangle)$  renormalises  $\rho_l$  (see equation (1.19) for the definition of  $S_{ii}$ ,  $\gamma$  and  $\Gamma$ ). Thus the effects coming from neighbouring resonances and the opening of the system due to the antennas are taken into account. These effects are important as they modify the baseline.

Finally we got an idea on how to measure the DOS for our dielectric disc system. The graphene-lattice we are going to investigate is shown in figure 2.12. We will position the moveable loop antenna (orange circle in figure 2.12) above each disc and measure the reflection, which corresponds in the chosen notation to  $S_{22}$ , in the frequency range shown in figure 2.12. This allows us to calculate the  $g$ -function according to equations (2.25, 2.26), which refers to the local density of states in the way shown above. Since we measure at all disc positions we have the full information about the DOS, which is calculated by integrating the local density of states over all obtained positions. We end up with the DOS shown in figure 2.12 for a graphene-like lattice of 216 dielectric discs.

We chose a lattice with special edges, so called armchair edges. These edges are chosen, because honeycomb lattices with these edges do not have 'edge-states' whose energies lie typically at or close to the Dirac point and which are mainly localised at the boundaries of the lattice (see [Bel14] for a detailed discussion). As we want to perform the quantum search close to the Dirac point using a distributed grid state, the appearance of these localised edge states should be avoided.



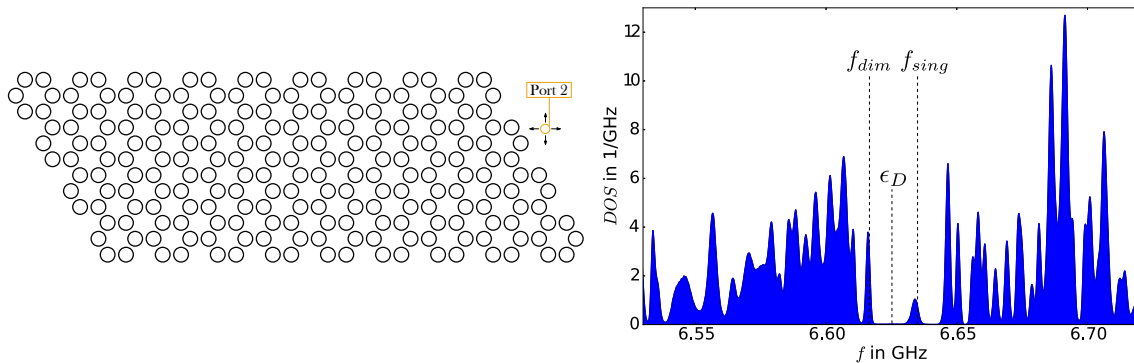


**Figure 2.12** – *Left*: Sketch of the graphene-lattice of 216 discs. The distance between the discs within the flake is 10 mm. The orange circle indicates the moveable loop antenna, which is connected to port 2 of the vector network analyser. **Right**: Measured DOS for the shown lattice. The DOS is normalised so that the frequency integral is equal to one ( $\int \rho_l(\mathbf{r}, f) d\mathbf{r} / \int \rho_l(\mathbf{r}, f) d\mathbf{r} df$ ). The Dirac point energy  $\epsilon_D$  is indicated according to the previous section. Later on, we will add two dimer discs (lower resonance of this dimer is indicated with  $f_{dim}$ ) and a single disc (resonance is indicated with  $f_{sing}$ ) (see section 2.2.5 and figure 2.13).

## 2.2.5 Quantum Search on the Graphene-lattice

As we are now able to identify the Dirac point, the point where the two bands merge (see figure 2.12). We can look for isolated resonances in its vicinity to find distributed grid states to perform the quantum search. Indeed looking at the measured DOS (figure 2.12) we can identify two isolated resonances. One above and one below the Dirac point. We will use two different localised search states to couple to these isolated grid states. One localised state will be the lowest state of a two disc system. Two coupled discs form what is called a dimer. Such a dimer shows, just like two coupled pendula, two eigenstates, a totally symmetric state and a totally anti-symmetric one. One has a good experimental control of these two appearing dimer resonances. Their eigenenergies (resonance positions) can be easily modified just by changing the intra dimer distance between the two discs [Bar13]. The eigenfrequency of the lower dimer state is indicated with a dashed line denoted with  $f_{dim}$  in figure 2.12. The other localised state we are going to use is the one of a single disc, whose eigenfrequency is close to a resonance above the Dirac point. The eigenfrequency of the single disc is marked with a dashed line (denoted with  $f_{sing}$ ) in figure 2.12.

Experimentally we established the same situation as before for the quantum search on the linear chain (see section 2.2.1). Again we will measure the transmission between the kink antenna and the loop antenna which is positioned above each disc (see figures 2.12 and 2.13). Once we have the full transmission information we can perform a Fourier transform to get the time development of the beating between the grid state and the search state. We will perform two separate Fourier transforms for small frequency windows ([6.611 GHz, 6.622 GHz] and [6.630 GHz, 6.639 GHz]) around the dimer resonance and around the single disc resonance. The result of this procedure is shown in figure 2.14.

## 2.2. Quantum Search and its Experimental Implementation

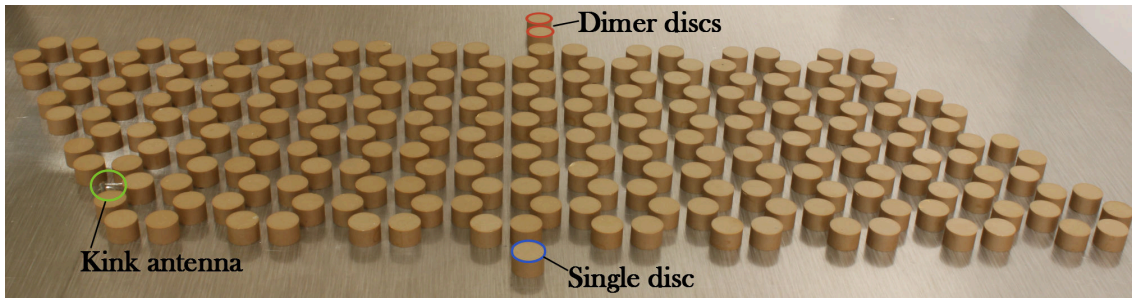


**Figure 2.13** – Picture of the set-up of the used graphene-lattice (compare with figure 2.12), where we added two discs forming a dimer (top) and a single disc (bottom) carrying the localised search states. The intra dimer distance is 9.5 mm.

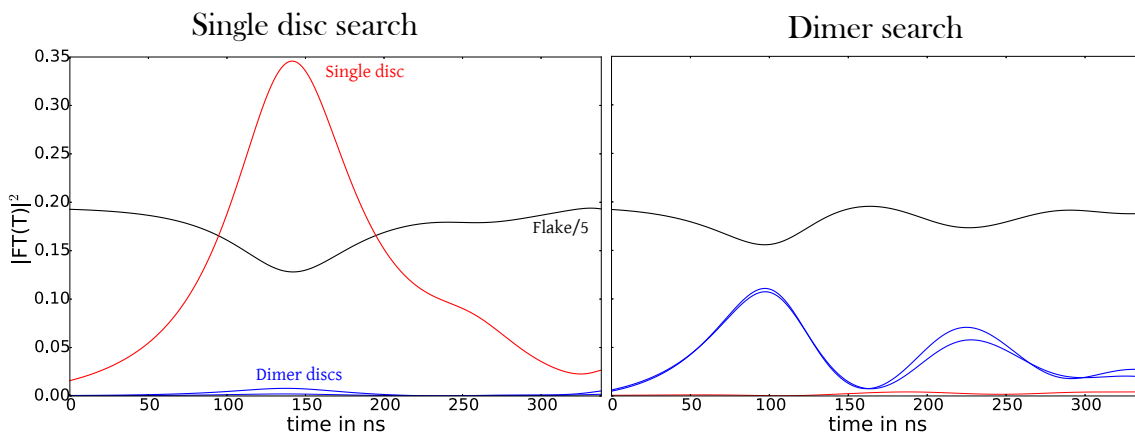


**Figure 2.14** – Result of the Fourier transform for the two frequency windows around the two search states (see details in the main text). The single disc search is shown on the **left**. The dimer search is shown on the **right**. The black line is the integrated intensity of the Fourier transform of the transmission matrix:  $T \int |FT(T)|^2 dx dy$  over the disc positions  $(x, y)$  of the graphene lattice divided by a factor of 5 to make it easier to compare it with the other signals. The red(blue) line(s) is(are) the intensity(intensities) at the single disc(the dimer discs). The normalisation is done such that  $\int |FT(T)|^2 dx dy = 1$  for all times (integration is done over all disc positions).

The signal is at first localised in the grid ( $\approx 98\%$ ) for both search cases. In the case of the single disc search the signal arrives after 142 ns at the single disc, where it shows up as a localised state (see left hand side in figure 2.15). About 35% of the intensity localises at the disc. Which is far more than the intensity at any other given disc in the system ( $\approx 65/216\%$ ). This means we have undoubtedly found the single disc within our system. The fact that we reach about 35% and not 100% shows already that our frequency window we chose to create the time information already contained small contributions from other grid states, which nevertheless did not lead to a fail of the quantum search!

The same localisation takes place for the case where we search for the two dimer discs, where the intensity localises to 25% at the dimer discs, which is still enough to do a clear distinction between them and the rest of the grid as we can see in figure 2.15.

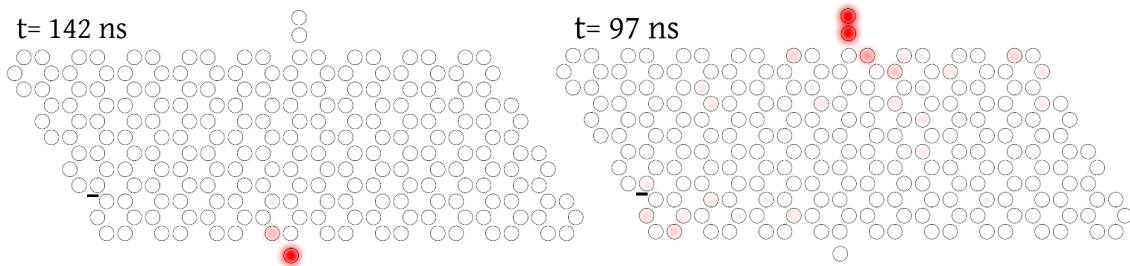


**Figure 2.15** – Intensity  $|FT(T)|^2$  plot showing the intensity distribution over the grid for the time when the search state is found. **Left:** The case where we search for the single disc (bottom of the lattice). **Right:** The case where we search for the dimer discs (top of the lattice).

One might ask why the search states are found at two different times, whereas the distance of the search items (dimer and single disc) is the same (12 nm see figure 2.14). To understand the difference in the search time one has to consider that the grid state we are using (states close to the Dirac point) are not necessary states which are uniformly distributed over the grid. It can be even worse in some cases. The grid states might include sites (discs) of 0 intensity. A search state coupled to these 'blind spots' can not be searched for as we already explained for the linear chain case. This is not the case for our graphene-lattice states as we see a clear localisation. The coupling of the search state and the grid state, however, which is proportional to  $\langle s|\Phi(\lambda)\rangle$ , does not have to be same for the two search cases neither. Therefore we end up with two different search times for the two cases. Note that the point of the excitation of the grid state must not be a blind spot of the grid state either, if one wants to perform a quantum search with this kind of set-up.

**Thus, one has to take carefully into account where one places the search items and where one excites the grid state, if one is working with a non-uniform-distributed grid state.** Our experiment can even be seen as a kind of switch. Depending on the energy with which one excites the grid, one can either direct a signal to one side of the flake or to another if one uses another excitation frequency. Therefore one could interpret the graphene-lattice itself as a switch directing a signal to a certain location.

In principle the defects can also be placed inside the grid [Fou14]. It was demonstrated that the search is still possible if one can achieve a small coupling between the search site, which is placed directly inside the lattice, and its neighbouring sites [Fou14]. In our experiment this is not a simple task, because if we introduce a search site into the grid, the coupling to the neighbouring discs are automatically defined by the distances between the search disc and its neighbours. Therefore we have no parameter to adjust the coupling with the current set-up. But one can think of course of modifying the set-up. One can introduce for example an antenna where the coupling is adjustable (by changing the length of the antenna for example) at the position where the search disc should be positioned in the lattice. This antenna could be connected with another antenna and this second antenna can be placed

in the vicinity of the search disc. By using two antennas with adjustable couplings we have again the possibility to establish an adjustable coupling between the search disc and the grid which can be tuned to be small enough so that the search can work.

## 2.3 CONCLUSION

In this chapter we showed that the quantum search is an interesting transport phenomena, which can be carried out in our tight binding analogue of coupled dielectric discs. I tried to convey the idea that one can understand our system of coupled dielectric resonators as a system of potential wells. We looked closely at the concept of quantum search which is a wave phenomenon using interference of an distributed lattice state  $|\Phi_0\rangle$  with a localised state  $|s\rangle$ . We could search for this localised state by exciting the lattice state to which the localised state couples and then look at the resulting beating pattern. At some point during this beating process the wave localised at the search state. We observed that the search time  $t_s$  can be understood as half of the beating time, which is defined by the re-occurrence time of the signal at the search state.

At first we investigated a linear chain of dielectric discs. To this chain we coupled an additional disc which represented the search state we wanted to look for. We demonstrated explicitly for a chain of 11 discs that we are able to make the distributed state of the lattice interact with the localised state of an additional disc, which resulted in the described beating phenomenon.

In a second step we enlarged these linear chains and investigated how the search time  $t_s$  depended on the total number  $N$  of chain discs. We found the theoretically predicted dependency of  $t_s \approx \sqrt{N}$ , where we varied  $N$  between 3 and 13. Using the chain arrangement of discs and two different search sites we demonstrated how a search for different sites can be performed.

In the following, we changed the lattice from a simple linear chain to a honeycomb lattice, which could be seen as an analogue of a graphene lattice. One speaks in this context of artificial graphene.

The graphene lattice with its Dirac point and its linear energy dispersion around this point is a two dimensional structure where an effective quantum search can be performed [Fou14]. We presented in a proof of principle experiment using 216 discs forming a graphene-lattice, that indeed a quantum search in the vicinity of this point can be performed. We even paved the way for a possible application of the quantum search by connecting it to the idea of a graphene based switch. Adjusting the frequency of the grid excitation we can direct a microwave signal to different additional sites located at the borders of our graphene-lattice. Our findings in this chapter can also be found in [Böh15]. During my PhD thesis I was also implicated in the implementations of what is called a two dimensional Penrose-tiled quasicrystal. More information on this topic can be found in [Vig16].



# 3 *The Q-Operator*

---

## Contents

---

<b>3.1</b>	<b>Wigner-Smith Time Delay Operator . . . . .</b>	<b>48</b>
<b>3.2</b>	<b>The Derivation of the <math>Q</math>-Operator . . . . .</b>	<b>49</b>
<b>3.3</b>	<b>Eigenvalues of the <math>Q</math>-Operator . . . . .</b>	<b>50</b>
<b>3.4</b>	<b>Construction of the <math>Q</math>-Operator - A Practical Approach . . . . .</b>	<b>52</b>

---

We will now leave the context of transport in open cavities and look at transport phenomena in waveguide systems (see section 1.1). In this chapter I will lay down some theoretical concepts which have been developed to extract certain informations from a scattering system by looking at its scattering matrix  $S$  (see section 1.2). This information will help us then to use wave front shaping techniques described in chapter 4 to form a special input, which leads to an interesting behaviour of this wave front travelling through the system.

### 3.1 WIGNER-SMITH TIME DELAY OPERATOR

Eisenbud, in his PhD thesis [Eis48] from 1948, investigated the scattering of wavepackets during a collision process. He demonstrated that their time-delay  $\Delta t$  was related to the energy derivative of the scattering phase  $\delta$ . He found:

$$\Delta t = \hbar \frac{d\delta}{dE}.$$

The same result was further discussed in [Boh51] by Bohm and later on also obtained by Wigner 1955 [Wig55] (with a difference of a factor 2).

Finally, in 1959 Smith proved an alternative approach of the hermitian lifetime matrix  $Q$  which describes the residence (life) time of a scattered wavefunction  $\Psi$  in a quantum mechanical system [Smi60]. He used directly the energy derivative of the scattering matrix  $S$  (as it was defined in section 1.2) and showed that  $Q$  is related to  $S$  as a function of the energy  $E$  by

$$Q = -i\hbar S^\dagger \frac{dS}{dE}.$$

In general,  $Q$  is called the Wigner-Smith time delay operator or alternatively Eisenbud-Wigner-Smith operator. It can be represented as a matrix, the so called Wigner-Smith time delay matrix (**WSTDM**), if one assumes that  $S$  denotes the scattering matrix given in a certain basis (plane wave basis for example, as in section 1.2). If one assumes that the scattering matrix  $S$  is unitary meaning  $S^\dagger S = \mathbb{1}$  ( $\mathbb{1}$  is the identity matrix) one can deduce that:

$$\begin{aligned} \frac{dS^\dagger S}{dE} &= \frac{d\mathbb{1}}{dE} = 0 \\ \Rightarrow \frac{dS^\dagger S}{dE} &= \frac{dS^\dagger}{dE} S + S^\dagger \frac{dS}{dE} = 0 \\ \Rightarrow \frac{dS^\dagger}{dE} S &= -S^\dagger \frac{dS}{dE} \\ \Rightarrow Q^\dagger &= Q. \end{aligned} \tag{3.1}$$

This means that the WSTDM for unitary scattering matrices  $S$  is hermitian and posses only real eigenvalues. Because of its hermiticity one finds sometimes alternative expression for  $Q$  like in [Rot11]:

$$Q = i\hbar \frac{dS^\dagger}{dE} S.$$

The scattering matrix normally contains all informations about the scattering system, i.e., it contains the reflection parts  $S_{ii}$  and the transmission parts  $S_{ij}$  (see section 1.2). Regarding experiments, one has often access to the transmission quantities  $S_{ij}$  ( $T$ ,  $T'$ ) only (see definition in section 1.2). This inspired Ambichl and Brandstötter to define an operator similarly to the WSTDM, but taking into ac-

## 3.2. The Derivation of the $Q$ -Operator

---

count only the transmission matrix  $T$ . They called their operator the  $q$ -operator (see [Amb12, Bra16, Gir16]):

$$q_\alpha = -iT^{-1}(\alpha) \frac{dT(\alpha)}{d\alpha}. \quad (3.2)$$

They introduced their operator depending on a parameter  $\alpha$ . If this parameter  $\alpha$  is the energy/frequency, we recover information about the time a scattering state stays within the scattering area as we will see in section 3.3 and chapter 6. The new idea is that  $\alpha$  can be a coordinate in space. The eigenvalues of such a  $q$ -operator can be associated with a kind of momentum transfer (see section 3.3).  $T^{-1}$  denotes the inverse matrix of  $T$  (see details in section 3.4).

## 3.2 THE DERIVATION OF THE $q$ -OPERATOR

In the following I explain how Ambichl and Brandstötter came up with the idea of the  $q$ -operator. The transmission matrix  $T$  maps incoming channels  $\mathbf{j}$  onto outgoing channels  $\mathbf{o}$  (see section 1.2). These channels can correspond to open modes or to single antenna sources when one thinks in terms of local excitation.

The transmission matrix  $T$  and the output  $\mathbf{o}$  shall depend on a parameter  $\alpha$  so that

$$\mathbf{o}(\alpha) = T(\alpha)\mathbf{j}. \quad (3.3)$$

The input  $\mathbf{j}$  is assumed to be constant with regard to  $\alpha$  ( $\mathbf{j}(\alpha) \equiv \mathbf{j}$ ). The input is freely adjustable as we will demonstrate in section 4.2.3 where we perform simple input shaping/wave shaping experiments.

The Taylor expansion of  $\mathbf{o}(\alpha)$  around an value  $\alpha_0$  yields:

$$\mathbf{o}(\alpha) \approx \mathbf{o}(\alpha_0) + \left. \frac{d\mathbf{o}}{d\alpha} \right|_{\alpha_0} \Delta\alpha \quad (3.4)$$

$$\stackrel{\mathbf{j}(\alpha) \equiv \mathbf{j}}{\approx} T(\alpha_0)\mathbf{j} + \left. \frac{dT(\alpha)}{d\alpha} \right|_{\alpha_0} \mathbf{j} \Delta\alpha. \quad (3.5)$$

$\Delta\alpha$  is a small change of the parameter  $\alpha$ . We demand in the following that the zero order and the first order term differ not in orientation but only by a complex factor  $c$  adding a phase and an amplitude to the vector components. Our demand can be formulated as

$$T(\alpha_0)\mathbf{j} = c \left. \frac{dT(\alpha)}{d\alpha} \right|_{\alpha_0} \mathbf{j} \Delta\alpha. \quad (3.6)$$

We can transform this in an eigenvalue problem by multiplying both sides with  $T^{-1}(ic\Delta\alpha)^{-1}$ :

$$-iT^{-1}(\alpha) \frac{dT(\alpha)}{d\alpha} \mathbf{j} = \lambda \mathbf{j}, \quad (3.7)$$

where  $\lambda$  is defined as  $\lambda = (ic\Delta\alpha)^{-1}$ .



The left side of equation (3.7) can be identified as the  $q$ -operator defined in equation (3.2). The eigenvectors of the  $q$ -operator  $\mathbf{i}_q$  are also called  $q$ -states following:

$$q_\alpha \mathbf{j}_q = \lambda_q \mathbf{j}_q, \quad \mathbf{o}_q = T \mathbf{j}_q. \quad (3.8)$$

**Note that  $q_\alpha$  in general is not Hermitian any longer, i.e., its eigenvalues are complex.** The assumption used to get to equation (3.6) is widely used in optics for example, where the  $q$ -state correspond to so called principal modes [Fan05], where  $\alpha$  is replaced by the frequency. These modes remain by construction in first order approximation unaffected by small frequency changes and so they are of great interest for multimode-fiber-communication where they help to avoid dispersive effects.

### 3.3 EIGENVALUES OF THE $q$ -OPERATOR

To understand the meaning of the eigenvalues  $\lambda$  of the  $q$ -operator, one can rewrite equation (3.7) into:

$$\begin{aligned} -i \frac{dT(\alpha)}{d\alpha} \mathbf{j} &= \lambda T(\alpha) \mathbf{j} \\ -i \frac{d\mathbf{o}}{d\alpha} &= \lambda \mathbf{o}. \end{aligned} \quad (3.9)$$

We can decompose the output  $\mathbf{o}$  into its amplitude  $|\mathbf{o}|$  and phase  $\phi$  so that  $\mathbf{o} = |\mathbf{o}(\alpha)| e^{i\phi(\alpha)}$ . The derivative of  $\mathbf{o}$  leads to:

$$\frac{d\mathbf{o}}{d\alpha} = \frac{d|\mathbf{o}|}{d\alpha} e^{i\phi(\alpha)} + i\mathbf{o} \frac{d\phi}{d\alpha} \quad (3.10)$$

$$\stackrel{(3.9)}{=} i\lambda \mathbf{o}. \quad (3.11)$$

Therefore we can derive for the eigenvalues  $\lambda$  by dividing equation (3.10) and equation (3.11) by  $i\mathbf{o}$  to obtain:

$$\lambda = \frac{d\phi}{d\alpha} - i \frac{d \ln(|\mathbf{o}|)}{d\alpha}. \quad (3.12)$$

Equation (3.12) is showing that the real part of the eigenvalue is determined by the change of the phase of the output which is also referred to as scattering phase, whereas the imaginary part is determined by the change of the amplitude of the output.

If  $\alpha$  corresponds to the angular frequency  $\omega = 2\pi f$  (energy), the derivative of the scattering phase  $d\phi/d\omega$  is related to the travelling time (delay time, see equation (3.1) and section 6.1.1 for more details) of the state passing through the scattering part of the system and the imaginary part of the eigenvalue explains how strong the scattered amplitude  $|\mathbf{o}|$  is influenced by small frequency changes. I want to give a first and simple example illustrating the connection between the derivative of the

### 3.3. Eigenvalues of the $Q$ -Operator

---

scattering phase and the travelling time (time delay). Let us assume that we have a plan wave with a wavenumber  $k$  travelling freely in  $x$ -direction. This wave can be described via:

$$P(x) = Ae^{-i(k_x x - \omega t)} = Ae^{i\Phi} \quad \text{with} \quad k_x = \sqrt{k^2 - k_y^2} = \sqrt{\frac{\omega^2}{c^2} - k_y^2}, \quad \omega = 2\pi f. \quad (3.13)$$

We assumed here an additional quantisation in  $y$ -direction which can also be set to 0. But with this example we follow the description of sinusoidal waves in a quasi one dimensional waveguide, which we will come across again in chapter 4. For the moment  $k_y$  is nothing else than just a quantisation number.

If there is no scattering and no absorption, the wave propagates freely and according to equation (3.13) we get for the phase  $\Phi$  of the wave at the position  $L$ , where  $L$  is the position where the output is defined:

$$\Phi = k_x L = \left( \sqrt{\frac{\omega^2}{c^2} - k_y^2} \right) L.$$

We set  $t = 0$ , because we are just interested in the phase change accumulated while travelling a certain distance  $L$ . This phase is indeed the scattering phase as we can write:

$$P(x = L) = TP(x = 0) \rightarrow T = 1e^{-i\Phi}, \quad (3.14)$$

where  $T$  is the transmission matrix describing free propagation with no absorption. The derivative of the transmission/scattering phase yields

$$\frac{d\Phi}{d\omega} = \frac{\omega L}{c^2 \sqrt{\frac{\omega^2}{c^2} - k_y^2}} = \frac{L}{c} \frac{\frac{\omega}{c}}{\sqrt{k^2 - k_y^2}} = \frac{L}{c} \frac{k}{\sqrt{k^2 - k_y^2}}. \quad (3.15)$$

Classically we can assume that the travelling time  $t$  equals  $L/v_x$ , where  $v_x$  is the speed in  $x$ -direction. We know that

$$\frac{k_x}{k} = \frac{v_x}{c}, \quad (3.16)$$

so we derive for the travelling time  $t$ , which is the time the wave needs to get to position  $L$ .

$$t = \frac{L}{v_x} = \frac{L}{c} \frac{k}{k_x} = \frac{L}{c} \frac{k}{\sqrt{k^2 - k_y^2}}. \quad (3.17)$$

Comparing equation (3.15) and equation (3.17) for our rather simple example one can understand the accordance of the travelling time  $t$  of the plane wave and the frequency derivative of the phase. A general derivation of the connection of the travelling time (time delay) and the derivative of the phase in the presence of a scattering potential can be found in section 6.1.1.

No matter the parameter  $\alpha$ , looking at equation (3.12) makes clear that a  $q$ -state with  $|\lambda| \ll 1$  is not sensitive to the variation of the parameter  $\alpha$ .

If we assume for example that  $\alpha$  represents the position  $x$  of an obstacle/scatterer within the scattering region, one can understand that  $q$ -states with small eigenvalues  $\lambda$  are less sensitive to the movement of this obstacle. We assume here of course that the size of the shift  $\Delta x$  is small compared to the used wavelength. Such types of  $q$ -states try to avoid the region of the obstacle (as we will see experimentally in section 4.3). Whereas for  $q$ -states with high values of  $\lambda$  the  $q$ -states focus on the central scatterer so that they are strongly affected by changing the scatterer position.

For the case  $\alpha = x$  one can look at the example of a travelling plane wave, as well. Here the scattering phase derivative  $d\Phi/dx$  can be understood as a measure of the momentum change (momentum flux change, see [Bra16] for a detailed derivation). If momentum is conserved, one can also speak of a momentum transfer onto a certain target which is positioned at  $x$ .

### 3.4 CONSTRUCTION OF THE $q$ -OPERATOR - A PRACTICAL APPROACH

To calculate the  $q$ -operator  $q_\alpha$ , one needs to evaluate  $T^{-1}$ . If  $T$  is singular or not quadratic, the inverse of  $T$  cannot be computed. This could be the case if a transport channel (for example a mode) is not transmitted or if one has more outgoing channels than incoming or vice versa.

The first step of computing  $T^{-1}$  is to compute its singular value decomposition so that  $T$  can be described as:

$$T = U\Sigma V^\dagger \quad \text{with} \quad \Sigma : \text{diagonal matrix.} \quad (3.18)$$

$U$ ,  $V$  denote complex unitary matrices.  $\Sigma$  is real and diagonal. If  $T$  is of the form  $(n_{out} \times n_{in})$ ,  $U$  has dimensions  $(n_{out} \times n_{out})$  and  $V$  has dimensions  $(n_{in} \times n_{in})$ .  $\Sigma$  is a  $(n_{out} \times n_{in})$ -matrix and contains the singular values  $\sigma_i$ .

These singular values  $\sigma$  introduce a kind of hierarchy as high singular values can be related to transmitting states showing high transmission.

We can look at the following example. Let us assume that  $n_{out} < n_{in}$  and  $N_b$  transport channels are blocked or are very low transmitting. If  $N_t = \min(n_{in}, n_{out})$ , we have  $N_t - N_b = N$  sigma values which are non zero. We can order the  $N$  sigma values such that  $\sigma_1 > \sigma_2 > \dots > \sigma_N$  and  $\Sigma$  looks like the following:

$$\Sigma = \begin{pmatrix} \sigma_1 & 0 & & & 0 \\ 0 & \ddots & 0 & & \\ & 0 & \sigma_N & & \\ 0 & & & \ddots & \dots & 0 \end{pmatrix}.$$

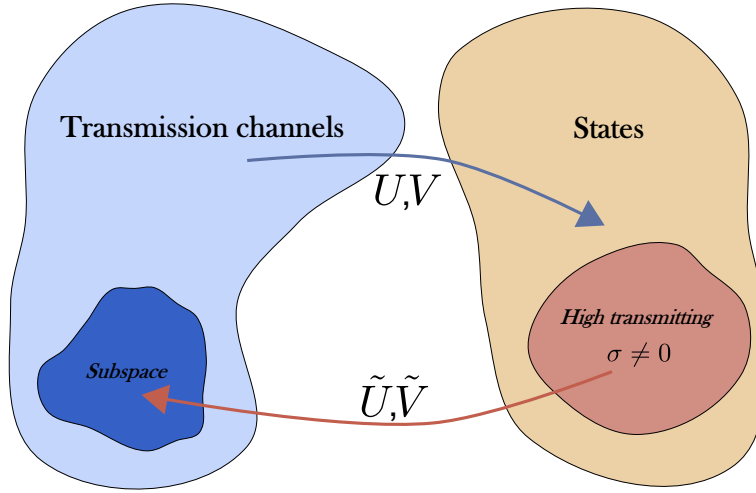


**Figure 3.1** – Scheme of reducing  $T$  to a subspace consisting of high transmitting states.

If  $T$  is diagonalisable, i.e.,  $N_b = 0$  and  $n_{out} = n_{in}$ ,  $\sigma_i$  correspond to the  $i$ -th eigenvalue of the transmission matrix  $T$ . In this case  $\sigma_1$  corresponds to the scattering state (eigenvector of  $T$ ) showing the highest transmission.

If  $N_b \neq 0$  or  $n_{out} \neq n_{in}$  we restrict ourselves to a reduced  $\Sigma$  which we call  $\tilde{\Sigma}$  and which contains only the  $N$  singular values which differ from 0. The dimension of  $\tilde{\Sigma}$  is  $(N \times N)$ . We define new transformation matrices  $\tilde{U}$  and  $\tilde{V}$  which correspond to the non zero  $\sigma$ -values. If we consider, for example, only the highest two  $\sigma$ -values to differ from 0,  $\tilde{U}$  and  $\tilde{V}$  are constructed from the original  $U$  and  $V$  by

$$U = \underbrace{\left( \begin{pmatrix} \circ \\ \circ \end{pmatrix} \begin{pmatrix} \circ \\ \circ \end{pmatrix} \cdots \right)}_{\tilde{U}}, \quad V = \underbrace{\left( \begin{pmatrix} \circ \\ \circ \end{pmatrix} \begin{pmatrix} \circ \\ \circ \end{pmatrix} \cdots \right)}_{\tilde{V}} \quad (3.19)$$

and we define the following transformation of  $T$  to get an invertible matrix by

$$\tilde{T} = \tilde{U}^\dagger T \tilde{V}, \quad T' = \tilde{U} \tilde{T} \tilde{V}^\dagger. \quad (3.20)$$

By construction we defined with this transformation a quadratic and diagonal matrix  $\tilde{T}$  which is therefore invertible. We are now working on a subspace of the original transmission channels. This is schematically illustrated in figure 3.1. To define this subspace in the original basis of  $T$ , which was of the form  $(n_{out} \times n_{in})$ , we have to re-transform  $\tilde{T}$ :

$$T_q = \tilde{U} \left( \tilde{U}^\dagger T \tilde{V} \right) \tilde{V}^\dagger. \quad (3.21)$$

$T_q$  is a reduced transmission matrix differing from the original transmission matrix  $T$ .  $T_q$  respects only high transmitting channels. Note also that  $T_q^{-1}$  remains invertible since it is defined by

$$T_q^{-1} = \tilde{V} \left( \tilde{U}^\dagger T \tilde{V} \right)^{-1} \tilde{U}^\dagger. \quad (3.22)$$

Note that  $\tilde{U}^\dagger T \tilde{V}$  is per construction invertible and that especially for  $\tilde{U}$  and  $\tilde{V}$  it is

$$\begin{aligned}\tilde{U}^\dagger \tilde{U} &= \mathbf{1}^{n_r \times n_r}, & \tilde{U} \tilde{U}^\dagger &\neq \mathbf{1}, \\ \tilde{V}^\dagger \tilde{V} &= \mathbf{1}^{n_r \times n_r}, & \tilde{V} \tilde{V}^\dagger &\neq \mathbf{1}.\end{aligned}$$

Finally, equations (3.21, 3.22) allow us to clearly define the  $q$ -operator using only the reduced transmission matrix  $T_q$  as

$$q_\alpha = -iT_q^{-1} \frac{dT_q}{d\alpha}. \quad (3.23)$$

**We are dealing now with a subspace of the transmission matrix meaning that the eigenvector of the  $q$ -operator does not necessarily have to be an eigenvector of the original transmission matrix!** The construction might not be unique, but it allows us to deal with systems showing a singular or non-quadratic transmission matrix. The construction depends on how many singular-values  $\sigma$  are taken into account.

We will see that this restriction is not a real restriction as we can still identify scattering states with special characteristics (see sections 4.3 and chapter 6). The scattering states in which we are interested are so called noiseless states of the transmitting type. These states, such as the particle-like scattering states for example (see chapter 6), are mainly living in the high transmitting subspace of the transmission matrix (as it is also discussed in [Two03, Sil03]).

It might happen that the distribution of the  $\sigma$ -values does not allow to define a clear cutting value for the small sigma values belonging to the low transmitting channels. In this case it is recommended to take into account all possible  $\sigma$ -value decompositions and to look at all the resulting eigenvalues of the  $q$ -operator. Since the real part and the imaginary part of these eigenvalues can be related to physical quantities, i.e., the time delay (see above), one can distinguish the resulting  $q$ -states in a second step according to these physical properties.

# 4 *Wave Front Shaping*

---

## Contents

---

<b>4.1</b>	<b>The Basic Idea . . . . .</b>	<b>56</b>
<b>4.2</b>	<b>Quasi-One-Dimensional Waveguide . . . . .</b>	<b>57</b>
4.2.1	<i>Experimental Realisation . . . . .</i>	57
4.2.2	<i>Theoretical Description . . . . .</i>	59
4.2.3	<i>The Empty Waveguide . . . . .</i>	63
4.2.4	<i>IQ-Modulators . . . . .</i>	70
4.2.5	<i>Waveguide Filled with Scatterers . . . . .</i>	72
4.2.6	<i>Mode Tuning . . . . .</i>	73
<b>4.3</b>	<b>Realising Q-States . . . . .</b>	<b>76</b>
4.3.1	<i>Transmission Matrix in a Scattering Environment . . . . .</i>	76
4.3.2	<i>Generating Q-States . . . . .</i>	77
4.3.3	<i>Experimental Realisation of Q-States . . . . .</i>	79
4.3.4	<i>A Coherent Perfect Absorber . . . . .</i>	83
<b>4.4</b>	<b>Conclusion . . . . .</b>	<b>86</b>

---

In the last chapter we have seen that we need experimental control about the input to generate specific scattering states,  $q$ -states, with a specific output. Designing the input to obtain a certain output is exactly in the spirit of wave front shaping. I will start to describe the basic idea behind wave front shaping and the microwave experiment (a quasi-one-dimensional waveguide) with which we are going to perform the shaping of the initial wave front. In section 4.2.6 the goal is to generate pure sinusoidal modes at the output, whereas in section 4.3.2 our aim is to focus or defocus microwaves on a target within the scattering region using only the information provided by the transmission matrix of the system. The results of this chapter will finally give us the possibility to create so called particle-like scattering states in a two-dimensional cavity (see chapter 6). But first of all we have to look closer in the basics of wave front shaping.

### 4.1 THE BASIC IDEA

Wave front shaping (alternative names: wave field shaping, optical phase conjugation) is a vast field and applied in many domains such as laser optics [Vel07, Mos12, His13, Nix13, Cha14, Ami16], the microwave domain [Hen04, Kai14, Dup15] or biomedicine [Hor15]. The typical set-up with which one performs wave front shaping is shown in figure 4.1.

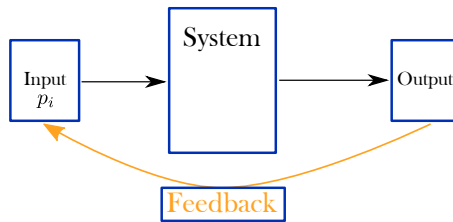


*Figure 4.1 – Sketch of a typical wave front shaping set-up.*

One needs to have an adjustable input, i.e., access to parameters  $p_i$  with which one is able to tune the input. These adjustable parameters for the input can be either phases or amplitudes or both. Phases and Amplitudes are nowadays controlled by spatial light modulators (SLMs) in optics or by IQ-modulators (see section 4.2.4) and spatial microwave modulators (SMMs) [Dup15] in the microwave domain. Once the input parameters are fixed one can emit a wave front which travels through a scattering system (like a strongly scattering opaque medium [Vel07]). After passing this scattering area an output is created depending on the properties of the scattering system.

The task is to optimise this very output. This optimisation can have different meanings. One might be interested in focussing the signal onto a specific point [Vel10] or in avoiding a certain point or region in the scattering system (see section 4.3 and [Kai14]) or in having no output at all (see coherent perfect absorber in section 4.3.4). To reach these goals one needs to adjust the input parameters  $p_i$ . This can be done by linear optimisation algorithms, that is to say one changes a single parameter,  $p_1$  for example, and one studies the changed outcome. If the outcome improves, in the sense that the output comes closer to what one wanted to achieve, one keeps the change of the parameter  $p_1$ . If one worsens our output one change  $p_1$  back to its initial value. In the next steps one goes through the other parameters in the same manner. After iterating this process for some time one might come to a point where no further improvement is achieved. This is normally the point when one stops the optimisation process. It is evident that one needs to establish a permanent feedback loop to do this kind of optimisation. (see [Kai14] for a deeper understanding of this optimisation process)

In this work we will present results which go beyond the tuning on the output by means of this kind of linear optimisation. The optimisation applied in our experiment is not based on an iterative optimisation routine, but on a single transmission

measurement, which is our basis measurement containing all the needed information to achieve various goals like avoiding a region (see section 4.3) or creating particle like scattering states (see chapter 6). But still we apply the basic concept of wave front shaping which is to tune the input based on the information of the output.

The role of what we called system before is played in this chapter by a multi-mode rectangular microwave waveguide with a tunable array of antennas as input (we make use of IQ-modulators) and variable scanning antennas to measure the output. Another concept I like to mention in this context is the concept of time-reversal [Fin92, Ler04], where the signal at the output is put in a memory, reversed in time and then send back into the system to create a specific behaviour at the input itself (see figure 4.2).

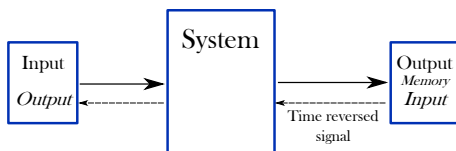


*Figure 4.2 – Sketch of a of time reversal set-up.*

This concept is quite similar to the one we are going to use. Similarly to our system the time reversal process is based on a 'basis' measurement which is basically the transmitted/reflected signal in the time domain, which contains all the necessary information.

## 4.2 QUASI-ONE-DIMENSIONAL WAVEGUIDE

### 4.2.1 Experimental Realisation

The experiment we are investigating in the following is designed to measure the transport of microwaves in a metallic multi-mode cavity. Our waveguide with a height of  $H = 8$  mm, a total length  $L = 2.38$  m, a width  $W = 10$  cm and an inter-antenna distance of  $L_a = 1.50$  m meets the waveguide condition which is defined as

$$H \ll W \ll L. \tag{4.1}$$

We have seen in section 1.1, that one distinguishes between two types of propagating modes in a rectangular waveguide system (polarisation of the electromagnetic wave). In our experiment we work with  $TE_0$  modes (see table 1.1). This means that the  $z$ -component of the electric field  $E_z$  is constant and does not depend of  $z$  (see figure 4.3).

To ensure that only the  $TE_0$  one has to work below a certain frequency limit, which is called the cut-off frequency  $\nu_c$  for the  $TE_0$  mode. Above the this limit one



would excite also the  $\text{TE}_1$  mode which we do not want in our experiment.  $k_z$  for the  $\text{TE}_1$  mode is defined according to equation (1.9) and table 1.1 ( $l = 1$ ):

$$\begin{aligned} k_z &= \frac{\pi}{H} = \frac{2\pi\nu_c}{c_0} \\ \Rightarrow \nu_c &= \frac{c_0}{2H} = 18.75 \text{ GHz.} \end{aligned} \quad (4.2)$$

Below this frequency only  $\text{TE}_0$  propagates and the other TE-modes as well as the TM-modes can only couple evanescently to the waveguide. Our set-up is shown in figures 4.3 and 4.4. We have an input antenna array of monopole antennas which is fed by a vector network analyser (VNA, Agilent E5071C). The VNA is connected with a power splitter (Microroot MPD16-060180) to support up to 16 IQ-modulators (GTM 1 M2L-68A-5 of GT Microwave Inc.) and up to 16 array antennas. The IQ-modulators allow us to change the phase and the amplitude of our microwave signal for each of the antennas (more details in section 4.2.5). We will see that in section 4.2.2 the confinement in the  $y$ -direction leads to a second quantisation of the modes, so that one can have multiple sinusoidal  $\text{TE}_0$  modes propagating in the system. With maximal 16 input antennas we can control up to 16 propagating sinusoidal  $\text{TE}_0$  modes.

The output monopole antenna is mounted on a movable metallic slide which can be shifted stepwise by a motor. It is used to scan the microwave signal along the  $y$ -axis in order to measure the superposition of the sinusoidal modes and to extract the strength of each component. Another monopole antenna, which is fixed to a moveable arm, can probe the electric field component  $E_z$  in the central part of the waveguide (see figure 4.3 and figure 4.4 for more details). The central part of the waveguide shows a grid of holes ( $5 \times 5$  mm) through which the movable antenna can enter the waveguide. The ends of the waveguide are filled with absorbing foam material (types: LS-14 and LS-16 from EMERSON&CUMING) to reduce reflections coming from the open ends. The distance between the absorbers and the antennas is large enough ( $\approx 2.5 \times W$ ), so that coupling between evanescent modes, emitted by the antennas, and the absorbers is prohibited. Otherwise one would have to deal with below cut-off transport coming from the other TE/TM-modes.

We can either choose to perform experiments in an empty waveguide or we can exchange the metallic boundaries to study a wobbly waveguide for example (see chapter 5), or we can introduce scatterers into the central part. In the experiment presented in this chapter, we use two kinds of scatterers; Teflon-scatterers with a radius of 2.5 mm and a metallic scatterers with a radius of 17.75 mm (see figure 4.19).

This type of set-up has already been used before in order to study the transport of propagating modes through systems with correlated disorder [Die11, Die12a, Die12b] and to investigate Anderson localisation via Loschmidt echoes [Bod09].

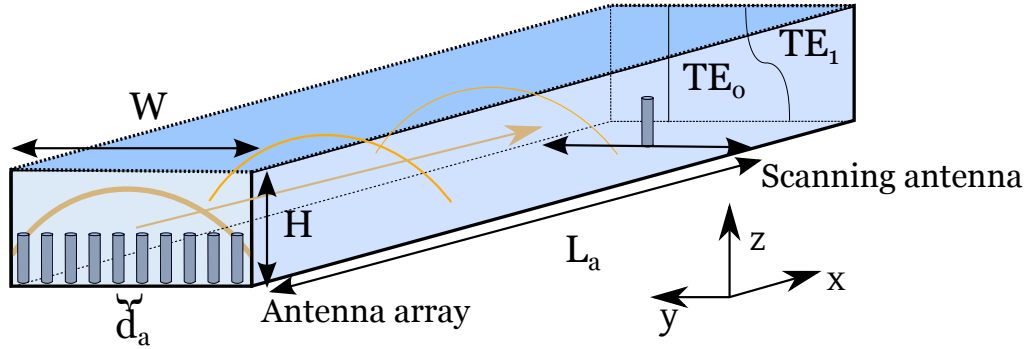


**Figure 4.3** – A sketch of the quasi-one-dimensional rectangular waveguide shown from the side. The arrangement of cylinders on the left side indicates the antenna-array of monopole antennas, whereas the single cylinder on the other side represents the single scanning monopole antenna which is movable in  $y$ -direction. The first propagating sinusoidal  $TE_0$  mode is shown in orange (see section 4.2.2). The field distribution of the electric field for  $TE_0$  and  $TE_1$  in the  $y$ -direction is drawn at the right end of the waveguide.

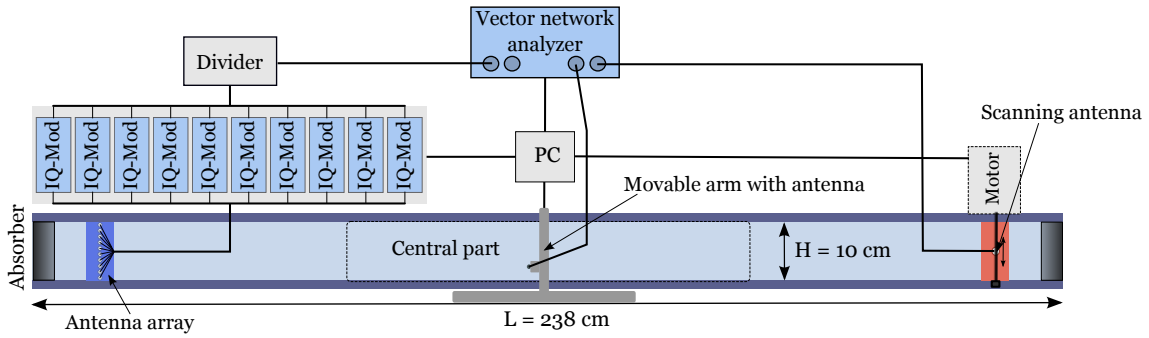


**Figure 4.4** – A sketch of the quasi-one-dimensional rectangular waveguide shown from the top view. Presented are IQ-modulators, vector network analyser (VNA), PC, cables, power divider and absorbing foam material at both ends of the guide.

## 4.2.2 Theoretical Description

As we work with  $TE_0$  modes, i.e.,  $k_z = l = 0$  (see chapter 1), equation (1.10) reduces to

$$(\Delta + k^2)\Psi(x, y) = 0. \quad (4.3)$$

If one excites this modes with an antenna for example, equation (4.3) gets inhomogeneous. For this type of equations it can be convenient to use the Green function formalism, which has already been formally introduced in chapter 1. Here we will try to find an explicit form for the Green function.

Let us assume that we have a point-like antenna which we treat as a point source at  $(\tilde{x}, \tilde{y})$  and we are interested in the signal strength at a position  $(x, y)$  (see coordinate system in figure 4.3).

## Chapter 4. Wave Front Shaping

---

To solve this problem we have to find the system's Green function  $g$  which we define according to equation (4.3) as

$$\begin{aligned} (\Delta + k^2) g(x, y|\tilde{x}, \tilde{y}) &= -\delta(x - \tilde{x})\delta(y - \tilde{y}) \\ \text{with } 0 < y, \tilde{y} < W \quad -\infty < x, \tilde{x} < \infty. \end{aligned} \quad (4.4)$$

As  $g$  represents  $E_z$  we must fulfil the following boundary conditions assuming perfect conducting walls:

$$g(x, 0|\tilde{x}, \tilde{y}) = g(x, W|\tilde{x}, \tilde{y}) \doteq 0, \quad (4.5)$$

$$\lim_{|x| \rightarrow \infty} g(x, y|\tilde{x}, \tilde{y}) \doteq 0. \quad (4.6)$$

To simplify equation (4.4) we perform a Fourier transform according to

$$G(k_x, y|\tilde{x}, \tilde{y}) = \int_{-\infty}^{\infty} g(x, y|\tilde{x}, \tilde{y}) e^{-ik_x x} dx, \quad (4.7)$$

$$g(x, y|\tilde{x}, \tilde{y}) = \frac{1}{2\pi} \int_{-\infty}^{\infty} G(k_x, y|\tilde{x}, \tilde{y}) e^{ik_x x} dk_x. \quad (4.8)$$

Applying the Fourier transform (4.7) to equation (4.4) leads to:

$$\frac{d^2 G}{dy^2} + (k^2 - k_x^2) G = -\delta(y - \tilde{y}) e^{-ik_x x}, \quad (4.9)$$

$$\text{with } G(k_x, 0|\tilde{x}, \tilde{y}) = G(k_x, W|\tilde{x}, \tilde{y}) = 0.$$

The conditions for  $G$  can be matched by assuming sinusoidal shaped modes which respect the boundary condition in the  $y$ -direction (similar to the case in section 1.1 for the TE-modes)

$$G(k_x, y|\tilde{x}, \tilde{y}) = \sum_{n=1}^{\infty} G_n \sin\left(\frac{n\pi y}{W}\right). \quad (4.10)$$

For  $\delta(y - \tilde{y})$  we use the ansatz

$$\delta(y - \tilde{y}) = \frac{2}{W} \sum_{n=1}^{\infty} \sin\left(\frac{n\pi y}{W}\right) \sin\left(\frac{n\pi \tilde{y}}{W}\right). \quad (4.11)$$

We plug equations (4.11), (4.10) into equation (4.9) and match the harmonics with regard to  $\sin\left(\frac{n\pi y}{W}\right)$  and derive:

$$\left(k^2 - k_x^2 - \left(\frac{n\pi}{W}\right)^2\right) G_n = -\frac{2}{W} \sin\left(\frac{n\pi \tilde{y}}{W}\right) e^{-ik_x x} \quad (4.12)$$

$$\Rightarrow G_n = \frac{2}{W} \sin\left(\frac{n\pi \tilde{y}}{W}\right) e^{-ik_x x} \frac{1}{\underbrace{k_x^2 + \left(\frac{n\pi}{W}\right)^2 - k^2}_{\kappa^2}}. \quad (4.13)$$

We found  $G$ . To obtain  $g$  we have to do a Fourier transform according to equation (4.8) leading us to

$$g(x, y|\tilde{x}, \tilde{y}) = \frac{1}{\pi W} \sum_{n=1}^{\infty} \sin\left(\frac{n\pi y}{W}\right) \sin\left(\frac{n\pi \tilde{y}}{W}\right) \int_{-\infty}^{\infty} \frac{e^{ik_x(x-\tilde{x})}}{k_x^2 + \kappa^2} dk_x. \quad (4.14)$$

The task is now to find the solution for the integral in equation (4.14). The integral is of the form

$$I = \int \frac{e^{izt}}{z^2 + z_1^2} dz = \int \frac{e^{izt}}{(z + iz_1)(z - iz_1)} dz, \quad (4.15)$$

where  $z = k_x$ ,  $t = x - \tilde{x}$  and  $z_1 = \kappa$ .

We perform the integration in the complex plane along the integration path  $C_1 + C_2$  as shown in figure 4.5. We assume the case where  $t$  is positive. In the case of a negative  $t$  one has to choose the correspondent integration path in the lower half plane.

In the following we perform the residue theorem stating

$$I = \oint_{C_1+C_2} \frac{e^{izt}}{z^2 + z_1^2} dz = 2\pi i \sum_k Res_k I. \quad (4.16)$$

According to equation (4.15) we get for the residue enclosed by the path:

$$Res_{iz_1} I = \lim_{z \rightarrow iz_1} (z + iz_1) I(z) = \frac{1}{2iz_1} e^{-z_1 t}. \quad (4.17)$$

This is why the integration results in

$$I = \frac{\pi}{z_1} e^{-z_1 t}. \quad (4.18)$$

For the chosen integral path  $C_2$  does not contribute to  $I$  as can be seen by the following argument:

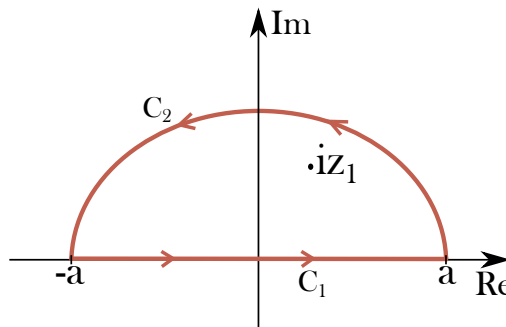


**Figure 4.5** – Sketch of the integration path.

$$\begin{aligned}
 \left| \int_{C_2} \frac{e^{izt}}{z^2 + z_1^2} dz \right| &\leq \int_{C_2} \left| \frac{e^{izt}}{z^2 + z_1^2} \right| dz \\
 &\stackrel{\text{see (4.20)}}{\leq} \int_{C_2} \frac{1}{|z^2 + z_1^2|} dz \\
 &\leq \int_{C_2} \frac{1}{a^2 - |z_1|^2} dz = \frac{\pi a}{a^2 - |z_1|^2} \xrightarrow{(a \rightarrow \infty)} 0. \quad (4.19)
 \end{aligned}$$

To justify the second step in equation (4.19) we need to verify the following:

$$\begin{aligned}
 |e^{izt}| &\stackrel{\text{polar}}{=} \stackrel{\text{coord.}}{=} |e^{it|z|(\cos(\phi) + i\sin(\phi))}| = |e^{-t|z|\sin(\phi)}| \\
 |e^{-it|z|\sin(\phi)}| &\leq 1 \quad \text{for } 0 \leq \phi \leq \pi. \quad (4.20)
 \end{aligned}$$

Note that equation (4.20) shows why we chose our integration path this way. Finally we found the result for  $g$  as it was defined in equation (4.4)

$$g(x, y | \tilde{x}, \tilde{y}) = \frac{1}{W} \sum_{n=1}^{\infty} \sin\left(\frac{n\pi y}{W}\right) \sin\left(\frac{n\pi \tilde{y}}{W}\right) \frac{1}{\kappa} e^{\kappa|x-\tilde{x}|}, \quad (4.21)$$

where  $\kappa$  is given by

$$\kappa = \sqrt{\left(\frac{n\pi}{W}\right)^2 - k^2} = i\sqrt{k^2 - \left(\frac{n\pi}{W}\right)^2}. \quad (4.22)$$

We can identify  $n\pi/W$  with a wavenumber  $k_y$  which takes the quantisation of the electric field in the  $y$ -direction into account.

Since our problem is two dimensional we can introduce a wavenumber  $k_x$  as

$$k_x = \sqrt{k^2 - k_y^2}, \quad k_y^2 = \left(\frac{n\pi}{W}\right)^2 \quad (4.23)$$

and thus write  $g$  as

$$g(x, y | \tilde{x}, \tilde{y}) = \frac{1}{W} \sum_{n=1}^{\infty} A_n \sin\left(\frac{n\pi y}{W}\right) \sin\left(\frac{n\pi \tilde{y}}{W}\right) \frac{1}{ik_x} e^{ik_x|x-\tilde{x}|}. \quad (4.24)$$

To properly describe the experimental situation we have to add effective coupling constants  $A_n$  which describe the coupling between the antennas and the sinusoidal modes. This is discussed in more detail in section 2 of [Tud08].

Note that  $g(x, y | x', y')$  can be considered as a transmission matrix  $T(x, y | x', y')$  in the spatial domain as it describes the transmission of the modes between two points of the waveguide (compare with section 1.2):

$$T(x, y | x', y') = g(x, y | x', y'). \quad (4.25)$$

We revisit equation (4.23). The total wavenumber  $k$  of the electromagnetic wave of frequency  $f$  is given by  $k^2 = (w/c_0)^2 = (2\pi f/c_0)^2$  (see equation (1.6)). We can write

$$k_x = \sqrt{\left(\frac{2\pi f}{c_0}\right)^2 - \left(\frac{\pi n}{W}\right)^2} = \frac{2\pi}{c_0} \sqrt{f^2 - \underbrace{\left(\frac{c_0 n}{2W}\right)^2}_{(f_c^{(n)})^2}}, \quad (4.26)$$

where  $n$  is the quantisation number defining the sinusoidal form of the wave in the  $y$ -direction. In other words,  $n$  is what is called mode number. If one works at a given frequency  $f$ , only  $N_W$  modes are propagating. This is due to the fact that for certain modes, certain values of  $n$ ,  $k_x$  gets imaginary and as a result these mode are exponentially damped. This be can seen by the factor  $e^{-|k_x||x-\hat{x}|}$  which would occur in equation (4.24) for these exponentially damped/evanescent modes. We denote  $f_c^{(n)}$  as lower cut-off frequency. It depends only on the quantisation number  $n$  and the waveguide width  $W$ . This frequency must be reached, so that the  $n$ -th mode becomes propagating.

The total number of propagating modes  $N_W$  for given frequency  $f$  in this kind of rectangular waveguide can be calculated as

$$N_W = \lfloor f/f_c^{(n)} \rfloor, \quad (4.27)$$

where  $\lfloor \dots \rfloor$  is indicating the floor function [Ive62].

In the context of scattering, one likes to think of how the sinusoidal modes are scattered. This is why one normally translates the transmission matrix  $T$  in its mode picture. This can be done in the following way:

$$T_{nm} = \int_0^W \int_0^W dy dy' \sin\left(\frac{n\pi y}{W}\right) \sin\left(\frac{m\pi y'}{W}\right) g(x, y|x', y'). \quad (4.28)$$

### 4.2.3 The Empty Waveguide

In this part we will concentrate on the information obtained by the transmission measurement between the antenna-array (10 antennas) and the scanning antenna (see figure 4.6) and how we can reconstruct the transmission matrix in the mode basis in the case of an empty waveguide (see section 4.2.2).

The positions of the antennas of the array are fixed. The distance between the array-antennas and the distance between the outermost antenna and the wall is 10/11 cm, i.e., we defined the  $y$  position of the  $i$ -th antenna of the array (relative to the inner wall of the waveguide) as  $y_i = i \times 10/11$  cm. The  $y$  positions of the scanning antenna, which we denote  $y'$ , are defined in an analogue way  $y'_i = i \times 10/11$  cm (see

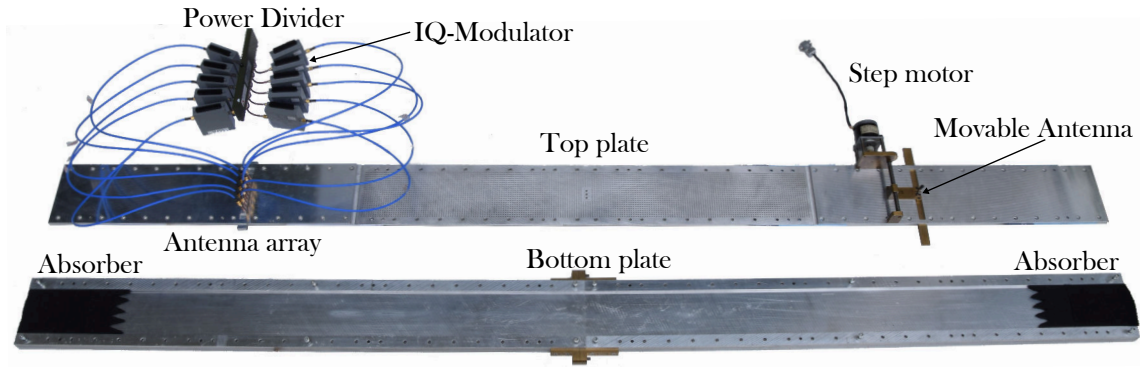


**Figure 4.6** – Photograph of the set-up using 10 antennas in the antenna array (left hand side) and one moveable antenna (right hand side). Compare with figure 4.4.

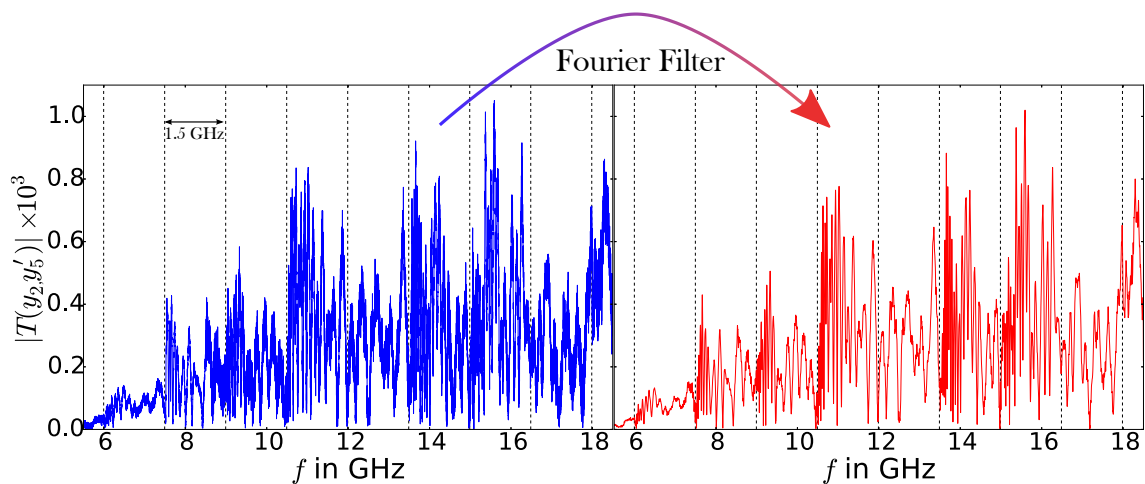


**Figure 4.7** – Two graphs which illustrate the absolute value of a single transmission measurement between an array-antenna at position  $y_2$  and the scanning antenna at a fixed position  $y'_5$  (see text for the definition of the positions). **Left:** Raw measurement. **Right:** Fourier filtered data. The dashed vertical lines indicate the opening of the modes.

figure 4.3 for the definition of the coordinate system). The precision we have to position the scanning antenna is about 0.25 mm.

A transmission measurement  $T(y_2, y'_5)$  between a single active antenna of the antenna array and the scanning antenna is shown in figure 4.7. We have seen in chapter 3 that we need the frequency derivative of the transmission matrix  $T$  to calculate the  $q$ -operator. Therefore we would like to deal with signals showing low signal noise. To guarantee that we apply a Fourier filter to the measured spectrum (see figure 4.7). Note that our measured microwave signal is complex, meaning that we measure amplitude and phase of our microwave signal.

The Fourier filtering is done in the following manner. We apply a Fourier transform to the measured frequency spectrum. This reveals how the corresponding pulse travels inside the waveguide. At some point in this time picture the pulse reaches the scanning antenna and is detected resulting in a peak in the time signal. When the measured peak intensity at the scanning antenna after the arrival of the pulse drops below  $\approx 5\%$  we set the time signal to zero. Afterwards we re-transform this modified time signal back into the frequency domain neglecting time components

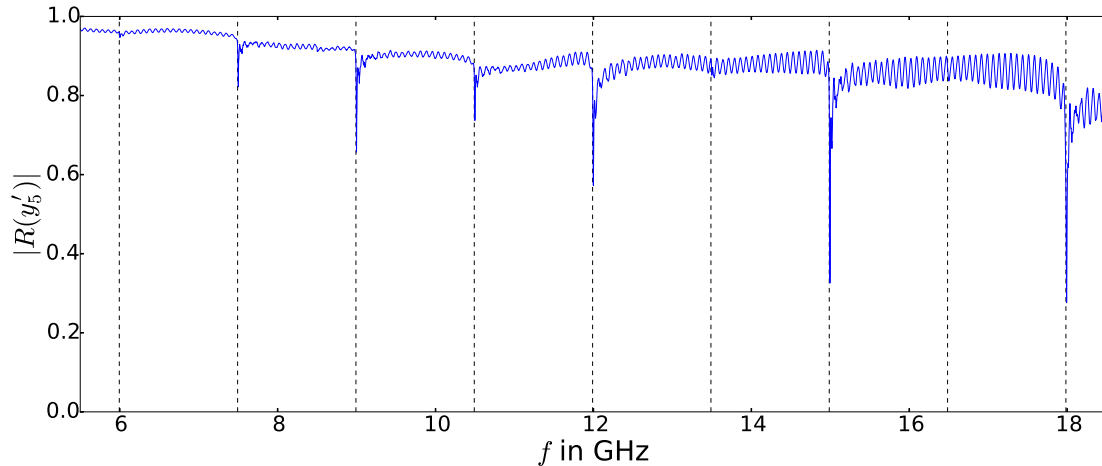


**Figure 4.8** – Absolute value of the reflection measured at the scanning antenna positioned at  $y'_2$ .

which are not related to the first arrival of the pulse. In other words, we are applying a high-pass filter.

The dotted vertical lines in figure 4.7 indicate the mode opening at the lower cut-off frequencies  $f_c^{(n)}$  (see 4.26). The opening frequencies differ by  $c_0/(2W) = f_c^1$  which is equal to 1.5 GHz for  $W = 10$  cm and  $c_0 = 3.0 \cdot 10^8$  m/s.

The different openings of the modes are clearly visible as peaks appear at these frequencies (see figures 4.7). The fast decrease of the transmission slightly after the mode opening corresponds to the factor  $1/(ik_x)$ . The transmission below 6 GHz is small. This is due to the fact that the IQ-modulators work within the frequency range of  $6 \text{ GHz} < f < 18 \text{ GHz}$ , so the presented spectra are cut according to these values. A reflection signal from the scanning antenna is presented in figure 4.8.

The reflection signal, like the transmission signal, is strongly position dependent. For instance, if the scanning antenna is positioned in a nodal line of a certain sinusoidal mode, one cannot couple to this mode and therefore it will not be visible. This means that some of the peaks/dips are not visible in the spectra neither in the reflection nor in the transmission signal. Also the antenna itself, its particular length and shape, changes the received signal. This is normally referred to as the coupling of the antenna to the waveguide. We can estimate this quantity by averaging the reflection spectrum  $R$  of the scanning antenna over all its positions  $y'$  and averaging over a small frequency window of  $\Delta f = 0.076$  GHz as it is shown in figure 4.9. The value for  $\Delta f$  is chosen manually, i.e., by choosing several values for  $\Delta f$  and verifying if the oscillations vanish (see fast oscillations in figure 4.9. Why this averaging is necessary becomes clear in the next step.

To eliminate the antenna coupling in a transmission signal one divides the measured spectra by

$$\left( \sqrt{(1 - \langle |R_1| \rangle)^2} \sqrt{(1 - \langle |R_2| \rangle)^2} \right), \quad (4.29)$$



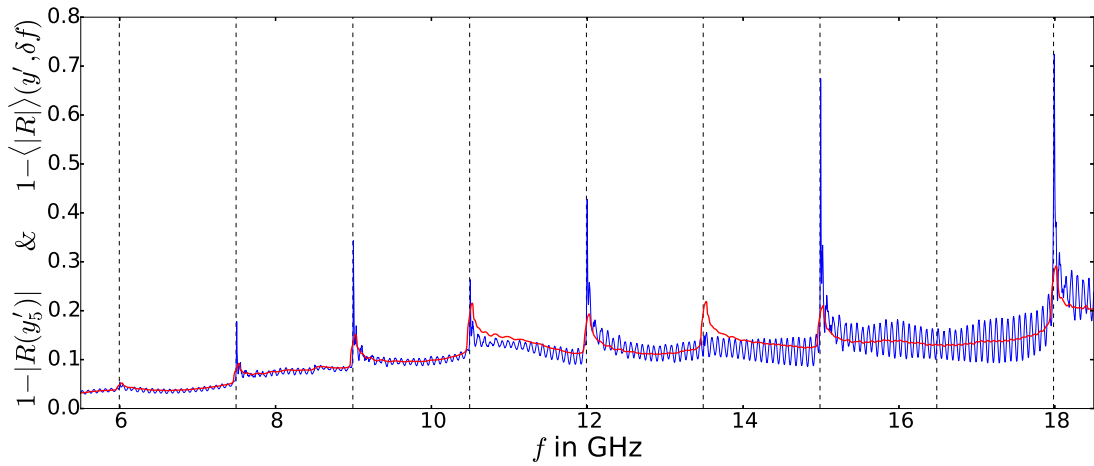


**Figure 4.9** – Absolute value of the reflection measured at the scanning antenna positioned at  $y_2$  (blue). Position and frequency averaged reflection signal (sliding average with a window of  $\Delta f = 0.076$  GHz) (red).

where  $\langle \dots \rangle$  stands for the mentioned averaging process.  $R_1$  and  $R_2$  are the reflection spectra measured at antenna 1 and antenna 2 which are used for the transmission measurement. This division allows us to compare the measured data in different frequency regimes eliminating the changed coupling of the antenna (see section 5.5). The averaging over the reflection spectra is necessary to not introduce oscillations to the transmission spectra artificially. For the moment we do not apply this kind of coupling elimination since we have only access to the reflections of the scanning antenna. We do not have direct access to the reflection of a single array-antenna due to the power divider (see position of the power divider in figure 4.4). But we will use this coupling elimination in chapter 5, where we use a second scanning antenna instead of the antenna array.

If we perform the sine transform as described in equation (4.28), we transform the transmission matrix in its mode picture. However, it turned out that this technique is not successful because of the array-antennas. The vicinity of the neighbouring antennas does not allow the simple point source description and therefore the double sinus transform described in equation (4.28) fails. This means that if one sends in for example a signal  $sig_8$  at the antenna array which corresponds to the 8th sinusoidal mode with  $\sin\left(\frac{8\pi}{d}y_i\right)$ , where  $y_i$  denotes the positions of the array antennas (see above), one measures at the output a share of 68% for the 8th mode. This points out that the antennas themselves lead to a scattering of the wave. As the intra-antenna distance for the array is smaller than the wavelength, the antennas are coupled evanescently. This means that we have to consider all the evanescent modes for the transport and we cannot just cut the sum at  $n = N_w$  in equation (4.24). By the means of mutual impedance calculation one can take into account this effect of mutual antenna coupling [Bal05]. Applying this type of calculation is not necessary though in our case as the antenna coupling leads only to a redefinition of the basis we are working in. Consequently, our basis is not orthogonal anymore but still complete as we will see below.

We will prove the fact that the 10 antennas are independent enough to fully control the 10 propagating modes. What we are going to do, mathematically speaking, is to apply a simple basis transformation to get back to the orthogonal basis. Experimentally this is done in the following way. In order to create a specific single mode output we solve a linear equation system of the following form (for each  $n$ -th mode individually):

$$\mathbf{o}_n = T(y, y', f)\mathbf{i}_n. \quad (4.30)$$

By measuring the transmission of each of the ten array-antennas to ten corresponding positions of the scanning antenna on the other side of the channel we have the information about the full  $10 \times 10$  transmission matrix  $T(y, y', f)^{10 \times 10}$ . This measurement of the transmission matrix is done in the following way. The IQ-modulator, which is connected with antenna 1 of the antenna array, is switched to (0 dB attenuation,  $0^\circ$  phase). This antenna is the emitting antenna. All other modulators are switched to (40 dB attenuation,  $0^\circ$  phase) and the corresponding antennas are considered as switched off. The scanning antenna is set to a fixed position on the  $y$ -axis and we measure the transmission signal from the emitting antenna 1 to the scanning antenna (see figure 4.4). Then all IQ-modulators are changed: Antenna 2 of the array is set to 0 dB and the others are switched to 40 dB attenuation. Again the transmission to the scanning antenna is measured, which is still at the very same position. After all 10 antennas have been switched in this manner, the scanning antenna moves to the next position. Finally, one gets in total  $10 \times 10$  measurements which form the transmission matrix  $T$  for a specific configuration of the scattering system. Once we have measured  $T$  we can use equation (4.30) which will help us to define  $\mathbf{i}_n$ .  $\mathbf{i}_n$  will be the input we have to generate with the help of our IQ-modulators to generate the wanted  $n$ -th mode  $\mathbf{o}_n$  as an output.

This ansatz will work out if  $T$  is of full rank or in other words, if, firstly, the signal emission by each single array-antenna is independent enough and if, secondly, the transporting medium is not blocking any energy transporting channel, i.e., mode. To test if this ansatz is valid we calculate  $\mathbf{i}_n$  according to (4.30), plug the settings which correspond to  $\mathbf{i}_n$  into our IQ-modulators and sine transform the output and compare it with the initial condition of a sinusoidal output  $\mathbf{o}_n$ . In the following we decided to work at a frequency of 15.5 GHz, where ten modes are propagating and where we are sufficiently far away from the mode opening of the 10-th mode at 15 GHz and of the 11-th mode at 16.5 GHz. The result of the sine transformed transmission after solving (4.30) and sending  $\mathbf{i}_n$  for each mode separately is shown in figure 4.10. The presented data is normalised so that the sum over all mode intensities is equal to one at any given frequency.

We obtained that our measured output follows the numerically expected one within the error of the noise. As we can see from figure 4.10 the transmission of a single mode works fine. We get transmissions amplitudes above 98%, except for the first mode where the transmission amplitude is about 93%. The reason for that is discussed below. To understand the scattering behaviour of a system one tends to

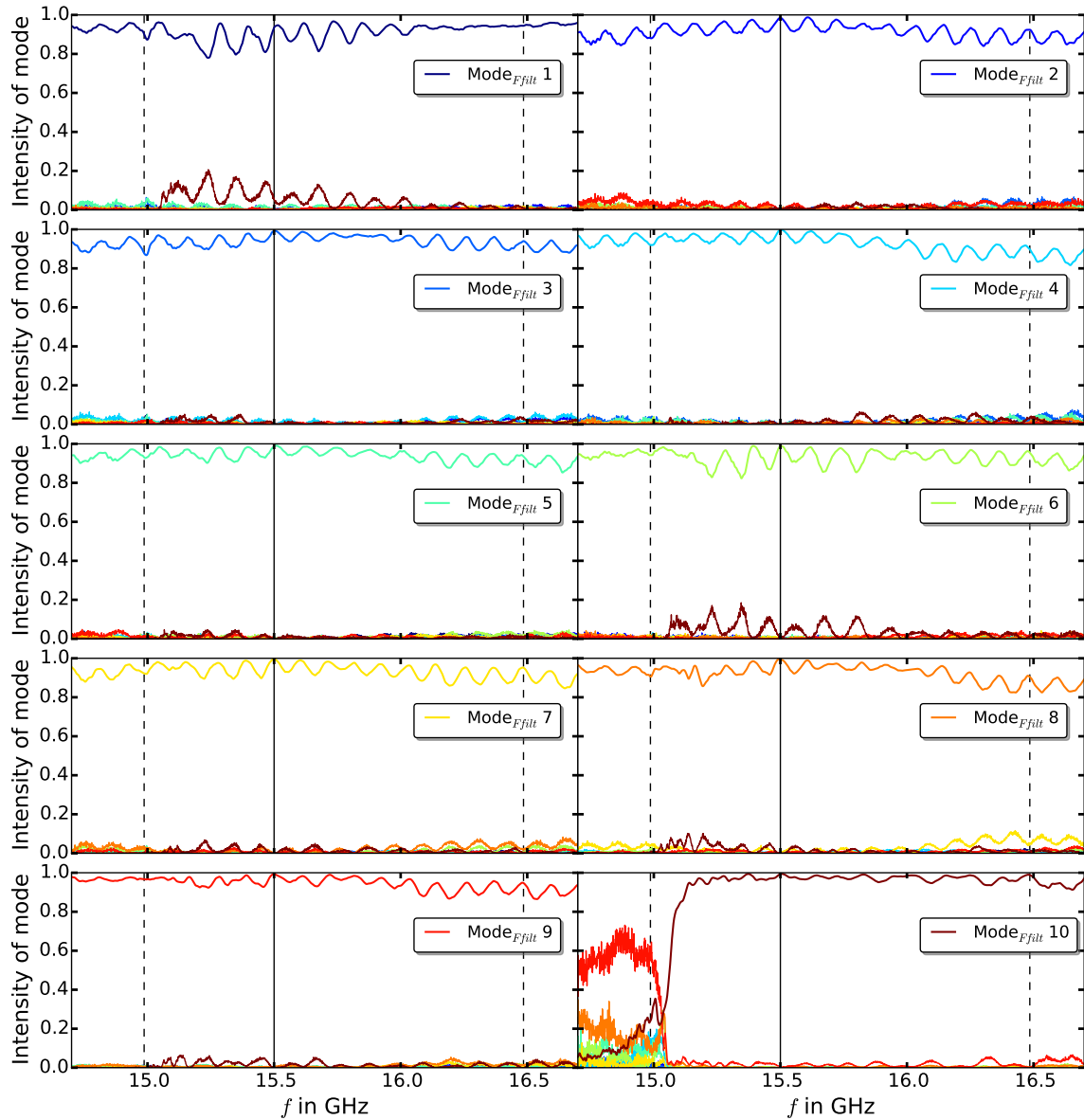


**Figure 4.10** – Fourier filtered intensity of the modes after measuring  $T^{10 \times 10}(y, y', f)$ , solving (4.30) and sending the resulting  $\hat{i}_n$  into the channel [for each mode individually]. The black vertical line indicates the frequency for which our system is tuned. The dashed vertical lines indicate the mode opening of the 10-th and 11-th mode. Each mode is indicated with its own color (see colour label in each cell).

think in the mode picture. In this context one tries to image how each single mode is scattered into the others. Therefore we can look at the transmission matrix  $T$  in its mode picture (see figure 4.11) defined according to equation (4.28).

As mentioned before we cannot perform the sine transform along the  $y$ -axis for the array-antennas, but since we have proven that the output follows the sinusoidal form of any mode we want (see figure 4.10 and results described above), we can assume that after a certain distance away from the antenna-array we established a stable sinusoidal mode.

We have to emphasise that although our system is only tuned to work at 15.5 GHz, the mode tuning in our system works broadband! This is because we used the same kind of antennas and cables to build up the input antenna array and because of the IQ-modulators which operate broadband.

The components  $T_{n,m}$  at 15.5 GHz are shown in figure 4.11. The index  $n$  of  $T_{n,m}$ , which corresponds to the sine transform along  $y$  positions of the array-antennas, is in a sense artificial. It can be seen as numeration of the modes sent into the channel. The analysis of these sent states is done by doing the sine transform along the positions  $y'$  of the scanning antenna. One recognises that we couple stronger to modes with high  $n$ , such as the 9-th or the 10-th mode. This is because of the factor  $1/ik_x$  which appears for the transmission (see equations (4.24), (4.26) and (4.28)). If we work at a frequency far from the mode specific cut-off frequency  $f_c^{(n)}$  (see equation (4.26)), like for the first mode for example, the factor  $1/ik_x$  gets small corresponding to a reduced coupling for the first mode at this frequency. Whereas for the 10th mode with a greater  $1/ik_x$ -value the coupling is higher leading also to a higher transmission. A nice feature which is clearly visible is the mode opening of the 10th mode close to its lower cut-off frequency of 15 GHz. We can conclude with this results that our transmission basis is of full rank and that therefore the emission from the array-antennas is sufficiently independent. We also notice that the scattering system does not block any of the 10 used modes.

Another, more hand-waving, explanation for the coupling behaviour of the modes in the waveguide is to look at their velocity in x-direction which is represented by  $k_x$  (see equation (3.16)). At the opening frequency of  $f_c^{(10)}$  the 10th mode has the smallest value of  $k_x$  (see equation (4.26)) when compared to the other modes. Therefore the dwell time of the 10th mode around the point of the excitation is larger than the ones of the other modes. Hence, the 10th mode can be feed for a longer time than the others leading to the observed fact that the 10th mode is the mode with the strongest transmission.

What we have done in this experiment can already be understood as **wave front shaping**. We used the transmission measurement in the spatial domain as basis to create our output. In this specific case we wanted to generate the pure sinusoidal modes. But in general any kind of output signal can be generated this way. By changing  $\mathbf{o}_n$  in equation (4.30) to a given output we can calculate the input  $\mathbf{i}_n$ .

It is worth mentioning at this point that the uniform loss introduced by the metallic walls of our cavity is present throughout the whole system. The travelling time of each mode is different which is a consequence of the different  $k_x$  values of the modes. The first mode spends less time in the cavity than the 10-th mode and undergoes therefore less absorption (for the frequency at which we are working at). Normally this effect is taken into account by adding a complex value to  $k_x$ . The absorption however is not dominant in our system as we will understand looking at figure 4.11. If the absorption was dominant, we would get an reversed picture for the left hand side of figure 4.11 in the sense that the first mode would be highest transmitting and the 10th mode would be the lowest.

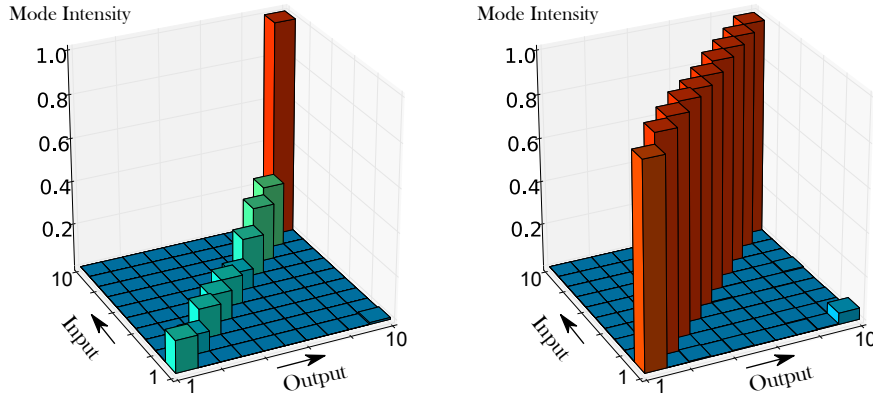


**Figure 4.11** – Result for the transmission matrix in the mode picture  $|T_{n,m}|^2$ . **Left:**  $|T|^2$  is normalised to  $|T|^2/|T_{max}|^2$ . **Right:**  $|T|^2$  is normalised to  $\sum_m |T_{n,m}|^2 = 1$ . The output axis describes the sinus transform along the positions  $y'_i$  of the scanning antenna. The input axis indicates which mode is actually send into channel.

#### 4.2.4 IQ-Modulators

We have seen previously that the necessary condition to perform wave front shaping is the control of the amplitude and the phase of our microwave signal emitted by each antenna. Experimentally this is achieved using IQ-modulators (see figure 4.12). These two parameters I and Q are encoded with a 12-bit precision and they are connected with the phase  $\Phi$  and the amplitude A in dB by

$$A = -10\log_{10}(I^2 + Q^2), \quad \Phi = \arctan\left(\frac{Q}{I}\right). \quad (4.31)$$

If our IQ-modulators worked perfectly we would have an maximal error of  $\approx 0.06$  dB for the amplitude and  $\approx 0.04^\circ$  for the phase due to the 12-bit precision.

Each IQ-modulator has two ports. Therefore one gets two transmission quantities called  $|t_{12}|$  and  $|t_{21}|$ , which describe the transmission amplitude from port 1 (left) to port 2 (right) or the other way round. Similarly, we get two reflection quantities. The quantities  $|r_{11}|$  and  $|r_{22}|$  describe the reflection amplitude at port 2 and port 1. The complete result of this two port measurement in the frequency range of the IQ-modulator is shown in figure 4.12.

We recognise that about 10% of the signal is reflected and the overall transmission attenuation for a setting of 0 dB is about 5 dB. It is worth noticing that the device has no preferred direction regarding the transmission as  $t_{12} \approx t_{21}$ .

In the following we will have a closer look on the transmission properties of the IQ-modulator. We measured the transmission through one of the IQ-modulators as a function of a **given** amplitude  $A_g$  and phase  $\Phi_g$  over the whole operating frequency range [6 GHz,18 GHz].

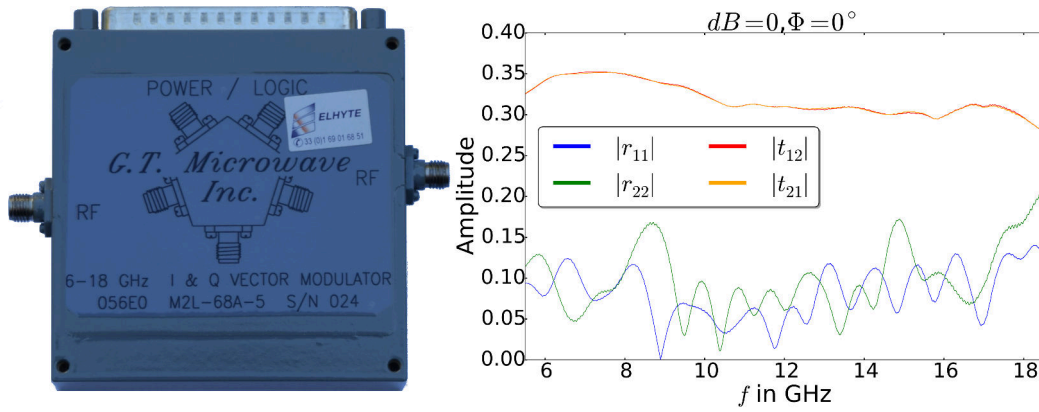


**Figure 4.12** – *Left*: Photo of an IQ-modulator. Entrance and exit for the microwaves are on the left and the right. *Right*: Amplitude of the transmission  $t_{12}$  between port 2 to port 1 (red). Amplitude of the transmission  $t_{21}$  between port 1 to port 2 (orange). Amplitude of the reflection at port 1  $r_{11}$  (blue) and at port 2  $r_{22}$  (green). The IQ-modulator is set to 0 dB and  $0^\circ \Phi$ .

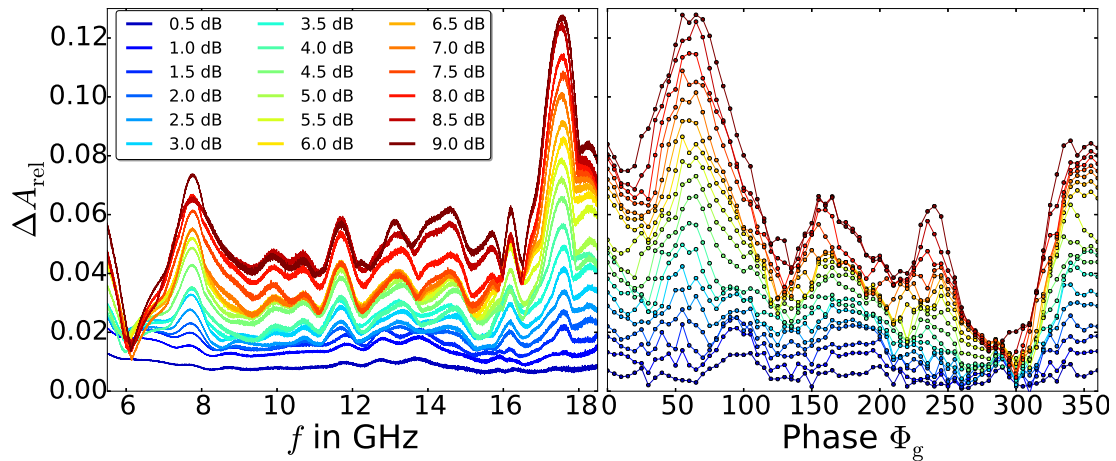


**Figure 4.13** – *Left*: Maximal  $\Delta A_{\text{rel}} = (A_r - A_g)/A_g$  for different given amplitudes  $A_g$  as a function of the frequency  $f$ . The maximum is obtained with regard to all possible  $\Phi_g$  values  $\Phi_g \in [0^\circ, 360^\circ]$ . *Right*: Maximal  $\Delta A_{\text{rel}} = (A_r - A_g)/A_g$  for different given amplitudes  $A_g$  as a function of given phase  $\Phi_g$ . The maximum is obtained with regard to frequency values  $f \in [5.5 \text{ GHz}, 18.5 \text{ GHz}]$ .

It turned out that the received transmission amplitude  $A_r$  depends on the frequency  $f$ ,  $A_g$  and  $\Phi_g$ . The received phase  $\Phi_r$  is also a function of the three parameters  $\Phi_r(f, A_g, \Phi_g)$ .

In figure 4.13 we show the relative deviation of the Amplitude  $\Delta A_{\text{rel}} = (A_r - A_g)/A_g$  for different  $A_g$  ( $A_g \in [0 \text{ dB}, 9 \text{ dB}]$ ) and different  $\Phi_g$  ( $\Phi_g \in [0^\circ, 360^\circ]$ ). Figure 4.14 describes the maximal phase error  $\Delta\Phi = \Phi_r - \Phi_g$  for the investigated amplitudes  $A_g$ . The shown results justify that we have a well controlled phase and amplitude definition, which is the very basis of doing wave front shaping. Additionally the

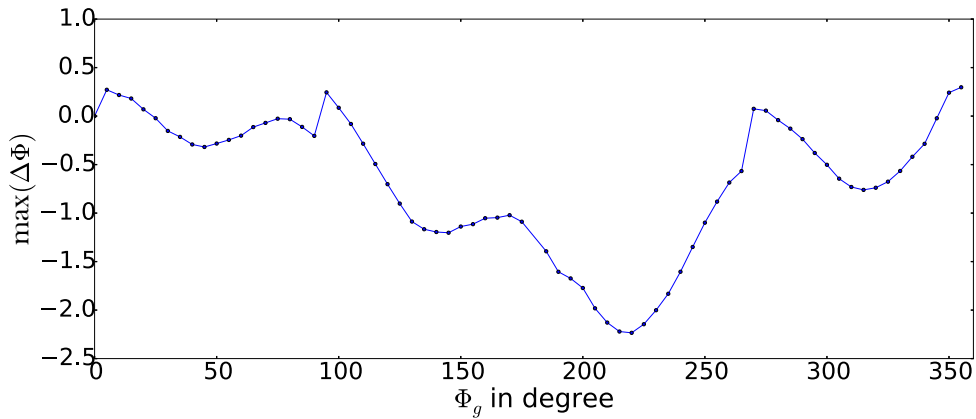


**Figure 4.14** – Maximal  $\Delta\Phi = \Phi_r - \Phi_g$ . The maximum is obtained with regard to all possible frequency values  $f \in [5.5 \text{ GHz}, 18.5 \text{ GHz}]$  and to given amplitudes  $A_g \in [0 \text{ dB}, 9 \text{ dB}]$ .

results show also that we can use the IQ-modulators also in a slightly broader frequency range  $\approx [5.5 \text{ GHz}, 18.5 \text{ GHz}]$  which goes beyond the original frequency of  $[6 \text{ GHz}, 18 \text{ GHz}]$  specified by the manufacturer.

It turned out that the IQ-modulators are quite sensitive to temperature changes. This is why it is strongly recommended to use temperature stabilisation. In our case we set up the IQ-modulators on a large copper plate, which keeps the temperature stable with respect to the temperature of the air-conditioned environment.

#### 4.2.5 Waveguide Filled with Scatterers

So far we worked with an empty channel. Now we introduce 18 Teflon-scatterers (radius of 2.5 mm, index of refraction  $n \approx 1.44$ ) and one brass scatterer (radius of 8.85 mm) by placing them in the central part of the waveguide (see figures 4.15 and 4.4). For sure, these scatterers will effect the transport of the sinusoidal modes. One no longer expects a diagonal shape of the transmission matrix as it was the case for the empty channel in figure 4.11.

The modes scatter into each other leading to a rather complicated scattering behaviour which strongly depends on the frequency we are working at and the

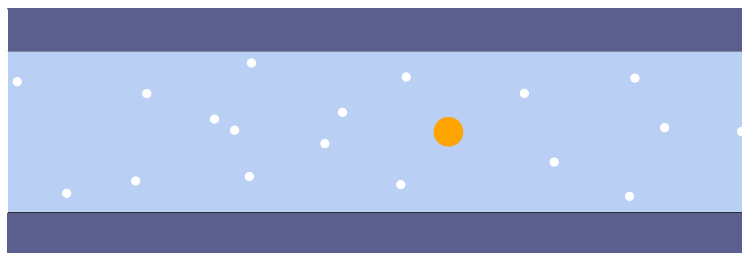


**Figure 4.15** – Scheme of the Teflon scatterers (white circles) and the brass scatterer (orange circle) in the central part of the cavity (see figure 4.4 for the whole set-up).

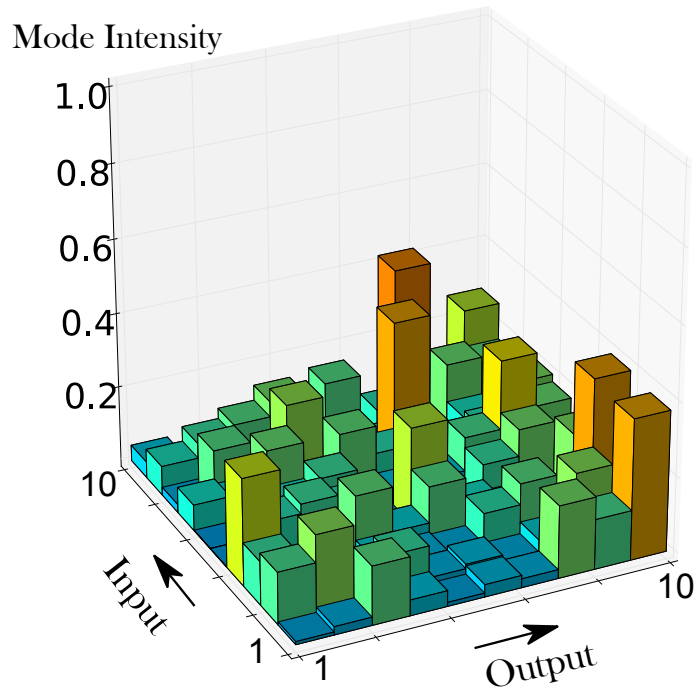


**Figure 4.16** – Result for the transmission matrix in the mode picture  $|T_{n,m}|^2$  for the waveguide filled *with scatterers*. The output axis describes the sinus transform along the positions  $y_i^j$  of the scanning antenna. The input axis indicates which mode is actually send into the channel.

scattering system itself, i.e., mean distance between scatterers, size of the scatterers, additional absorption induced by the scatterers and their index of refraction.

From the empty channel measurement (see section 4.2.3) we learned how to tune the IQ-modulators so that the antenna array produces a specific mode output. Based on this information we send the single modes into the scattering region and we measure the resulting mode output received at the moveable antenna. Since we inflict scattering, we do not expect the modes to reappear in their initial sinusoidal shape after the scattering region. At the tuned frequency of 15.5 GHz we can look again at the transmission matrix elements like we have done for the empty case (compare figure 4.11 and figure 4.16). Due to the scattering between the modes the transmission matrix  $T_{n,m}$  is not diagonal any more and we obtain a complex inter-mode scattering behaviour instead.

#### 4.2.6 Mode Tuning

Nevertheless, we can follow the same procedure as the one for the empty channel and readjust our antenna array signal to change the output to a single outgoing mode after the scattering area. In order to do so, we measure the transmission of each



single antenna through the scattering region. This allows us to recalculate what we have to send from the antenna array to retune the single sinusoidal modes, just as we have done it for the empty waveguide. The result of these retuning towards the sinusoidal modes is shown in figures 4.17 and 4.18.

As it can be seen from figure 4.18 the retuning works for some modes in a broader frequency range. Modes 1, 9 and 10 are rather narrowband, whereas, modes 6, 7 and 8 show broadband transmission. The investigation of the bandwidth of the transmitted mode as a function of the properties of the scattering system like correlation length for example might offer the possibility to compare theoretical work (like [Hsu15]) with experimental data.

At the working frequency of 15.5 GHz, we managed to retune the sinusoidal modes even in the case of scattering. From the point of view of an observer who is located at the movable antenna position the received signal looks like the one of an empty waveguide with a reduced overall transmission. The reduced overall transmission is the result of the backscattering caused by the scatterers.

This kind of output tuning by shaping the initial wave front is working as long as all modes are transmitted. If a mode is not transmitted we do not have access to a full basis meaning that we can not tune our output due to this now reduced subspace spread by the remaining modes.

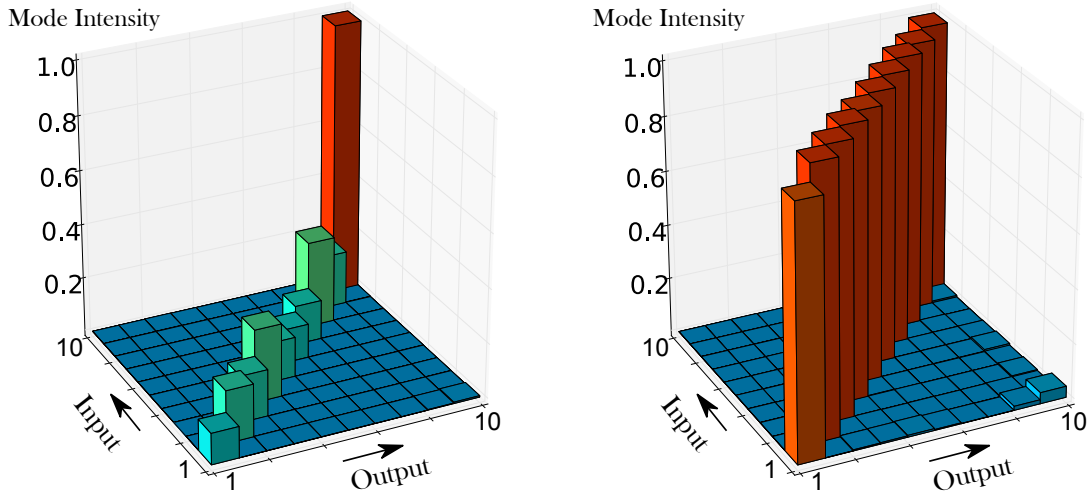


**Figure 4.17** – Result for the retuned transmission matrix in the mode picture  $|T_{n,m}|^2$  for the case of the a scattering region filled with scatterers. **Left:**  $|T|^2$  is normalised to  $|T|^2/|T_{max}|^2$ . **Right:**  $|T|^2$  is normalised to  $\sum_m |T_{n,m}|^2 = 1$ . The output axis describes the sinus transform along the positions  $y'_i$  of the scanning antenna. The input axis indicates which mode is actually send into channel.

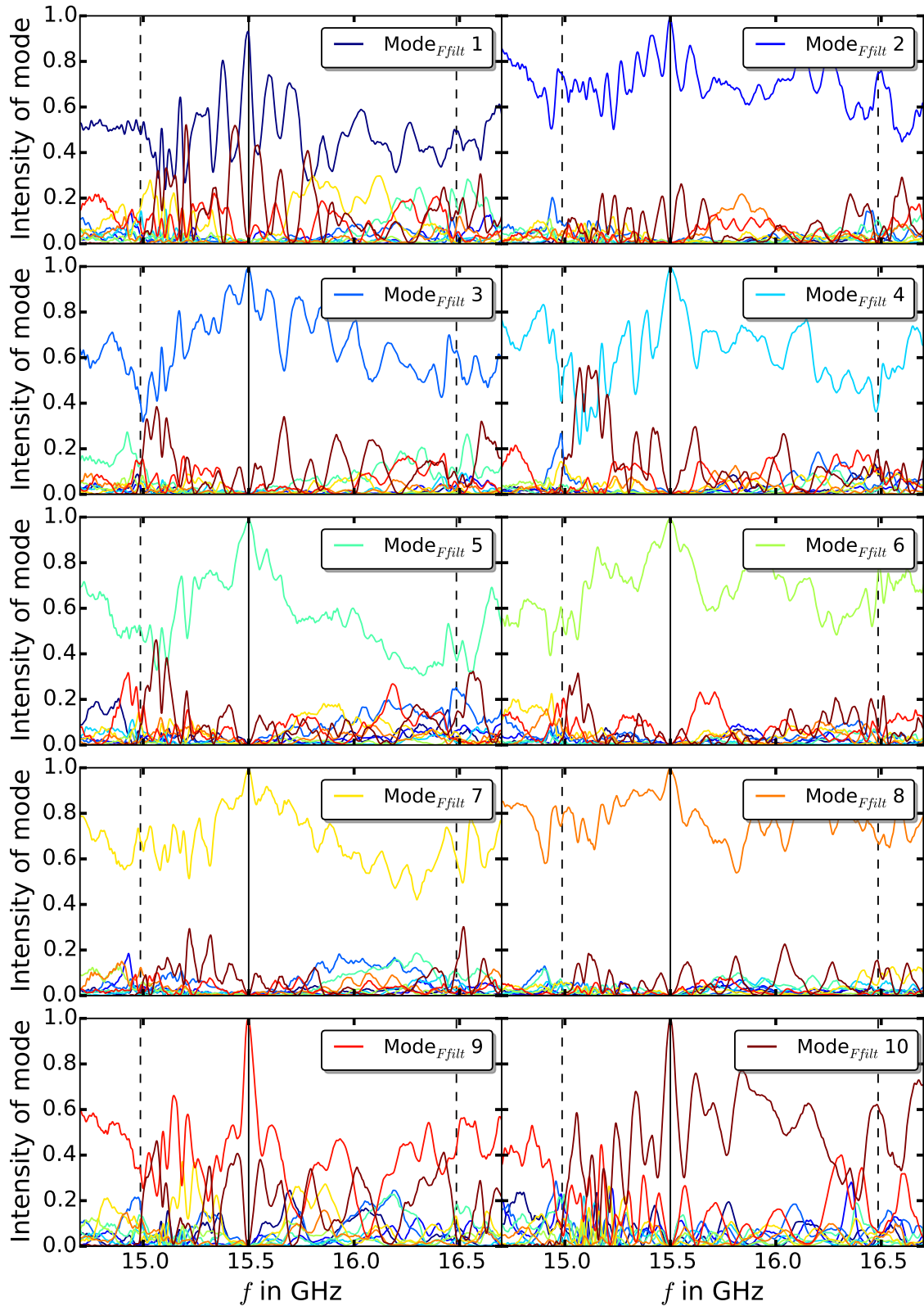


**Figure 4.18** – Fourier filtered intensity of the modes after measuring  $T^{10 \times 10}(y, y', f)$  through the waveguide filled with scatterers, solving (4.30) for a pure sinusoidal output and sending the resulting  $\mathbf{i}_n$  into the channel (for each mode individually). The dashed vertical lines indicate the mode opening of the 10-th and 11-th mode and the vertical solid line shows the frequency for which the IQ-modulators were tuned. Each mode is shown in a different color (see colour label in each cell and compare with figure 4.10).

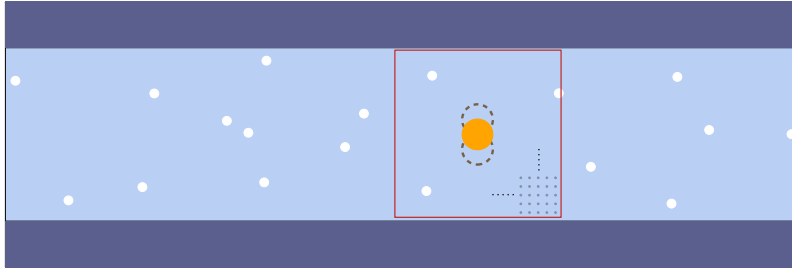


**Figure 4.19** – Sketch of the central part, where white circles denote the 18 Teflon-scatterers (radius of 2.5 mm) and the orange solid circle denotes the brass scatterer (radius of 8.85 mm) at its central position. The dashed grey lines around the brass scatterer indicate the movement of the scatterer to the top (bottom). The grid of holes (5mm×5mm) for the antenna attached to the moveable arm (see figure 4.4) is indicated in the lower right corner of the red square. This grid reaches all over the area marked with the red square.

### 4.3 REALISING Q-STATES

We will keep the very same set-up with its Teflon and brass scatterers inside and we will try to create scattering states which are eigenstates of the  $q$ -operator. In order to do so, we need to have an adjustable parameter. In this case we will use the position of the brass scatterer (orange circle in figure 4.15). We will measure the transmission matrix  $T$  for three slightly different positions of the brass scatterer. This allows us to calculate the  $q$ -operator and its eigenstates ( $q$ -states) according to section 3.4. Once we have calculated these, we have the necessary parameters for the IQ-modulators in order to emit those states from the antenna array. The intensity of these states will be measured around the brass scatterer with the use of the full set-up shown in figure 4.4. We will see specific outcomes depending on the corresponding eigenvalue and the measured overall transmission.

#### 4.3.1 Transmission Matrix in a Scattering Environment

We considered three positions for the central metallic scatterer (down, center, up: indicated in orange in figure 4.19). The size of the brass scatterer ( $r = 8.85$  mm) and the size of the position variation ( $\delta_y = 8.85$  mm) are smaller than the used wavelength  $\lambda = 1.93$  cm  $\leftrightarrow$   $f = 15.5$  GHz. In that way we ensure that the position changes of the brass scatterer do not influence the transmission matrix too strongly, as we need to compute the derivative of  $T$ ,  $dT(y_{\text{brass}})/dy_{\text{brass}}$  (see equation (3.23)). This derivation with regard to the position of the brass scatterer  $y_{\text{brass}}$  is approximated by:

$$\frac{dT(y_{\text{brass}})}{dy_{\text{brass}}} \approx \frac{T(y_{\text{brass}} + \delta_y) - T(y_{\text{brass}} - \delta_y)}{2\delta_y}. \quad (4.32)$$

For each of the positions of the brass scatterer we measure the transmission matrix

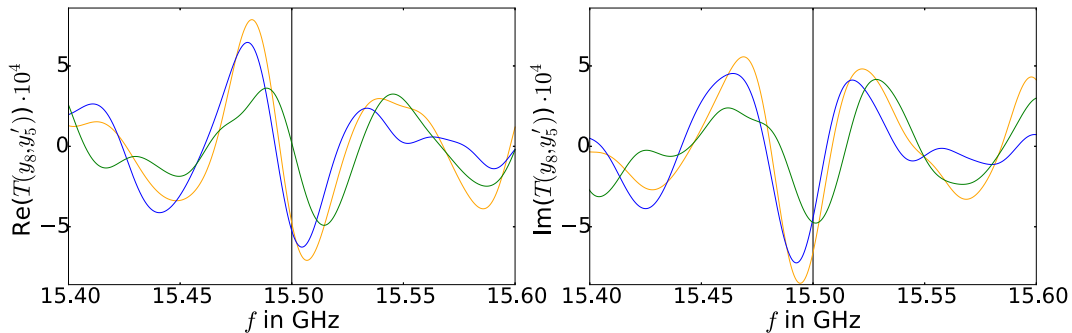


**Figure 4.20** – Fourier filtered real part and imaginary part of one entry of the transmission matrix for 3 positions of the central metallic scatterer [blue: Lower position of the scatterer, orange: Central position of the scatterer, green: Upper position of the scatterer]. The solid vertical line indicates the frequency of 15.5 GHz at which we are working at.

$T$  in the spatial domain. Figure 4.20 shows the same entry of the measured transmission matrix for the three positions of the brass scatterer. We obtain that the chosen position change of the brass scatterer does not fully destroy the correlation between the spectra. In fact the difference in the spectra is on the one hand large enough and on the other hand it is not too great, so that one can guarantee that the derivative  $dT(y_{\text{brass}})/dy_{\text{brass}}$  is still a well defined quantity. We measured the transmission matrix  $T$  and its derivative. In the next step we are going to compute the  $q$ -operator with this information.

### 4.3.2 Generating Q-States

The  $q$ -operator for our case where the parameter  $\alpha$  is replaced by the  $y$ -coordinate of the brass scatterer (see definition and discussion of the  $q$ -operator in chapter 3) can be written as

$$q = -iT^{-1} \frac{dT}{dy_{\text{brass}}}, \quad (4.33)$$

where  $y_{\text{brass}}$  stands for the position of the brass scatterer. We follow the calculation procedure described in chapter 3.  $T$  is a  $10 \times 10$  matrix which describes the transmission through the system at 15.5 GHz.  $T$  is not transformed in the mode picture here, since the computation of the eigenvalues and eigenvectors works for every chosen basis. We calculate all the possible eigenvalues  $\lambda$  and eigenstates  $\mathbf{i}_q$  of the  $q$ -operator, where we consider 1 to 10 singular-values in our calculation. This means in the first calculation we consider only the greatest singular-value and the highest transmitting eigenstate  $\sigma_1$  (for details see section 3.4). Then we consider two singular-values  $\sigma_1$  and  $\sigma_2$  leading to 2 eigenvalues and 2 eigenstates of the corresponding  $q$ -operator and so on. In total there are  $\sum_{i=1}^{10} i = 55$  eigenvalues and eigenstates possible taking into account up to 10 singular values. These eigenvalues of the  $q$ -operator are ordered with

$$\text{ord}_q = \frac{|\lambda_q|}{|\mathbf{o}_q|^2} \quad \text{with} \quad \mathbf{o}_q = T\vec{q}. \quad (4.34)$$

$\lambda_q$  denotes the eigenvalue of the  $q$ -state and  $|\mathbf{o}_q|^2$  is the measure for the total transmitted energy (compare with equation (3.8)). We chose this criterion as we are looking for two types of  $q$ -states (eigenstates of the  $q$ -operator). The first type of  $q$ -states shows high transmission and is weakly influenced by the movement of the scatterer. In section 3.3 we have seen that this sensitivity of a  $q$ -state is encoded in the modulus of his eigenvalue  $|\lambda_q|$ . This means that  $q$ -states of the first type will show large values for  $|\mathbf{o}_q|^2$  and small values for  $|\lambda_q|$ , so we can associate these types of states with small values of  $\text{ord}_q$ . One can assume that  $q$ -states of the first type, as they show high transmission and low sensitivity to the change of the position of the scatterer, try to avoid the region of the brass scatterer. In this context we like to speak of **avoiding states**.

For the other type of states it is exactly the other way around. They are strongly influenced by the change of the position of the brass scatterer and they show low transmission resulting in a high value for  $\text{ord}_q$ .  $Q$ -states of the second type are strongly affected by the position change. This together with the low transmission lets us assume that these states are focused onto the brass scatterer, where they are experiencing back-reflection. We refer to these states as **focussing states**.

The result of the calculation of  $\text{ord}_q$  is shown in figure 4.21. We arrange the values of  $\text{ord}_q$  in an ascending order. As explained before, we are especially interested in the smallest and the greatest values of  $\text{ord}_q$ . To verify our assumptions we will have to look at the intensity profiles around the brass scatterer of these two types of states. Note that the avoiding and focusing states are still  $q$ -states but they differ in their  $\text{ord}_q$ -value.

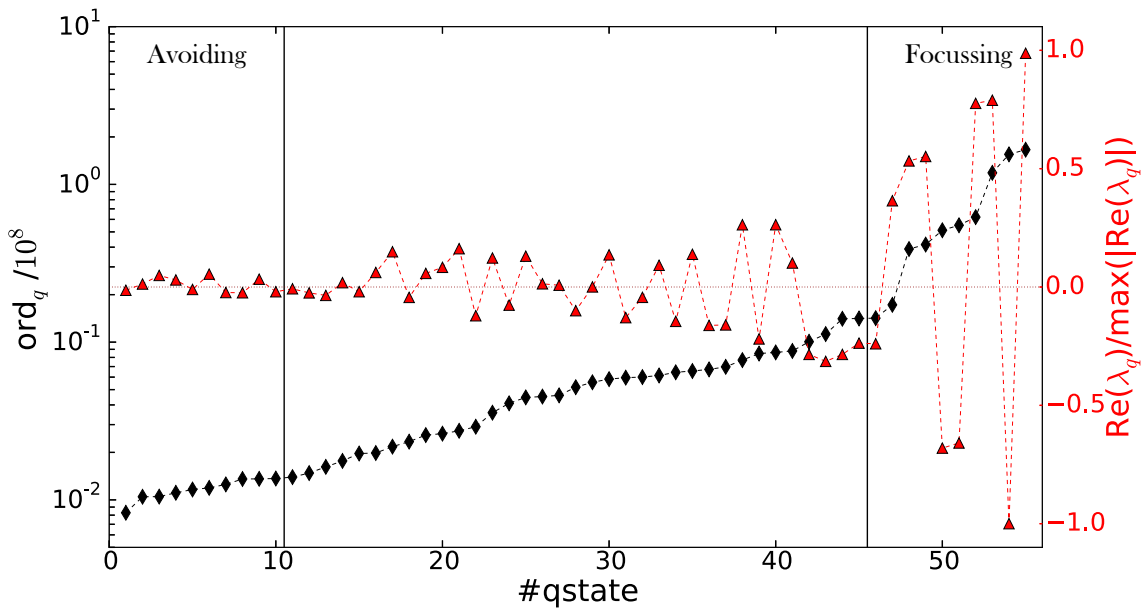


**Figure 4.21** – Result of the calculation of  $\text{ord}_q = |\lambda_q|/|\mathbf{o}_q|^2$  of all the 55 possible eigenstates (see main text). **The black diamonds** represent the  $\text{ord}_q$ -values and **the red triangles** are the corresponding real parts of the eigenvalues of the  $q$ -states (important at the end of section 4.3.3). The left and right parts separated by solid black lines contain the avoiding and focussing states, respectively.

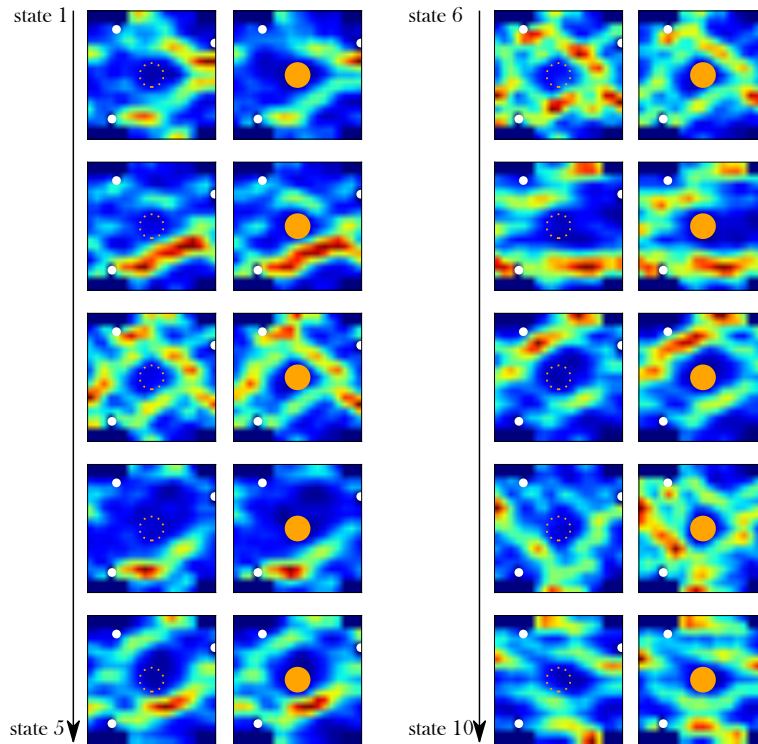


**Figure 4.22** – Transmission intensity measured between the antenna array and the antenna attached to the moveable arm (see figure 4.4) for the first 10  $q$ -states ordered according to equation (4.34). These states are referred to as avoiding states. Each state is measured two times using the same input. On the left without the brass scatterer present and on the right with the brass scatterer. The solid orange circle represents the brass scatterer. The dashed circular line represents only indicates the former position of the brass scatterer. The generating process of the images and the colour bar is shown in figure 4.23.

### 4.3.3 Experimental Realisation of Q-States

Once we have calculated the eigenvectors in the basis of our antenna array, we can create the calculated states and send them into the waveguide. The additional scanning antenna attached to the movable arm in the center (see figure 4.4) of the waveguide allows us to measure the intensity profile of these  $q$ -states around the brass scatterer in the red square indicated in figure 4.19.

The resulting intensity profile for the **avoiding states** (the 10 first states according to the order introduced in section 4.3.2) is presented in figure 4.22. Each of these states are measured with the brass scatterer present (positioned in the central position; see figure 4.19) in the waveguide and later on without the brass scatterer. **The sent signal from the array antennas stays the same for the two cases.**

Further details on the image processing can be found below. The intensity profiles presented in figure 4.22 show clearly that no matter if the scatterer is present or not, the area around the scatterer is poorly occupied by the state (dark blue colour

in the dashed circles in figure 4.22). One can call this an avoiding of the area since the intensity which is stored within the region of the scatterer (in the case where the scatterer is not present, dashed line in figure 4.22) is for all measured avoiding states less than 1% of all the intensity stored in the whole measurement field (red square in figure 4.19). The avoiding states show a hole around the brass scatterer.

At this point I would like to discuss shortly how the intensity pictures are created. We start measuring the transmission between the array antennas and the scanning antenna positioned in the waveguide. This transmission signal is then Fourier filtered (see section 4.2.3) and the resulting intensity is treated with a discrete two dimensional convolution of the form

$$c_s(x, y) = s * k(x, y) = \sum_{x'} \sum_{y'} k(x', y') s(x - x', y - y') \quad (4.35)$$

with  $k = \begin{pmatrix} 0.0625 & 0.125 & 0.0625 \\ 0.125 & 0.25 & 0.125 \\ 0.0625 & 0.125 & 0.0625 \end{pmatrix}$ .

$s$  denotes the intensity of measured transmission signal and  $k$  is called the convolution kernel, which in our case takes only the nearest neighbour measurements (pixels) into account. Note that  $x$ ,  $y$ ,  $x'$  and  $y'$  are discrete quantities (more details can be found in [Pre92, Jay09]).

Afterwards we add a bilinear interpolation to smooth the images. The steps are shown in figure 4.23.

Note that all the calculations presented in this chapter deal with the Fourier filtered data. The convolution and the bilinear interpolation is only used for generating the images. The bilinear interpolation can be useful though. Especially for the case where one works with a measurement grid well below the wavelength. Our grid however with its distance of  $\Delta x = \Delta y = 5$  mm is of the same order as the

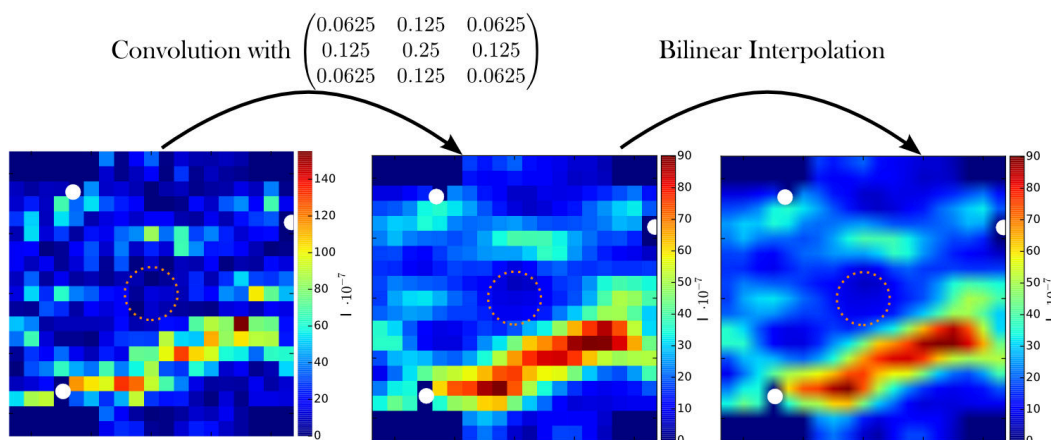


**Figure 4.23** – Work flow of the image processing for the state 2 (compare with figure 4.22).

wavelength  $\lambda(15.5 \text{ GHz}) = 1.93 \text{ cm}$ . This is why we do not use the bilinear interpolation for the further quantitative investigation. We use it only as a measure to improve the visualisation qualitatively.

To be more precise on the fact that the avoiding states seem unaffected by the presence of the metallic scatterer we study the spatial correlations of the  $q$ -states, where we combine the case where the brass scatterer is present with the one where it is not present. In this sense we define the spatial correlation of the  $q$ -state as:

$$\text{Corr}(f) = \frac{|\int \Psi_a^*(f) \Psi_p(f) dA|}{\sqrt{\int |\Psi_p(f)|^2 dA \int |\Psi_a(f)|^2 dA}}. \quad (4.36)$$

$\Psi_a(f)$  [ $\Psi_p(f)$ ] is the frequency dependant complex transmission signal obtained for each  $q$ -state in the case of the absent [present] brass scatterer.

The result of the correlation calculation for all the 20 interesting  $q$ -states is shown in figure 4.24. For the frequency of 15.5 GHz at which we are working **the correlation function shows values from 90% to 95% for the avoiding states**. Moreover, the correlation stays on a high level even for the whole measured frequency window, which indicates that the sent  $q$ -states keep their particular shape for a rather large frequency window. Of course the width of the correlation peak depends strongly on the scattering system. If one introduces more and more scatterers to the system the width of the peak is supposed to become smaller and smaller.

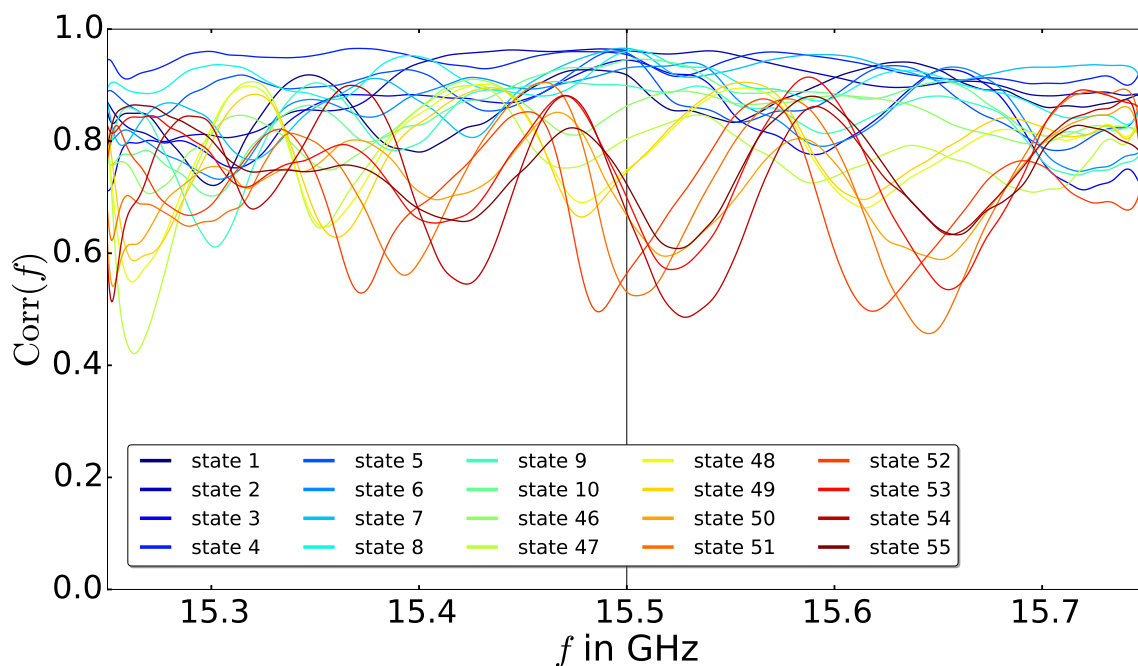


**Figure 4.24** – The frequency dependent correlation function for the 20 selected  $q$ -states (see also figure 4.21 and equation (4.36)).



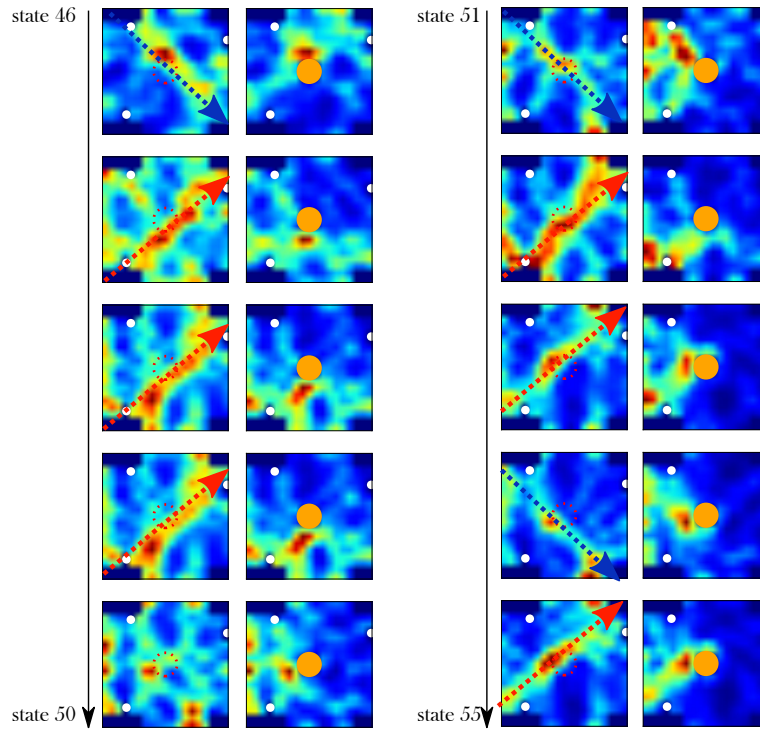


**Figure 4.25** – Transmission intensity measured between the antenna array and the antenna attached to the moveable arm (see figure 4.4) for the last 10  $q$ -state ordered according to equation (4.34). These states are referred to as focussing states. Each state is measured two times. On the left without the brass scatterer and on the right with the brass scatterer. In state 54 and 55 two arrows are shown indicating two different directions in perfect correlation with the sign of the real part of the associated eigenvalue (see figure 4.21). The generating process of the images and the colour bar is shown in figure 4.23

Figure 4.24 also reveals that the **focussing states (states 46-55) are still quite correlated with values well above 50%**. One can understand this fact if one looks at the intensity profiles shown in figure 4.25.

The focussing states show high intensities in the vicinity of the brass scatterer. If the brass scatterer is not present the state shows a strong intensity line going through the area where the brass scatterer was placed before. If the brass scatterer is present, it acts as an obstacle where the focussing states are directly reflected. Especially the states 51 to 55 show strong reflection characteristics when the scatterer is present in the waveguide. These  $q$ -states hardly pass the brass scatterer, so the right half of the image shows very low intensity (dark blue colours right from central scatterer in figure 4.25). The correspondence of the wave functions of the focussing states, especially on the left half of the measured field, leads to a fairly high correlation for these states when one compares the scatterer-present and scatterer-absent case.

Another aspect is the **directivity of the focussing**. It has been shown in [Bra16] that the sign of the real part of the eigenvalue  $\lambda_q$  of the  $q$ -state can be associated to a direction, if the shift of the obstacle is done in the transversal direction to the propagation direction of the mode (as it is the case here). A rigorous theo-

retical explanation is not yet available, but I mentioned in section 3.3, that the real part of  $q_y$  can be related to the momentum transfer onto the obstacle with regard to the  $y$ -direction (since the derivation of  $T$  is done with  $\partial/\partial y$  which leads to a  $k_y$  dependency of the  $q$ -operator, [Bra16]). Therefore the sign of the real part of the eigenvalue can be connected to the direction from which the state is focussing onto the obstacle. This argument is in full agreement with the experimental observations.

We can fix a certain direction to the state 55 (red arrow in figure 4.25) which we connect to the positive value of the real part  $\text{Re}(\lambda_q)$ . The direction indicated in the intensity plot of state 54 (blue arrow in figure 4.25) is associated with the negative value of  $\text{Re}(\lambda_q)$ . As we look at the direction of the intensity lines of the focussing states in figure 4.25 (indicated with two coloured arrows defined after the state 54 and 55), we recognise that they are in perfect agreement with the sign changes of  $\text{Re}(\lambda_q)$  shown in figure 4.21. An exact theory for obstacle movements in the longitudinal direction ( $x$ -direction) can be found in [Bra16].

#### 4.3.4 A Coherent Perfect Absorber

In this context, I would like to introduce the concept of coherent perfect absorption as it was presented in [Cho10b]. A perfect coherent absorber is appearing when a wave injected into a lossy and finite system is fully absorbed in the sense that the back reflected parts of the wave are undergoing destructive interference. Such a system would therefore, viewed from outside, mimic a perfect absorber. As we have seen before, we can describe a scattering system with its scattering matrix  $S$ . Of special interest in physics are the poles and zeros of the scattering matrix, which can be calculated as points lying in the complex  $k$ -plane (see [Fon72, Sit71] for an introduction on zeros/poles of the scattering matrix). One can show that coherent perfect absorption occurs whenever a zero located in the upper half plane of the  $k$ -plane is moved downwards close to the real  $k$ -axis [Cho10b]. This is done by adding loss to the system. In fact this is the exact contrary to what people do when they try to construct lasers. Laser engineers try to move poles of the lower half plane upwards by adding gain to the system. This is why this phenomenon of coherent perfect absorption can be associated with a time reversed version of a laser, a so called "anti-laser" [Gma10]. Assuming we have a system where a zero is lying on the real  $k$ -axis. If we injected a wave which corresponds to the eigenvector of this zero-eigenvalue, the outgoing wave would vanish and the injected wave would be perfectly absorbed within the system itself.

We think such a system can be realised with our quasi-one-dimensional channel. A proposal for an implementation of such a coherent perfect absorber (CPA) using the already known components of our set up is shown in figure 4.26. The idea is that we have a well controlled injection of waves coming from two opposite leads attached to the scattering region. The reflected parts of the waves will interfere with the transmitted parts in such a way that the intensity is trapped within the scattering region, where it is absorbed by a lossy material. In our case this is an

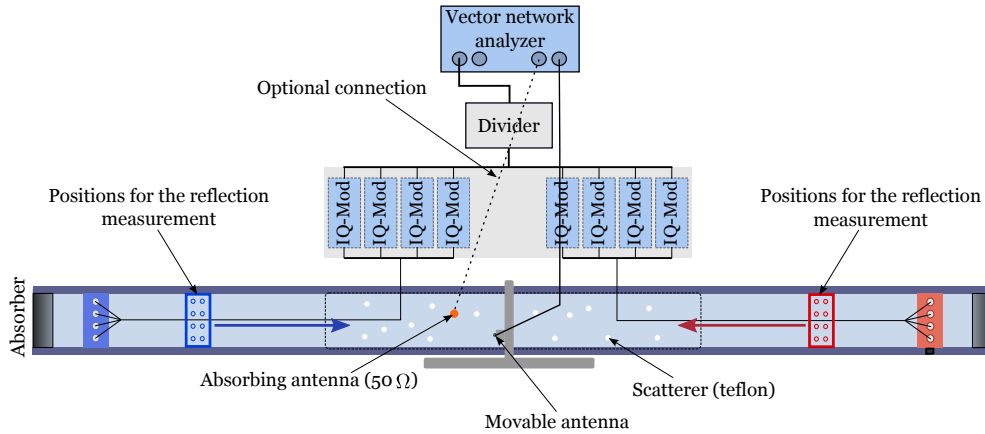


**Figure 4.26** – Sketch illustrating the idea of measuring coherent perfect absorption with the accessible equipment. Compare with figure 4.4. The number of propagating modes is 4.

antenna with a  $50 \Omega$  resistance attached. This means that the reflected part of the wave injected from the right lead interferes destructively with parts of the wave transmitted from the left and vice versa. It is clear that one needs precise control of the phases and amplitudes of the injected waves so that the coherent parts interfere exactly in the manner described before. An 'anti-laser'-system with two attached channels has been constructed using uniform distributed lossy material (a uniform silicon waver) in [Wan11].

Our idea differs strongly in this point, as we want to use scattering together with a highly non-uniform absorption given by a point-like absorption introduced by an additional antenna.

In the lasing community it is known that using disordered potentials together with gain helps to increase the path length of the light within the system and leads to an enhancement of the amplification [Cao06, Wie08]. This type of laser is referred to as random laser. In this sense we propose here an experiment as model for an anti-random laser, where the scattering enhances the absorption. Such an anti-random laser has not yet been achieved experimentally (to the best of my knowledge).

### Discussion of the experimental realisation

If one compares the microwave waveguide we want to use for the measurement of the CPA and the waveguide we used before (compare figure 4.26 with figure 4.4), one recognises that the set-up supports now signal injection from both leads, where we positioned 4 antennas on each side. These antennas give us full control about the four propagating modes which we are going to inject from both sides. We will use Teflon cylinders as scattering objects and an additional antenna connected to a 50 Ohm resistance to introduce strong point-like absorption. A possibility to prove the existence of a CPA is to verify that all injected energy is fully focussed into

the absorbing material. With our experiment we have the great possibility to prove exactly that. In fact, we can quantify the amount of absorption by connecting the absorbing antenna to the vector network analyser and by measuring the transmission from the leads into the antenna.

But before one can do that, one has to overcome the difficulty to meet the CPA condition. One has to prove that the scattering matrix  $S(f)$  has an eigenvalue  $\lambda_{CPA}$  of value zero. Then, in a second step, one can inject the corresponding eigenvector  $\mathbf{i}_{CPA}$  and show maximal absorption by the absorbing antenna. From the previous experiments we know how to extract the transmission matrix  $T$  of the system. If we want also to gain access to the reflection matrix  $R$  we have to introduce additional measurement points, shown as 8 additional measurement point on each side in figure 4.26 (marked with "positions for the reflection measurement"). The movable antenna can address these eight points and we can measure the transmission from the outermost antennas to the point where the moveable antenna is located. The measurement protocol would be to measure the complex propagation constants  $\beta_n$  of the four propagating modes  $\Psi_n =$  for  $n = 1, 2, 3, 4$  (see equation (4.37)) in the empty waveguide (no scatterer and no absorption antenna):

$$\Psi_n \propto \sin(k_{y,n}y) e^{i\beta_n x}. \quad (4.37)$$

$k_{y,n}$  is the k-value for the  $y$ -direction defined in equation (4.23) (the coordinate system was defined in figure 4.3).  $\beta_n$  in general is complex even in the case of an empty waveguide. The imaginary part of  $\beta_n$  accounts for the losses which are mainly related to the metallic surfaces of the cavity. The empty-measurement allows us to specify the propagation constants and the size of possible reflections of the absorbers, whose presence cause small back reflections (but no inter-mode scattering).

As a second step, we can plug in the scattering system and the absorbing antenna and measure all entries of the scattering matrix where we use the additional measurement points and the information about the  $\beta_n$  to specify the reflections coming from the scattering system. It was shown in [Bra16] theoretically that these additional 8 measurement points on each side together with the information of an empty waveguide measurement are enough to construct the full scattering matrix.

Once we have measured the frequency dependant scattering matrix, we can calculate its eigenvalues. If we find an eigenvalue which is 0 for a certain frequency  $f_{CPA}$ , we can calculate the corresponding eigenvector  $\mathbf{i}_{CPA}$ . Since we can measure the transmission from the outer antennas (antennas connected to the IQ-modulators) into the absorbing antenna, we can calculate the maximal possible transmission into the absorbing antenna by solving a simple linear equation system of the size  $8 \times 1$ , where we used the transmission from each single outer antenna to the absorbing central antenna. This resulting optimal transmission state has to coincide with  $\mathbf{i}_{CPA}$ . If it is the case one can be sure that the back reflections interfere destructively with the transmitted parts of the injected wave and that all the intensity is stored within the scattering region (absorbing antenna), which is the proof of an coherent perfect absorber realised with non uniform absorption and additional scattering. This would correspond to the creation of an anti-random laser.

### 4.4 CONCLUSION

The presented set-up shows how wave front shaping can be performed in a quasi-one-dimensional rectangular waveguide. We used IQ-modulators to modulate the wave front emitted by an array of ten monopole antennas. I showed that we are able to excite individual sinusoidal modes in the waveguide, no matter if this waveguide was empty or filled with dielectric/metallic scatterers. All this was possible using the information of the systems transmission matrix  $T$  and shaping the initial wave front accordingly. In a second step we went beyond simple mode tuning. We measured the transmission matrix for various positions of a metallic scatterer (slight position movements of the scatterer perpendicular to the direction of the mode propagation) and used the scatter position  $y_{scat}$  as parameter  $\alpha$  (see chapter 3) to construct the  $q$ -operator. The eigenvectors, called  $q$ -states, of this operator have unique properties. We could identify two types of  $q$ -states which are clearly distinguishable by our used criteria  $\text{ord}_q$  (see equation (4.34)). Eigenvectors with a low value of  $\text{ord}_q$  are of avoiding character. This means that they significantly avoid the space occupied by the moved scatterer and they are very robust. These  $q$ -states with a low value of  $\text{ord}_q$  stayed basically the same, no matter if the scatterer was present or not (see figures 4.22 and 4.24). The second type of  $q$ -states was of focussing character and the corresponding states showed a strong dependency on the position of the scatterer. We could even associate a direction to these focussing states. The direction was found to be a function of the sign of the real part of the eigenvalue of the corresponding  $q$ -state.

This new concept of using a generalised  $q$ -operator together with a spatial parameter  $\alpha$  seems very promising. Especially if one thinks of possible applications. As our system can be seen as fully analogue to other wave based systems, such as acoustic systems [Ede05] and optical ones [Xio16], one can translate our findings into these domains.

One can think of the problem for wireless communication systems [Ral98], where one is always interested in finding solutions to focus a signal on a certain spot like a phone for example. With our approach it is possible either to focus on a spot/area or to avoid a certain region using the same kind of information. This can be useful under the aspect of security as well, where one wants to leave out possible intruders. Our results might also be interesting for applications in medicine, where one tries on the one hand side to kill tumours by intense focussed radiation (such as ultrasound [Coc09]) and on the other hand side to leave vulnerable areas untouched. The idea of measuring the transmission as a function of the position of a scatterer might also be interesting in the closely related context of time reversal [Fin92, Ler04], where one is also interested in achieving a focussing or avoiding effect. Further information on our set-up and a detailed discussion of the obtained results for the mode tuning are also available in [Böh16].

# 5 *Dynamical Encircling of an Exceptional Point*

---

## Contents

---

<b>5.1</b>	<b>Exceptional Points and their Experimental Realisation . . . . .</b>	<b>88</b>
<b>5.2</b>	<b>Dynamical Encircling with a Waveguide . . . . .</b>	<b>92</b>
	<i>5.2.1 Bloch Modes . . . . .</i>	92
	<i>5.2.2 Using Perturbation Theory . . . . .</i>	94
<b>5.3</b>	<b>Experimental Realisation in a Waveguide . . . . .</b>	<b>96</b>
<b>5.4</b>	<b>Microwave Set-up . . . . .</b>	<b>100</b>
<b>5.5</b>	<b>The Dynamical Encircling - Experimental Results . .</b>	<b>102</b>
<b>5.6</b>	<b>Parametric Encircling . . . . .</b>	<b>105</b>
<b>5.7</b>	<b>Conclusion . . . . .</b>	<b>110</b>

---

A very peculiar transport phenomena arises when one encircles a so called exceptional point (**EP**). We will show in this chapter that we can address this transport phenomena with our one dimensional waveguide set-up, where we introduced wavy boundaries and additional loss. The propagating modes will perform the mentioned encircling and this causes them to show the typical flipping behaviour. The great advantage of our set-up is that a full dynamical encircling around an exceptional point can be achieved, which leads to an asymmetric mode switching when comparing different injection directions.

## 5.1 EXCEPTIONAL POINTS AND THEIR EXPERIMENTAL REALISATION

Exceptional points raised the interest of the physics community since they are the origin of quite peculiar phenomena such as state flips [Uzd11, Mil15, Gao15, Xu16, Din16]. Exceptional points (also called branch points) are observed in physical systems which can be modelled by a non-Hermitian Hamiltonian, which takes into account that these system experience gain or loss leading to a non-conservation of energy.

EPs arise in open systems following the Schrödinger equation ( $i\partial_t\Psi = H\Psi$ ) once two resonant states coincide [Rot09, Moi11, Hei12]. An example can be given by investigating a  $2\times 2$  Hamiltonian, e.g., the Hamiltonian of two coupled damped oscillators. This Hamiltonian can be written as (I follow the notation of [Dop16a]):

$$H = \begin{pmatrix} \delta - i\gamma_1/2 & g \\ g & -i\gamma_2/2 \end{pmatrix}, \quad \delta, g, \gamma_1, \gamma_2 \in \mathbb{R}, \quad (5.1)$$

where  $g$  is the coupling and  $\delta$  is the detuning between the two states.  $\gamma_1$  and  $\gamma_2$  are the loss rates destroying the Hermitian property of  $H$  so that  $H \neq H^\dagger$ .

The eigenvalues  $E_{1,2}$  of  $H$  can be calculated as

$$E_{1,2} = \frac{\delta}{2} - i\frac{\gamma_1 + \gamma_2}{4} \pm \frac{1}{2}\sqrt{\Delta} \quad \text{with} \quad \Delta = \left(\delta - i\frac{\gamma_1 - \gamma_2}{2}\right)^2 + 4g^2. \quad (5.2)$$

The behaviour of the eigenvalues as a function of the coupling  $g$  and the detuning  $\delta$  is presented in figure 5.1.

For the eigenvectors  $\Phi_{1,2}$  one finds [Dop16b]

$$\Phi_1 = \begin{pmatrix} \cos\left(\frac{\Omega}{2}\right) \\ \sin\left(\frac{\Omega}{2}\right) \end{pmatrix}, \quad \Phi_2 = \begin{pmatrix} -\sin\left(\frac{\Omega}{2}\right) \\ \cos\left(\frac{\Omega}{2}\right) \end{pmatrix} \quad (5.3)$$

$$\text{with} \quad \tan\left(\frac{\Omega}{2}\right) = \frac{g}{E_1 + i\gamma_2/2}. \quad (5.4)$$

An exceptional point occurs if  $\Delta = 0$ . This happens for  $g = g_{EP}$  and  $\delta = \delta_{EP}$  with

$$g_{EP} = \begin{cases} g_{EP}^+ = \frac{|\gamma_1 - \gamma_2|}{4} \\ g_{EP}^- = -\frac{|\gamma_1 - \gamma_2|}{4} \end{cases}, \quad \delta_{EP} = 0. \quad (5.5)$$

Note that the chosen Hamiltonian (equation (5.1)) contains two exceptional points.

For unequal loss rates  $\gamma_1 \neq \gamma_2$  one finds one complex eigenvalue  $E_{EP} = -i(\gamma_1 + \gamma_2)/4$  and one complex eigenvector  $\Phi_{EP}$  for each of the two exceptional points,

## 5.1. Exceptional Points and their Experimental Realisation

---

which are defined according to [Dop16b] as (see also [Kat13] for more mathematical details):

$$\Phi_{EP} = \begin{cases} \Phi_{EP}^+ = \begin{pmatrix} 1 \\ -i \end{pmatrix} & \text{if } g = g_{EP}^+ \\ \Phi_{EP}^- = \begin{pmatrix} 1 \\ +i \end{pmatrix} & \text{if } g = g_{EP}^- \end{cases} \quad (5.6)$$

This means that the two eigenvectors (eigenstates) and the two eigenvalues **coalesce** at the EP. This is especially different from a degeneracy, where only the eigenvalues coalesce. A remarkable effect is also that the norm of  $\Phi_{EP}$  is zero, which is formally known as self-orthogonality [Moi11]. A more rigorous approach including different coupling configurations for  $g$  to calculate exceptional points can be found in [Hei12].

In figure 5.1 one can examine the resulting eigenvalue spectrum of  $H$  depending on the detuning  $\delta$  and the coupling  $g$ . Physically interesting is the fact that for  $\delta = \delta_{EP}$  the two energy levels of the two eigenstates, corresponding to  $\text{Re}E$  in figure 5.1, undergo an avoided crossing for  $g > g_{EP}$  and a real crossing for  $g < g_{EP}$ . The widths of the eigenstates, corresponding to  $\text{Im}E$ , show exactly the opposite behaviour. These two properties are typical while passing an exceptional point.

An interesting feature which occurs when following a state encircling the exceptional point is the state flip feature. In order to observe this one has to parametrise a path around the exceptional point. Therefore we introduce the time parameter  $t$  so that  $g$ ,  $\delta$  and  $\Psi$  are now time dependent variables and their dynamics is described via the time-dependant Schrödinger equation  $i\partial_t\Psi(t) = H(t)\Psi(t)$ .

A possible circular path parametrisation around an exceptional point with a distance  $r$  and an angle  $\phi$  is

$$g(t) = g_{EP} + r\cos(\phi(t)), \quad \delta(t) = -2r\sin(\phi(t)). \quad (5.7)$$

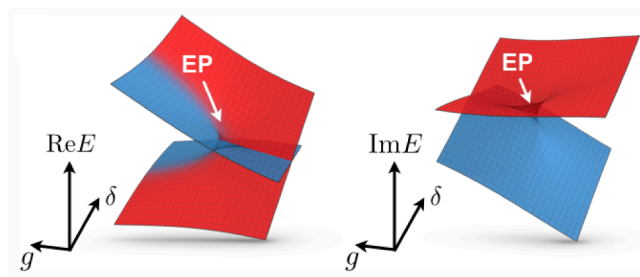


**Figure 5.1** – Eigenvalue spectrum of  $H$  around an exceptional point (white arrow) depending on the coupling  $g$  and the detuning  $\delta$ . **Left:** Real part of the eigenvalues  $E_{1,2}$  (see equation (5.2)). **Right:** The imaginary part of the eigenvalues  $E_{1,2}$ . The red (blue) colour corresponds to an eigenvalue with relative gain (loss). [Dop16b]



## Chapter 5. Dynamical Encircling of an Exceptional Point

---

For  $r$  small,  $r^2 \rightarrow 0$ , the dependency of the eigenvalues  $E_{1,2}$  as a function of  $r$  and  $\phi$  at  $g_{EP} = g_{EP}^+$  is described by

$$E_{1,2} \approx r \sin(\phi) - i \frac{\gamma_1 + \gamma_2}{4} \pm \sqrt{2r g_{EP}^+} e^{i\phi/2}. \quad (5.8)$$

The phase term  $\exp(i\phi/2)$  is the reason for the interchanging of the eigenvalues as shown in figure 5.1 for an encircling of the EP  $\phi \rightarrow \phi \pm 2\pi$ . Doppler concluded in [Dop16b] with the help of [Kec03] (chapter 3.2) for the angle  $\Omega$  (see equation (5.3))

$$\text{Re} \left( \frac{\Omega}{2} \right) \approx \frac{\pi}{4} - \frac{\phi(t)}{4}. \quad (5.9)$$

This means that a full encircling of the exceptional point leads only to a  $\pi/2$  shift of the eigenvector phase  $\Omega$ :

$$\frac{\Omega}{2} \rightarrow \frac{\Omega}{2} - \frac{\pi}{2} \quad \text{for} \quad (2\pi)^+, \quad (5.10)$$

$$\frac{\Omega}{2} \rightarrow \frac{\Omega}{2} + \frac{\pi}{2} \quad \text{for} \quad (2\pi)^-. \quad (5.11)$$

where  $(2\pi)^+$  indicate an encircling in the positive mathematical sense and  $(2\pi)^-$  in the negative sense. The eigenvectors  $\Phi_i$  defined by equation (5.3) undergo a flip while traversing the loop. This is the widely observed state flip phenomenon:

$$\begin{pmatrix} \Phi_1 \\ \Phi_2 \end{pmatrix} \xrightarrow{(2\pi)^+} \begin{pmatrix} \Phi_2 \\ -\Phi_1 \end{pmatrix}, \quad \begin{pmatrix} \Phi_1 \\ \Phi_2 \end{pmatrix} \xrightarrow{(2\pi)^-} \begin{pmatrix} -\Phi_2 \\ \Phi_1 \end{pmatrix}. \quad (5.12)$$

Only after 4 round trips ( $8\pi$ ) the state (eigenvector) comes back to the original state (eigenvector) [Dem04, Mai05, Kec03]:

$$\begin{pmatrix} \Phi_1 \\ \Phi_2 \end{pmatrix} \xrightarrow{(2\pi)^+} \begin{pmatrix} \Phi_2 \\ -\Phi_1 \end{pmatrix} \xrightarrow{(2\pi)^+} \begin{pmatrix} -\Phi_1 \\ -\Phi_2 \end{pmatrix} \xrightarrow{(2\pi)^+} \begin{pmatrix} -\Phi_2 \\ \Phi_1 \end{pmatrix} \xrightarrow{(2\pi)^+} \begin{pmatrix} \Phi_1 \\ \Phi_2 \end{pmatrix}. \quad (5.13)$$

In this context, I would like to mention two microwave experiments which used two real experimental parameters for the discrete encircling of an exceptional point [Dem01, Dem04]. The first parameter was the coupling between two halves of a metallic cavity (corresponds to  $g$  in our case), i.e., they modified the width of a slit connection between the halves. The second parameter was the variation of energy levels (which corresponds to  $\delta$  in our case) by moving a metallic scatterer in one of the two halves of the metallic cavity. In this experiment they were able to confirm the state flip and that a fourfold encircling of the exceptional point recreates the initial state according to equation (5.13). Other experiments used coupled electronic circuits [Ste04], optical micro-cavities [Lee09] or cold atoms [Cho10a] to perform what is called a **parametric encircling** of the exceptional point.

This picture of state flips stays valid as long as the system dynamics can be described fully adiabatically. However, it turned out that also non-adiabatic effects have to be considered when encircling an exceptional point dynamically.

## 5.1. Exceptional Points and their Experimental Realisation

It has been shown in [Uzd11], that an encircling of a state can either follow an adiabatic transition towards its flipped equivalent or a non-adiabatic. The preferred transition for a fixed encircling direction depends on the initial state. Due to non-adiabatic coupling an eigenstate can undergo a non-adiabatic transition. We can look for example on the clockwise encircling of the state which is initially placed on the lossy part of the upper eigenvalue plane (also called upper Riemann sheet). This is shown in figure 5.2. This state follows a non adiabatic behaviour encircling the EP (solid line in figure 5.2) which leads to the fact, that the state comes back to its initial position (see figure 5.2). The adiabatic transition following the lossy plane all the time is heavily suppressed and therefore only the non-adiabatic transition enters predominantly. In figure 5.3 all prominent transitions for all possible initial conditions and all encircling directions are presented. **Thus the final state of an eigenstate encircling an exceptional point depends only on the direction of the encircling, not on the initial state.**

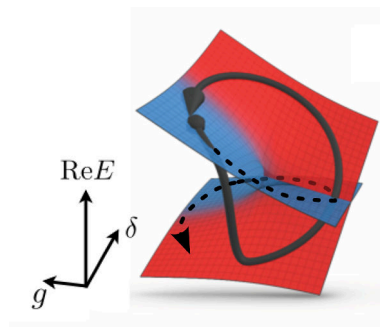


**Figure 5.2** – Dynamics of an eigenstate starting from the lossy part of the upper eigenvalue plane and encircling an exceptional point in the counter-clockwise direction. The coloured sheets indicate the two different eigenvalues of  $H$  (see equation (5.1) and figure 5.1). Path taken due to non-adiabatic coupling (solid line). Path which would correspond to an adiabatic behaviour (dashed line). The red (blue) colour corresponds to the eigenvalue-sheet with relative gain (loss).

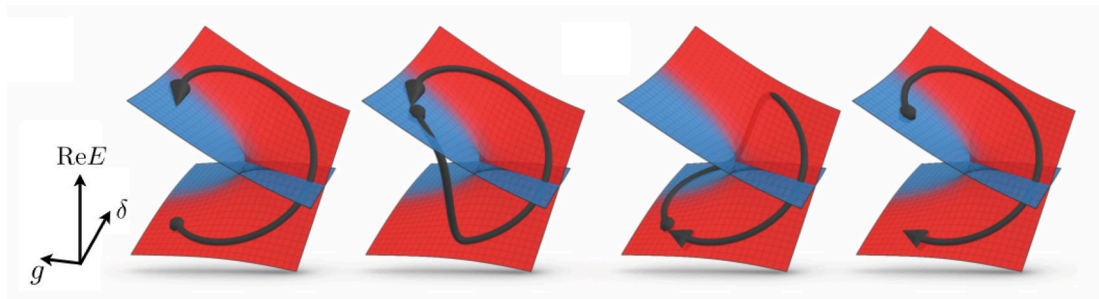


**Figure 5.3** – Dynamics of eigenstates encircling an exceptional point of the non-Hermitian Hamiltonian  $H$  (see equation (5.1)). The coloured sheets indicate the two different eigenvalues of  $H$  (see figure 5.1). Depending on the encircling direction **only**, the eigenstate reaches always the same final state. The red (blue) colour corresponds to the eigenvalue-sheet with relative gain (loss). [Dop16a]

Assume a system where one has two eigenstates (or modes) which perform a loop around the exceptional point in the manner described above. If this system followed the dynamics described above, one would create an asymmetric switch. The system would react in such a way that state (mode) 1 scatters into state (mode) 2, whereas state (mode) 2 scatters into itself. One has to note here that this asymmetric switching effect arises due to non-adiabatic transitions. Therefore it can only be observed in an experiment performing a dynamical encircling rather than a parametric one done by the Darmstadt group [Dem01, Dem04]. This idea of an asymmetric switch marks the aim of our system we want to design in the following. Thus we have to think of how to perform a dynamical encircling of an exceptional point.

### 5.2 DYNAMICAL ENCIRCLING WITH A WAVEGUIDE

In this chapter we will translate the ideas presented above into a waveguide system similar to the one presented in chapter 4. The waveguide of chapter 4 will be modified to fit its new purpose. We will exchange the straight borders and we insert instead smoothly and periodically deformed walls and we place absorbing material inside to introduce the loss which correspond to the  $\gamma_i$  of equation (5.1). The boundary parameters (amplitude and frequency of the boundary) will define our parameter space through which the states (in our case Bloch-modes) are performing the round-trip around the EP. The width and the working frequency are adjusted in such a way that only the first two Bloch modes can propagate along the x-axis (following the coordinate system introduced in section 4.2).

#### 5.2.1 Bloch Modes

These newly introduced periodic boundaries (see figure 5.4) will lead to the appearance of so called Bloch modes  $\Lambda$  with their wavenumber  $K$ . We will see that these Bloch modes will represent the states which coalesce at the exceptional point and that their wavenumbers correspond to the eigenenergies which will coincide as described above.

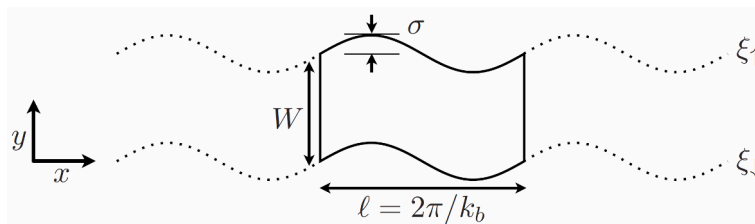


**Figure 5.4** – Scheme of an infinite waveguide with a periodically changing border. [Dop16b]

## 5.2. Dynamical Encircling with a Waveguide

---

The harmonically oscillating electric field  $\Phi(x, y, t)$  within this periodic waveguide can be described as

$$\Phi(x, y, t) = \Lambda(x, y)e^{-i(\omega t - Kx)} = \phi(x, y)e^{-i\omega t}. \quad (5.14)$$

Note that  $K$  is defined up to an integer multiple of  $k_b$ , such as  $K \bmod k_b$ , where  $k_b$  denotes the boundary wave number defined in figure 5.4 (see details below).

As we have shown in section 1.1 this field has to obey the two dimensional Helmholtz equation (see equation (1.6) for  $\mu = 1$ ):

$$\Delta\phi(x, y) + \epsilon(x, y)\frac{\omega^2}{c_0^2}\phi(x, y) = 0. \quad (5.15)$$

where  $\epsilon$  is here a complex dielectric function,  $c_0$  is the speed of light. If  $\epsilon$  is just a real constant, i.e., it is not position dependant, one finds the sinusoidal modes, which have been discussed in detail in chapter 4. In this notation the sinusoidal modes are written with

$$\Phi_n = \sin\left(\frac{n\pi y}{W}\right) e^{ik_n x}, \quad \text{with} \quad k_n = \sqrt{\frac{\omega^2}{c^2} - \left(\frac{n\pi}{W}\right)^2}, \quad (5.16)$$

where  $n$  is a simple integer (compare with section 4.2.2) and  $W$  is the constant waveguide width (see figure 5.4).

But in order to reproduce a Hamiltonian similar to the one in equation (5.1) one has to introduces position dependant losses to the system this means  $\epsilon(x, y) = 1 + i\eta(x, y)/k$  is now complex and depends on the dissipation coefficient  $\eta(x, y)$ .  $\eta$  takes into account the losses from the waveguide walls as well as from the absorbing material introduced in the waveguide itself.

At the border the field  $\phi(x, y)$  follows Dirichlet boundary conditions so that  $\phi(x, y = \xi_\uparrow) = 0 = \phi(x, y = \xi_\downarrow)$  with (see also figure 5.4 where  $\xi$  is indicated)

$$\xi_\downarrow(x) = \sigma \sin k_b x, \quad \xi_\uparrow(x) = W + \sigma \sin k_b x, \quad (5.17)$$

where the boundary wavenumber  $k_b$ , given by

$$k_b = k_1 - k_2 + \delta = k_r + \delta, \quad (5.18)$$

introduces near resonant scattering.  $\delta$  is the detuning parameter ( $\delta \ll k_b$ ). We will see that this wobbly waveguide will be attached to a simple rectangular one, where the basic excitation of the sinusoidal modes is done. The frequency  $\omega_w$  where we are working at is chosen, so that the corresponding wavenumber  $k_w$  fulfils  $2\pi/W < k_w = \omega^2/c^2 < 3\pi/W$  (see equation (5.16)), leaving us with two propagating modes.  $\phi$  is defined to be Bloch-periodic. Therefore it fulfils the following periodicity:

$$\Lambda(x + l, y) = \Lambda(x, y) \quad \text{with} \quad l = \frac{2\pi}{k_b}. \quad (5.19)$$

### 5.2.2 Using Perturbation Theory

The initial state is prepared in a rectangular waveguide so we set  $\sigma = \nu = \delta = 0$  leading to:

$$\phi^0 = \Lambda^0(x, y)e^{ik_1x}, \quad (5.20)$$

$$\Lambda^0(x, y) = a_1 \sin\left(\frac{\pi}{W}y\right) + a_2 \sin\left(\frac{2\pi}{W}y\right) e^{-ik_r x}. \quad (5.21)$$

where  $\Lambda^0$  is periodic with regard to  $l_0 = 2\pi/k_r$ . One refers to this as a degenerate Bloch mode of multiplicity two with the wavenumber  $k_1$ .

Now we switch on the boundary amplitude  $\sigma$ , the detuning parameter  $\delta$  and the dissipation coefficient  $\eta$  and therefore we have to consider corrections appearing in equation (5.19) like

$$\Lambda(x, y) = \Lambda^0(x, y) + \Lambda^1(x, y), \quad K = k_1 + s, \quad (5.22)$$

$$l = \frac{2\pi}{k_b} = l_0 + l_1\delta + \mathcal{O}(\delta^2), \quad \text{with } l_0 = \frac{2\pi}{k_r}, \quad l_1 = \frac{-2\pi}{k_r^2}. \quad (5.23)$$

$s$  is a small correction for the wavenumber and of the same order as  $\sigma$ ,  $\delta$  and  $\eta$ . Using the definition of  $\phi$  (equation (5.14)) and developing  $\phi$  for small  $s$  and neglecting higher order terms of  $\sigma$ ,  $\delta$  and  $\eta$  and also neglecting products of those one derives

$$\phi(x, y) = [\Lambda^0(x, y) + \Lambda^1(x, y) + ix\Lambda^0(x, y)s]e^{ik_1x} \quad (5.24)$$

Taking this result and using the Helmholtz equation (5.15), the boundary conditions such as  $\phi(x, y = \xi_\uparrow) = \phi(x, y = \xi_\downarrow) = 0$  and the periodicity condition for  $\Lambda$  in equation (5.19) one derives two equations (see details in [Dop16b])

$$\left(i\frac{\eta}{2}\frac{k}{k_1} - s\right)a_1 + i2\frac{\sigma}{k_1}\frac{\pi^2}{W^3}a_2 = 0 \quad (5.25)$$

$$-i2\frac{\sigma}{k_2}\frac{\pi^2}{W^3}a_1 + \left(\delta + i\frac{\eta}{2}\frac{k}{k_2} - s\right)a_2 = 0 \quad (5.26)$$

One can recognise here that if one writes equations (5.25, 5.26) in their matrix form, one ends up almost with a matrix similar to the Hamiltonian defined in equation (5.1). The equation system (5.25, 5.26) is solvable if its determinant is 0, i.e.,

$$\left(s - i\frac{\eta}{2}\frac{k}{k_1}\right)\left(s - \delta - i\frac{\eta}{2}\frac{k}{k_2}\right) - \frac{4\pi^4}{W^6}\frac{\sigma^2}{k_1k_2} = 0. \quad (5.27)$$

The three equations (5.25, 5.26, 5.27) are sufficient to define  $s$ ,  $a_1$  and  $a_2$  so that we can approximate  $\phi$  by [Dop16b]:

$$\phi(x, y) \approx \left(a_1 \sin\left(\frac{\pi}{W}y\right) + a_2 \sin\left(\frac{2\pi}{W}y\right) e^{-ik_r x}\right) e^{i(k_1+s)x}, \quad (5.28)$$

## 5.2. Dynamical Encircling with a Waveguide

---

with

$$c_1(x) = a_1 \sqrt{k_1} e^{i\pi/4} e^{-i(\delta-s)x}, \quad c_2(x) = a_2 \sqrt{k_2} e^{-i\pi/4} e^{-i(\delta-s)x}. \quad (5.29)$$

$c_1(x)$  and  $c_2(x)$  are coefficients solving a Schrödinger equation (see equation (5.30) and the explanation given below). The solution (5.28) shows that the components of the Bloch modes are expressed as slightly modified sinusoidal modes. In the following we will refer to the first component of the Bloch mode as Bloch mode 1 and the second one will be named Bloch mode 2.

The presented approximation for  $\phi(x, y)$  holds for small  $\sigma$ ,  $\delta$ ,  $\eta$  and  $s$ . With the use of equations (5.25, 5.26, 5.27) and a similarity transformation which gives symmetric diagonal elements one can define a Hamiltonian which is similar to the one in equation (5.1) and one can show that  $\phi$  (5.28) fulfils the Schroedinger equation where **the time dependency  $t$  was replaced by the spatial coordinate  $x$**  [Dop16b]

$$i \frac{\partial}{\partial x} \begin{pmatrix} c_1 \\ c_2 \end{pmatrix} = H \begin{pmatrix} c_1 \\ c_2 \end{pmatrix}, \quad H = \begin{pmatrix} \delta - i \frac{\eta}{2} \frac{k}{k_1} & B\sigma \\ B\sigma & -i \frac{\eta}{2} \frac{k}{k_2} \end{pmatrix}, \quad B = 2 \frac{\pi^2}{W^3} \frac{1}{\sqrt{k_1 k_2}}. \quad (5.30)$$

This  $2 \times 2$  Hamiltonian shows a very nice correspondence with equation (5.1). The amplitude modulation  $\sigma$  of the wavy boundary turns out to be related to the coupling  $g$ . The frequency modulation  $\delta$  manipulates the detuning of the two resonances and  $\eta$  plays the role of  $\gamma$  (compare equation (5.1) with equation (5.30)). We see in the Hamiltonian of equation (5.30) that the loss  $\gamma_j = i \frac{\eta}{2} \frac{k}{k_j}$  differs for the two modes due to the factor of  $k/k_j$  for the case of non-position-dependant loss  $\eta$ . But in our experiment it is possible to introduce absorbing foam material (see section 5.4) and therefore we can make the loss  $\eta$  position dependant  $\eta = \eta(x, y)$ . We need to design  $\eta$  in such a way that the absorption gets mode dependent. This can be done by placing absorbing material in the nodal spots of one mode, for example.

In order not to loose the Bloch-formalism  $\eta(x, y)$  has to fulfil the following condition:

$$\eta = \eta_0 \tilde{\eta}(x, y), \quad \tilde{\eta}(x + l, y) = \tilde{\eta}(x, y), \quad \text{with } l = 2\pi/k_b. \quad (5.31)$$

In fact this leads to the modified Hamiltonian [Dop16b]:

$$H = \overbrace{\begin{pmatrix} \delta & B\sigma \\ B\sigma & 0 \end{pmatrix}}^{H_0} - i \frac{\eta_0}{2} \begin{pmatrix} \Gamma_{11} & \Gamma_{12} \\ \Gamma_{12}^* & \Gamma_{22} \end{pmatrix}, \quad (5.32)$$

$$\Gamma_{nm} = \frac{e^{i\pi(m-n)/2}}{\pi W} \frac{k k_b}{k_n k_m} \int_0^W \int_0^l \tilde{\eta}(x, y) \sin\left(\frac{n\pi}{W}\right) \sin\left(\frac{m\pi}{W}\right) e^{-i(k_n - k_m)x} dx dy \quad (5.33)$$

A clever way to introduce asymmetric mode scattering is to place the absorbing material in the maximum of an eigenstate  $v_1$  of  $H_0$ , meaning that:

$$H_0 v_1 = E_1 v_1. \quad (5.34)$$

We can construct now an anti-Hermitian Hamiltonian  $H$  so that  $v_1$  is heavily suppressed along its propagation. One way to do it is to define  $H$  as

$$H = H_0 - i\frac{\eta}{2}v_1v_1^\dagger. \quad (5.35)$$

Since  $v_1^\dagger v_2 = 0$ , by construction, only  $v_1$  is heavily absorbed, when one looks at the propagation of the eigenvectors by the means of  $\exp(-iHx)v_i$ . We obtain that  $v_1$  undergoes a heavy damping (factor of  $\exp(-\eta x/2)$ ) during the propagation.

Numerically, one can show that the absorption description by  $\Gamma_{nm}$  works well for the description of Bloch mode propagation [Dop16b]. Experimentally we will follow our considerations above and we will place the absorber at the nodal line of one of the modes (line of the maximum of the other mode). This is exactly what can be seen in the experimental realisation (see figure 5.9). By adjusting the length of this absorbing line we can regulate the absorber strength to ensure that we are still in the regime of small  $\eta$ , so that the perturbation description presented in this chapter is still valid.

### 5.3 EXPERIMENTAL REALISATION IN A WAVEGUIDE

At this point we have all necessary ingredients to design a waveguide where an encircling of an exceptional point is possible. We will choose the  $x$ -dependent parameters  $\sigma(x)$ ,  $\delta(x)$ ,  $\eta(x)$  (see coordinate system in figure 5.4) such that an encircling can be achieved within in the limits of our experiment. Concretely, this means

$$\sigma(x) = \frac{\sigma_0}{2} \left( 1 - \cos \frac{2\pi}{L} x \right), \quad \delta(x) = \delta_0 \left( 2 \frac{x}{L} - 1 \right) + \rho, \quad (5.36)$$

$$\eta(x) = \frac{\eta_0}{4} \left( 1 - \cos \frac{2\pi}{L} x \right)^2 = \frac{\eta_0}{4} \left( 1 + \cos \left( \pi \frac{\delta - \rho}{\delta_0} \right) \right)^2. \quad (5.37)$$

Note that  $0 \leq x \leq L$ , where  $L$  is the finite waveguide length. Normally the Bloch formalism deals with infinite system length, but is justified to move to systems with a finite length if the length  $l$  connected to the periodicity of the Bloch modes (see equation (5.19)) follows  $l \ll L$ .  $\sigma_0$  is the maximal roughness and  $\delta_0$  the maximal detuning strength of the boundary modified by a constant detuning of  $\rho$ .  $\eta_0$  is the dissipation constant. The system part corresponding to  $x = 0$  and  $x = L$  are **identical** as they describe a **uniform rectangular waveguide without absorption**. In the following we will use the wobbly waveguide Hamiltonian equation (5.30) together with the result of section 5.1 and the parametrisation of  $\eta$  in equation (5.37). Note that  $g = B\sigma$  and  $\gamma_1 = \eta(x)k/k_i$  (compare equation (5.1) and equation (5.30)). One can calculate the exceptional point coordinates in the  $(\delta, \sigma)$ -plane as :

$$\delta_{EP} = 0, \quad \sigma_{EP} = \frac{|\gamma_1 - \gamma_2|}{4B} = \frac{\eta_0}{16B} \left( 1 + \cos \left( \pi \frac{\rho}{\delta_0} \right) \right)^2 \left| \frac{k}{k_1} - \frac{k}{k_2} \right|. \quad (5.38)$$

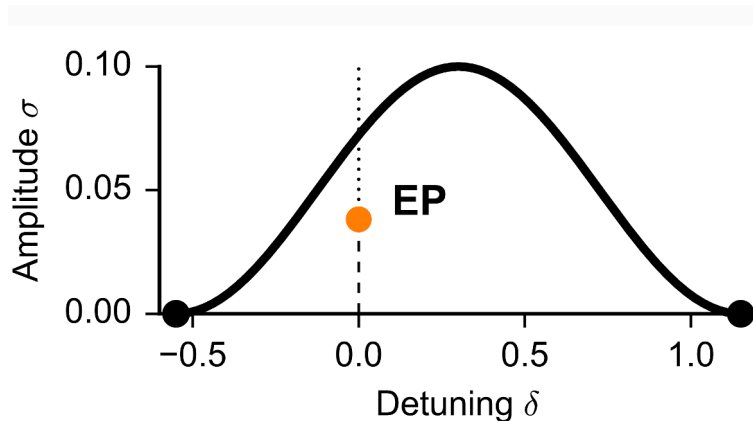


**Figure 5.5** – Scheme of the encircling of the exceptional point (EP) in the  $(\delta, \sigma)$ -plane. The path defined by the parameter equation (5.36) follows the solid black line. The chosen parameters are  $L/W = 100$ ,  $kW/\pi = 2.05$ ,  $\sigma_0/W = 0.1$ ,  $\delta_0 W = 0.85$ ,  $\rho W = 0.3$ ,  $\eta_0 W = 0.6$ . The dashed line indicates where  $\text{Re}(E_1) = \text{Re}(E_2)$  and the dotted line shows the line for  $\text{Im}(E_1) = \text{Im}(E_2)$  (compare with section 5.1). [Dop16b]

Since we know the Hamiltonian  $H$  (equation (5.30)) we can calculate the eigenvalues for  $H$  in the whole  $(\delta, \sigma)$ -plane. Together with the path determined with equation (5.36) one gets a similar picture than those presented in section 5.1. The exceptional point for the wobbly waveguide encircled by the parametric path defined by equation (5.36) is presented in figure 5.5. Note that if the amplitude of the boundary  $\sigma$  vanishes,  $\delta$  can have an arbitrary value and still all this waveguide configurations with  $\sigma = 0$  correspond to the simple rectangular waveguide. Since the losses follow  $\eta(x) = \eta(L - x)$  (see equation (5.37)), the two black dots indicated in figure 5.5 really describe the same physical system. One can define the following parameter transformation for which the encircling path is closed in a mathematical sense [Dop16a]:

$$\begin{pmatrix} p_1 \\ p_2 \end{pmatrix} = \begin{pmatrix} r \sin(2\alpha) \\ r \cos(2\alpha) \end{pmatrix} \text{ with} \\ r = \sqrt{\left(\frac{\sigma}{\sigma_0}\right)^2 + \left(\frac{\delta - \rho}{\delta_0}\right)^2}, \quad \alpha = \arctan\left(\frac{\delta - \rho}{\delta_0} / \frac{\sigma}{\sigma_0}\right). \quad (5.39)$$

Following an eigenstate (eigenvector) around an EP, theoreticians look at what they call eigenvector populations [Uzd11, Dop16a]. It turns out that one can understand these eigenvector populations in the waveguide context as entries of the transmission matrix  $T$  describing how the Bloch modes (eigenvectors) are scattered into each other while going around the exceptional point (see definition of the transmission matrix in section 1.2). The development of these entries, while encircling the EP, is schematically shown in figure 5.6. The encircling direction can be understood as direction of the injection. Injection from the left side of the waveguide can be associated with a counter clockwise encircling, whereas injection from the right describes the clockwise encircling. The initial state on the lower (upper) half plane corresponds to the injection of Bloch mode 2 (1).



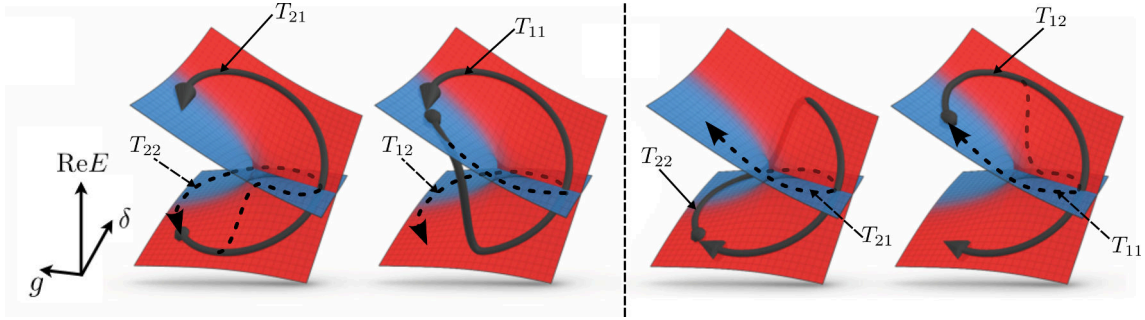


**Figure 5.6** – Encircling the exceptional point for different initial Bloch modes. Dominant transitions are shown with a solid line. Damped transitions are shown with dashed lines. **Left:** Counter clockwise encircling of the two eigenmodes (Bloch modes). On the outer (inner) left Bloch mode two (one) is injected. **Right:** Clockwise encircling of two eigenmodes. On the outer (inner) right Bloch mode one (two) is injected. The red (blue) colour corresponds to the eigenvalue-sheet with relative gain (loss).

Let us concentrate first on the outer left picture of figure 5.6 describing the injection of Bloch mode 2 into the system. The adiabatic transition (solid line) follows the eigenvalue sheet corresponding to the one of relative gain (red sheet in figure 5.6). While encircling the exceptional point this mode (as it is representing an eigenvector of  $H$ ) will undergo a state flip at the end of his round trip. Following the amplitude (intensity) of the initially sent mode means in this context that we are looking at transmission matrix elements  $T_{ij}$ . Therefore the transition described by the solid line represents  $T_{21}$  since the adiabatic transition of Bloch mode 2 ends up in Bloch mode 1.

In section 5.1 we saw that also non-adiabatic process come into play here. The non-adiabatic transition is represented by the dashed line in figure 5.6 and it corresponds to  $T_{22}$ . This state flip back into the initial state is a direct result of the non-adiabatic coupling. Since this transition follows the lossy eigenvalue sheet (see blue sheet in figure 5.6) it is heavily suppressed so that  $T_{21} > T_{22}$ .

Similarly, following the amplitude of the initial first Bloch mode (inner left picture in figure 5.6) one observes an immediate adiabatic transition which is followed by a rather long trajectory on the sheet associated with gain. Following the amplitude of this state gives the size of  $T_{11}$ . The adiabatic transition corresponding to  $T_{12}$  is following the lossy sheet during all its encircling. Meaning that  $T_{12}$  is heavily suppressed and  $T_{12} < T_{11}$ .

One can also make a comparison between the two pictures.  $T_{21}$  is following the gain sheet most of the time (especially when compared to the other possible transitions), whereas  $T_{12}$  does the same on the lossy sheet.

Therefore  $T_{21}$  has to be the greatest obtained quantity and  $T_{12}$  the smallest, i.e.,  $T_{21} \gg T_{12}$  (compare with the actual obtained experimental results in section 5.5).

In figure 5.6, I also show the scheme for the clockwise encircling of the exceptional point (the two pictures on the right). This corresponds in our case to an injection

### 5.3. Experimental Realisation in a Waveguide

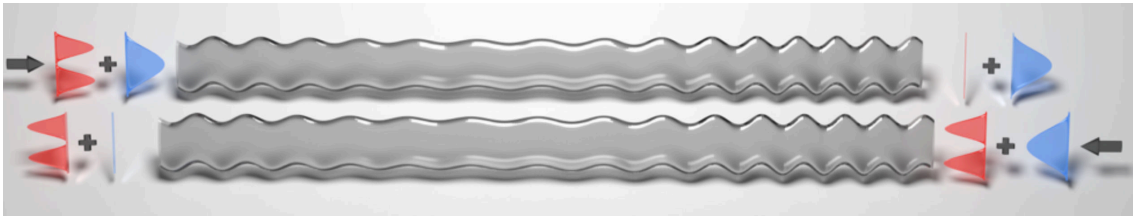


**Figure 5.7** – Scheme of a waveguide with damping and smoothly deformed boundaries (see equations (5.17, 5.36, 5.37)) supporting two sinusoidal modes undergoing scattering as an illustration of the asymmetric switch effect. **Upper panel:** Injection of two modes from the left with mode 1 surviving. **Lower panel:** Injection of two modes from the right with mode 2 surviving. [Dop16a]

from the right side of the waveguide (as described above). These pictures for the clockwise encircling can be understood in the same way as discussed for the counter clockwise encircling. Following the discussion above we can derive relations between the quantities  $T_{ij}$  in an analogue way, i.e.,  $T_{21} < T_{22}$  (from the inner right figure of figure 5.6),  $T_{11} < T_{12}$  (from the outer right figure of figure 5.6) and  $T_{21} \ll T_{12}$  (comparison of the two).

It might be written in a cryptic way so far, but at this point we have realised an asymmetric switch, which shows different preferred transitions depending on the injection direction. The observations from above are sum up in figure 5.7.

Finally we realised an asymmetric switch, which generates depending on the injection (encircling) direction a different output at its end. If we inject a combination of the two modes from the left of the waveguide, (almost) only the first mode (Bloch mode 1) will reach the output (see upper panel in figure 5.7). Whereas, if we inject a combination of the two modes from the right, only the second mode (Bloch mode 2) will survive the transition.

This kind of waveguides can be of great interest when one thinks of possible applications. The great advantages with this kind of technique is that it can serve as a very efficient filter, which does not simply suppress certain components, but instead it transforms these unwanted components into the desired ones. In practice such a wobbly waveguide system can be realised in any kind of wave system such as an optical or an acoustical system for example.

The important thing here is that we use non uniformly distributed loss to perform this asymmetric switching behaviour. It has been shown in [Dop16b] that an asymmetric switching effect can be performed with uniform distributed loss only as well. But this method shows two major draw backs. First the overall output intensity is very poor  $I \propto 10^{-20}$  and the waveguide itself is very long ( $L/W \gg 100$ ).

The uniform absorption can be replaced by a highly localised one however. Using strong localised absorption reduces the system size  $L$  to a level realisable in an experiment  $L/W \approx 25$ . Absorbing material is placed at the nodes of the second eigenvector (Blochmode) of  $H_0$  as it is defined in equation (5.32) (see also figure 5.9). Note that  $H_0$  describes the case where no absorption is present, i.e,  $\eta_0 = 0$ .

Numerically the damping of the output of the Bloch mode, which corresponds to the damped transition, is of the order of 5 magnitudes [Dop16b] (non-scattering Gaussian shaped absorbing dots exactly placed in the nodal points of Bloch mode 2).

Note that changing the absorber position means also to change the position of the exceptional point within the  $(\delta, \sigma)$ -plane. Numerically it was shown that this new loop-trajectory taking into account the changed condition  $\eta$  corresponding to our used absorber configuration still encircles an exceptional point which itself remains within the encircled area [Dop16b]. However, the Gaussian shaped absorbing dots used for the numerics are not a good idea for the microwave experiment. Distributing many absorbing dots throughout the nodal points would cause high back reflections and therefore we decided to use a continuous stripe-absorber. The stripe-shape is a good compromise. For sure it will lead to parasitic absorption of both Bloch modes, but it will create the necessary loss to establish an encircling and it minimises the back-scattering-effect.

## 5.4 MICROWAVE SET-UP

For the experimental realisation we fixed the parameters according to equations (5.36, 5.17):

$$W = 5 \text{ cm}, \quad L = 25W, \quad \sigma_0 = 0.16W, \quad \delta_0 = 1.25/W, \quad \rho = -1.8/W$$

$$k_b = k_r + \delta(x) \quad \text{with} \quad k_r = \frac{\pi}{W}(\sqrt{N^2 - 1} - \sqrt{N^2 - 4}), \quad N = 2.6. \quad (5.40)$$

I developed a CAD-model of the cavity using these fixed parameters so it can be fabricated by CNC-machines (computerised numerical control machines). A sketch of the fabricated cavity can be seen in figure 5.8. Due to the limited size of the accessible CNC-machine we had to divide the waveguide in multiple parts. The

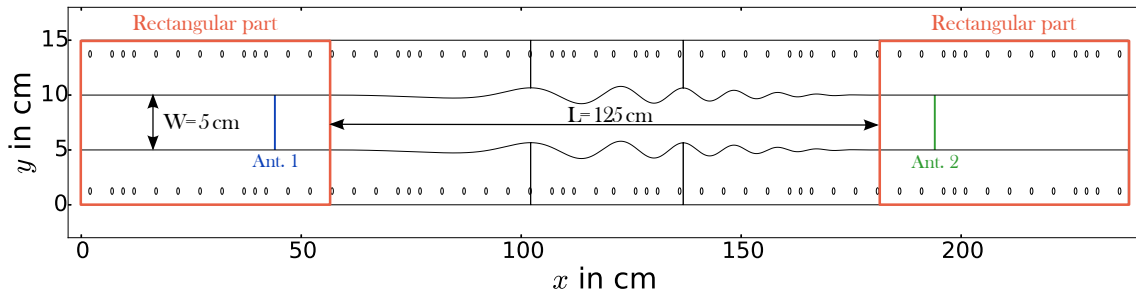


**Figure 5.8** – Sketch of the waveguide. The central part following the boundary parameter equation (5.40) is placed in between two rectangular waveguide parts containing the antennas. The blue and the green vertical lines on the left and on the right present the possible positions for the two scanning antennas (compare with figure 5.9 for the position of the absorber-stripe).

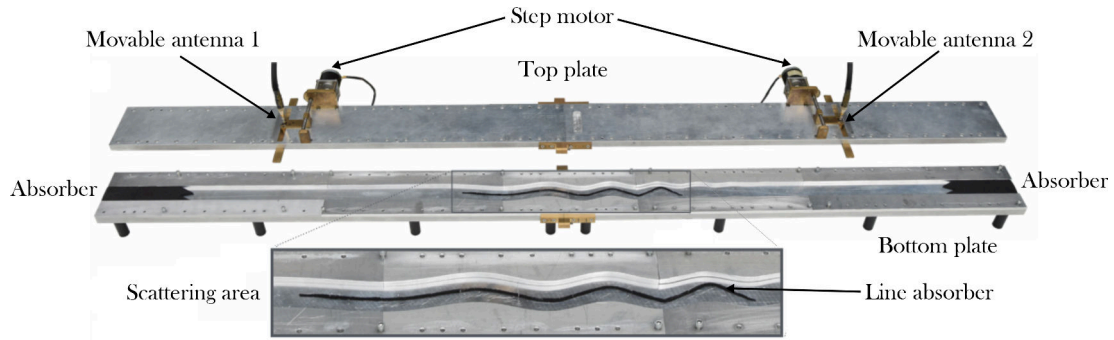


**Figure 5.9** – Photo of the experimental set-up showing the two step motor driven scanning antennas which were connected to a vector network analyser. Black absorbing foam is placed at the end of the waveguide to minimise reflections from the open ends. The stripe of absorbing foam material introduces the necessary mode dependent loss for the encircling (see figure 5.8 and table 5.1 for more details).

overall precision of the fabricating machine of  $\delta \approx 0.01$  mm for aluminium material is way below the wavelength  $\lambda = 3.84$  cm at the frequency  $f = 7.8$  GHz, where our experiment is supposed to work. The different sections of the cavity are hold in place by precisely placed pins. This leaves no gap and the positioning error with less than 1 mm is well below the wavelength. We will see that the eventual inter-mode scattering and backscattering by the junctions plays only a minor role in the experiment as the general transmission behaviour follows exactly the theoretical predictions. For sure if one thinks of building a commercial device with high output efficiency, the control of the boundary is crucial.

Once the 3d-modeling was done using *OpenSCAD*, the real waveguide could be fabricated using aluminium as basis material. A photo of the fabricated aluminium waveguide is presented in figure 5.9.

All the important parameters of the final aluminium waveguide are listed in table 5.1. As already explained in section 4.2.3 we use foam absorber to suppress reflections from the ends of the channels, i.e, to mimic a quasi infinite waveguide. They show a saw-tooth form in order to minimise back reflections coming from the absorber itself. The absorber stripe in the center introduces the necessary loss for the exceptional point encircling. The absorber-stripe is sloped so that reflections happening at the edges of the absorber are minimised. The two measurement antennas are mounted onto movable slides which are moved by step motors with a total precision of  $\approx 0.25$  mm.

The height of the waveguide of 8 mm ensures that we work only with the  $TE_0$  mode (see sections 1.1 and 4.2.2). At 7.8 GHz and a width  $W = 5$  cm we deal with two open sinusoidal modes (see section 4.2.2). The lower frequency cut-off  $f_c^1$  is at  $\approx 3$ GHz. This means that the frequency distance between two modes (see equation (4.26)) is also at  $\approx 3$ GHz. For more details concerning the microwave waveguide revisit sections 1.1 and 4.2.2.

Total length	[cm]	238
Antenna Distance	[cm]	150
Width	[cm]	5
Height	[mm]	8
Central Absorber		LS-10211 [ <i>ARC Technologies</i> ]
Central Absorber Width	[mm]	2.5
Central Absorber Height	[mm]	5 (ascending/descending at the end)
End-Absorber		LS-14, LS-16 [ <i>EMERSON&amp;CUMING</i> ]
End-Absorber Length	[cm]	17.5
End-Absorber Width	[cm]	5
End-Absorber Height	[mm]	6-6.5

**Table 5.1** – Details on the experimental parameters.

## 5.5 THE DYNAMICAL ENCIRCLING - EXPERIMENTAL RESULTS

We have seen in section 5.3 that the relevant experimental quantities are the transmission matrix elements  $T_{ij}$ . The measurement of these elements is done in the following way. We measure the transmission at  $2 \times 2$  positions of the scanning antennas. These points are defined as  $(y_0, y_1 = (5 \text{ cm} + W/3, 5 \text{ cm} + 2W/3)$  (see figure 5.8). First antenna 1 (left antenna) is moved to position  $y_0$ . After that antenna 2 moves to  $y_0$  and  $y_1$  and we measure each time the transmission. Once these two measurements are done, antenna 1 moves to  $y_1$  and antenna 2 repeats its movement like before. In total we have four transmission measurements and eight reflection measurements, i.e., four reflection measurements for each antenna. Such a reflection/transmission measurement for a given position of the two antennas is shown in figure 5.10.

Since we want the transmission data to be comparable in a large frequency window, we have to remove the frequency dependant coupling of the used antennas. This calibration technique of the transmission matrix has been established in [Die10]. Therefore we calibrate the transmission data following:

$$T'(y_i, y_j) = \frac{T(y_i, y_j)}{\sqrt{(1 - \langle | \langle R_1 \rangle_{sl} | \rangle_{pos}^2)(1 - \langle | \langle R_2 \rangle_{sl} | \rangle_{pos}^2)}}, \quad (5.41)$$

where  $T(y_i, y_j)$  stands for the transmission measured between antenna 1 (at position  $y_i$ ) and antenna 2 (at position  $y_j$ ).  $\langle R_k \rangle_{sl}$  describes the sliding average over frequency window of  $\Delta f = 0.0735$  GHz for the reflection signal at antenna  $k$ . The value for  $\Delta f$  was chosen manually, i.e., by choosing several values for  $\Delta f$  and verifying if the oscillations in the reflection spectra vanish (see also section 4.2.3).  $\langle \cdot \rangle_{pos}$  denotes an additional averaging over all measured four reflection measurements, which should

## 5.5. The Dynamical Encircling - Experimental Results

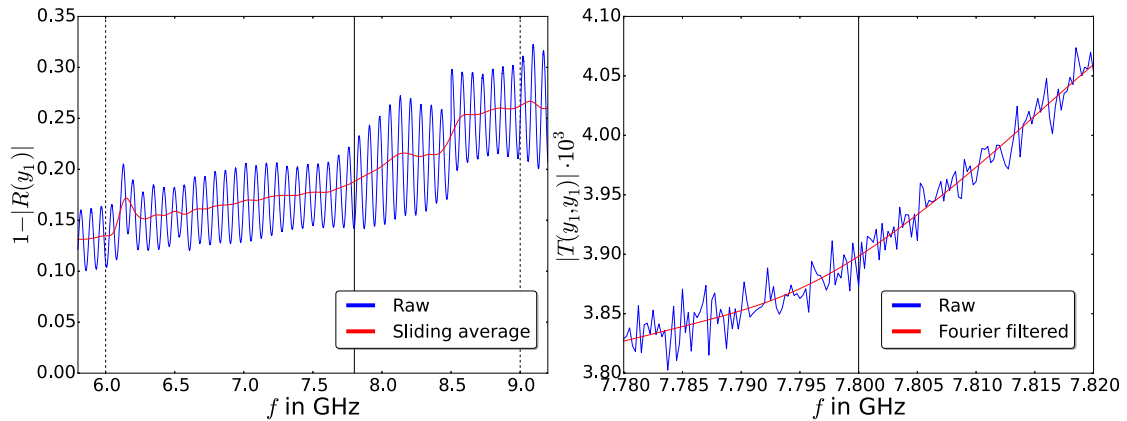


**Figure 5.10 – Left:** A measured reflection for antenna 2 at position  $y_1$ . The blue line represents the raw data and the red line represents the raw data after the sliding average treatment (average window is  $\Delta f = 0.0735$  GHz; see also section 4.2.3). The dashed line indicates the mode opening for the second (third) mode. The solid vertical line represents the frequency where our set up should perform an encircling of an exceptional point. **Right:** A measured transmission signal between antenna 1 at  $y_1$  and antenna 2 at  $y_1$ . The raw data is shown in blue and the Fourier filtered data in red. The solid vertical line represents the working frequency.

be the same due to the symmetry of the chosen positions. This calibration can also be seen as removing the impedance mismatch between the antenna and the waveguide. We did not apply any further renormalisation of  $T(y_i, y_j)$ . For instance, one could think of measuring a rectangular waveguide with the same total boundary length (no absorbing foam material) to get a measure for the intrinsic losses in the waveguide, which can be seen as additional parasitic losses. We disregard here the effect of the overall intrinsic losses on the absolute transmission efficiency as it is not important for the observation of the characteristic mode scattering behaviour described in section 5.3

Once the data is calibrated we can transform the transmission matrix  $T$  into the mode picture  $T_{nm}$  by using a two dimensional sinus transform (compare with section 4.2.2) defined here as

$$T_{nm} = \frac{1}{2} \sum_{y_i, y_j} T'(y_i, y_j) \sin\left(\frac{n\pi}{W} y_i\right) \sin\left(\frac{m\pi}{W} y_j\right). \quad (5.42)$$

The result of this transformation (see figure 5.11) reveals a very nice agreement with the theoretical considerations of section 5.3. The expected behaviour for the injection of the left which corresponds to the counter clockwise encircling of the EP (see figure 5.6). The condition  $T_{11} > T_{12}$  is fulfilled (factor of 20 in between them).  $T_{21} > T_{22}$  is fulfilled also (factor of 20). We observe for the relation  $T_{21} \gg T_{12}$  a difference of 4 orders of magnitude! We also measured the transmission matrix for the case that the signal is injected from the right. This transmission matrix is denoted with  $\tilde{T}$  in figure 5.11.

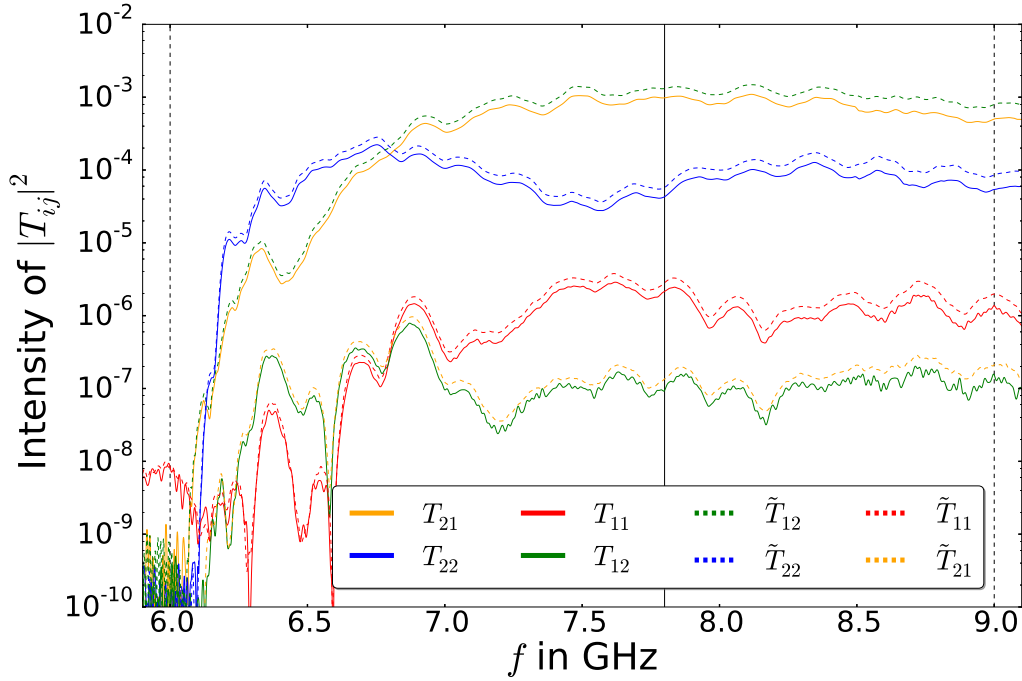


**Figure 5.11** – Intensity of the transmission matrix elements  $T_{nm}$  (mode picture) as a function of frequency. Dashed lines indicate the mode openings of the second and third mode. The solid line shows the frequency for which the set-up was designed to work at.  $\tilde{T}_{nm}$  is the transmission matrix measured for the signal that is injected from the right.

We note that we have a slight break of reciprocity (dashed and solid lines are not falling onto each other in figure 5.11). We observed that this breaking is an effect of the line absorber, who seems to be slightly magnetised. This causes a directional dependence of the absorption and therefore the transmission gets direction dependent as well. In case of no line absorber, we do not observe any difference between the two injection directions. The transmissions signal from both directions are still strongly correlated, so this directional dependence of the transmission can be assumed as a constant factor, which is not related to the theory of the encircling of the exceptional point.

Nevertheless, looking at the injection from the right side of the waveguide we also get the expected behaviour for the  $T_{ij}$ :  $\tilde{T}_{21} < \tilde{T}_{22}$ ,  $\tilde{T}_{11} < \tilde{T}_{12}$ ,  $\tilde{T}_{21} \ll \tilde{T}_{12}$ . **This is in fact the proof of the asymmetric switching behaviour due to the presence of an EP.**

To justify that our system behaves fully adiabatically in the case of the absence of the EP, one would need to follow the same parameter loop in parameter space without the presence of the EP. However, as our fixed system parameters  $\delta(x)$ ,  $\sigma(x)$  and  $\eta(x)$  fully determine the position of the EP, we do not have the possibility to carry out such a measurement. But the results allow us to claim that the system dynamics is not fully non-adiabatic, since  $T_{1,2}$ ,  $T_{2,1}$  ( $\tilde{T}_{12}$ ,  $\tilde{T}_{21}$ ) are related to adiabatic transitions along the parametric loop.

## 5.6 PARAMETRIC ENCIRCLING

As we have clearly confirmed the dynamical encircling of the exceptional point. Thus one can ask oneself if it also possible to relate this kind of waveguide experiments back to a parametric encircling of an exceptional point (see section 5.1).

This is indeed possible. To do that, we have to construct a periodic waveguide for each of the parameter points of our encircling trajectory in the  $(\delta, \sigma)$ -plane. This is possible because each point on the trajectory around the EP represents a well defined waveguide with a well defined boundary.

We chose 5 equidistant points on the trajectory and constructed 5 waveguides corresponding to the specific boundary parameters at these points (see figures 5.12 and 5.13).

One could also say that we are going to translate 5 points of the waveguide with periodically changing boundary  $\xi = \sigma \sin(k_b(x)x)$  (see equation (5.17)) into five waveguides with boundary  $\tilde{\xi} = a \sin(\Omega x)$  of a constant frequency  $\Omega \neq \Omega(x)$ . To find the appropriate estimation for the constant boundary frequency  $\Omega$ , we will have a look at the Taylor expansion of  $\xi$  and  $\tilde{\xi}$  around an arbitrary point  $x_0$ .

This expansion can be written as

$$\begin{aligned} \xi(x_0) &\approx \sigma \left[ \sin(k_b(x_0)x_0) + \cos(k_b(x_0)x_0) \left( \frac{\partial k_b}{\partial x} x + k_b \right) \Big|_{x_0} (x - x_0) + \dots \right] \\ \tilde{\xi}(x_0) &\approx a \left[ \sin(\Omega x_0) + \cos(\Omega x_0) \Omega (x - x_0) + \dots \right]. \end{aligned} \quad (5.43)$$

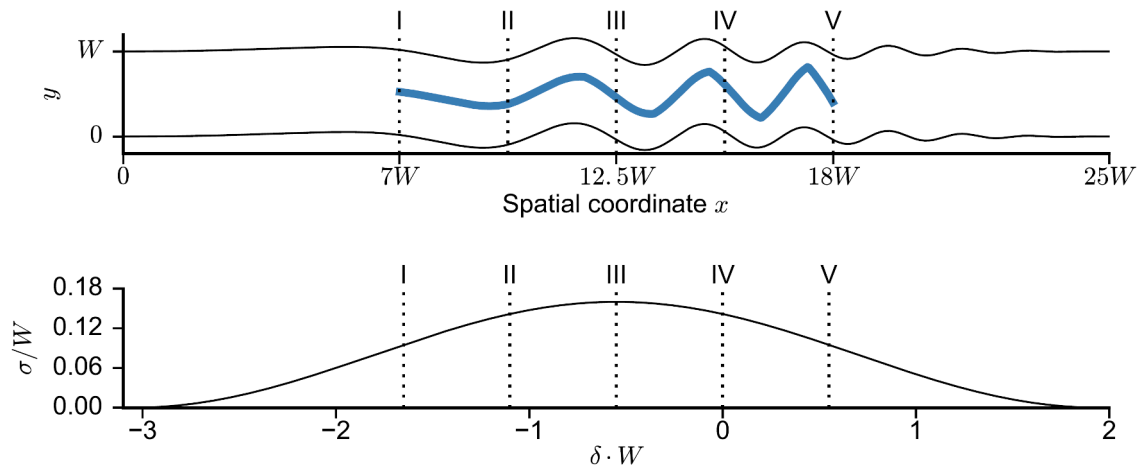


**Figure 5.12 – Top:** Scheme of the set-up for the dynamical encircling (compare with figure 5.8). The absorber is highlighted with a blue color. **Bottom:** The encircling path in the  $(\delta, \sigma)$ -plane related to the waveguide. The dotted lines with the Roman numbers I to V connect positions in real space with points on the parameter-trajectory in the  $(\delta, \sigma)$ -space. [Dop16a]



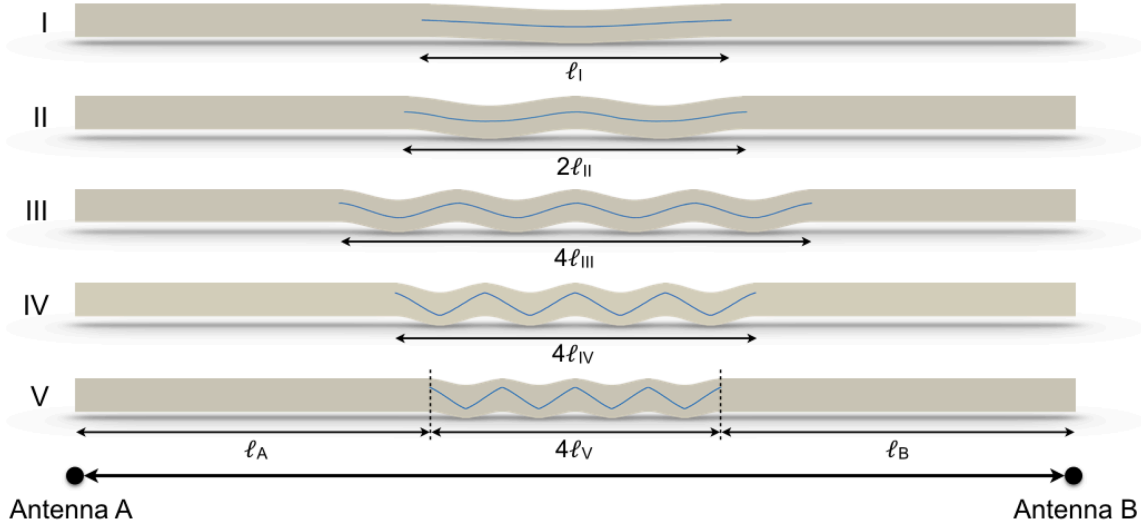


**Figure 5.13** – Picture of the 5 realised waveguides according to the parameter sets defined in figure 5.12 and table 5.2.  $l_A, l_B$  describe the length of the rectangular parts of the waveguide ( $l_A = l_B$  for the experiment; see also figure 5.8)).  $l_n$ , where  $n$  stands for a Roman numeral, is the period length of the  $n$ -th-configuration, i.e.,  $l_n = 2\pi/\Omega_n$ . The number in front of  $l_n$  indicates the number  $m$  of realised periods for each configuration. The line absorber is indicated in blue color. [Dop16a]

By comparing the two lines of equation (5.43) we have to demand that  $a$  and  $\Omega$  of the new boundary  $\tilde{\xi}$  follow:

$$a = \sigma = \sigma_n, \quad \Omega = \frac{\partial k_b}{\partial x} x|_{x_n} + k_b(x_n), \quad (5.44)$$

where the index  $n$  represents the 5 different positions according to which we are going to construct the 5 new waveguides where we do the translation (see figure 5.12).  $\Omega$  becomes using equations (5.18, 5.36):

$$\Omega = k_r + 2\delta_0 \left( \frac{2x_n}{L} - 1 \right) + \rho + \delta_0 = k_r + \delta_n. \quad (5.45)$$

This matching of a constantly changing boundary  $\xi$  to a boundary  $\tilde{\xi}$  with constant boundary frequency is illustrated in figure 5.14 for the case III (compare with figure 5.12).

We constructed 5 different waveguides of constant boundary frequency representing 5 points on the encircling path around the exceptional point. The parameters of these five chosen waveguides are shown in table 5.2 and their spatial form is presented in figure 5.13.

Once the waveguides were realised, we measured again the transmission matrix  $T$  in the spatial domain for  $2 \times 2$  points. This time we worked exclusively at 7.8 GHz, so we just calibrate the data according to equation (5.41), where we left out averaging

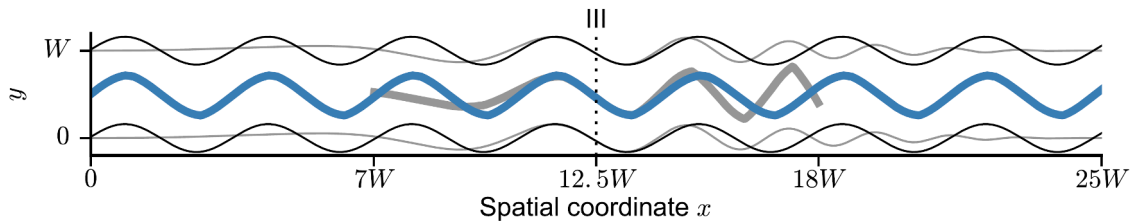


**Figure 5.14** – Schematic transformation from a waveguide with  $x$ -dependant boundary frequency towards a waveguide with a constant boundary frequency at position III (see figure 5.12 and approximations in the main text). [Dop16a]

configuration n	I	II	III	IV	V
$x_n/W$	7	9.75	12.5	15.25	18
$\delta_n/W$	-1.65	-1.1	-0.55	0.0	0.55
$\sigma_n/W$	0.094	0.1416	0.16	0.1416	0.094
$l_A = l_B$ [cm]	51.57	49.26	39.51	47.93	53.11
Width of the line absorber [mm] ( $\pm 0.5$ )	1	2.5	2.5	2.5	1
Height of the line absorber [mm] ( $\pm 0.1$ )	5	5	5	5	5

**Table 5.2** – Experimental parameters  $x_n, \delta_n, \sigma_n$  as a function of the waveguide width  $W = 5$  cm. The length  $l_A = l_B$  specify the length of the rectangular parts of the waveguide (see figure 5.8). Parameters of the used line absorber.

since we do not want to compare the signal in a large frequency window. This calibrated transmission data is again transformed into its mode picture by applying the discrete sine transformation following equation (5.42).

In this experiment we are not performing a continuous encircling. Therefore we can not just look at the transition elements corresponding to the entries of  $T_{ij}$  of the transmission matrix. Instead we have to study the eigenvectors of the transmission matrix  $T_{ij}$  in which the components of the Bloch modes are encoded.

The propagation of the Bloch mode through the regular oscillating waveguide can be described via the translation operator  $U_{l_n}$  that translates a Bloch mode  $\Phi_n(x, y)$  by a full period  $l_n = 2\pi/\Omega_n$  so that

$$U_{l_n} \Phi_n(x, y) = \Phi_n(x + l_n, y) = e^{iKl_n} \Phi_n(x, y). \quad (5.46)$$

Once the Bloch mode has propagated through  $m$  periods of length  $l_n$ ,  $U_{l_n}^m$  contains the full transmission information such that

$$T = U_{l_n}^m, \quad (5.47)$$

where  $T$  is the transmission matrix in the mode representation. This becomes clear when one realises that the (distorted) sinusoidal modes with their amplitudes  $c_1$  and  $c_2$  are the basis of the Bloch modes (see equations (5.28, 5.29)). This means also that the vector  $(c_1, c_2)^T$  has to be an eigenvector of  $T$ :

$$\begin{pmatrix} T_{11} & T_{21} \\ T_{12} & T_{22} \end{pmatrix} \begin{pmatrix} c_1^{(n)} \\ c_2^{(n)} \end{pmatrix} = \tau_n \begin{pmatrix} c_1^{(n)} \\ c_2^{(n)} \end{pmatrix}. \quad (5.48)$$

The index  $n$  is again the index representing the 5 realised waveguides. For the parametric encircling we have to study the eigenvectors and eigenvalues of the measured transmission matrix  $T$  in order to obtain the characteristic state-flip.

To eliminate the effect that the modes travel through rectangular parts before entering (after leaving) the periodic part of the waveguide (see figure 5.13), we apply phase factors to the transmission matrix  $T$ :

$$T_{\text{phcal}} = \begin{pmatrix} T_{11}e^{2ik_1l_B} & T_{21}e^{ik_1l_B}e^{ik_2l_B} \\ T_{12}e^{ik_1l_B}e^{ik_2l_B} & T_{22}e^{2ik_2l_B} \end{pmatrix}. \quad (5.49)$$

The definition of  $l_B$  can be found in figure 5.13.

The question is now what behaviour of the eigenvectors one would expect for the case of a parametric encircling of an EP. In each investigated configuration it is always the first sinusoidal mode component which undergoes the heavy loss. So the low transmission eigenvalue  $t_l$  is mainly related to the first sinusoidal mode (corresponding to  $c_1$ ). **Note that this is only true when there is no state flip.** If there is no state flip at all in the system, the small eigenvalue before the flipping point  $\tau_{b_l}$  and the small eigenvalue after the flipping point  $\tau_{a_l}$  will show both a high fraction of  $|c_1|$ . If there is an EP present the relation between the eigenvalues and eigenvectors will be of course different. In the following the indices  $b$  and  $a$  indicate 'before' and 'after' the flipping point and the indices  $l$  and  $h$  denote a 'low' and a 'high' value. If one has a closer look on  $\tau_{b_l}$  and  $\tau_{a_l}$  for the case where an EP is encircled, one will notice that  $\tau_{b_l}$  is composed mainly of the first sinusoidal mode (high value of  $|c_1|$ ), whereas  $\tau_{a_l}$  is suddenly mainly composed of  $|c_2|$  which is associated with the second sinusoidal mode. This is the state flip effect. Similarly, the high eigenvalue  $\tau_{b_h}$  before the flipping point is related to  $|c_2|$ , whereas  $\tau_{b_h}$  corresponds to  $|c_1|$ . The described behaviour is visualised in table 5.3.

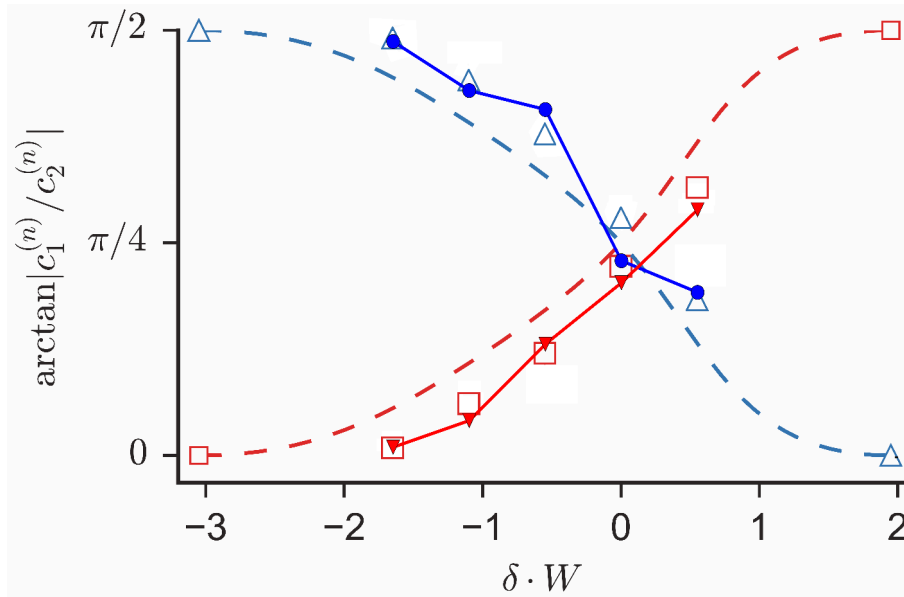
In the experiment we were looking at the ratio of  $|c_1^{(n)}/c_2^{(n)}|$  for the two eigenvalues  $\tau_i$  as a function of the fabricated waveguide configurations. If our configurations are equivalent to a parametric encircling of an EP, state flip behaviour will be encountered. This state flip behaviour proves the presence of an exceptional point in the same way as it was done in [Dem04, Lee09, Gao15]. Following the ratio  $|c_1^{(n)}/c_2^{(n)}|$  we should see a crossing of the two lines as it is schematically explained in table 5.3. This is exactly what we observe experimentally (see figure 5.15). The crossing behaviour is clearly visible in our experimental data and therefore the parametric encircling around an exceptional point is indeed proven. Also the comparison with the numerical results and the results of the effective  $2 \times 2$  Hamiltonian (according to table 5.2 and equations (5.32, 5.33) obtained by Doppler et al. are in good agreement with our experimental results.

<i>excep. point</i>		$\tau_{bl}$	$\tau_{bh}$	$\tau_{al}$	$\tau_{ah}$
1 <sup>st</sup> sine mode comp.	$ c_1^{(n)} $	↑	↓	↓	↑
2 <sup>nd</sup> sine mode comp.	$ c_2^{(n)} $	↓	↑	↑	↓
ratio	$ c_1^{(n)}/c_2^{(n)} $	↑	↓	↓	↑

<i>no excep. point</i>		$\tau_{bl}$	$\tau_{bh}$	$\tau_{al}$	$\tau_{ah}$
1 <sup>st</sup> sine mode comp.	$ c_1^{(n)} $	↑	↓	↑	↓
2 <sup>nd</sup> sine mode comp.	$ c_2^{(n)} $	↓	↑	↓	↑
ratio	$ c_1^{(n)}/c_2^{(n)} $	↑	↓	↑	↓

**Table 5.3** – Visualisation of the behaviour of  $c_1^{(n)}$  and  $c_2^{(n)}$  under the presence/absence of an exceptional point (see definition of  $c_i^{(n)}$  in equations (5.28, 5.29)).  $\tau_n$  are the eigenvalues defined in equation (5.48). The indices  $b$  and  $a$  stand for a waveguide configuration "before" and "after" experiencing the exceptional point/state flip. The indices  $l$  and  $h$  indicate a 'low' or a 'high' value of the eigenvalue.  $\uparrow(\downarrow)$  stands for a high(low) value of the eigenvector component  $|c_i|$  belonging to  $\tau$  according to equation (5.48).



**Figure 5.15** – Ratio of the eigenvector components  $c_i^{(n)}$  (see equation (5.48)) as a function of the measured waveguide configurations belonging to the high/low transmission eigenvalue  $\tau_h$  (red curve)/ $\tau_l$  (blue curve) (compare with table 5.3). **Experimental data:** Red filled triangles, blue filled circles. **2×2 Hamiltonian** according to table 5.2 and equations (5.32, 5.33): Dashed lines. The end points denote analytical solutions (empty waveguide). **Numerics:** Blue empty upwards pointing triangles, red empty squares. [Dop16a]

### 5.7 CONCLUSION

The minimal model, where an exceptional point (EP) arises, is a physical system which is described by a  $2 \times 2$  non-Hermitian Hamiltonian of the form of equation (5.1). One can think of a system of coupled damped oscillators for example. The EP is a point in the parameter space of the Hamiltonian where the two eigenvectors **and** the two eigenvalues coalesce.

If one follows an eigenvector on its path encircling an exceptional point the state flip phenomenon arises and the eigenvector is flipped into his counterpart (mind the sign; see equation (5.12)). This flipping behaviour can be even more complicated as non-adiabatic transitions might occur when the EP is **encircled dynamically** [Uzd11]. As a consequence of these non-adiabatic transitions, one observes that the final state of an eigenstate encircling an exceptional point depends only on the direction of the encircling and not on the initial state. This effect can be assigned to as an asymmetric switching effect.

We showed that this dynamical encircling of an exceptional point is experimentally feasible using a waveguide with a wavy boundary (see figure 5.9). The propagation of Bloch modes in such a wavy waveguide can be explained by a  $2 \times 2$  non-Hermitian Hamiltonian which is a complete analogue to the Hamiltonian studied before theoretically (compare equations 5.1 and 5.30). We could relate the encircling direction of the EP with the injection direction of our microwave signal. Therefore we could make direct use of the asymmetric switching effect to construct a mode filter which changes its filtering behaviour upon injection direction (see figure 5.7). By investigating the scattering behaviour of the two modes propagating in our system, we clearly proved that we have realised an asymmetric mode switch based on the encircling of an EP (see figure 5.11). Not only did we prove that such an asymmetric switch can be realised, but we also showed that a dynamical encircling of an EP, where non-adiabatic transitions occur, is experimentally feasible [Dop16a]. This is a great progress with respect to previous experiments which have realised only a parametric encircling.

To study the connection between the parametric and the dynamical encircling, we built five different waveguides corresponding to five sets of parameters of the encircling trajectory in the parameter space of the Hamiltonian. With these five waveguides we could reproduce the same state flip behaviour as it was observed by other experiments describing a parametric encircling [Dem01, Dem04, Ste04, Lee09, Cho10a]. Therefore our experiment links in a nice way the results of dynamical and parametric encircling. Additionally, our experiments paves the way for various possible applications as our system can be realised in other wave systems as well. An optical waveguide with a wavy boundary and additional loss introduced in the same manner as described in this chapter would feature the same asymmetric switching/filtering behaviour.

# 6 *Particle-like Scattering States*

---

## Contents

---

<b>6.1</b>	<b>Theoretical Background and Motivation . . . . .</b>	<b>112</b>
6.1.1	<i>Group Delay and Dwell Time . . . . .</i>	112
6.1.2	<i>Particle-like Scattering States . . . . .</i>	115
<b>6.2</b>	<b>Microwave Set-up . . . . .</b>	<b>118</b>
<b>6.3</b>	<b>Experimental Findings . . . . .</b>	<b>120</b>
6.3.1	<i>Determining the <math>Q</math>-operator . . . . .</i>	120
6.3.2	<i>Generating Particle-like Scattering State 1 . . . . .</i>	124
6.3.3	<i>Other Particle-like Scattering States . . . . .</i>	126
6.3.4	<i>Perturbation of Particle-like Scattering States . . . . .</i>	128
<b>6.4</b>	<b>Conclusion . . . . .</b>	<b>131</b>

---

In this chapter we will revise the  $q$ -operator in its original form of the Wigner-Smith time delay operator (see section 3.1). We will show that the eigenvalues and eigenvectors of the corresponding Wigner-Smith time delay matrix (WSTDm) have special properties which can be very useful for the transmission of a wave signal through a two dimensional scattering system.

## 6.1 THEORETICAL BACKGROUND AND MOTIVATION

### 6.1.1 Group Delay and Dwell Time

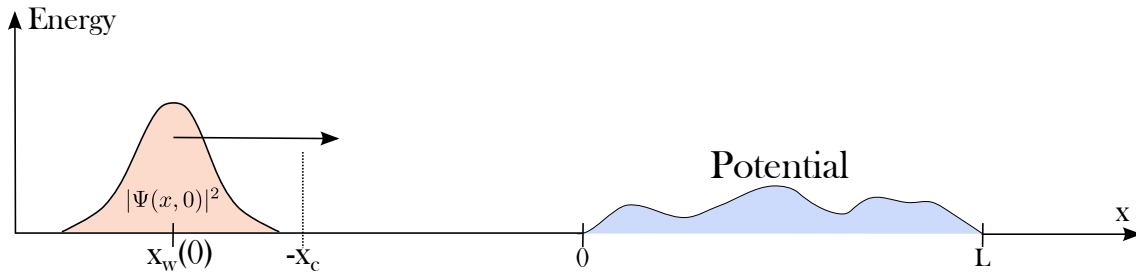


**Figure 6.1** – An initial wave packet  $\Psi(x, t)$  travelling through a one-dimensional system and undergoing scattering at a stationary potential  $V(x)$ , which is spatially limited between  $[0, L]$ .  $x_w(t)$  indicates the position of the maximum of the wave packet at time  $t$ .  $x_c$  is the critical distance up to which a free propagation of the wave packet can be assumed (see text).

In section 3.1, I have already introduced the WSTD and I have given an interpretation of its eigenvalues. In this chapter I would like to present a more general view on the time information encoded in a scattering problem of waves. We will investigate in the following the connection between the time delay of a wave packet undergoing scattering and its connection to the WSTD in more detail.

Let us assume an arbitrary wave packet  $\Psi(x, t)$  in one dimension which is propagating in the positive  $x$ -direction. An arbitrary stationary potential  $V(x)$ , which the wave packet has to pass, introduces scattering (see figure 6.1). The wave packet  $\Psi$  can be decomposed in its plane wave components  $\Gamma(k)$  outside the potential by applying

$$\Psi(x, t) = \frac{1}{\sqrt{2\pi}} \int dk \Gamma(k) e^{i(kx - \omega(k)t)}. \quad (6.1)$$

$\omega$  is  $k$  dependent and the relation between  $\omega$  and  $k$  is called dispersion-relation  $\omega(k)$ . Initially  $\Psi$  is localised outside of the potential (see figure 6.1). As the wave packet is propagating it will undergo scattering, so that some components of the wave packet will be reflected and others transmitted.

We call the transmitted part of the wave packet  $\Psi_{\text{tr}}(x, t)$  and its corresponding plane wave components  $\Gamma_{\text{tr}}(k)$  such as

$$\Psi_{\text{tr}}(x, t) = \frac{1}{\sqrt{2\pi}} \int dk \Gamma_{\text{tr}}(k) e^{i(k(x-L) - \omega(k)t)}, \quad x > L. \quad (6.2)$$

where  $L$  denotes the limit of the spatial distribution of the potential (see figure 6.1). The scattering of the wave due to the potential can be described by the relation of

## 6.1. Theoretical Background and Motivation

---

the plane wave components before and after the scattering (if the distance to the potential is sufficiently large)

$$\Gamma_{\text{tr}}(k) = A_{\text{tr}} e^{i\phi_{\text{tr}}(k)} \cdot \Gamma(k), \quad A_{\text{tr}}, \phi_{\text{tr}} \in \mathbb{R}. \quad (6.3)$$

$A_{\text{tr}} e^{i\phi_{\text{tr}}(k)}$  is a complex transmission coefficient which refers to the scattering process. These coefficients can be condensed into a complex scattering matrix  $T$  as we have seen in chapter 4.

For the reflected part of  $\Psi$  one can introduce complex reflection coefficients with  $\Gamma_{\text{re}} = A_{\text{re}} e^{i\phi_{\text{re}}(k)}$ , respectively, and derive similar relations than the ones for the transmission equations (6.2, 6.3).

Now we are restricting the problem to its asymptotic limit, i.e.,  $t \rightarrow \infty$ . In general it can be assumed that the phase factor is rapidly fluctuating as a function of  $k$ . Therefore in the limit of large  $t$  one can apply the stationary phase approximation as it was used in [Hau89] (see chapter 6.1 of [Ble75] for a rigorous mathematical description). In this case mainly those plane wave components contribute to  $\Psi_{\text{tr}}(x, t)$  whose  $k$ -values are located close to the stationary point of the phase. All the components far from the stationary point of the phase add incoherently leading only to minor contributions. The stationary phase approximations for our equation (6.2) can be written as

$$\begin{aligned} \frac{\partial}{\partial k} (k(x - L) - \omega(k)t + \phi_{\text{tr}}(k)) &= 0 \\ \Rightarrow x - \frac{\partial \omega}{\partial k} t + \frac{\partial \phi_{\text{tr}}}{\partial k} &= 0 \\ \Rightarrow x_w(t) = \frac{\partial \omega}{\partial k} t + \frac{\partial \phi_{\text{tr}}}{\partial k}, \end{aligned} \quad (6.4)$$

where  $x_w$  describes the position of the maximum of the wave packet after the scattering (one can use also any other significant point of the wave packet).  $\partial \omega / \partial k$  is called the group velocity of the wave packet. This velocity can be seen as the velocity with which the maximum is travelling along the x-axis.

Equation (6.4) states that a wave packet undergoing scattering accumulates an additional spatial delay  $\Delta x$  of  $\partial \phi_{\text{tr}} / \partial k$  which is caused by the phase of the complex transmission coefficient. This spatial delay leads to a time delay.

$$t_{\text{del}} = \Delta x \frac{m}{p} = \frac{m}{\hbar k} \frac{\partial \phi_{\text{tr}}}{\partial k} = \frac{m}{\hbar k} \frac{\partial E}{\partial k} \frac{\partial \phi_{\text{tr}}}{\partial E} = \hbar \frac{\partial \phi_{\text{tr}}}{\partial E} \quad \text{for} \quad E = \frac{\hbar^2 k^2}{2m}. \quad (6.5)$$

This time delay can also be understood as a kind of dwell time, since it marks the difference between the travelling time of a not-scattered state and a scattered one both travelling at the speed of the group velocity, i.e., the time the wave spends inside the scattering region. This is a more general derivation of the dependency of the delay time on the derivative of the phase than the hand-waving example given in section 3.3. In the same manner one can derive a reflection phase time  $t_{\text{re}} = \hbar \partial \phi_{\text{re}} / \partial E$ .



Such a definition of the dwell time has certain drawbacks. First, the used stationary phase approximations is only valid in the limit of large  $t$ (or  $x$ ). Second, to keep a clear definition of the dwell time one needs to assume a free propagation of the followed significant point  $x_w$  before entering the scattering region. This is formally done by enlarging the scattering region from  $-x_c$  to  $L$  (see figure 6.1). For sufficiently large  $x_c$  one can be sure that no parts of the wave packet have interfered with the already back scattered parts. Third, what happens if the significant point is lost during the scattering process? It can happen for example that one can not define a clear maximum value after the scattering of the wave packet. Fourth, what happens if parts of the wave packet remain trapped inside the potential?

Nevertheless the concept of time delay and the related concept of group delay, are well studied subjects in literature (e.g. see [Win03a, Ili09]). The group delay is a more generalised version of the simple time delay. It contains the information about the phases of the reflection and transmission coefficients and puts them together as a weighted sum:

$$t_g = \hbar \left( |r|^2 \frac{d\phi_{re}}{dE} + |t|^2 \frac{d\phi_{tr}}{dE} \right). \quad (6.6)$$

The weighting factors  $|r|^2 = |A_{re}|^2$  and  $|t|^2 = |A_{tr}|^2$  represent the reflectivity and the transmittance. The group delay describes the time of any significant point of the wave packet to appear after the potential (obstacle) **and** to reappear after reflection weighted by the corresponding scattering intensities. The group delay can easily be further generalised as it was done in [Amb12, Bra16] to describe multichannel scattering:

$$t_g = \hbar \sum_{l=1}^{n_{in}+n_{out}} |(S\mathbf{i})_l|^2 \frac{d\phi_l}{dE}. \quad (6.7)$$

where  $n_{in} + n_{out}$  is the total number of flux carrying channels (injection from both sides),  $S$  is the full scattering matrix and  $\mathbf{i}$  is a vector containing the coefficients of the incident waves (see section 1.2). The index  $l$  denotes the  $l$ -th component of  $S\mathbf{i}$ .  $\phi_l$  is the phase of the  $l$ -th component of  $(S\mathbf{i})_l$  such as  $(S\mathbf{i})_l = |S\mathbf{i}_l|e^{i\phi_l}$ .

Ambichl showed in [Amb12] that the **expectation value of the Wigner-Smith time delay operator is identical with the multi-channel group delay (in case of a unitary scattering matrix)**. In the following I will restrict myself to the investigation of the group delay (time delay). But since I raised certain drawbacks I want to shortly introduce the theoretical concept of dwell time, which answers the raised questions. The dwell time  $t_d$  as it is used in [Hau89, Win03a, Win03b, Ili09, Amb12] is defined as

$$t_d = \frac{W}{j_{in}}, \quad (6.8)$$

where  $j_{in}$  labels the stationary flux injected into the scattering region and  $W$  is the intensity of a wave packet injected with a  $k$ -vector  $\mathbf{k}$ .  $W$  reflects only the intensity stored within the scattering region, i.e.,  $W = \int_0^L dx |\Psi(x, \mathbf{k})|^2$ . Since this description is based on Feynman's path integral formalism of quantum mechanics also fictitious paths describing non unitary processes (loss) can be taken into account.

## 6.1. Theoretical Background and Motivation

---

It was shown in [Hau89, Win03a, Win03b] that the connection between the group delay  $t_g$  and the dwell time  $t_d$  follows:

$$t_g = t_d + t_i, \quad (6.9)$$

where  $t_i$  describes the self-interference effects of the wave packet entering the scattering region (as discussed before). This means the group delay can be understood as the sum of the time the wave packet stays inside the scattering region plus a correction term for the self-interference at the entrance (see [Hau89] or [Amb12] for further details).

### 6.1.2 Particle-like Scattering States

The important point to remember is the fact that the group delay is the expectation value of the Wigner-Smith time delay matrix. Therefore all the eigenstates of this matrix have a well defined group delay which refers to the corresponding eigenvalue. The central points discussed in this chapter are based on the work of Rotter et al. in [Rot11].

The system we are studying is shown in figure 6.2. We have two rectangular leads attached to a two dimensional billiard of arbitrary shape. Each lead shall contain  $N$  sinusoidal TE<sub>0</sub> modes (compare with chapters 1 and 4). Rotter uses flux normalised modes (flux normalised transport channels) this can be translated to our sinusoidal modes  $\phi_n(x, y)$  so that

$$\phi_n(x, y) = \frac{1}{\sqrt{k_x}} \sin(k_y y) e^{ik_x x}. \quad (6.10)$$

$k_x$  and  $k_y$  are the wave vectors in  $x$  and  $y$  direction as they were defined in equation (4.3). The factor  $1/\sqrt{k_x}$  is called flux normalisation.

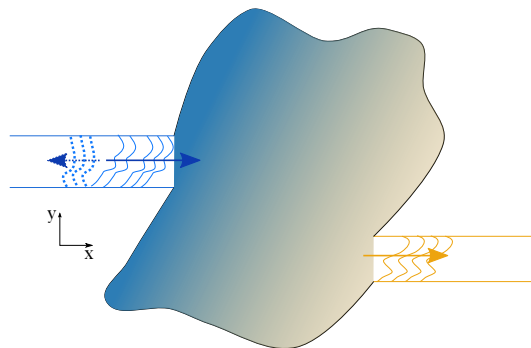


**Figure 6.2** – Wave scattering in a cavity, where a wave front is injected from the left and transmitted to the right. The dotted wave front shall indicate the reflected part of the initially injected one. The blue lead on the left denotes the incoming lead. The orange one on the right is the outgoing lead.

According to section 1.2 we connect the modes entering and leaving the billiard using a scattering matrix  $S$

$$S = \begin{pmatrix} R & T' \\ T & R' \end{pmatrix}. \quad (6.11)$$

Note that  $S$  contains four  $N \times N$  blocks representing the transmission matrices  $T$  and  $T'$  and the reflection matrices  $R$  and  $R'$  for the  $N$  propagating modes (compare with section 1.2).  $R$  and  $T$  describe the signal injection from the left lead and the primed quantities  $R'$  and  $T'$  are related to the injection from right lead. Note that we deal with as many incoming than outgoing modes (In the experiment  $N = 16$  in both leads). According to section 3.1 we can define the WSTD  $Q$  as

$$Q = i\hbar \frac{\partial S^\dagger}{\partial E} S = i\hbar \begin{pmatrix} \dot{R}^\dagger R + \dot{T}^\dagger T & \dot{R}^\dagger T' + \dot{T}^\dagger R' \\ \dot{T}'^\dagger R + \dot{R}'^\dagger T & \dot{R}'^\dagger R' + \dot{T}'^\dagger T' \end{pmatrix} = \begin{pmatrix} Q_{11} & Q_{12} \\ Q_{21} & Q_{22} \end{pmatrix}, \quad (6.12)$$

where the dots denote the energy derivative  $\partial/\partial E$ . Particle-like scattering states (PLSSs) are the eigenvectors of this matrix. We have seen above that their eigenvalues correspond to the group delay  $t_g$ . These state have two additional properties which are quite interesting.

**First**, particle-like scattering states belong to the class of noiseless states [Two03, Sil03], meaning that their transmission values are either close to 0 (reflecting type) or to 1 (transmitting type). It turns out, that the PLSSs are living in the subspace of eigenstates of the transmission matrix  $T$  with corresponding eigenvalues  $\tau$  close to 0 or 1 [Rot11]. The total transmission is defined as

$$Tr(T^\dagger T) = \sum_{n=1}^N \tau_n \quad \text{with} \quad \tau_n \in [0, 1]. \quad (6.13)$$

**Second**, particle-like scattering states show a beam-like propagation, i.e., highly collimated wave fronts occupying classical paths. Thus their propagation is limited to certain regions and they are not distributed over the whole scattering region.

We will restrict ourselves in the following to the injection of states from the left (see figure 6.2) and we are looking for PLSSs which link the incoming lead to the outgoing one. A state  $\mathbf{w}$  injected from the left can be described as  $\mathbf{w} = (\mathbf{p}^T, 0)^T$ . Such a state shows  $N$  zero components.  $Q$ -states are eigenstates of the  $q$ -operator. The eigenvalue problem gets for the injection from the left:

$$Q\mathbf{w} = \begin{pmatrix} Q_{11}\mathbf{p} \\ Q_{21}\mathbf{p} \end{pmatrix} = q \begin{pmatrix} \mathbf{p} \\ 0 \end{pmatrix} = q\mathbf{w}. \quad (6.14)$$

This leaves us to solve the same two equations as they were found in [Rot11]:

$$Q_{11}\mathbf{p} = q\mathbf{p}, \quad Q_{21}\mathbf{p} = 0. \quad (6.15)$$

This means a particle-like scattering state has to be an eigenstate of  $Q_{11}$  and it has to lie in the kernel of  $Q_{21}$ . For unitary scattering systems Rotter et al. in

## 6.1. Theoretical Background and Motivation

---

[Rot11] could show that a state  $\mathbf{p}$  solving the two conditions in equation (6.15) is either fully reflected or fully transmitted. In [Rot11] these states are referred to as 'NOTEs' (Noiseless Time Delay Eigenstates). These states are known in the field of quantum chaotic transport as states whose shot-noise vanishes (see for example [Jac06,Sil03] for more details). In [Amb12] the particle-like scattering states are explicitly calculated for unitary systems and systems with uniform loss.

However, the direct calculation of the eigenstates of  $Q_{11}$  is not possible in our case, since in our experiment only the transmission matrix  $T$  is accessible (see section 6.2). We have seen in section 3.2, where we used the information of the transmission matrix **only**, that this information is sufficient. In section 3.2 we defined a generalised  $q$ -operator  $q_\alpha$  (see equation (3.23)) as an analogue of the Wigner-Smith time delay matrix containing only  $T$ . We showed that the real part of the eigenvalue  $\lambda$  of this now reduced operator contains the derivative of the scattering phases (see equation (3.12)  $\alpha = \omega$ ) and, as we have seen in this chapter (see equation (6.5)), the scattering phases are the essential information in which the delay time (travelling time of a wave packet) is encoded. This theoretical result was checked numerically by Brandstötter in [Bra16], where he compared directly the shortest PLSS calculated with the help of the full scattering matrix  $S$  (reflection and transmission information) with the states calculated with  $q_{\alpha=\omega}$  (see Figure 3.2 of [Bra16]). For both cases he was able to construct a highly collimated beam-like scattering state following the shortest classical path.

The result that one needs only the information stored in the transmission matrix is a blessing for experimentalists, since the transmission matrix is easier accessible from the experimental side.

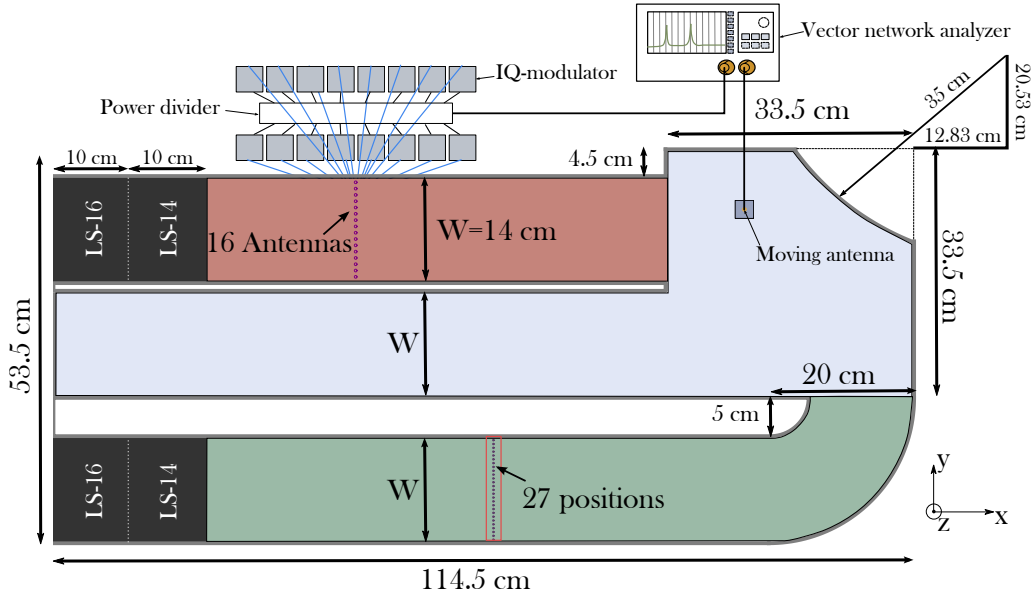


**Figure 6.3** – Two dimensional microwave cavity excited by 16 antennas (left upper corner), which are placed in the incoming lead (red coloured area). The injected signal passes the scattering area/billiard (blue area) and reaches the outgoing lead (green area). The incoming and the outgoing lead are closed with absorbing foam material (LS-14, LS-16; see section 4.2). The scattering region is closed (except for the connection to the incoming and outgoing lead). The 27 positions for the moving antenna for the measurement of the transmission matrix  $T$  are marked with a red rectangle. Vector network analyser, power divider and IQ-modulator have been already discussed in chapter 4. Compare with figure 6.5.

## 6.2 MICROWAVE SET-UP

The scattering system in which we are going to observe the particle-like scattering states is shown in figure 6.3. The chaotic scattering region (blue area in figure 6.3) is attached to an incoming lead (red area in figure 6.3) and an outgoing lead (green area in figure 6.3). The large peculiar shape of the scattering area/billiard ensures that we have enough billiard states to generate a particle-like accumulation of intensity along a classical path. This is why the shape of the scattering region is not only limited to a rectangular form but extended with an arm to fully exploit the space available in the experimental set-up.

The width of the lead  $W$  is 14 cm and its lower cut-off frequency  $f_c^1$  equals 1.07 GHz (see equation (4.26)), i.e., the first sinusoidal mode opens at 1.07 GHz. We want to work in the frequency range, where 16 modes are available, this is to say,  $17.12 \text{ GHz} < f < 18.20 \text{ GHz}$ . Our working frequency will be at 17.5 GHz  $\rightarrow \lambda = 1.71 \text{ cm}$  ( $\lambda$  is wavelength), leaving us enough space between the working frequency and the limit of the IQ-modulator which is at  $\approx 18.0 \text{ GHz}$ . The excitable 16 modes provides us with the basis to generate the wave front whose outcome will form the PLSSs in the cavity.

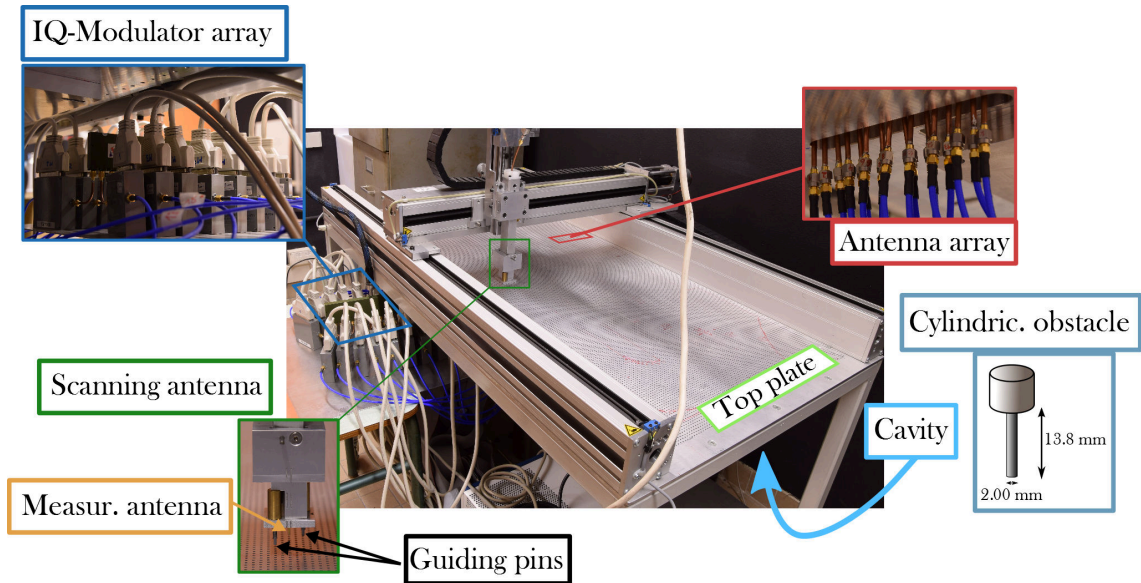


**Figure 6.4** – Pictures of the set-up showing the central components. The cavity as shown in figures 6.3 and 6.5 is put underneath the top plate. Optionally one can put additional cylindrical obstacle in the holes of the top plate to introduce additional scattering.

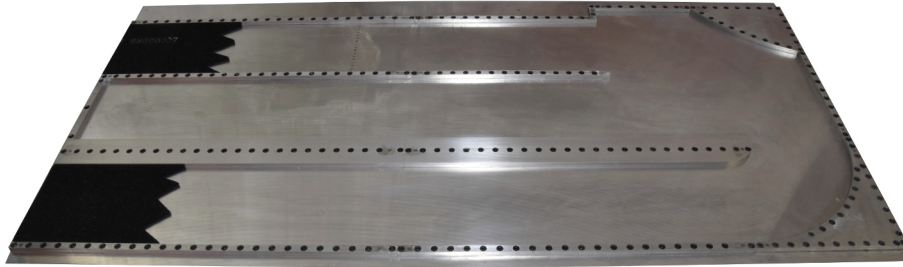


**Figure 6.5** – Picture of the fabricated cavity with the absorbers in the injecting and outgoing lead. For more details about the dimensions and the used experimental devices (see the sketch presented in figure 6.3).

Figures 6.3 and 6.5 show only the bottom plate of the cavity. The cavity is closed with another aluminium plate containing a grid of holes ( $5 \text{ mm} \times 5 \text{ mm}$ ) with a hole radius of 2 mm (see figure 6.4). The height of the cavity, which is sandwiched under the measurement table (see arrow in figure 6.4) is 8 mm. This fixes the upper cut-off frequency for the  $\text{TE}_0$  mode to  $f_{cut} = 18.75 \text{ GHz}$ , which is  $\approx 1 \text{ GHz}$  above the working frequency (see sections 1.1 and 4.2 for details on the  $\text{TE}_0$  modes). The holes in the top plate allow us to introduce a moveable antenna and to measure the  $z$ -component of the electric field  $E_z$  at any given hole position in the cavity.

The excitation of the  $\text{TE}_0$  mode forming the wave front is done using simple monopole-antennas as they have already been introduced in section 4.2. We use 16 of these monopole antennas which are each connected to an IQ-modulator to modify their amplitude and phase (compare with section 4.2). We use absorbing foam material (LS-14, LS-16 from EMERSON&CUMING) to avoid backscattering from the open ends of the incoming and the outgoing lead.

In contrast to the quasi one dimensional waveguide experiments (section 4.2) we use the moving antenna to measure the transmission matrix at 27 positions in the outgoing waveguide and not an additional sliding antenna (see red rectangle marked with 27 positions in figure 6.3, compare with figure 4.4). To avoid opening and closing the cavity for introducing additional scattering by placing obstacles, we had the idea to use the measurement holes (grid holes in the top) to insert cylindrical obstacles leading to additional scattering within the cavity. Such a cylindrical obstacle is presented in figure 6.4. This gives us the flexibility to test the robustness of the particle-like scattering states with regard to a local perturbation in the billiard.

### 6.3 EXPERIMENTAL FINDINGS

#### 6.3.1 Determining the $Q$ -operator

To calculate the  $q$ -operator we need the transmission matrix for a frequency window around the frequency of 17.5 GHz, where we want to work at (see definition of the  $q$ -operator in section 3.1). The positions where we inject the microwave signal (16 antennas connected to the IQ-modulators) and the positions to where we measure the transmission with the moving antenna (27 positions) are marked in figure 6.4.

To get rid of the white noise we perform a Fourier filter as it was already discussed in section 4.2.3. The transmission matrix  $T$  is of the form  $27 \times 16$ . We can follow the practical approach described in chapter 3 to calculate the eigenvalues  $\lambda_q$  and eigenvectors  $\mathbf{i}_q$  for which we get the output  $\mathbf{o}_q$  as  $T\mathbf{i}_q = \mathbf{o}_q$  (The  $q$ -eigenstate is not necessarily an eigenstate of the transmission matrix (see section 3.2) according to how many singular values  $\sigma_i$  are considered for the calculation. Since we have seen in chapter 3 that the travelling time is encoded within the real part of the eigenvalue  $\text{Re}(\lambda_q)$ , we ordered the eigenvalues after their real parts. We considered up to 5 eigenvalues (rising order) depending on how many singular values  $\sigma_i$  are considered (see chapter 3 for more details). We will call all the eigenvalues belonging to the same number of considered  $\sigma$  values a  **$\sigma$ -block of eigenvalues** or simply  **$\sigma$ -block**.

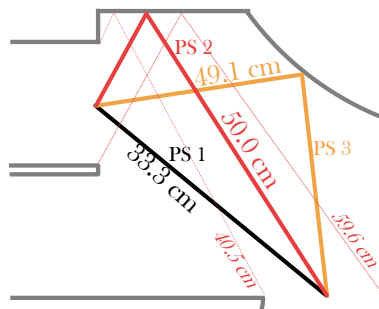


**Figure 6.6** – Definition of the Particle-like scattering states named PS 1, PS 2 and PS 3. The numbers correspond to the path-lengths of the states.

Note that the number of  $\sigma$  values goes together with the number of eigenvalues. Especially for just one  $\sigma$  value you can create only one eigenvalue which is related to one eigenstate.

The result of the calculations of the different  $\lambda_q$  values together with the total transmitted energy, which is given by  $|\mathbf{o}_q|^2$ , is shown in figure 6.7. The oscillations we see in figure 6.7 are due to the ordering of the states according to  $\text{Re}(\lambda)$ . Taking into account only five states per  $\sigma$  value we end up with in total 70 states, which are numbered from 0 to 69.

In the following, I would like to restrict our considerations only on finding the  $q$ -state which describes the direct path between the incoming lead on the top and the outgoing lead on the bottom. This state shall be named particle-like scattering state 1 (PS 1) (see figure 6.6). PS 1 has the shortest time delay between entering and exiting the cavity, so its real part should be the smallest for each considered  $\sigma$ -block. The states with this property are located on the dashed lines in figure 6.7.

In addition to the property delay time we look at the stability of the  $q$ -eigenstate. This means that we look on the effect of small frequency changes  $\delta f$  on the output. In section 3.3, I showed that this property is associated to the modulus of the imaginary part of the eigenvalue  $|\text{Im}(\lambda)|$ . A small imaginary part is linked to output-stability

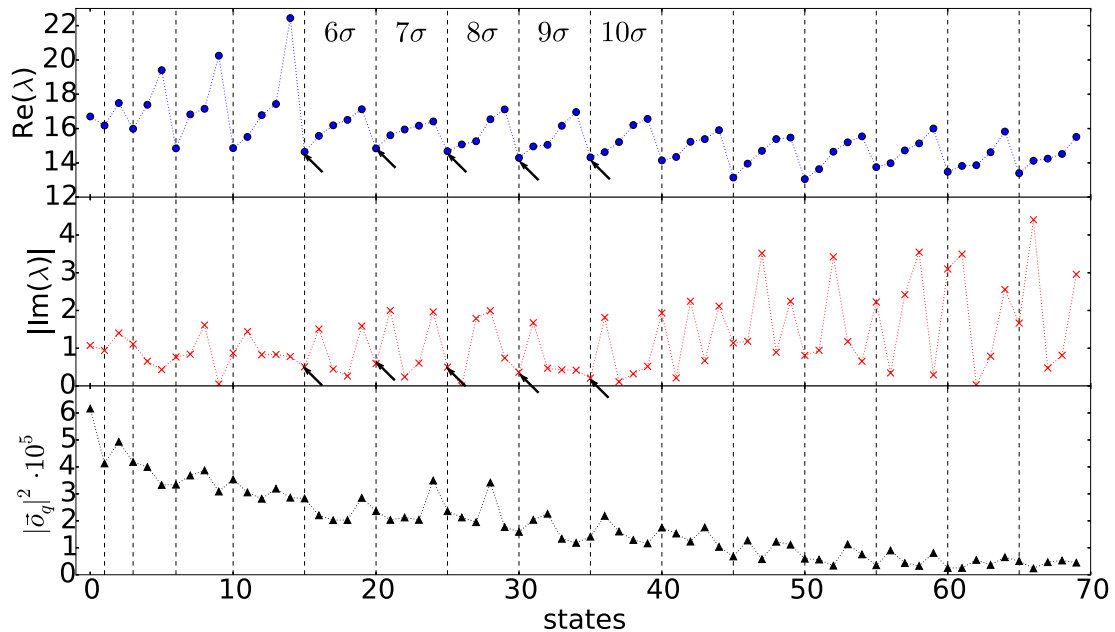


**Figure 6.7** – Result of the eigenvalues of the  $q$ -operator calculated using the measured transmission matrix  $T$ . **Top:** Real part of the eigenvalues  $\text{Re}(\lambda)$  corresponding to a time in ns. **Centre:** Imaginary part of the eigenvalues  $\text{Im}(\lambda)$ . **Bottom:** Total transmission calculated from  $|\mathbf{o}_q|^2$  using the relation  $T\mathbf{i}_q = \mathbf{o}_q$ . The  $n\sigma$  on top shall indicate, that  $n$   $\sigma$ -values were taken into account for the calculation. The dashed lines indicate the borders of a  $\sigma$ -block. The arrows show the positions of the expected particle-like scattering state 1 (see text for further details).



against frequency change  $\delta f$  (see section 3.3). So our second condition for the PS 1 is a small value of the imaginary part. If we order the states according to these two criteria we get the five states marked by arrows in figure 6.7. The exact order of the found states according to the two criteria is 35, 30, 25, 15 and 20 (35 has the lowest value  $|\text{Im}(\lambda)|$  and 20 the greatest one).

In figure 6.7 one observes an overall decline of the total transmission  $|\mathbf{o}_q|^2$  for ascending  $\sigma$ -blocks. This is due to the fact that one enlarges the subspace in which one looks for the PLSSs. This larger basis must not necessary increase the precision on the definition of the PLSSs. In fact this enlargement of the frequency dependant basis elements perturbs the definition of the PLSSs as more non path-like components enter the calculation.

This can also be seen in the imaginary values  $|\text{Im}(\lambda)|$  after the 10-th  $\sigma$ -block, where one observes larger oscillations and much greater values for the PS 1 states (values on the dashed lines in figure 6.7). However, our chosen states show intermediate transmission values and very high frequency stability values (low  $|\text{Im}(\lambda)|$  values).

Despite the three mentioned a priori properties ( $\text{Re}(\lambda)$ ,  $\text{Im}(\lambda)$  and  $|\mathbf{o}_q|^2$ ), one has another a priori information which one can use to specify PLSSs. This information is stored in the following auto-correlation function which describes the output change of the eigenvector  $\mathbf{o}_q(f)$  with changing frequency:

$$\text{corr}(f) = \frac{|\mathbf{o}_q^\dagger(f)\mathbf{o}_q(f_0)|}{|\mathbf{o}_q(f)||\mathbf{o}_q(f_0)|} \quad \text{with} \quad T\mathbf{i}_q = \mathbf{o}_q, \quad (6.16)$$

where  $y$  denotes the spatial axis along the 27 antenna holes (see figure 6.3).  $f_0$  denotes the working frequency of 17.5 GHz.  $\text{corr}(f)$  can be seen as a frequency broadband criteria for the stability of the  $q$ -eigenstates, whereas  $\text{Im}(\lambda)$  is more like a narrowband stability criteria as it contains only the information in the vicinity of  $f_0$  ( $\partial T/\partial f$  at  $f_0$  in the definition of the  $q$ -operator equation (3.2) with  $\alpha=f$ ). The result of this correlation for the different  $q$ -eigenstates is shown in figure 6.8.

One can conclude that all the  $q$ -eigenstates show a quite large frequency stability. To quantify the differences between them we performed a parabolic fit within the frequency range of [17.497GHz, 17.503 GHz] and looked at the opening width  $\text{corropen}_{fit}$  of the parabola which is shown in figure 6.9 as a function of the  $q$ -eigenstates.

Small  $|\text{corropen}_{fit}|$ -values correspond to a large opening of the parabola and this represents broadband frequency stability. The chosen states (35, 30, 25, 15 and 20) show  $|\text{corropen}_{fit}|$ -values close to the mean value (state 15) or well above (20, 25, 30 and 35). Therefore we consider them to be frequency stable which is another indicator that we are looking at the right  $q$ -eigenstate, i.e., we are looking at PS 1.

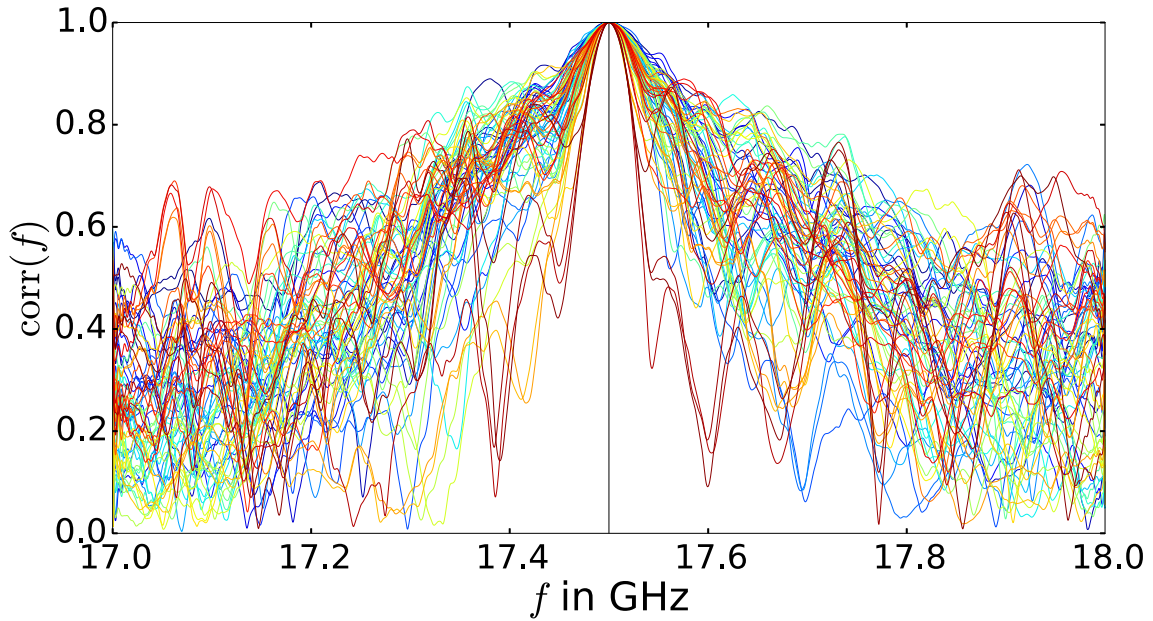


**Figure 6.8** – Result of the calculation of  $\text{corr}(f)$  (see equation (6.16)) for all 70 eigenstates of the  $q$ -operator.

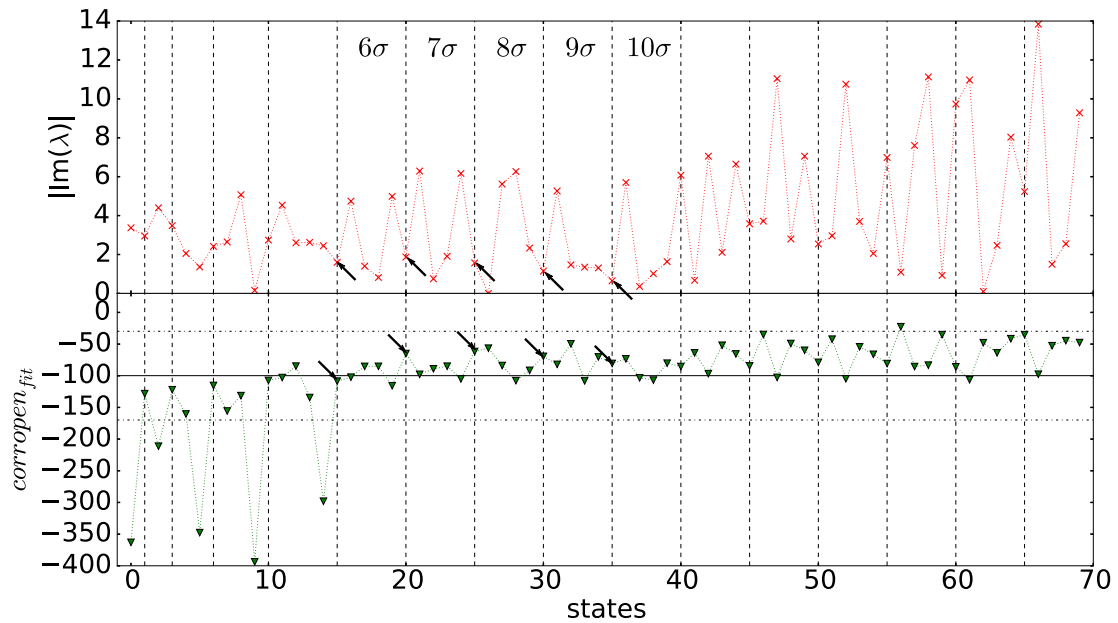


**Figure 6.9** – **Top:** Imaginary part of the eigenvalue  $\text{Im}(\lambda)$  (same as shown in figure 6.7). **Bottom:** Result of the calculation of  $\text{corr}(f)$  for all 70  $q$ -eigenstates. The solid horizontal line marks the mean value of  $\text{corropen}_{fit}$  and the dashed horizontal lines mark the standard deviation around the mean value (see also figure 6.7).

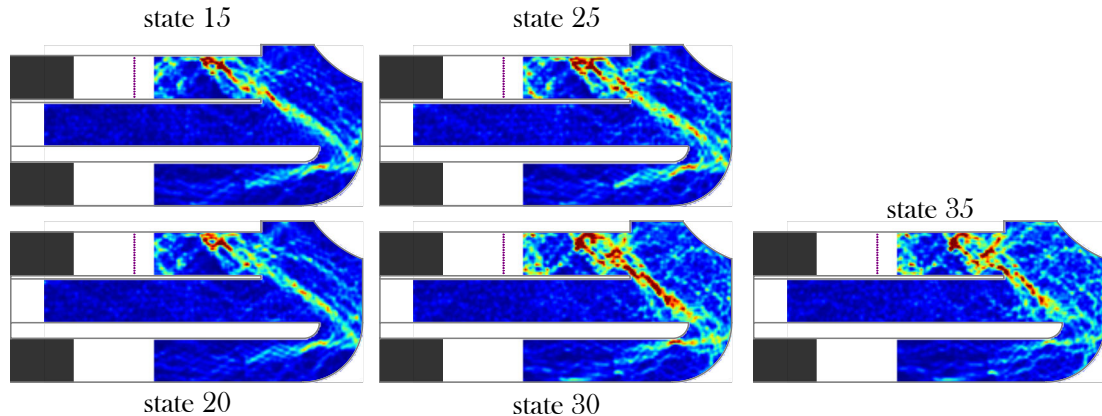


**Figure 6.10** – Intensity profile of the  $q$ -eigenstate 15, 20, 25, 30, 35 within the cavity (compare with figure 6.7). Red stands for high intensity and blue stands for low intensity.

### 6.3.2 Generating Particle-like Scattering State 1

We fixed our consideration onto these 5 states. To prove that they show a particle-like accumulation of intensity along classical paths we have to investigate their spatial intensity distribution/profile. We will start our investigation by sending the respective eigenvectors to the antenna array (see figure 6.3). This is done using the IQ-modulators. The states are injected and the moving antenna scans the interior of the cavity. The picture processing follows the exact same steps as already implemented in section 4.3.3. The intensity profiles for the  $q$ -eigenstates 15, 20, 25, 30 and 35 are shown in figure 6.10.

The intensity of the chosen states is clearly accumulated on a classical path which connects directly the incoming with the outgoing path. State 35 is already showing that its basis already contains non-path like contributions and it has the largest basis of all the shown states. This is why it is the most stable state, but it is at the limit of being a PS 1. This could have been already observed in figure 6.9, where state 40 (only one  $\sigma$ -block further) is very unstable (high  $|\text{Im}(\lambda)|$ -value). This means state 35 is at the limit of being a stable PS 1. Nevertheless, we showed that we are able to create states of type PS 1 only by using the information from the transmission matrix showing high accumulated intensity along the shortest classical path.

A quantitative measure for the localisation of the particle-like scattering state can be introduced by looking at the ratio of the intensity of the scattering state which is actually located on the classical path. The idea is to define a mask which corresponds to the classical trajectory between the leads (width of the trajectory is about the width of the waveguide) and to compare the integrated intensity within the mask with the total intensity stored within the billiard. The mask which define the PS 1 path and the billiard itself are shown in figure 6.11.

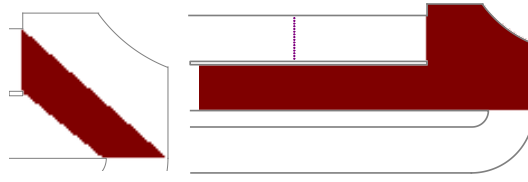


**Figure 6.11** – Pictures of the two mask used to calculate  $s_{loc}$ . **Left:** Mask for the path of the particle-like scattering state 1. **Right:** Mask describing the scattering part of the cavity.

Using these masks we define the following quantity (see equation (6.17)), which we call localisation strength  $s_{loc}$  or normalised localisation strength  $s_{loc_n}$ :

$$s_{loc}^i = \frac{\int_{A=path_i} I dA}{\int_{A=cav} I dA}, \quad s_{loc_n}^i = s_{loc}^i \cdot \frac{\int_{A=cav} dA}{\int_{A=path_i} dA}. \quad (6.17)$$

The index  $i$  describes the type of the PLSS. Later on we will discuss also PS 2 and PS 3 with this criteria.  $path_i$  describes the mask of PS  $i$ , i.e., the area occupied by the classical path corresponding to PS  $i$  and  $cav$  denotes the whole measured cavity area (see right hand side of figure 6.11).  $I$  denotes the measured intensity and  $A$  is the area in the  $(x,y)$ -plane. The normalised localisation strength  $s_{loc_n}^i$  is the factor of which the measured intensity distribution differs from an uniform distributed intensity profile.  $s_{loc_n}^i$  allows us to easily discriminate the quality of different types of PLSSs as they are area-normalised.

The values for  $s_{loc}^i$  and  $s_{loc_n}^i$ , which we calculated for the states 15, 20, 25, 30 and 35 are presented in table 6.1. The values in table 6.1 state that we are able to locate about 40% of the intensity onto the classical path of PS 1. State 35 which was supposed to be the most stable shows the lowest quality regarding our new quantitative measure. This is what we have already observed (see figure 6.11). Therefore our introduced measure seems reasonable. The reasons for the low quality of state 35 has already been discussed above. Our observation of the intensity is not only limited to the frequency domain. Since we measured the states for a frequency window of  $17.3 \text{ GHz} < f < 18 \text{ GHz}$ , we have the possibility to look into the time evolution of the scattering states. In figure 6.12 we compared the time evolution of state 20, which corresponds to a PS 1, with a random state, which is created using random settings for the IQ-modulator.

state	15	20	25	30	35
$s_{loc}^1$	0.41	0.38	0.38	0.40	0.36
$s_{loc_n}^1$	2.3	2.1	2.1	2.3	2.0

**Table 6.1** – Values of  $s_{loc}^1$  and  $s_{loc_n}^1$  (see definition in equation (6.17)) for the states representing particle-like scattering state 1.

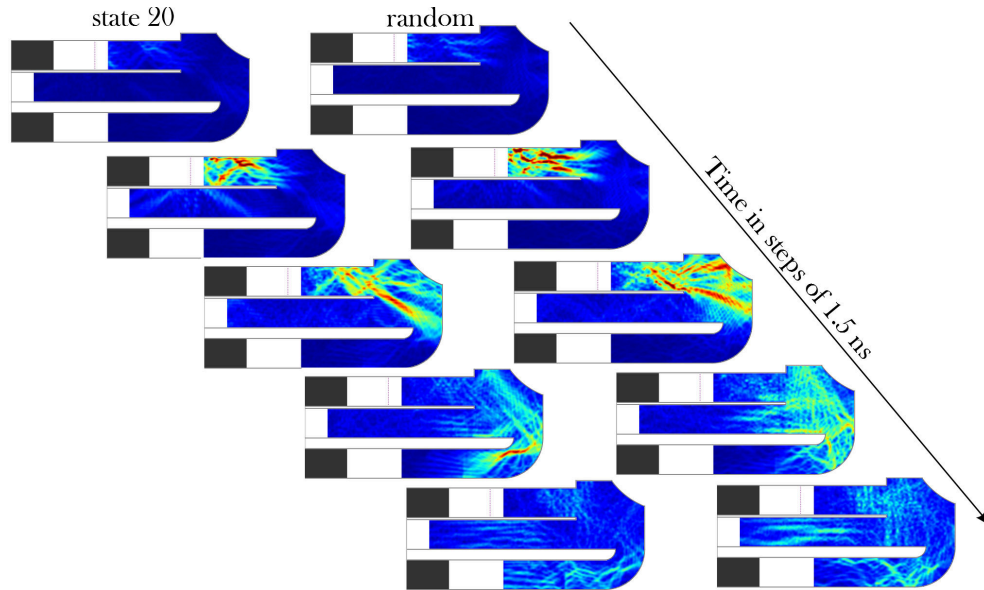


**Figure 6.12** – Time evolution of the intensity profile of the state 20 and a random state. **Red** for high intensity and **blue** for low intensity.

We observe in figure 6.12 how the random state is filling up almost the whole rectangular part of the scattering area (see pictures in the third row of figure 6.12), whereas state 20 is more focused onto the direct path pointing towards the outgoing lead. After 4.5 ns state 20 is strongly localised in the outgoing lead. The random state is more distributed among the entire scattering part of the cavity especially in the additional arm (see pictures in the last row of figure 6.12).

We showed in this section that we were able to identify a scattering state which accumulates its intensity onto the shortest classical path connecting the leads and we found a quantitative criteria to describe the quality of such a state by looking at the integrated intensity of the area occupied by classical path of width  $\approx W$  (lead width see figure 6.3).

### 6.3.3 Other Particle-like Scattering States

As it has been already indicated in figure 6.6 there are two other short PLSSs present in our system. We name them PS 2 and PS 3. Before we used a priori information only. Now we use directly the mask-criteria (according to equation (6.17)) which we introduced above to identify these two type of states. Therefore we need two new masks which describe the classical paths of PS 2 and PS 3. These masks are shown in figure 6.13. Why we can not use a similar a priori argument than it was the case for the particle-like scattering state 1 is discussed below.

What we did was that we injected 70 eigenstates of the  $q$ -operator (described in figures 6.7 and 6.9) and measured the intensity profile with the scanning antenna. In a second step we calculated for each measured state the normalised localisation

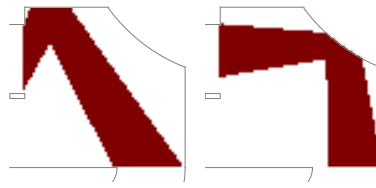


**Figure 6.13** – Pictures of the two masks used to calculate  $s_{loc}$  and  $s_{loc_n}$  corresponding to PS 2 and PS 3 (compare with figure 6.6). **Left:** Mask for the path of the PS 2. **Right:** Mask for the path of the PS 3.

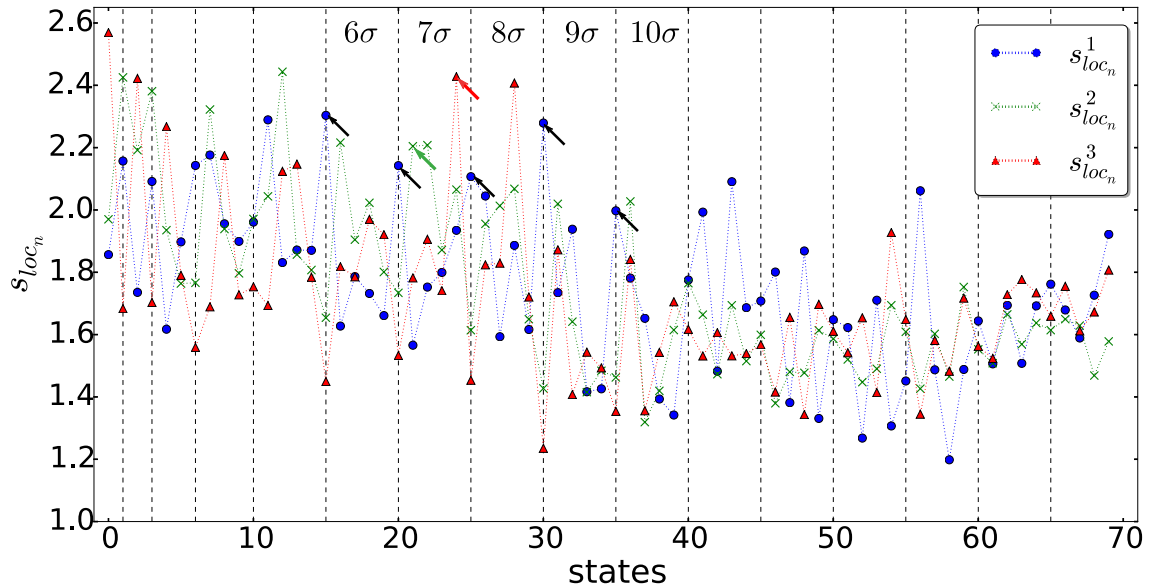


**Figure 6.14** – Normalised localisation strength  $s_{loc_n}^i$  for  $i = 1, 2, 3$  for 70 measured states (same order as in figures 6.7 and 6.9). **Black arrows** indicate the states associated with a particle-like scattering state 1. The **Red arrow** and the **green arrow** refer to PS 2 and PS 3.

strength  $s_{loc_n}^i$  for  $i = 1, 2, 3$  for the three types of PLSSs. The result is shown in figure 6.14. This means that we have associated three numbers with each measured state. Each of these numbers describe to which extend the measured state is really a PLSS of type PS  $i$  ( $i = 1, 2, 3$ ). For example state 21 and state 24 (see red and green arrow in figure 6.14) show a strong particle like behaviour. State 21 corresponds to a PS 2 and state 24 refers to a PS 3.

We can also look directly at their intensity profiles which are shown in figure 6.15. It is evident that state 21 and state 24 show an accumulated intensity onto the path of PS 2 and PS 3. The question I would like to answer in the following is why we can not apply the same method for finding the PS 1.

We restrict the problem on the states in the  $7\sigma$ -block (see figures 6.7 and 6.9). States 21 and 24 are particle like as we have seen before, i.e., they reflect trajectories of a classical particle staying in the billiard for a certain time (delay time).

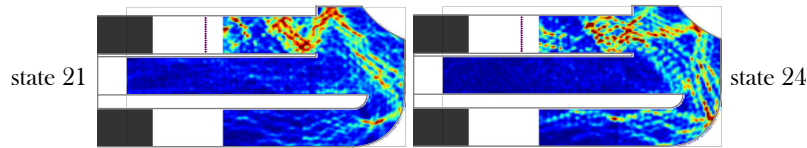


**Figure 6.15** – Intensity profile of the states 21 and 24 (compare with figure 6.7). **Red** for high intensity and **blue** for low intensity.

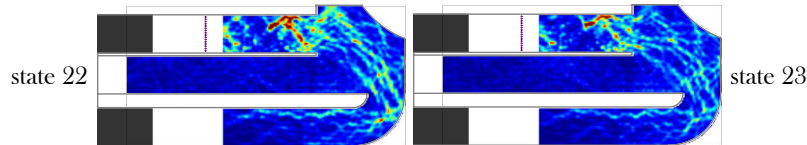


**Figure 6.16** – Intensity profile of state 22 and state 23 belonging to the  $7\sigma$ -block (compare with figure 6.7). **Red** stands for high intensity and **blue** stands for low intensity.

Consequently the states 22 and 23 should reflect paths which have a delay time  $t$  which follows  $t_{21} < t < t_{24}$ , where  $t_{21}$  and  $t_{24}$  are the delay times of the states 21 and 24. However, if one looks at the intensity profiles of state 22 and 23 (see figure 6.16), one recognises that these states are more less superposition of state 21 and 24.

The reason for that can be found when one looks at the path lengths of the PLSSs associated with the states 21 and 23 (see figure 6.6). One finds that PS 2 and PS 3 have quite similar path lengths especially when one takes into account a certain width of the trajectories (see red dashed lines in figure 6.6). Similar path lengths mean of course similar delay times since the wave front is always travelling with the full  $k$ -vector depending only on the speed of light  $c$  within the central cavity. The problem is that the  $q$ -operator can only discriminate eigenstates with **different** delay times. Since this is not the case here one observes always a superposition of PS 2 and PS 3. If one looks close enough, even state 21 and state 24 show features of both PS 2 and PS 3.

Experimentally, one could overcome this delay time degeneracy by putting obstacles (scatterers) into the path of either PS 2 or 3. Brandstötter showed numerically in [Bra16] that the insertion of obstacles (size is of the order of the wavelength) does not effect those PLSSs whose trajectory is not passing through the obstacle, i.e., one can switch in between several PLSSs so that one can always ensure an unaffected communication between the incoming and the outgoing lead.

### 6.3.4 Perturbation of Particle-like Scattering States

In the following we like to verify this numerical observation of Brandstötter, so we are going to introduce obstacles in the scattering part of the cavity. If the obstacle is placed within the path of an PLSS, the transmitted signal will be blocked and the overall transmission for this state will drop down. In this section we will restrict

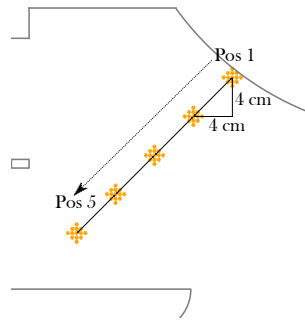


**Figure 6.17** – Cylindrical pins (a bundle of 13) are placed in the holes of the top plate at 5 given positions. Note that only one position is filled at a time. The distance between the positions is the same.

the investigations to the states 20, 21 and 24 which represent the PS 1, 2 and 3, respectively (see figures 6.10 and 6.15).

We will study how these states react to perturbations introduced by additional obstacles within the cavity. Cylindrical pins will play the role of the obstacles (see figure 6.5). We put 13 of them together to a rectangular shape and place them inside the holes of the top plate (see figure 6.17). We chose 5 equidistant positions for this rectangle of pins (see figure 6.17). This rectangular ensemble of pins can be seen as a local perturbation (site length of the rectangle  $\approx 1.5$  cm) of the order of the wavelength  $\lambda = 1.7$  cm, i.e., the perturbation is greater than the size of possible nodal spots of the scattering state.

Before placing the obstacles we measure the transmission matrix  $T$  at 5 rows around the central line where we measured the transmission matrix in section 6.3.1 (two rows to the left and two to the right of the one indicated with a red square in figure 6.3). These are in total 135 measurement points to measure the transmission from the injection lead to the exit lead. After having measured the empty waveguide we have created a reference to which we will compare the transmission in the case where we placed the pins. The measurement procedure is the following. We place the 13 pins at position  $i$  (denoted with Pos  $i$  in figure 6.17,  $i = 1, 2, 3, 4, 5$ ) and we measure each time the transmission at the 135 given measurement points. Then we quantify the difference between the measurement with and without the obstacles. To do that we use the following intensity relation:

$$\Delta I_{rel}^{tot} = \frac{\int (I_{ob} - I_{em}) dA}{\int I_{em} dA}. \quad (6.18)$$

$I_{ob}$  and  $I_{em}$  denote the measured intensity at the 135 measurement points in case of the presence or absence of the pins. We calculated  $\Delta I_{rel}^{tot}$  for each obstacle position using the obtained measurement data. The calculated  $\Delta I_{rel}^{tot}$  for the states 20, 21 and 24 is shown in figure 6.18.

Once the pins are placed such that they are sitting in the path of PS 1, 2 or 3, the transmission drops down. This observation is explained in figure 6.19, which shows



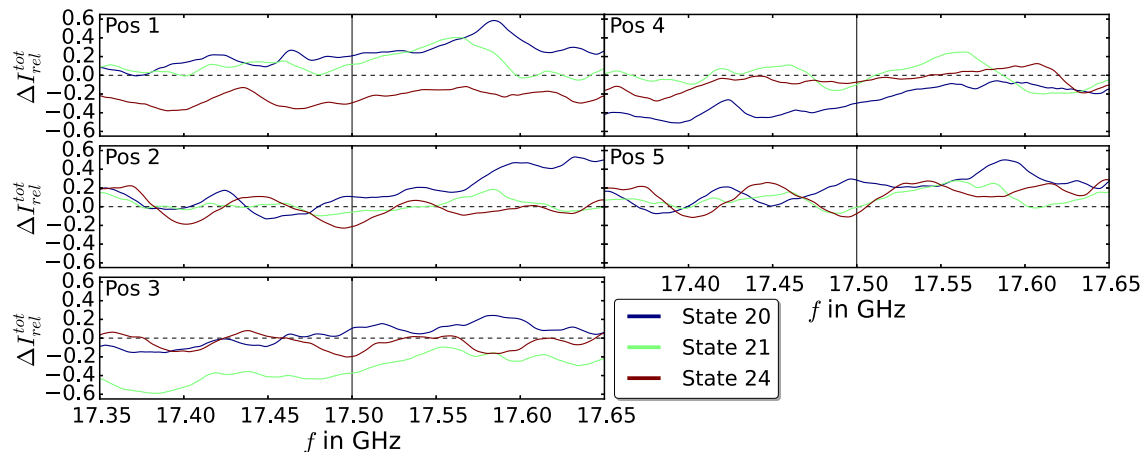


**Figure 6.18** – Obtained  $\Delta I_{rel}^{tot}$  (definition in equation (6.18)) for 5 positions of the rectangular pin obstacle (see figure 6.17) for the states 20, 21 and 24 which correspond to PS 1, 2 and 3 (see figures 6.10 and 6.15).

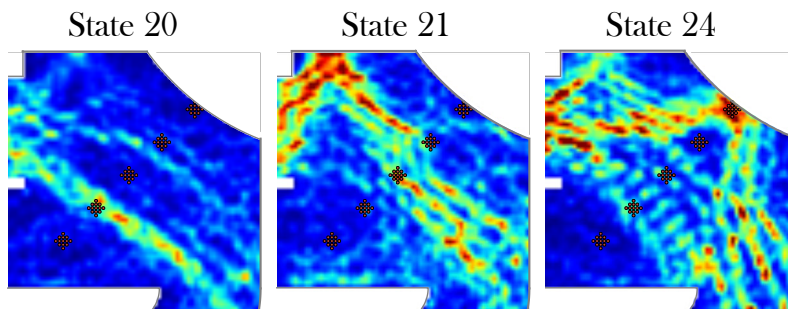


**Figure 6.19** – Overlay of the obtained intensity of the scattering state for the **empty** scattering region with positions of the cylindrical obstacles. The red dots symbolise the possible positions of the obstacles (compare with figure 6.17). **Left:** State 20. **Center:** State 21. **Right:** State 24.

an overlay of the intensity of the scattering states of the **unperturbed** system together with the positions of the obstacles. Once we position the obstacle onto the path of a PLSS (PS 1, 2 or 3) the state is highly perturbed and therefore the transmission of this state drops down significantly ( $\geq 28\%$ ). The important thing we observe is that the other PLSSs, which are not directly affected by the obstacle do not drop down at all or drop down only slightly.

The reason for that behaviour is that each PLSS is living on a certain subspace of the transmission matrix  $T$ . This subspace is spanned by path-like high transmitting scattering states (see section 3.4). Perturbations lying outside of the corresponding path are automatically not included in the subspace. Therefore this perturbation does not influence the PLSS. This is not obvious in first place, since we changed the scattering system significantly by introducing this kind of pin-obstacles. Nevertheless, we showed that the PLSSs are rather stable against perturbations which are not directly associated with their classical path. Just like for classical particles the PLSS is only influenced by obstacles which are placed onto his trajectory.

**This opens up the possibility to circumvent local obstacles or perturbations by switching between different PLSSs.** This way also intruders or unwanted listeners in a wave based communication system can be avoided!

## 6.4 CONCLUSION

In this chapter I tried to deepen the insight on the relation of the  $q$ -operator defined in chapter 3 and the realm of particle-like scattering states which are related to the Wigner-Smith time delay operator. These particle-like states, which are eigenstates of the  $q$ -operator, show highly collimated intensities occupying classical paths. Their corresponding eigenvalue contains the information about the delay time (travelling time of the wave). Therefore we are able to distinguish between different particle-like scattering states (PLSSs) occupying different classical trajectories. We showed that we are able to construct these states using the information stored in the frequency dependant transmission matrix  $T$  only, where we used the formalism of the  $q$ -operator (see chapter 3), which can be seen as a generalised version of the Wigner-Smith time delay operator (using only  $T$ ).

Our aim was to use this knowledge and to perform an in situ generation of these states by the means of incident wave front shaping (see also chapter 4). We constructed a two dimensional cavity (see figure 6.3) with two attached leads which defined our input and our output.

At first, we measured the transmission matrix and constructed the  $q$ -operator and calculated its eigenstates. We ordered the obtained eigenstates according to their eigenvalues  $\lambda$  and their total transmission and we were able to identify the PLSS which corresponds to the shortest classical path connecting incoming and outgoing lead (called PS 1, see figure 6.6). To verify the classical nature of the state we injected this state with our antenna array, where we can shape the incident wave front using IQ-modulators.

This in situ shaping is the prominent difference compared to recent work [Gér16] dealing with PLSSs. G eradin et al. showed that they are able to measure the full scattering matrix  $S$  of a scattering system, which was realised with an elastic plate and excited with laser pulses. They could create the initial conditions for the realisation of PLSSs in a similar way than we did. However, their experimental set-up did not allow an in situ injection of the states. Instead, they measured the basis of the scattering states by exciting the plate at multiple positions at the input side. With this basis measurement they could virtually create the intensity patterns of the particle-like scattering states.

Our experiment shows the first in situ realisation of PLSSs by means of incident wave front shaping using multiple well defined antenna sources as input. We have also access to higher order PLSSs (PS 2 and 3, see figure 6.6), i.e., we can address PLSSs which correspond to the second and third shortest classical paths possible

in our cavity. We observed that these states are nearly degenerated eigenstates of the  $q$ -operator as their path length (delay time) is nearly equal. Especially if one assigns a certain width to the classical trajectory.

By introducing cylindrical obstacles into the billiard, we were able to confirm the stability of PS 1, 2 and 3 with regard to local perturbations. Our set-up enables us to easily switch between different paths. These paths can also be interpreted as communication paths offering the possibility to avoid obstacles or intruders which occupy a certain region of the system. This might be useful with regard to possible applications like in wireless communications using multiple inputs and multiple outputs (MIMO) [Sal85, Sam02] for example. Our results can be related in fact to any kind of wave based system, where one is able to measure the transmission matrix of the scattering system as a function of the frequency (energy) and where one has full control about the incident channels (amplitude and phase control in our case).

# General Summary

---

In this thesis I presented different atypical transport phenomena. The first one was the Quantum Search, where we realised a focussing of energy onto a distinct search site. This focussing could be understood as spectral wave shaping to search out for specific sites in a tight binding system. We showed with our experiment that we were able to perform such a search in an open cavity system in which we placed dielectric resonators. We measured a linear chain of variable length ( $N$ ) for which the search time followed  $\mathcal{O}(\sqrt{N})$ . For large systems one has to move to two dimensional graphene-like lattices (Dirac point with linear energy dispersion) so that an effective search is possible  $\mathcal{O}(\sqrt{N \ln(N)})$  [Fou14]. For a proof of principle experiment we arranged 216 dielectric resonators to a graphene-like lattice (arm-chair edges only) where we successfully looked for two different search sites which were coupled to eigenstates of the graphene-lattice in the vicinity of the Dirac point. Since the grid was excited within a spectrally selected frequency window, we could speak of incident spectral wave shaping which was used to localise a certain object within an arrangement of other objects. We paved the way for a possible application of the quantum search by connecting this concept to the idea of a graphene based switch, i.e., one can localise energy on two different sites of the lattice by exciting two different lattice states (see chapter 2).

We moved to experiments studying wave front shaping in quasi one dimensional waveguides. Our set-up was able to produce any of the present sinusoidal modes of the guide at the output. We demonstrated this by producing the diagonalised transmission matrix in the mode picture. This diagonalisation was possible even for the case in which we have introduced dielectric/metallic scatterers inside the waveguide. The control of the incident wave front, which is the basis for any kind of tuning, was established by an array of antennas. Each antenna was tunable (phase and amplitude) by an IQ-modulator, which was experimentally characterised (see section 4.2.4). To use the full potential of our set-up, we looked at the  $q$ -operator (chapter 3), which is a modified version of the Wigner-Smith time delay operator (WSTDO) where energy and  $S$  (scattering matrix) are replaced by a parameter  $\alpha$  and  $T$  (transmission matrix). If  $\alpha$  corresponds to the transversal coordinate of a scatterer and if we are able to measure the transmission matrix for three slightly different positions, we are capable to construct the  $q$ -operator. The eigenstates of the  $q$ -operator incorporate the information about the position of the scatterer naturally. This enables us to shape the initial wave in the way that the wave either avoids the region of the moved scatterer or focuses on it. We could also confirm that the eigenvalue of the corresponding focussing state contains information from which direction the state focusses (see chapter 4).

In the next step I presented a two dimensional chaotic cavity with two attached leads. The input lead contained an array of 16 antennas which were tunable due to the IQ-modulators. By measuring the transmission matrix  $T$  between the incoming lead and the outgoing lead in a certain frequency window we could construct the  $q$ -operator ( $\alpha$  is the frequency). The eigenstates of this operator represented particle-like scattering states, which are originally defined as eigenstates of the WSTD0. It had been numerically shown [Bra16] that the eigenstates of the  $q$ -operator and the eigenstates of the WSTD0 lead to almost the same particle-like behaviour. We could proof experimentally that the a priori information provided by the frequency dependant transmission matrix is enough to create a scattering state whose intensity is strongly accumulated on the shortest classical trajectory connecting incoming and outgoing lead. In addition, we discovered higher order particle-like scattering states corresponding to second and third shortest paths present in the system. We checked the stability of these states by placing an arrangement of cylindrical obstacles which formed a local perturbation. We observed that those states were mainly affected by the perturbation whose corresponding classical paths were intersected by the obstacles (see chapter 6). These results can be related in fact to any kind of wave based system leading to possible applications like applications in wireless communication, for example, where one already uses multiple input and multiple output (MIMO) techniques [Sal85, Sam02].

The last atypical transport phenomenon we studied was the phenomenon which arises when a system features an exceptional point (EP). We described how the simple model of a  $2 \times 2$  non-Hermitian Hamiltonian, which incorporates these special points, can be translated into a quasi one dimensional wavy waveguide system with additional position dependant loss supporting two propagating modes. In this waveguide the two appearing Bloch modes encircle such an EP during their propagation through the guide. Our waveguide system represented a dynamical encircling leading to the observation of non-adiabatic transitions. This non-adiabatic transitions were experimentally observed by looking at the transmission matrix  $T$  in the sinusoidal mode picture. Theoretically an asymmetric mode scattering behaviour depending on the injection direction had been predicted. This was exactly what we obtained in our experiment. Furthermore, we performed a parametric encircling of the EP by building five different periodical waveguides corresponding to five points on the continuous trajectory around the EP which had been studied before in the dynamical case. We detected a flipping behaviour for the two propagating Bloch modes. This flipping behaviour was in total agreement with the results observed by the other experimental groups who had already realised such a parametric encircling of an EP [Dem01, Dem04, Ste04, Lee09, Cho10a] (see chapter 5).

# Conclusion

---

Dans cette thèse, nous avons étudié différents phénomènes de transport atypiques. Le premier concerne la « recherche quantique », dans le cadre de laquelle nous avons réalisé une focalisation d'énergie sur un site bien déterminé. Ce résultat peut être interprété comme une mise en forme spectrale spécifique de l'onde dans le but de rechercher des sites distincts dans un système traité par le modèle des liaisons fortes. Nous avons démontré expérimentalement notre capacité à réaliser ces « recherches » dans un système en cavité ouverte dans laquelle nous avons préalablement placé des résonateurs diélectriques. Nous avons entre autres mesuré une chaîne linéaire de longueur variable ( $N$ ) pour laquelle le temps de recherche est de l'ordre de  $\mathcal{O}(\sqrt{N})$ . Pour des systèmes de grande taille, nous devons utiliser des réseaux bi-dimensionnels de type graphène (possédant un point de Dirac et une relation de dispersion linéaire) de manière à ce qu'une recherche efficace soit réalisable dans un temps de l'ordre de  $\mathcal{O}(\sqrt{N \ln(N)})$  [Fou14]. Comme preuve de principe, nous avons réalisé un arrangement de 216 résonateurs diélectriques sous forme de graphène (avec uniquement des bords de type “arm-chair”) dans lequel nous avons cherché avec succès deux sites différents qui étaient couplés à des états propres du réseau de graphène se situant proches du point de Dirac. Dans la mesure où le réseau n'était excité que sur une gamme de fréquences bien déterminée, nous pouvons parler de mise en forme spectrale de l'onde incidente pour localiser un objet pré-sélectionné parmi un arrangement d'autres objets. Nous avons ainsi ouvert la voie à une possible application de l'algorithme de « recherche quantique » en reliant ce concept à l'idée d'un router à base de graphène : il est possible de localiser de l'énergie sur deux sites différents en excitant deux états distincts du réseau (cf. chapter 2).

Nous avons ensuite étudié expérimentalement la mise en forme de front d'ondes dans des guides d'ondes quasi-unidimensionnels. Notre dispositif permet d'obtenir en sortie n'importe lequel des modes sinusoidaux du guide. Nous en avons fait la démonstration en calculant la matrice de transmission diagonalisée dans la base des modes propres du système. Cette diagonalisation a également été réalisée pour un guide d'onde dans lequel étaient inclus des diffuseurs diélectriques/métalliques. Le contrôle du front d'onde incident, qui est à la base du processus d'ajustement, a été effectué par un ensemble d'antennes. Chaque antenne est programmable en phase et en amplitude par un modulateur IQ préalablement caractérisé (cf. section 4.2.4). Pour utiliser tout le potentiel de notre dispositif, nous avons étudié le  $q$ -operator (cf chapitre 3), qui constitue une version modifiée de l'opérateur de retard de Wigner-Smith (WSTDO) dans lequel l'énergie et la matrice de diffusion  $S$  sont respectivement remplacées par un paramètre  $\alpha$  et la matrice de transmission  $T$ . Si  $\alpha$  correspond aux coordonnées transverses d'un diffuseur et si nous sommes capables

## Conclusion

---

de mesurer la matrice de transmission pour trois positions légèrement différentes du diffuseur, nous sommes alors capables de construire le  $q$ -operator. Ses états propres contiennent naturellement l'information sur la position du diffuseur. Cela nous permet de mettre en forme la condition initiale de manière à ce que l'onde soit en capacité soit d'éviter la région contenant le diffuseur, soit au contraire de se focaliser sur ce dernier. Nous avons aussi confirmé que la valeur propre correspondant à l'état focalisé contient l'information sur la direction suivant laquelle l'état se focalise (cf. chapitre 4).

Ensuite, j'ai présenté une cavité chaotique à deux dimensions à laquelle nous avons ajouté une entrée et une sortie. L'entrée contient un ensemble de 16 antennes ajustables grâce aux modulateurs IQ. En mesurant la matrice de transmission  $T$  entre l'entrée et la sortie dans une certaine gamme de fréquences nous avons pu construire le  $q$ -operator ( $\alpha$  étant ici la fréquence). Les états propres de cet opérateur sont des états de type "particle-like scattering states" qui sont originellement définis comme des états propres du WSTDO. Il a été démontré numériquement [Bra16] que les états propres du  $q$ -operator et du WSTDO mènent à des comportements identiques de type "particle-like". Nous avons pu prouver expérimentalement que l'information fournie a priori par la matrice de transmission (dépendant de la fréquence) est suffisante pour créer des états de diffusion dont l'intensité est fortement accumulée sur la trajectoire classique la plus courte connectant l'entrée à la sortie du système. De plus, nous avons découvert des ordres plus élevés de ces "particle-like scattering states" qui correspondent à la deuxième et troisième trajectoire la plus courte existant dans le système. Nous avons par ailleurs vérifié la stabilité de ces états en plaçant un arrangement d'obstacles cylindriques, créant ainsi une perturbation locale. Nous avons alors observé que ces états étaient surtout affectés lorsque les perturbations croisent les trajectoires classiques qui leurs sont associées (cf. chapitre 6). Ces résultats peuvent être associés à n'importe quel système ondulatoire, ce qui mène à de potentielles applications par exemple dans le domaine des télécommunications sans fil, où les techniques d'entrées et sorties multiples (MIMO, Multiple Input Multiple Output) sont déjà largement utilisées [Sal85, Sam02].

Le dernier phénomène de transport atypique que nous avons étudié apparaît lorsque le système possède un « point exceptionnel » (PE). Nous avons considéré un guide d'ondes quasi-unidimensionnel oscillant et possédant des pertes dépendant de la position et exploité un modèle simple basé sur un Hamiltonien non-Hermitien  $2 \times 2$  incluant ces points spéciaux. Dans ce système, deux modes de Bloch entourent un PE le long de leur propagation dans le guide. Notre dispositif exhibe un encerclement dynamique, ce qui mène à des transitions non-adiabatiques qui ont été observées expérimentalement en considérant la matrice de transmission  $T$  décrite dans la base des modes sinusoïdaux. Théoriquement, la diffusion de modes asymétriques, dépendant de la direction d'injection, est prédite et c'est exactement ce que nous obtenons expérimentalement. De plus, nous avons réalisé un encerclement paramétrique d'un PE en construisant 5 guides différents correspondant à 5 points sur la trajectoire continue qui encercle le PE étudié dynamiquement auparavant. Nous avons observé un saut d'un mode de Bloch à l'autre durant leur propagation.

---

Ce comportement est en accord parfait avec les résultats obtenus par différents groupes qui ont déjà réalisé un tel encerclement paramétrique d'un PE [[Dem01](#), [Dem04](#), [Ste04](#), [Lee09](#), [Cho10a](#)] (cf. chapitre 5).





# A *The Central Eigenstate for a Resonator Chain*

---

In this chapter we will prove that the state  $\Psi_k$  is an eigenstate of the Hamiltonian  $H_{i,j}$  describing a linear chain of  $N$  tight bound resonators, where  $N$  is an odd number.  $\Psi_c$  is defined as (see also equation (2.6)):

$$\Psi_c = \cos\left(\frac{l+1}{2}\pi\right) \quad \text{with } l = 1, 2, \dots, N \text{ with } N \in 2\mathbb{N} + 1, \quad (\text{A.1})$$

$$H_{i,j} = \nu\delta_{i,j} + \kappa(\delta_{i,j-1} + \delta_{i,j+1}) \quad \text{with } i, j = 1, 2, \dots, N. \quad (\text{A.2})$$

$\nu$  corresponds to the central frequency of a single resonator (dielectric disc) and  $\kappa$  describes the nearest neighbour coupling.

It is to show that  $H\Psi_c = \nu\Psi_c$  for a chain with an odd number of elements. In general it is:

$$z_l = \sum_{i=1}^N H_{l,i}\Psi_i = \left( \sum_i \nu\delta_{l,i} + \kappa(\delta_{l,i-1} + \delta_{l,i+1}) \right) \cos\left(\frac{l+1}{2}\pi\right). \quad (\text{A.3})$$

*Case 1:  $1 < l < N$*

$$\begin{aligned} z_l &= \nu\cos\left(\frac{l+1}{2}\pi\right) + \kappa\left(\cos\left(\frac{l+2}{2}\pi\right) + \cos\left(\frac{l}{2}\pi\right)\right) \\ &= \nu\cos\left(\frac{l+1}{2}\pi\right) + \kappa\left(-\cos\left(\frac{l}{2}\pi\right) + \cos\left(\frac{l}{2}\pi\right)\right) \\ &= \nu\Psi_c. \end{aligned}$$

*Case 2:  $l = 1$*

$$\begin{aligned} z_1 &= \nu\cos(\pi) + \kappa\left(\cos\left(\frac{3}{2}\pi\right)\right) \\ &= \nu\cos(\pi) = \nu\Psi_{c,l=1}. \end{aligned}$$

*Case 3:  $l = N$*

$$\begin{aligned} z_N &= \nu\cos\left(\frac{N+1}{2}\pi\right) + \kappa\left(\cos\left(\frac{N}{2}\pi\right)\right) \\ &\stackrel{N \text{ odd}}{=} \nu\cos\left(\frac{N+1}{2}\pi\right) = \nu\Psi_{c,l=N}. \end{aligned}$$

## Appendix A. The Central Eigenstate for a Resonator Chain

---

We proofed at this point that  $\Psi_c$  is an eigenstate of  $H$  with the eigenvalue of the central frequency  $\nu!$

In a next step we want to show that  $|\Psi_c|^2 = (N + 1)/2$ . This proof is done by induction.

For  $N = 5$   $\Psi_c$  is:

$$\sum_{i=1}^5 \left| \cos \left( \frac{i+1}{2} \pi \right) \right|^2 = 1 + 0 + 1 + 0 + 1 = 3 = \frac{5+1}{2}.$$

We assume that:

$$\sum_{i=1}^N \left| \cos \left( \frac{i+1}{2} \pi \right) \right|^2 = \frac{N+1}{2}.$$

For  $N+2$  (We investigate odd numbers):

$$\begin{aligned} \sum_{i=1}^{N+2} \left| \cos \left( \frac{i+1}{2} \pi \right) \right|^2 &= \sum_{i=1}^N \left| \cos \left( \frac{i+1}{2} \pi \right) \right|^2 \\ &+ \left| \cos \left( \frac{N+2}{2} \pi \right) \right|^2 \rightarrow 0 \\ &+ \left| \cos \left( \frac{N+3}{2} \pi \right) \right|^2 \rightarrow 1 \\ &= \frac{N+1}{2} + \frac{2}{2} = \frac{(N+2)+1}{2}. \end{aligned}$$

This means:

$$\Psi_c = \frac{1}{\sqrt{\frac{(N+1)}{2}}} \cos \left( \frac{l+1}{2} \pi \right). \quad (\text{A.4})$$

The amplitude of  $\Psi_c$  follows the pattern  $(1,0,-1,0,1,0,\dots)$ . It populates the edges of the chain and each second disc. Its eigenvalue corresponds to the central frequency of a single resonator.

# Bibliography

---

- [Ali16] M. Aliofkhazraei, N. Ali, W.I. Milne, C.S. Ozkan, S. Mitura, and J.L. Gervasoni: *Graphene Science Handbook: Electrical and Optical Properties*. CRC Press 2016.  
*1 citation on page 40*
- [Amb04] A. Ambainis: Quantum walks and their algorithmic applications. *International Journal of Quantum Information* **01**, 507–518 (2004).  
*3 citations: page 5, 11, and 29*
- [Amb12] Philipp Ambichl: *Delay Times and Beam-Like Scattering States in Coherent Wave Transmission Through Resonators*. Diploma Thesis, Technische Universität Wien 2012.  
*8 citations: page 6, 7, 12, 14, 49, 114, 115, and 117*
- [Ami16] L. V. Amitonova, A. Descloux, J. Petschulat, M. H. Frosz, G. Ahmed, F. Babic, X. Jiang, A. P. Mosk, P. S. J. Russell, and P. W. H. Pinkse: High-resolution wavefront shaping with a photonic crystal fiber for multimode fiber imaging. *Optics Letters* **41**, 497 (2016).  
*3 citations: page 6, 12, and 56*
- [Bal05] C.A. Balanis: *Antenna Theory: Analysis and Design*. John Wiley & Sons third edition 2005.  
*1 citation on page 66*
- [Bar10] Sonja Barkhofen: *Mikrowave Measurements on Graphene-like Structures*. Diploma Thesis, Philipps Universität Marburg 2010.  
*2 citations: page 33 and 35*
- [Bar13] S. Barkhofen, M. Bellec, U. Kuhl, and F. Mortessagne: Disordered graphene and boron nitride in a microwave tight-binding analog. *Physical Review B - Condensed Matter and Materials Physics* **87**, 035101 (2013).  
*6 citations: page 5, 11, 26, 28, 31, and 42*
- [Bel13a] M. Bellec, U. Kuhl, G. Montambaux, and F. Mortessagne: Tight-binding couplings in microwave artificial graphene. *Physical Review B* **88**, 115437 (2013).  
*10 citations: page 5, 11, 21, 26, 27, 28, 31, 37, 39, and 41*
- [Bel13b] M. Bellec, U. Kuhl, G. Montambaux, and F. Mortessagne: Topological Transition of Dirac Points in a Microwave Experiment. *Physical Review Letters* **110**, 033902 (2013).  
*3 citations: page 5, 11, and 28*

## Bibliography

---

- [Bel14] M. Bellec, U. Kuhl, G. Montambaux, and F. Mortessagne: [Manipulation of edge states in microwave artificial graphene](#). *New Journal of Physics* **16**, 113023 (2014).  
*5 citations: page 5, 11, 28, 31, and 41*
- [Ben11] C. Bena and L. Simon: [Dirac point metamorphosis from third-neighbor couplings in graphene and related materials](#). *Physical Review B* **83**, 115404 (2011).  
*1 citation on page 39*
- [Bla52] J.M. Blatt and V.F. Weisskopf: *Theoretical Nuclear Physics*. John Wiley & Sons 1952.  
*1 citation on page 21*
- [Ble75] N. Bleistein and R.A. Handelsman: *Asymptotic Expansions of Integrals*. Dover Books on Mathematics Series. Dover Publications 1975.  
*1 citation on page 113*
- [Bod09] J. D. Bodyfelt, M. C. Zheng, T. Kottos, U. Kuhl, and H.-J. Stöckmann: [Probing Localization in Absorbing Systems via Loschmidt Echos](#). *Physical Review Letters* **102**, 253901 (2009).  
*1 citation on page 58*
- [Boh51] D. Bohm: *Quantum Theory*. Dover books in science and mathematics. Prentice-Hall 1951.  
*3 citations: page 6, 12, and 48*
- [Böh15] J. Böhm, M. Bellec, F. Mortessagne, U. Kuhl, S. Barkhofen, S. Gehler, H.-J. Stöckmann, I. Foulger, S. Gnuzman, and G. Tanner: [Microwave Experiments Simulating Quantum Search and Directed Transport in Artificial Graphene](#). *Physical Review Letters* **114**, 110501 (2015).  
*3 citations: page 5, 11, and 45*
- [Böh16] J. Böhm and U. Kuhl: [Wave Front Shaping in Quasi-One-Dimensional Waveguides](#). *Accepted for publication* , arXiv:1607.01221 (2016).  
*3 citations: page 6, 12, and 86*
- [Bra16] Andre Brandstötter: *Wave Control in Complex Media: from System Design to Wave Front Shaping*. Diploma Thesis, Technische Universität Wien 2016.  
*12 citations: page 6, 12, 49, 52, 82, 83, 85, 114, 117, 128, 134, and 136*
- [Cao06] H. Cao: [Review on latest developments in random lasers with coherent feedback](#). *Journal of Physics A: Mathematical and General* **39**, 467–467 (2006).  
*1 citation on page 84*
- [Cas09] A. H. Castro Neto, F. Guinea, N. M R Peres, K. S. Novoselov, and A. K. Geim: [The electronic properties of graphene](#). *Reviews of Modern Physics* **81**, 109–162 (2009).  
*5 citations: page 5, 11, 29, 31, and 40*

- [Cha14] T. Chaigne, J. Gateau, O. Katz, E. Bossy, and S. Gigan: [Light focusing and two-dimensional imaging through scattering media using the photoacoustic transmission matrix with an ultrasound array](#). *Optics letters* **39**, 2664–7 (2014).  
3 citations: page 6, 12, and 56
- [Chi04] A. Childs and J. Goldstone: [Spatial search by quantum walk](#). *Physical Review A* **70**, 022314 (2004).  
3 citations: page 5, 11, and 31
- [Chi10] A. Childs: [On the Relationship Between Continuous- and Discrete-Time Quantum Walk](#). *Communications in Mathematical Physics* **294**, 581–603 (2010).  
1 citation on page 29
- [Cho10a] Y. Choi, S. Kang, S. Lim, W. Kim, J. R. Kim, J. H. Lee, and K. An: [Quasieigenstate Coalescence in an Atom-Cavity Quantum Composite](#). *Physical Review Letters* **104**, 153601 (2010).  
6 citations: page 7, 13, 90, 110, 134, and 137
- [Cho10b] Y. D. Chong, L. Ge, H. Cao, and A. D. Stone: [Coherent Perfect Absorbers: Time-Reversed Lasers](#). *Physical Review Letters* **105**, 053901 (2010).  
3 citations: page 6, 13, and 83
- [Coc09] E. Cochard, C. Prada, J. F. Aubry, and M. Fink: [Ultrasonic focusing through the ribs using the DORT method](#). *Medical Physics* **36**, 3495 (2009).  
1 citation on page 86
- [Dem01] C. Dembowski, H.-D. Gräf, H. L. Harney, A. Heine, W. D. Heiss, H. Rehfeld, and A. Richter: [Experimental Observation of the Topological Structure of Exceptional Points](#). *Physical Review Letters* **86**, 787–790 (2001).  
7 citations: page 7, 13, 90, 92, 110, 134, and 137
- [Dem04] C. Dembowski, B. Dietz, H.-D. Gräf, H. L. Harney, A. Heine, W. D. Heiss, and A. Richter: [Encircling an exceptional point](#). *Physical Review E* **69**, 056216 (2004).  
8 citations: page 7, 13, 90, 92, 108, 110, 134, and 137
- [Die10] Otto Dietz: *Transport in Quasi-One-Dimensional Systems*. Diploma Thesis, Philipps Universität Marburg 2010.  
1 citation on page 102
- [Die11] O. Dietz, U. Kuhl, H. J. Stöckmann, N. M. Makarov, and F. M. Izrailev: [Microwave realization of quasi-one-dimensional systems with correlated disorder](#). *Physical Review B - Condensed Matter and Materials Physics* **83**, 134203 (2011).  
1 citation on page 58

## Bibliography

---

- [Die12a] O. Dietz, U. Kuhl, J. C. Hernández-Herrejón, and L. Tessieri: [Transmission in waveguides with compositional and structural disorder: Experimental effects of disorder cross-correlations](#). *New Journal of Physics* **14**, 013048 (2012).  
*1 citation on page 58*
- [Die12b] O. Dietz, H. J. Stöckmann, U. Kuhl, F. M. Izrailev, N. M. Makarov, J. Doppler, F. Libisch, and S. Rotter: [Surface scattering and band gaps in rough waveguides and nanowires](#). *Physical Review B - Condensed Matter and Materials Physics* **86**, 201106 (2012).  
*1 citation on page 58*
- [Din16] K. Ding, G. Ma, M. Xiao, Z. Zhang, and C. Chan: [Emergence, Coalescence, and Topological Properties of Multiple Exceptional Points and Their Experimental Realization](#). *Physical Review X* **6**, 021007 (2016).  
*3 citations: page 7, 13, and 88*
- [Dop16a] J. Doppler, A. Mailybaev, J. Böhm, U. Kuhl, A. Girschik, F. Libisch, T. J. Milburn, P. Rabl, N. Moiseyev, and S. Rotter: [Dynamically encircling an exceptional point for asymmetric mode switching](#). *Nature* **537**, 76–79 (2016).  
*11 citations: page 7, 13, 88, 91, 97, 99, 105, 106, 107, 109, and 110*
- [Dop16b] Jörg Doppler. *Encircling of exceptional points: theory and applications*. Dissertation Technische Universität Wien 2016.  
*12 citations: page 7, 13, 88, 89, 90, 92, 94, 95, 96, 97, 99, and 100*
- [Dup15] M. Dupré, P. del Hougne, M. Fink, F. Lemoult, and G. Lerosey: [Wave-Field Shaping in Cavities: Waves Trapped in a Box with Controllable Boundaries](#). *Physical Review Letters* **115**, 017701 (2015).  
*3 citations: page 6, 12, and 56*
- [Ede05] G.F. Edelmann, H.C. Song, S Kim, W.S. Hodgkiss, W.A. Kuperman, and T Akal: [Underwater Acoustic Communications Using Time Reversal](#). *IEEE Journal of Oceanic Engineering* **30**, 852–864 (2005).  
*1 citation on page 86*
- [Eis48] Leonard Eisenbud. *The Formal Properties of Nuclear Collisions*. Dissertation Princeton University 1948.  
*3 citations: page 6, 12, and 48*
- [Fan05] S. Fan and J. M. Kahn: [Principal modes in multimode waveguides](#). *Optics letters* **30**, 135–137 (2005).  
*1 citation on page 50*
- [Fin92] M. Fink: [Time reversal of ultrasonic fields. I. Basic principles](#). *IEEE Transactions on Ultrasonics, Ferroelectrics and Frequency Control* **39**, 555–566 (1992).  
*2 citations: page 57 and 86*

- [Fon72] L. Fonda: [On the Connection between Particles and Poles of the S-Matrix](#). *Fortschritte der Physik* **20**, 135–144 (1972).  
1 citation on page 83
- [Fou14] I. Foulger, S. Gnutzmann, and G. Tanner: [Quantum Search on Graphene Lattices](#). *Physical Review Letters* **112**, 070504 (2014).  
8 citations: page 5, 11, 29, 31, 44, 45, 133, and 135
- [Fyo05] Y. V. Fyodorov, D. V. Savin, and H.-J. Sommers: [Scattering, reflection and impedance of waves in chaotic and disordered systems with absorption](#). *Journal of Physics A: Mathematical and General* **38**, 10731–10760 (2005).  
1 citation on page 19
- [Gao15] T. Gao, E. Estrecho, K. Y. Bliokh, T. C. H. Liew, M. D. Fraser, S. Brodbeck, M. Kamp, C. Schneider, S. Höfling, Y. Yamamoto, F. Nori, Y. S. Kivshar, A. G. Truscott, R. G. Dall, and E. A. Ostrovskaya: [Observation of non-Hermitian degeneracies in a chaotic exciton-polariton billiard](#). *Nature* **526**, 554–558 (2015).  
4 citations: page 7, 13, 88, and 108
- [Gér16] B. Gérardin, J. Laurent, P. Ambichl, C. Prada, S. Rotter, and A. Aubry: [Particle-like wave packets in complex scattering systems](#). *arXiv* , 1602.05812 (2016).  
1 citation on page 131
- [Gir16] A. Girschik, A. Brandstätter, P. Ambichl, and S. Rotter: [Control of Branched Flow in Optics](#). *in preperation* (2016).  
3 citations: page 6, 12, and 49
- [Gma10] C. F Gmachl: [Laser science: Suckers for light](#). *Nature* **467**, 37–39 (2010).  
3 citations: page 6, 13, and 83
- [Gro97] L. Grover, B. Labs, M. Avenue, and M. Hill: [Quantum Mechanics Helps in Searching for a Needle in a Haystack](#). *Physical Review Letters* **79**, 325–328 (1997).  
3 citations: page 5, 11, and 29
- [Gro02] L. Grover and A. M. Sengupta: [Classical analog of quantum search](#). *Physical Review A* **65**, 032319 (2002).  
4 citations: page 5, 11, 29, and 30
- [Hau89] E. H. Hauge and J. A. Støvneng: [Tunneling times: A critical review](#). *Reviews of Modern Physics* **61**, 917–936 (1989).  
5 citations: page 7, 14, 113, 114, and 115
- [Hei09] B. Hein and G. Tanner: [Wave Communication across Regular Lattices](#). *Physical Review Letters* **103**, 260501 (2009).  
3 citations: page 5, 11, and 30



## Bibliography

---

- [Hei12] W. D. Heiss: [The physics of exceptional points](#). *Journal of Physics A: Mathematical and Theoretical* **45**, 444016 (2012).  
*4 citations: page 7, 13, 88, and 89*
- [Hen04] B. E. Henty and D. D. Stancil: [Multipath-Enabled Super-Resolution for rf and Microwave Communication using Phase-Conjugate Arrays](#). *Physical Review Letters* **93**, 243904 (2004).  
*1 citation on page 56*
- [His13] T. Hisch, M. Liertzer, D. Pogany, F. Mintert, and S. Rotter: [Pump-Controlled Directional Light Emission from Random Lasers](#). *Physical Review Letters* **111**, 023902 (2013).  
*3 citations: page 6, 12, and 56*
- [Hor15] Roarke Horstmeyer, Haowen Ruan, and Changhui Yang: [Guidestar-assisted wavefront-shaping methods for focusing light into biological tissue](#). *Nature Photonics* **9**, 563–571 (2015).  
*3 citations: page 6, 12, and 56*
- [Hsu15] C. W. Hsu, A. Goetschy, Y. Bromberg, A. D. Stone, and H. Cao: [Broadband Coherent Enhancement of Transmission and Absorption in Disordered Media](#). *Physical Review Letters* **115**, 223901 (2015).  
*1 citation on page 74*
- [Ili09] I. Ilić, P. P. Beličev, V. Milanović, and J. Radovanović: [Modeling of dwell time and group delay in dispersive and absorptive media](#). *Physica Scripta* **T135**, 014040 (2009).  
*3 citations: page 7, 14, and 114*
- [Ive62] K.E. Iverson: [A programming language](#). Wiley 1962.  
*1 citation on page 63*
- [Jac98] J.D. Jackson: [Classical Electrodynamics](#). Wiley third edition 1998.  
*2 citations: page 17 and 26*
- [Jac06] P. Jacquod and R. S. Whitney: [Semiclassical theory of quantum chaotic transport: Phase-space splitting, coherent backscattering, and weak localization](#). *Physical Review B* **73**, 195115 (2006).  
*1 citation on page 117*
- [Jay09] S. Jayaraman: [Digital Image Processing](#). Tata McGraw Hill Education 2009.  
*1 citation on page 80*
- [Kai14] N. Kaina, M. Dupré, G. Lerosey, and M. Fink: [Shaping complex microwave fields in reverberating media with binary tunable metasurfaces](#). *Scientific Reports* **4**, 6693 (2014).  
*3 citations: page 6, 12, and 56*

- [Kat13] T. Kato: *Perturbation theory for linear operators*. Grundlehren der mathematischen Wissenschaften. Springer Berlin Heidelberg 2013.  
*1 citation on page 89*
- [Kec03] F. Keck, H. J. Korsch, and S. Mossmann: *Unfolding a diabolic point: a generalized crossing scenario*. *Journal of Physics A: Mathematical and General* **36**, 2125–2137 (2003).  
*3 citations: page 7, 13, and 90*
- [Kit53] C. Kittel: *Introduction to Solid State Physics*. John Wiley & Sons 1953.  
*2 citations: page 24 and 36*
- [Köb11] B. Köber, U. Kuhl, H.-J. Stöckmann, A. Goussev, and K. Richter: *Fidelity decay for local perturbations: Microwave evidence for oscillating decay exponents*. *Physical Review E* **83**, 016214 (2011).  
*1 citation on page 15*
- [Kuh13] U. Kuhl, O. Legrand, and F. Mortessagne: *Microwave experiments using open chaotic cavities in the realm of the effective Hamiltonian formalism*. *Fortschritte der Physik* **61**, 404–419 (2013).  
*1 citation on page 19*
- [Kun11] R. Kundu: *Tight-Binding Parameters for Graphene*. *Modern Physics Letters B* **25**, 163–173 (2011).  
*1 citation on page 39*
- [Lee09] S. Lee, J. Yang, S. Moon, S. Lee, J. Shim, S. W. Kim, J. Lee, and K. An: *Observation of an Exceptional Point in a Chaotic Optical Microcavity*. *Physical Review Letters* **103**, 134101 (2009).  
*7 citations: page 7, 13, 90, 108, 110, 134, and 137*
- [Ler04] G. Lerosey, J. de Rosny, A. Tourin, A. Derode, G. Montaldo, and M. Fink: *Time Reversal of Electromagnetic Waves*. *Physical Review Letters* **92**, 193904 (2004).  
*2 citations: page 57 and 86*
- [Lin10] Y.-M. Lin, C. Dimitrakopoulos, K. A. Jenkins, D. B. Farmer, H.-Y. Chiu, A. Grill, and P. Avouris: *100-GHz Transistors from Wafer-Scale Epitaxial Graphene*. *Science* **327**, 662–662 (2010).  
*1 citation on page 40*
- [Mai05] A. A. Mailybaev, O. N. Kirillov, and A. P. Seyranian: *Geometric phase around exceptional points*. *Physical Review A* **72**, 014104 (2005).  
*3 citations: page 7, 13, and 90*
- [Mil15] T. J. Milburn, J. Doppler, C. A. Holmes, S. Portolan, S. Rotter, and P. Rabl: *General description of quasiadiabatic dynamical phenomena near exceptional points*. *Physical Review A* **92**, 052124 (2015).  
*3 citations: page 7, 13, and 88*

## Bibliography

---

- [Moi11] N. Moiseyev: *Non-Hermitian Quantum Mechanics*. Cambridge University Press 2011.  
*4 citations: page 7, 13, 88, and 89*
- [Mos12] A. P. Mosk, A. Legendijk, G. Lerosey, and M. Fink: *Controlling waves in space and time for imaging and focusing in complex media*. *Nature Photonics* **6**, 283–292 (2012).  
*3 citations: page 6, 12, and 56*
- [Nix13] M. Nixon, O. Katz, E. Small, Y. Bromberg, A. a. Friesem, Y. Silberberg, and N. Davidson: *Real-time wavefront shaping through scattering media by all-optical feedback*. *Nature Photonics* **7**, 919–924 (2013).  
*3 citations: page 6, 12, and 56*
- [Nov04] K. S. Novoselov, A. K. Geim, S. V. Morozov, D. Jiang, Y. Zhang, S. V. Dubonos, I. V. Grigorieva, and A. A. Firsov: *Electric Field Effect in Atomically Thin Carbon Films*. *Science* **306**, 666–669 (2004).  
*1 citation on page 40*
- [Pol15] C. Poli, M. Bellec, U. Kuhl, F. Mortessagne, and H. Schomerus: *Selective enhancement of topologically induced interface states in a dielectric resonator chain*. *Nature Communications* **6**, 6710 (2015).  
*3 citations: page 5, 11, and 28*
- [Pop10] S. M. Popoff, G. Lerosey, R. Carminati, M. Fink, a. C. Boccara, and S. Gigan: *Measuring the transmission matrix in optics: An approach to the study and control of light propagation in disordered media*. *Physical Review Letters* **104**, 100601 (2010).  
*2 citations: page 6 and 12*
- [Por13] R. Portugal: *Quantum Walks and Search Algorithms*. Quantum Science and Technology. Springer New York 2013.  
*3 citations: page 5, 11, and 29*
- [Pre92] W.H. Press, B.P. Flannery, S.A. Teukolsky, and W.T. Vetterling: *Numerical Recipes in FORTRAN: The Art of Scientific Computing*. Cambridge University Press second edition 1992.  
*1 citation on page 80*
- [Ral98] G.G. Raleigh and J.M. Cioffi: *Spatio-temporal coding for wireless communication*. *IEEE Transactions on Communications* **46**, 357–366 (1998).  
*1 citation on page 86*
- [Roh94] J. W. Rohlf: *Modern Physics from a to Z0*. Wiley 1994.  
*1 citation on page 40*
- [Rot09] I. Rotter: *A non-Hermitian Hamilton operator and the physics of open quantum systems*. *Journal of Physics A: Mathematical and Theoretical* **42**, 153001 (2009).  
*3 citations: page 7, 13, and 88*

- [Rot11] S. Rotter, P. Ambichl, and F. Libisch: [Generating particlelike scattering states in wave transport](#). *Physical Review Letters* **106**, 120602 (2011).  
6 citations: page 7, 14, 48, 115, 116, and 117
- [Sal85] J. Salz: [Digital Transmission Over Cross-Coupled Linear Channels](#). *AT&T Technical Journal* **64**, 1147–1159 (1985).  
3 citations: page 132, 134, and 136
- [Sam02] H. Sampath, S. Talwar, J. Tellado, V. Erceg, and A. Paulraj: [A fourth-generation MIMO-OFDM broadband wireless system: design, performance, and field trial results](#). *IEEE Communications Magazine* **40**, 143–149 (2002).  
3 citations: page 132, 134, and 136
- [Sav06] D. V. Savin, O. Legrand, and F. Mortessagne: [Inhomogeneous losses and complexness of wave functions in chaotic cavities](#). *Europhysics Letters* **76**, 774–779 (2006).  
1 citation on page 19
- [Sch05] R. Schäfer, H.-J. Stöckmann, T. Gorin, and T. H. Seligman: [Experimental Verification of Fidelity Decay: From Perturbative to Fermi Golden Rule Regime](#). *Physical Review Letters* **95**, 184102 (2005).  
1 citation on page 15
- [Sch10] A. Schreiber, K. N. Cassemiro, V. Potoček, A. Gábris, P. J. Mosley, E. Andersson, I. Jex, and C. Silberhorn: [Photons Walking the Line: A Quantum Walk with Adjustable Coin Operations](#). *Physical Review Letters* **104**, 050502 (2010).  
1 citation on page 29
- [Sch12] A. Schreiber, A. Gábris, P. P. Rohde, K. Laiho, M. Stefanak, V. Potoček, C. Hamilton, I. Jex, and C. Silberhorn: [A 2D Quantum Walk Simulation of Two-Particle Dynamics](#). *Science* **336**, 55–58 (2012).  
1 citation on page 29
- [Sil03] P. Silvestrov, M. Goorden, and C. Beenakker: [Noiseless scattering states in a chaotic cavity](#). *Physical Review B* **67**, 241301 (2003).  
5 citations: page 7, 14, 54, 116, and 117
- [Sin01] J. Singleton: [Band Theory and Electronic Properties of Solids](#). Oxford Master Series in Condensed Matter Physics. OUP Oxford 2001.  
1 citation on page 24
- [Sir00] L. Sirko, S. Bauch, Y. Hlushchuk, P. M. Koch, R. Blümel, M. Barth, U. Kuhl, and H.-J. Stöckmann: [Observation of dynamical localization in a rough microwave cavity](#). *Physics Letters A* **266**, 331–335 (2000).  
1 citation on page 15

## Bibliography

---

- [Sit71] A. G. Sitenko and P. J. Shepherd: *Lectures in Scattering Theory: International Series of Monographs in Natural Philosophy*. International series of monographs in natural philosophy. Elsevier Science 1971.  
*1 citation on page 83*
- [Sla54] J. C. Slater and G. F. Koster: Simplified LCAO Method for the Periodic Potential Problem. *Physical Review* **94**, 1498–1524 (1954).  
*3 citations: page 5, 11, and 24*
- [Smi60] F. T. Smith: Lifetime matrix in collision theory. *Physical Review* **118**, 349–356 (1960).  
*3 citations: page 6, 12, and 48*
- [Ste95] J. Stein, H.-J. Stöckmann, and U. Stoffregen: Microwave Studies of Billiard Green Functions and Propagators. *Physical Review Letters* **75**, 53–56 (1995).  
*2 citations: page 15 and 21*
- [Ste04] T. Stehmann, W. D. Heiss, and F. G. Scholtz: Observation of exceptional points in electronic circuits. *Journal of Physics A: Mathematical and General* **37**, 7813–7819 (2004).  
*6 citations: page 7, 13, 90, 110, 134, and 137*
- [Stö90] H.-J. Stöckmann and J. Stein: “Quantum” chaos in billiards studied by microwave absorption. *Physical Review Letters* **64**, 2215–2218 (1990).  
*2 citations: page 15 and 21*
- [Stö99] H.-J. Stöckmann: *Quantum Chaos - An Introduction*. Cambridge University Press 1999.  
*3 citations: page 20, 21, and 40*
- [Tay05] J.R. Taylor: *Classical Mechanics*. University Science Books 2005.  
*1 citation on page 24*
- [Tud08] T. Tudorovskiy, R. Höhmann, U. Kuhl, and H.-J. Stöckmann: On the theory of cavities with point-like perturbations: part I. General theory. *Journal of Physics A: Mathematical and Theoretical* **41**, 275101 (2008).  
*1 citation on page 62*
- [Two03] J. Tworzydło, A. Tajic, H. Schomerus, and C. W. J. Beenakker: Dynamical model for the quantum-to-classical crossover of shot noise. *Physical Review B* **68**, 115313 (2003).  
*4 citations: page 7, 14, 54, and 116*
- [Uzd11] R. Uzdin, A. Mailybaev, and N. Moiseyev: On the observability and asymmetry of adiabatic state flips generated by exceptional points. *Journal of Physics A: Mathematical and Theoretical* **44**, 435302 (2011).  
*6 citations: page 7, 13, 88, 91, 97, and 110*

- 
- [Vel07] I. M. Vellekoop and A. P. Mosk: [Focusing coherent light through opaque strongly scattering media](#). *Optics letters* **32**, 2309–2311 (2007).  
*3 citations: page 6, 12, and 56*
- [Vel08] I. M. Vellekoop and A. P. Mosk: [Universal Optimal Transmission of Light Through Disordered Materials](#). *Physical Review Letters* **101**, 120601 (2008).  
*2 citations: page 6 and 12*
- [Vel10] I. M. Vellekoop, A. Lagendijk, and A. P. Mosk: [Exploiting disorder for perfect focusing](#). *Nature Photonics* **4**, 320–322 (2010).  
*1 citation on page 56*
- [Vig16] P. Vignolo, M. Bellec, J. Böhm, A. E. Camara, J. Gambaudo, U. Kuhl, and F. Mortessagne: [Energy landscape in a Penrose tiling](#). *Physical Review B* **93**, 075141 (2016).  
*4 citations: page 5, 11, 28, and 45*
- [Wal47] P. R. Wallace: [The Band Theory of Graphite](#). *Physical Review* **71**, 622–634 (1947).  
*3 citations: page 5, 11, and 24*
- [Wan11] W. Wan, Y. Chong, L. Ge, H. Noh, A. D. Stone, and H. Cao: [Time-Reversed Lasing and Interferometric Control of Absorption](#). *Science* **331**, 889–892 (2011).  
*3 citations: page 6, 13, and 84*
- [Wie08] D. S. Wiersma: [The physics and applications of random lasers](#). *Nature Physics* **4**, 359–367 (2008).  
*1 citation on page 84*
- [Wig55] E. P. Wigner: [Lower limit for the energy derivative of the scattering phase shift](#). *Physical Review* **98**, 145–147 (1955).  
*3 citations: page 6, 12, and 48*
- [Win03a] H. G. Winful: [Delay Time and the Hartman Effect in Quantum Tunneling](#). *Physical Review Letters* **91**, 260401 (2003).  
*4 citations: page 7, 14, 114, and 115*
- [Win03b] H. G. Winful: [Group delay, stored energy, and the tunneling of evanescent electromagnetic waves](#). *Physical Review E* **68**, 016615 (2003).  
*4 citations: page 7, 14, 114, and 115*
- [Xio16] W. Xiong, P. Ambichl, Y. Bromberg, S. Rotter, and H. Cao: [Spatio-temporal Control of Light Transmission through a Multimode Fiber with Strong Mode Coupling](#). *arXiv* , 1601.04646 (2016).  
*1 citation on page 86*

- [Xu16] H. Xu, D. Mason, L. Jiang, and J. G. E. Harris: [Topological energy transfer in an optomechanical system with exceptional points](#). *arXiv* , 1602.06881 (2016).

*3 citations: page 7, 13, and 88*

## Abstract

Transport of waves plays an important role in modern communication systems like Wi-Fi or optical fibres. Typical problems in such systems concern security against possible intruders, energy consumption, time efficiency and the possibility of mode filtering. Microwave experiments are suited to study this kind of problems, because they offer a good control of the experimental parameters like sub-wavelength precision or phase and amplitude adjustment of the signals. Thus we can implement the method of wave shaping to investigate atypical transport phenomena, which address the mentioned problems.

Wave front shaping solely based on the transmission together with the Wigner-Smith time delay formalism allows me to establish special scattering states in situ. These scattering states avoid a pre-selected region, focus on a specific spot or follow trajectories of classical particles, so called particle-like scattering states. Energy efficient transport and avoiding possible intruders are the most interesting features of these states.

Mode filtering is induced inside a waveguide with wavy boundaries and position dependent loss. The boundary profiles are chosen in such a way that the two propagating modes describe an encircling of an exceptional point in the Bloch picture. The asymmetric mode filtering is found due to the non-adiabatic transitions occurring during this encircling. This is the first experimental realisation of a dynamical encircling of an exceptional point.

Another part of my work deals with Grover's quantum search. I put such a search into practice in a two-dimensional graphene-lattice using coupled resonators, which form a tight-binding analogue. In this proof of principle experiment we search for different resonators attached to the graphene-lattice. Changing the transmission direction of the signal according to the initially shaped wave can be seen as a graphene based switch. Furthermore, the scaling behaviour of the quantum search is quantified for a linear chain of resonators.



## Résumé

Le transport des ondes joue un rôle majeur dans les systèmes modernes de communication comme le Wifi ou les fibres optiques. Les principaux problèmes rencontrés dans ces systèmes concernent la protection contre les intrusions, la consommation d'énergie, la rapidité de traitement et le filtrage modal. Les expériences menées dans le domaine des micro-ondes sont particulièrement bien adaptées pour aborder ces situations. Elles offrent, en effet, un excellent contrôle des paramètres expérimentaux, notamment une précision inférieure à la longueur d'onde sur la géométrie du système et un ajustement précis de l'amplitude et de la phase du signal. Nous proposons ainsi dans cette thèse différentes expériences micro-ondes mettant toutes en œuvre une mise en forme des ondes, pour traiter les problèmes identifiés plus haut.

Dans une cavité micro-ondes, des états de diffusion particuliers sont générés en s'appuyant uniquement sur des mesures de transmission et sur le formalisme du temps de retard de Wigner-Smith. Ces états sont capables d'éviter une région déterminée de la cavité, de se concentrer sur un point particulier, ou de suivre une trajectoire typique d'une particule classique. Tous ces états présentent un avantage certain en matière de sécurité et de transport efficace de l'énergie.

Le filtrage de mode est mis en œuvre dans un guide d'ondes aux frontières ondulées et en présence de pertes dépendant de la position. Le profil du guide est choisi de façon à ce que les deux modes qui se propagent encerclent un point exceptionnel dans l'espace des états de Bloch. Cette trajectoire s'accompagne d'une transition non-adiabatique entre les deux modes et d'un filtrage asymétrique de ces modes. Ce travail constitue la première réalisation expérimentale de l'encerclement dynamique d'un point critique.

La thèse présente également des travaux liés à la problématique des algorithmes de « recherche quantique », notamment l'algorithme de Grover. Cette recherche est mise en œuvre dans un réseau en nid d'abeilles de résonateurs micro-ondes couplés, bien décrits par un modèle de liaisons fortes (le système constitue un analogue micro-ondes du graphène). Une expérience de preuve de principe propose la recherche de deux résonateurs distincts reliés au réseau. Selon son façonnage initial, le signal envoyé dans le réseau peut s'orienter vers l'un ou l'autre des résonateurs cibles ; les propriétés particulières de transport du graphène sont exploitées pour créer un commutateur. La loi d'échelle attendue pour un algorithme de Grover est expérimentalement obtenue dans une chaîne linéaire.

